Synthesis and Investigation of Multi-Phase DNA Microspheres

Karuna Skipper

A thesis submitted to The University of Sydney
in fulfilment of the requirements for the degree of
Doctor of Philosophy

School of Chemistry
Faculty of Science
The University of Sydney
Australia
September 2025

Supervisor: Dr. Shelley Wickham

Co-Supervisor: Dr. Anna Waterhouse

Statement of Originality

This is to certify that the content of this thesis is my own work. This thesis has not been submitted for any other degree or purpose.

I certify that the intellectual content of this thesis is the product of my own work, and that all assistance received in preparing this thesis and all sources have been acknowledged.

Karuna Skipper

27 May 2025

Abstract

Synthetic cells have potential use as platforms to investigate cellular machinery, micro-reactors, or drug-delivery vehicles. These may be formed from a variety of top-down or bottom-up synthesis methods. Of particular interest is the process of liquid-liquid phase separation (LLPS), a mechanism by which dissolved solutes spontaneously condense together to form liquid droplets in a larger liquid solution. LLPS can be applied to DNA nanotechnology, a field which sees the synthesis of nano- to micro-scale structures through rational design. Nanostars, comprised of a discrete number of partially complimentary DNA oligonucleotides, self-assemble into micro-scale coacervate droplets through temperature annealed LLPS.

This thesis presents a new method for the formation of DNA nanostar (NS) synthetic cells, with chemically and structurally distinct core and shell regions. First, modifications to the physical structure of nanostars were investigated. The inter-related effects of NS size, shape, inter-star binding strength, and environmental conditions on coacervate properties were investigated. A method for the experimental determination of NS phase-separation temperature was presented.

Orthogonal nanostars were combined in solution and shown to form distinct populations of coacervates. Selective modification of one NS population to induce limited interaction with the other resulted in increasing interfacial contact. The degree of contact or co-localisation was dependent on the energy profiles of each nanostar and

the strength of inter-phase complementarity. Techniques for the prediction and formation of patchy, two-layer, and three-layer coacervates were presented, with each phase consisting of distinct nanostars. Results showed that the majority of experimental micro-architectures aligned with predictions. Effects of key NS variables on the resulting coacervate micro-architecture were investigated.

Differences in nanostar design allowed for control over the physical properties of the micro-scale coacervates. The encapsulation of a nanostar droplet in a two-layer core-shell system was shown to prevent core fusion over time at elevated temperatures. The targeted capture of cargo in multi-phase coacervates was demonstrated, using ssDNA-functionalised biomolecules. The location and degree of capture was controlled through the selective functionalisation of the cargo, along with selective release of cargo through toehold-mediated strand displacement reactions. The shell of a core-shell coacervate was shown to selectively prevent the infiltration of core-targeted cargo, acting as a switchable filter. Finally, proof-of concept designs were presented for the dynamic switching of cargo compartmentalisation and coacervate micro-architecture.

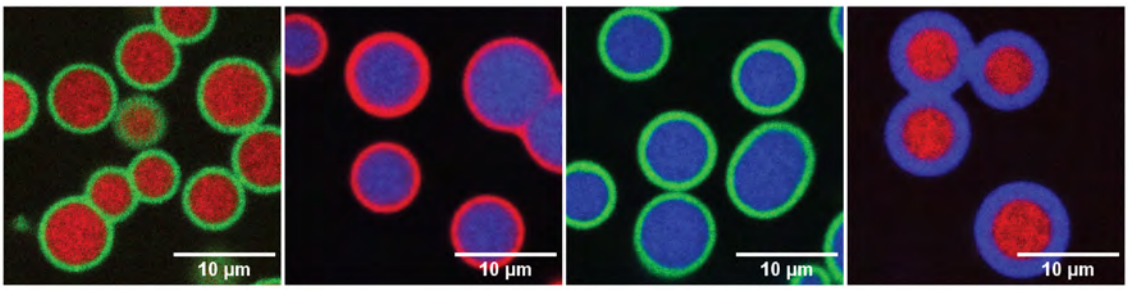

Figure 1: A technique was developed for the production of core-shell coacervates, through the staggered phase separation of DNA nanostars.

Statement of Contribution

Project design and data interpretation throughout this Thesis were performed with insight and feedback from Associate Professor Shelley Wickham and Associate Professor Anna Waterhouse.

In Chapter 2, **Dr Minh Tri Luu** and **JB Chen** assisted in designing and implementing the oxDNA simulations in section 2.4. **Dr Bradley Harding** assisted in conducting the PAGE experiment in figure 2.3. **Dr Toby Passioura** gave insight when designing qPCR experiments in section 2.6.

In Chapter 3, **Zach Martin** provided assistance in data analysis and statistical interpretation in sections 3.4 and 3.5.4.

In Chapter 4, **Dr Bradley Harding** and **Dr Taylor Szyszka** assisted in conducting the PAGE experiment in figure 4.22, and the plate reader experiment in figure 4.4.

In Chapter 5, **Byunghwa Kang** and **Eli Kengmana** provided assistance in understanding the T7 polymerase strand displacement reaction in section 5.2.3. **Sally Gao** and **Dr Tiffany Goh** assisted in designing and testing proof-of-concept microfluidic experiments in the same section.

I designed and conducted all other experimental work described. No generative AI or LLMs were used at any point during this work. The Thesis was written with structural and editorial feedback from **Associate Professor Shelley Wickham, Associate Professor Anna Waterhouse, Rita Skipper, Zach Martin, Dr Qianyi Zhang, Dr Bradley Harding, Sreelakshmi Meppat, Brandon de Moraes**, and **Alisha Skipper**.

Acknowledgements

I acknowledge the Gadigal people of the Eora Nation as the Traditional Owners and Custodians of the land where this was research conducted, and I pay respects to their Elders past, present and emerging.

There are multiple organisations who generously funded or provided aid during my PhD candidature. This research was supported by an Australian Government Research Training Program (RTP) Scholarship. My personal stipend was provided by the L E R Tonnet and Family Scholarship in Chemistry. My work was funded by ARC grant DP220101528. I additionally received support from the University of Sydney Nano Institute, the School of Chemistry, the Sydney University Graduates Union of North America, the International Society for Nanoscale Science, Computation, and Engineering, and the University of Sydney itself.

I would like to acknowledge the Australian Centre of Microscopy and Microanalysis (ACMM) at the University of Sydney for their microscopy facility and training. In particular, I thank **Dr Yingying Su** and **Dr Neftali Flores-Rodriguez** for all their assistance and support. Furthermore, I thank Sydney Analytical for use of their equipment and resources, and for the indispensable advice provided by **Dr Toby Passioura**.

Now, onto the emotions. There are certain people without whom this thesis would

not exist. Despite being the one whose name is on the cover, I was perhaps the least vital individual involved in the process.

First, foremost, and forever: my supervisor, **Associate Professor Shelley Wickham**. Your support and guidance have allowed me to grow as a scientist and as a person. You allowed me to pursue any esoteric thought that came to mind, allowing my research to develop far beyond anything I could have imagined; you pushed me to take so many academic and professional opportunities, letting me learn and grow outside of the lab; and when I would go off the deep end, you would hit me with a required dose of sanity. Thank you.

My thanks also go to my co-supervisor **Associate Professor Anna Waterhouse**, for allowing me to take part in this project. Particularly in the early years of my candidature, you and your group were vital to my development as a researcher. You always brought a fresh, insightful perspective to any question or problem I may have posed. Thank you very much for your continuous support and goodwill.

During my candidature, I was able to spend two months at Johns Hopkins University in the lab of **Associate Professor Rebecca Schulman.** Thank you so much for the incredible opportunity, and all the support you provided.

Next to science, my second great passion is science communication. Luckily enough, I was able to work with the incomparable **Professor Alice Motion** in all number of outreach and education projects. These were some of my most memorable times in Sydney, and you truly helped me develop vital skills.

In the same vein, thank you to all of my students and mentees. It is true when they say you never learn so much as when you are trying to teach.

There are countless lab-mates and science friends without whom university life would have been unbearable. **Bradley, Eli, Felicia, Gut, Jas, Johnathan, Kanako,**

Lachlan, Minh, Rezwan, Sally, Sheena, Sree, Taylor, Tiffany. Have I forgotten anyone? That would be embarrassing. Thank you for the help, the support, the tears.

My first year in Sydney - thank you, covid - I didn't know a single person. This made me desperate enough to sign up to a silly little theatre group. I am not and shall never be a thespian. It was still the best mistake of my life. Thank you for the laughs, the memories, the lifelong friendships. Thank you for reminding me there is life outside of work; for the games; for eating my baked goods. I love you all.

The rat pack. Do you remember why we are called that? I was so desperate to see you that I considered orchestrating a heist for rapid antigen tests, to barter my way across the border. You played every possible role: distraction, entertainment, sounding-board, therapist, philosopher. Beloved friends. Do you know what you'll be playing next? Soon? Please?

Finally, my family. **Alisha, Andrew, Rita, Rupert.** It is not an exaggeration to say I could not have done this without you. Each one of you deserves a lifetime of thanks for all you have done, and I shall spend my life trying to give it. For the big things, yes, the incredible, undeserved support and love. But for the small things, too. Keeping me company on my midnight walks home. Conversations of nonsense noises. Tarot reading. Supporting my worthwhile insanities and putting a stop to the worthless ones. Thank you, thank you, thank you. I love you.

Contents

List of Figures

List of Tables

List of Terms

Nanostar variables

J_{nt}	Number of unpaired bases at the central junction
R_{nt}	Number of unpaired bases at the arm terminus
SE_L	Sticky end length in nt
SE_{GC}	Percentage of GC nucleotides in a sticky end
%C	Degree of complementarity between two nanostar populations
Geometry, G	The length of a NS arm between central junction and terminus
NS	Nanostar
s-Star	Surfactant star
SE	Sticky ends
Tetravalent	Nanostar with $f = 4$ arms
Trivalent	Nanostar with $f = 3$ arms
Valency, f	The number of arms of a nanostar

General definitions

bp	Base pairs

dsDNA	Double-stranded DNA
HCA	Hybridisation curve analysis
HJ	Holliday Junction
LLPS	Liquid-liquid phase separation
MCA	Melt curve analysis
nt	Nucleotides
SA	Streptavidin
ssDNA	Single-stranded DNA
TMSD	Toehold mediated strand-displacement reaction

Temperature terms

ΔT	Annealing rate in ^{o}C/min
ΔT_{PS}	Difference in phase separation temperature between two nanostars
T_E	Evaporation temperature of a nanostar condensate
T_g	Gelation temperature of a nanostar condensate
T_M	Computationally determined melting temperature of a DNA sequence
T_{Hy}	Hybridisation temperature of an individual nanostar
T_{PS}	Phase separation temperature of a nanostar condensate

Chapter 1

Introduction

1.1 Motivation for developing DNA coacervates as synthetic cells

Self-assembly is a key facet of molecular, cellular, and materials sciences. The spontaneous formation of ordered assemblies, from the complexation of ligand and receptor to the arrangement of polymeric crystals, is vital to a range of natural and synthetic technologies [1] [2]. In a biological context, innumerable cellular structures assemble in a bottom-up manner without external direction or instruction, relying solely upon complex combinations of inherent physical properties. For instance, phospholipid membranes and polypeptides use hydrophilic and -phobic partitioning, while molecular machines and protein aggregates use non-covalent bonds and pi-pi stacking [3] [4] [5].

Similar principles have been leveraged in the creation of synthetic structures, such as polymer nanoparticles used in optics, electronics, and bioimaging [6] [7] [8]. However, these synthetic structures cannot yet approach the level of complexity seen in

the biological realm, with self-directed organisation occurring from the molecular to the macro scales. Biological systems exist outside of thermodynamic equilibrium, possessing components constantly in a state of chemical flux or change. Replication of such unstable systems is difficult, with most synthetic structures instead proceeding to a thermodynamic minimum. Trapping synthetic systems through kinetic control is thus desired.

Biological systems self-assemble structural, organisational, and functional components. It is a central aim of synthetic biology to replicate such systems. This would allow for deepened understanding of these mechanisms, by removing the inherent complexity of the *in vivo* context and focusing on a single form of interaction at a given time. Furthermore, the study and imitation of biomolecule self-assemblies allows for the creation of ever more intricate micro- and nanostructures and molecular technologies.

DNA, the genetic material of life, is a uniquely programmable polymer material. The same properties that allow it to act as the cellular information carrier – chemical stability, programmable sequence, and reliable replication – make it an ideal candidate for building self-assembling materials [9] [10]. Through leveraging the base-pairing specificity of nucleic acids, nanostructures have been created for a range of investigative and practical applications: molecular microscopy, drug delivery, and material templating [11] [12] [13] [14]. The specificity of the base-pairing mechanism allows for nano-scale precision when designing synthetic structures, and allows for location-specific binding of cargo molecules through DNA-functionalisation.

Furthermore, beyond the synthesis of individual DNA nanoparticles, it is possible to design self-assembling DNA nanostructures that then assemble amongst themselves into higher-order microscale structures [15] [16] [17] [18] [19]. For instance, a cellular process that has garnered significant interest in recent years is the formation

of membraneless organelles, liquid coacervates of highly concentrated proteins and nucleic acids [1]. Studies of such systems – responsible for processes from carbon fixation to apoptosis – suggest several required features, including protein disorder and complexity, multivalency, solution concentration, and specific environmental conditions [5] [20] [21]. Reproducing the formation of similar micro-scale coacervates using DNA nanostructures allows for the comprehensive investigation of each of these features in isolation. In synthetic DNA systems, each parameter can be individually replicated in a manner impossible to achieve in a protein system, due to the unique programmability of nucleic acids.

Protein coacervates are thought to concentrate enzymes and reagents into close proximity, modulating the rate of cellular reactions. Synthetic versions of such structures, created through rational design, would allow the creation of novel bioreactors to enhance or control the rate of chosen chemical processes. If multiple coacervates were combined into a larger super-structures, discrete reactions could be linked in a self-directing circuit [22] [23]. DNA nanostructures are eminently suitable for such a task, as the functionalisation of biomolecules to selectively localise with particular nucleic acid sequences is relatively straightforward [24] [25].

In practice, the creation of liquid coacervates using DNA nanostructures results in nano- to micro-scale spheres, the latter of which are studied as synthetic cells. In this case, instead of modelling subcellular behaviour, DNA nanostructure coacervates are used to replicate the cellular structure itself – a large liquid body which creates a unique chemical environment for its internal contents, sometimes separated into distinct layers or compartments. These may variously be used to mimic cellular functions or study cellular structures, for which the ability to impart higher-order complexity is vital. In its most basic form, a synthetic cell must consist of an outer boundary separating a unique internal environment from the broader solution [26].

A fundamental characteristic of both cells and cellular organisation is their controlled stability over time in a complex environment. However, a limitation of DNA-based coacervate systems is their tendency towards fusion. While cellular coacervates maintain their size and structure until externally directed, indicating a level of physical stability, DNA coacervates are seen to fuse over time [27] [28]. Here we attempt to address this limitation by implementing a kinetic trap to capture coacervate droplets within an outer boundary or 'shell' to increase stability by preventing fusion.

Methods for making core-shell DNA coacervates exist, but have limitations - a key one is reliance on non DNA-DNA interactions. To address this gap, this thesis focuses on the formation of layered synthetic cells from simple, self-assembling DNA nanostructures in an aqueous environment, relying only on defined DNA base-pairing as the assembly mechanism. The outer layer is proposed as a boundary between adjacent inner cores, maintaining the separation of chemically and physically distinct regions.

This thesis presents a comprehensive investigation of self-assembling DNA nanostructures, *nanostars*, that undergo phase separation to form coacervates under appropriate environmental conditions [29] [30] [31]. The overall aim is the creation of layered coacervates through staggered phase separation, achieved through rational design of DNA nanostar structure and sequence. It is envisioned that this will result in areas of controllable physical and chemical identities, which allow for long-term stability of liquid coacervates, selective cargo capture of biomolecules, and structural switching for mimicry of cellular behaviours.

This thesis seeks to understand the fundamental interactions and properties of DNA coacervates, and to develop methods to design and predict the self-assembly of new nano- and micro-structures. These results may be expanded beyond the phase-

separation of DNA nanostars to engineer self-assembling liquids on a broader scale.

The remaining sections of Chapter 1 include an overview of current research in synthetic cells, providing insight into the motivations behind this work (section 1.3); the theory and principles of phase separation, particularly liquid-liquid phase separation (section 1.4); and the key aspects of nucleic acid nanotechnology upon which this research is based (section 1.5). A literature review of phase-separated nucleic acid coacervates and DNA nanostar coacervates is provided (section 1.6), highlighting the history, function, and design considerations of these structures. These particular features are emphasised as they form the basis of the experimental work conducted in this thesis. Finally, the specific research questions of this thesis are outlined and the thesis structure established (section 1.7).

1.2 Cells in nature

The basic unit of living organisms, the cell, exists in a staggering variety of phenotypes. Even within a single organism, genetically identical cells exhibit vast differences in size, structure, and appearance, depending on their intended function. These differences are not arbitrary – the physical form of cells is intrinsically linked to their biological purpose, and any deviation from their basic structure may inhibit their ability to perform their function. This connection between form and function is a basic tenet of biological research, with new links between the physical structure and biological purpose of cellular subunits constantly being found.

Cellular mechanisms behaving appropriately is a key aspect of homeostasis, the maintenance of a stable internal environment. This does not, however, imply a need for stasis, an unchanging internal environment. Leukocytes are a key component of the body's immune defence system (figure 1.1). When travelling through the blood, they may be signalled to attach to the wall of the blood vessel. From here, they pass through the endothelium in order to reach an area of inflammation or infection [32]. A key step in this process is a change in the leukocyte's cytoskeleton, giving it a flat, amoeba-like structure with the ability to crawl along and through the vascular endothelium [33]. This process, vital for the functioning of the immune system, involves a complex series of intra- and intercellular signals and mechanical changes in membrane and structural proteins. Slight changes at different points of these signal cascades have the ability to disrupt the immune process entirely [34]. Complete understanding of this signal cascade is important for the treatment and prevention of disease.

Of particular importance to this thesis is the cell's ability to isolate chemical reactions in a confined environment. The compartmentalisation of reagents allows for the production of specialised reaction chambers with tailored chemical conditions,

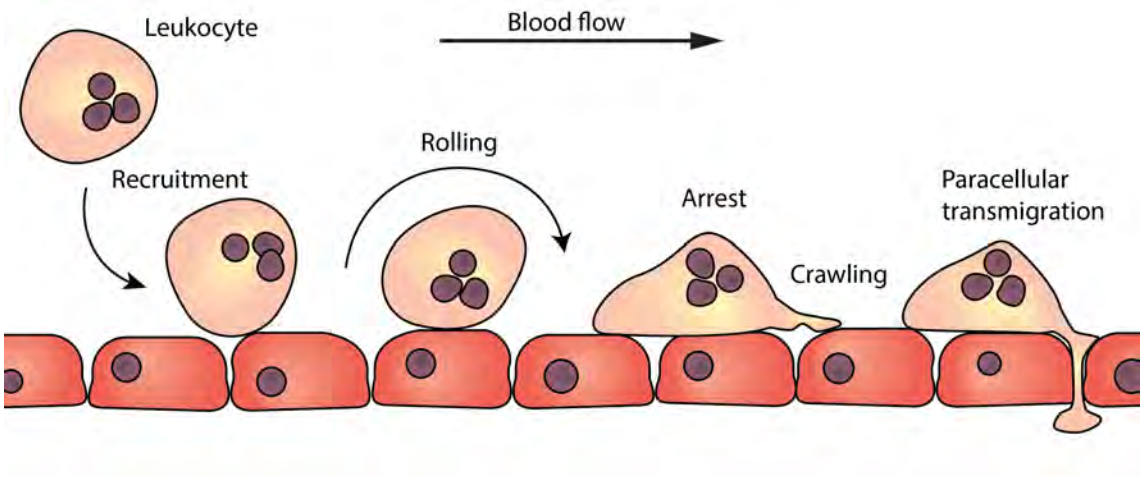

Figure 1.1: When moving through the bloodstream, leukocytes undergo a number of state changes initiated by biochemical signalling. Endothelial cells recruit free-flowing leukocytes, which weakly adhere to the wall of the blood vessel. Shear flow from the passage of blood causes the leukocyte to roll along the endothelium, until it reaches an area of interest. Here, a signal cascade causes the leukocyte to halt in place, becoming tightly bound to the endothelium. Transformation of the cell's cytoskeleton deforms it from a roughly spherical structure to one spread across the wall of the blood vessel. It moves in an ameboid fashion, extending pseudopods to crawl across the surface. Finally, it penetrates the blood vessel wall to reach the site of inflammation, passing either between or through the endothelial cells. Figure adapted from [35].

allowing for the selective enhancement of the reaction [36]. Alternatively, the sequestration of reagents allows for selective up- or down-regulation of their chemical pathways. It is this ability to selectively capture or exclude cargo which guides the work in this thesis.

The study of cellular networks is made difficult by the complex, interconnected nature of these systems. When performing *in vitro* investigations or *in vivo* genetic modifications, the distinction between a natural behaviour and a stress response may be difficult to ascertain. It was once thought that initial leukocyte adhesion to the endothelium led to further white blood cell recruitment through leukocyte-leukocyte contact [37]. Further investigations revealed that this behaviour only occurred to any significant degree in *in vitro* contexts, thus requiring a reassessment of the assumed behaviours [38]. The ability to study any singular aspect of cellular behaviour in isolation is thus beneficial. If the function of a particular protein or

cellular mechanism is in question, investigating it in a synthetic environment with fewer external effectors will allow an in-depth analysis of its specific behaviours. This knowledge can be integrated with *in vivo* data sets to form a comprehensive understanding. To increase the level of abstraction, creating a purely synthetic model of a proposed mechanism allows one to interrogate the key aspects of these forms and functions.

1.3 Synthetic cells

In order to gain enhanced understanding of the processes which take place inside living cells, it can be helpful to isolate functions from their complex, interacting networks. The methods to achieve this are generally assigned to one of two categories: top-down or bottom-up approaches. In the former, natural organisms are genetically modified to reduce complexity, leaving behind only the structures to be studied and those vital for life [39]. In the latter approach, synthetic cells are constructed from basic molecular subunits in order to model or replicate organic functions [26] [40]. For some researchers in this field, one of the eventual goals of this realm of synthetic biology is to create a living synthetic cell, defined as one that possesses the five hallmarks of life. These are: (1) a membrane to control environmental exchange; (2) internal organisation through compartmentalisation; (3) the production of and response to communication signals; (4) self-directed movement; (5) the ability to metabolise energy, grow, and divide [41] [42]. In parallel, the creation of cell-like structures allows for the study of cellular machinery and the modelling of related mechanisms.

Synthetic cells may also be synthesised for functional, rather than investigative, purposes. Synthetic cells have been designed to act as microreactors, spaces in which chemical reagents are confined to enhance their rate of reaction [40] [43] [44] [45]. Confining enzymes and substrates while excluding competitors or antagonists can promote the desired reaction pathway. This concept was inspired by existing cellular structures, and will be discussed in section 1.4. In synthetically replicating this confinement, chains of artificial microreactors may be linked together to create multi-stage reaction pathways [46] [47] [48]. This allows for the promotion of low-yield products or the creation of novel reaction pathways.

Synthetic cells may alternatively be used in pharmaceutical contexts, acting as car-

riers to deliver drugs to target sites within the body [49]. This may direct the drug carrier to the targeted organ, to cells exhibiting particular disease phenotypes, or even to subcellular regions within specified cells [50] [49]. The targeted delivery of drugs has the dual benefits of reducing side-effects by minimising systemic distribution and off-target uptake of potentially toxic drugs, while simultaneously increasing therapeutic efficacy by increasing the amount of drug delivered to the target site. This function has been also combined with the earlier concept of microreactors, creating synthetic cells which travel to a target site within the body, synthesise the drug *in situ*, and immediately release it for maximum efficacy [51].

In designing for any of these intended applications - biological modelling, reaction vessels, or drug carriers - the basic physical attributes of the synthetic cell remain the same [52] [46] [49]. They must first possess an outer membrane or barrier, separating the bulk of the contents from the surrounding environment. This membrane must be capable of allowing selective entry of biomolecules and reagents, controlling molecular exchange into and out of the cell. The cell must display sufficient stability such that it is robust to changing environments or the passage of time, and it finally must create a suitable environment for the intended cargo biomolecules.

A popular method for making synthetic cells is using liposomes, vesicles that replicate the naturally occurring phospholipid bilayer. This creates the membrane of the synthetic cell, separating the vesicle's interior from the surrounding environment. These can be formed using thin-film hydration, emulsion templating, or microfludic device-based strategies [53] [54] [55] [56]. Liposomal technologies see significant use due to the breadth of their tunability: the method of production allows selection of the vesicle's size and membrane composition [57]; the biomimetic nature of the lipid membrane supports biocompatibilty [58]; and they can be internally or externally functionalised with proteins, enzymes, or nucleic acids [59] [60].

Despite the breadth of utility of liposomes in creating synthetic cells, the technology still possesses limitations. As mentioned by Elani *et al.*, reactions confined within vesicles are restricted in that the reagents must be added during the vesicle formation process [46]. In order to create sequential or step-based reactions, increasing numbers of cells must be linked together. This creates the need for inter-compartmental communication and transport, complicating the synthesis of these structures through the addition of detector and transport mechanisms.

Alternatively, membrane-free synthetic cells have also been investigated. Membraneless synthetic cells are formed of macromolecular coacervates, dense liquid droplets of phase-separated polymers, proteins, or nucleic acids [41]. These offer potential as microreactors, allowing selective compartmentalisation of molecules without the need for membrane-spanning transport complexes [61] [62]. They also act as model protocells, providing the ability to explore possible avenues of abiotic and pre-biotic cell formation, in effort to understand the evolution of life [63] [64].

1.4 Self-assembly

As a synthetic technique, self-assembling (SA) strategies are vital across the realms of chemistry, biochemistry, and nanotechnology. Although, when working with such concepts at the nanoscale, the rigid boundaries defining and separating the fields of science grow indistinct. Self-assembly may be simply defined as the spontaneous ordering or aggregation of molecular subunits. Distinct from molecular formation, SA structures form using non-covalent bonds, relying upon weaker forms of interaction to create their ordered assemblies [2]. Weak intermolecular forces include hydrogen bonds, Van der Waals forces, or hydrophobic interactions - associations weak enough that the structures may dynamically adjust to produce long-range order. This is in contrast to glass-based assemblies, which irreversibly bind upon initial contact and create an amorphous structure [65]. Most synthetic SA systems typically exist in thermodynamic equilibrium, reaching a minimum energy potential through either entropic or ethalpic pathways [66]. Their synthesis typically uses low-cost, bottom-up methods requiring little user input or complex equipment.

It is an aim of these fields to reach the level of complexity seen in biological SA structures, which exist as dynamic systems rather than static objects [67]. Biological systems use external energy sources to drive functional processes, often involving metastable states. For instance, while modern technologies can reliably synthesise DNA through top-down control of chemical coupling steps, cellular machinery can unwind, unzip, replicate, and ligate DNA strands in a repeating cycle at constant temperature [66].

Examples of self-assembling systems are wide-ranging, both naturally-occurring and synthetic. In aqueous environments, phospholipids spontaneously align to create lipid bilayers, arranged through the competing forces of hydrophobicity and -philicty, forming the basis of cellular membranes [3]. This principle is also used to synthe-

sise micelles, liposomes, and vesicles, each vital in biological and pharmacological research. In the realm of engineering, organic molecules may be synthesised as self-assembled monolayers (SAM): a two-dimensional plane of molecular structures arranged across a substrate through chemisorption, creating a homogenously functionalised surface. These structures find use in applications ranging from chemical treatment for surface protection to the engineering of nanoelectronics through layered lithography [68] [69]. Thus, the term "self-assembly" is used to describe a range of techniques as broad as they are vital.

1.4.1 Liquid-liquid phase separation

In this thesis, we are particularly concerned with phase-separating systems, the spontaneous assembly of regions of high and low concentrations of solutes dissolved in solution. This mechanism is well-studied in polymer solutions, which were noted as exhibiting colloidal behaviour as early as 1931 [70], with the thermodynamics of two-phase systems described by 1942 [71].

Polymer solutions undergo phase separation through either spinodal decomposition or nucleated growth [72]. The occurrence of either mechanism depends on the composition (e.g. concentration, cations, solvent) of the original mixture, and can be visualised through a phase diagram (figure 1.2 A). For a given polymer solution, there exists range a of concentration and environmental parameters (e.g. temperature, pressure, pH) for which the solution will be homogeneously mixed. When environmental parameters are changed, a boundary is crossed beyond which the system loses stability and will phase separate [1]. The extreme of this boundary is known as the critical point. The boundary between homogeneous and metastable states is called the binodal curve. A metastable state is one which will remain homogeneous until externally activated. It is a local minimum in the free energy plot of a system, separated by an energy barrier from the thermodynamic equilibrium

[73]. Further within the binodal curve is the spinodal curve, beyond which phase-separation spontaneously occurs. The shape, symmetry, and position of each curve depends heavily on the solute, solvent, and environmental conditions of the system.

In a system in which the solution temperature is varied, and instability occurs as temperature is decreased (figure 1.2 B), the critical point is termed upper critical solution temperature (UCST) [74]. When above the binodal curve (P_0), the solution remains stable and homogeneously mixed. When the temperature falls to between the binodal and spinodal curves (P_1), it enters a metastable region. A further decrease to below the spinodal curve (P_2) will result in an unstable system and immediate decomposition into dense and dilute phases.

Nucleated growth occurs in the case of a metastable system. Here, the homogeneous solution exists at a local free energy minimum, while the phase separated solution is an even lower global energy minimum. Low-amplitude fluctuations in local free energy cannot overcome the energy barrier of the local free energy minimum [1]. Instead, an inhomogeneity in the local environment will allow discrete phase-separated nuclei to form and grow into distinct droplets or spheres [75]

Spinodal decomposition occurs when the solution enters the unstable region within the spinodal curve [76] [74]. In a solution of a homogeneously mixed polymer at UCST, immediately upon quenching the temperature to beneath the spinodal curve, the solution exists at a maximum in free energy. This disfavoured energy state is resolved through the spontaneous initiation of separation between polymer phases throughout the solution. The solution rapidly separates into two distinct phases, producing interconnected networks of regions of high and low concentration. This phase transformation is described by the Cahn-Hilliard equation [77].

For a given environmental parameter, changes in polymer concentration will affect the solution's position within the phase diagram (figure 1.2 C-D) [21]. A homoge-

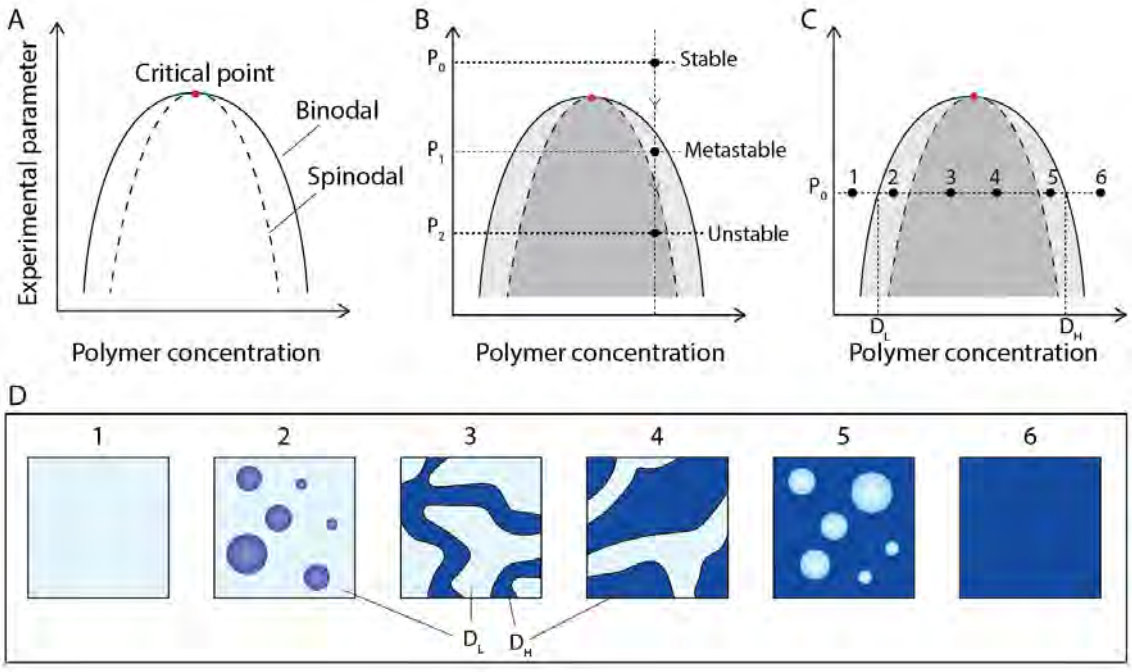

Figure 1.2: General representation of a polymer phase diagram, showing relationship between polymer concentration and a generic experimental parameter (P). **A** At high values of P or extremes of polymer concentration, a homogeneous solution forms. Beneath a critical point (red circle), phase separation may initiate. **B** If P is reduced to the region between the spinodal and binodal curves (solid line, light grey area), the solution enters a metastable state. If P is reduced to within the spinodal curve (dashed line, dark grey area), the solution spontaneously destabilises. **C-D** Extremes of polymer concentration outside the binodal curve will form homogeneous solutions (1, 6). In the metastable region, if phase separation is nucleated, the solution will form discrete droplets. If the solution is at a lower concentration than the critical point (2), highly dense polymer droplets will phase separate from a dilute solvent. If the solution concentration is above the critical point (5), low-density droplets in a highly-dense solvent will result. In the unstable region, the solution forms interconnected networks of high- and low-concentration phases (3-4). At a given value of P, an increase in polymer concentration will adjust the ratio of low:high density regions. The polymer concentration within those regions will remain constant, defined by the edges of the binodal curve as D_L and D_H. Figure adapted from [21].

neously low concentration mixed solution may exist at one extreme (figure 1.2 C-D position 1) while a homogeneously high concentration exists at the other (figure 1.2 C-D position 6). In the formation of phase-separated regions, the solution splits into low-density and high-density polymer phases. The concentration of polymer within these regions remains constant at a set environmental parameter. The low density (D_L) and high density (D_H) concentrations are defined by the binodal boundaries. Variation in the overall solution concentration does not affect polymer concentration in the two phases. Rather, the ratio of low:high density regions will vary. When polymer concentration changes for a fixed environmental parameter, the two binodal regions of the phase diagram will produce either high-density droplets within a low-density bulk (figure 1.2 C-D position 2), or low-density droplets within a high-density bulk (figure 1.2 C-D position 5). Similarly, within the spinodal curve, the system-spanning networks will either see high- in low-density structures (figure 1.2 C-D position 3) or vice versa (figure 1.2 C-D position 4).

Once phase-separated D_H droplets form, they grow over time through either fusion or ripening [78]. Fusion, otherwise termed coalescence, is the merging of droplets when they come into contact with one another. This mechanism is only possible when the surface tension of the droplets is such that droplet-droplet interactions are stronger than than droplet-solute. This is the case when the constituent polymers are self-attractive. Alternatively, the process of growth through ripening was first described by Ostwald in 1897 [79]. It describes the process of the dissolution of small particles in favour of larger ones [80]. In a solution containing both small and large droplets, an equal droplet volume may be contained within a single large droplet or multiple smaller ones. The smaller droplets would, together, possess a greater surface area than the single larger droplet, rendering them an energetically unfavourable structure. The small droplets can therefore dissolve, and their constituent particles will deposit on the surface of larger droplets. The processes of

fusion and ripening are not mutually exclusive, and can occur simultaneously in the same solution.

1.4.2 Phase separation in living cells

Recent studies show that phase separation also occurs inside living cells [81] [82]. A defining characteristic of eukaryotic organisms is the presence of membrane bound organelles [83]. These are cellular compartments enclosed within lipid bilayers that perform specific, specialised functions, such as mitochondria, endoplasmic reticula, or lysosomes. These structures are essential in coordinating the complex behaviours of the cell. Through the compartmentalisation of biomolecular operations and reactions, they greatly increase the efficiency of cellular functions. Non-membrane-bound organelles have also been identified in eukaryotes, molecule-rich liquid droplets that demix from the cytosol, formed through liquid-liquid phase separation (LLPS) [84] [85] [86].

From the synthesis of ribosomes in nucleoli to defining cellular structure with centrosomes, membraneless organelles are proposed to affect every aspect of cellular function. First described were the P granules of *Caenorhabditis elegans* germ cells, RNA-protein structures that have been suggested to carry RNA memory of gene expression across cellular generations [86]. Their liquid nature is essential to their function. During fertilisation, P granules partition away from the face of the nucleus towards the posterior side of the cell, where they become incorporated into the forming germline. This localisation is achieved by preferential dissolution of P granules in the anterior of the cell and condensation in the posterior, proposed to be a clear sign of phase separation and liquid characteristics.

The classification of phase-separated cellular coacervates as liquid droplets is dependent on the observation of three physical characteristics [81]. First, when coming

into contact, whether two cellular coacervates fuse and form a larger sphere, indicating liquid deformability and a shape driven by surface tension. Second, when observed under shear forces, whether cellular coacervates deform in a liquid-like manner. Third, whether photobleaching experiments show an active exchange of constituent particles inside and through cellular coacervates. The third criterion is a matter of some debate. Photobleaching is the process by which fluorescent molecules lose their ability to fluoresce following high-energy excitation [87]. If a portion of a coacervate is photobleached, recovery of fluorescence in the bleached region indicates the movement of particles within the coacervate, suggesting it is in a liquid phase. Similarly, bleaching of the full structure and a return of fluorescence indicates an exchange of particles with the dilute phase. However, fluorescence recovery after photobleaching is not a definitive indicator of liquid phase coacervates. A gel or crystalline structure with mobile subunits would appear to recover in a similar fashion [21]. Therefore, the ability to study cellular coacervates when confined within the complex cellular environment is limited.

The thermodynamics of cellular structures are many times more complex than simple polymer solutions, but can result in broadly similar physical behaviours. The distinction between soluble macromolecules and those that undergo phase separation relates to the comparative strengths of solute-solute and solute-solvent interactions [81] [1]. A non-interacting system is one in which solute-solute interactions are minimal, while in an interacting system, solute-solute interactions overpower solute-solvent interactions.

Any system will spontaneously minimise chemical potential through the passive diffusion of its contents. This may result in either a mixed or homogeneous solution, depending on the Gibbs free energy of the system under a given set of conditions [88]. In a non-interacting biomolecule system, free energy is minimised by homogeneous distribution of the particles throughout the solvent [1]. For an interacting system,

a multi-modal free energy curve favours the formation of areas of low- and high-concentration. In either state, the chemical potential remains equal across phases, allowing particle flux at equilibrium. Thus, concentrated liquid compartments can form and remain stable in cells without active energy input, through the physical process of liquid-liquid phase separation.

In interacting systems there is an entropy gain in multi-valent complexation, due to the release of solvent molecules, known in chemistry as the chelate effect. In the cellular context, biomolecule multivalency is thought to be a driving feature of phase separation. This often occurs through a combination of strong, specific binding forces and weak, general interactions [82]. For instance, the complexation of protein and ligands at multiple binding sites, or the presence of intrinsically disordered regions (IDRs), leads to the formation of oligo- or polymer structures [89].

The ability of biomolecules to bind to one another at multiple sites per particle, multivalency, is a key feature of many cases of LLPS observed in biology. Typically, the greater the number of binding sites per subunit, or the higher the binding strength, the larger the size of the resulting coacervate. In a keystone study, Li *et al.* demonstrated LLPS of synthetic, multivalent peptides, tying the formation of macroscopic structures to angstrom-scale molecular interactions [90]. They demonstrated key concepts in the cellular context, including the inverse relationship between valency and concentration required for phase separation; valency and size of coacervates; and a strong increase of biomolecule activity when condensed (figure 1.3).

In a cellular context, LLPS coacervates appear to hold particular importance in the regulation of RNA processes, including transcription, processing, and translation [91] [92]. Many cellular coacervates form through the interaction of RNA and proteins, taking advantage of the multivalency of RNA polymers. In certain cases,

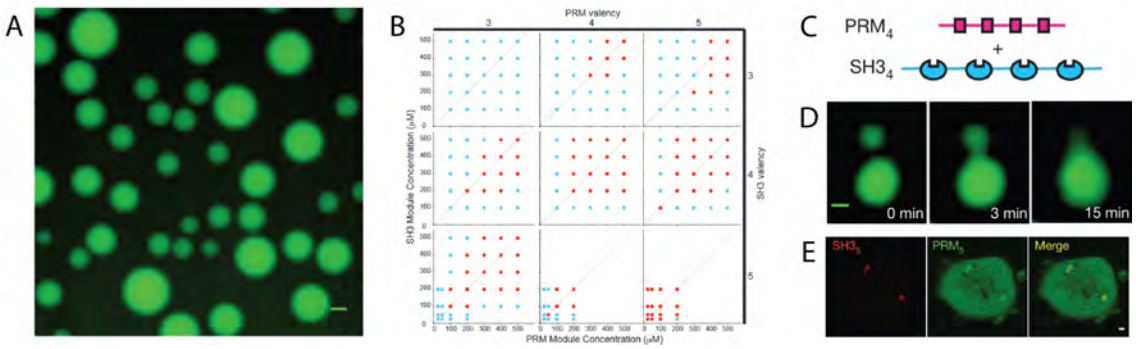

Figure 1.3: An example of biological phase separation of multivalent subunits. **A**: Dense coacervates formed from an equimolar solution of PRM_4 and $SH3_4$ peptides *in vitro*. **B**: Phase diagrams of PRM and SH3 peptides of varying length and concentration; coacervate formation indicated by red circles. In this study, phase separation was found to require subunits of high concentration and/or with multiple binding sites. **C**: Example oligomer structures. **D**: Fusion of coacervates over time suggests a liquid phase. **E**: Expression of PRM_5 and $SH3_5$ in cells forms discrete puncta. These were not associated with any vesicles or membranes. Rapid fluorescence recovery of puncta suggested liquid coacervates. Figure adapted from [90]

large mRNA molecules form extended networks through disordered binding [93]. This results in a dynamic mesh, creating the nucleation site around which proteins condense to form coacervate droplets.

1.4.3 Multi-phase droplets

Complex droplet systems are those containing more than one phase-separating polymer (figure 1.4). In these cases, the structure of the resulting droplets depends on the method of coacervate formation and the interactions between the various constituent molecules [94] [95]. The same coacervate formation technique may produce radically different droplet architectures, also termed morphology, depending on the relative attraction between the polymer phases and solvent [96].

Examples of such variants include discrete uniform droplets, when the polymers are universally repulsed from one another; co-localised, surface adhered, lensed, or co-continuous structures, when polymer-polymer and polymer-solvent attraction are both present; and core-shell structures, when the attraction between polymers is

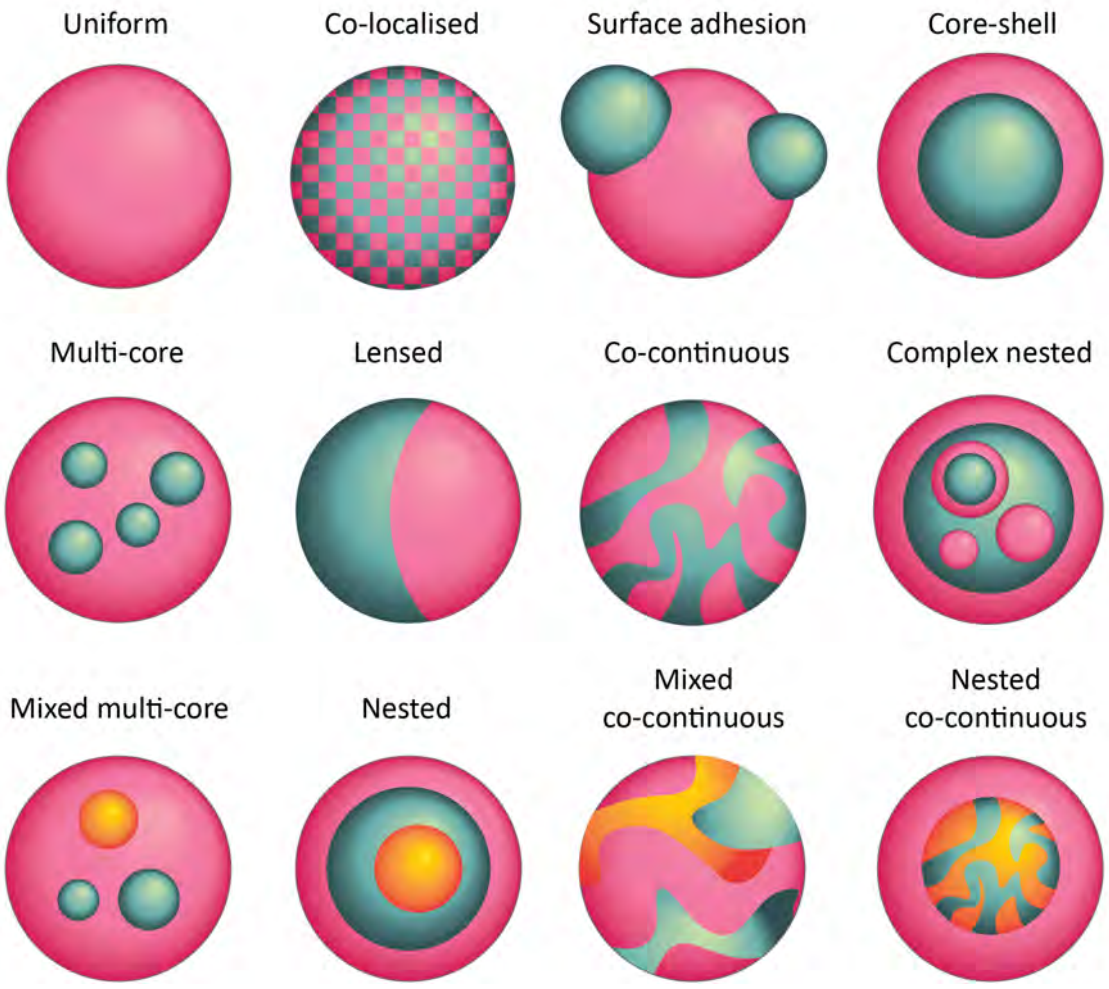

Figure 1.4: Examples of morphologically complex multi-polymer coacervate structures relevant to the work in this thesis. Figure adapted from [94].

greater than the attraction of the core to the solvent (figure 1.4) [94]. More complex structures are possible, when using additional polymers in the system or different droplet formation techniques.

In a multiphase coacervate system, three forces determine the degree of wetting of one against the other – the surface tension of each species of coacervate against the surrounding solvent ($\gamma 1$ and $\gamma 2$), and the interfacial tension between the two coacervates ($\gamma 12$). The greater the attraction between the two phases, the lower the interfacial tension experienced [94]. In a system with multiple interfacial tensions, the components will organise in such a way that interfaces with higher γ are

minimised in surface area [97].

If no attraction exists between the two populations, the interfacial tension between two droplets (γ_{12}) would be infinitely high. As such, the species will exist in isolation, as the sum of the surface tensions of individual droplets (γ_1 and γ_2) will be less than the interfacial tension between two droplets.

$$\gamma_1 + \gamma_2 < \gamma_{12} \tag{1.1}$$

Conversely, if the interfacial tension between coacervates is less than the surface tension of individual droplets, then they will be driven to form co-localised droplets.

$$\gamma_{12} < \gamma_1 + \gamma_2 \tag{1.2}$$

Lu and Spruijt posit that the partial wetting of two coacervates occurs when [97]:

$$\gamma_1 < \gamma_{12} \quad and \quad \gamma_2 < \gamma_{12} \tag{1.3}$$

Yewdall et al. extend the model, describing the phenomenon as occurring when [95]:

$$\gamma_1 < \gamma_{12} < \gamma_1 + \gamma_2 \tag{1.4}$$

If γ_1 and γ_2 are each individually lower than γ_{12}, no energy is saved through the formation of an interface between the two coacervates. However, if the sum of γ_1 and γ_2 is collectively greater than γ_{12}, then a small degree of stability is conferred to the system through the formation of partially wetted structures. The specific degree

of wetting represents a balance being struck between the three interfacial tensions.

Given a limited size difference between coacervates, species 2 will be encapsulated by species 1 if:

$$\gamma_1 + \alpha\gamma_{12} < \gamma_2 \tag{1.5}$$

with α representing a measure of the relative sizes of droplets 1 and 2 [97]. This results in a core-shell structure. Finally, multiple core coacervates (2 and 3) may be encapsulated within a single shell (1) if the sum of their individual interfacial tensions is less than the interfacial tension between the two.

$$\gamma_1 + \gamma_{12} < \gamma_2 \quad and \quad \gamma_1 + \gamma_{13} < \gamma_3 \quad and \quad \gamma_{12} + \gamma_{13} < \gamma_{23} \tag{1.6}$$

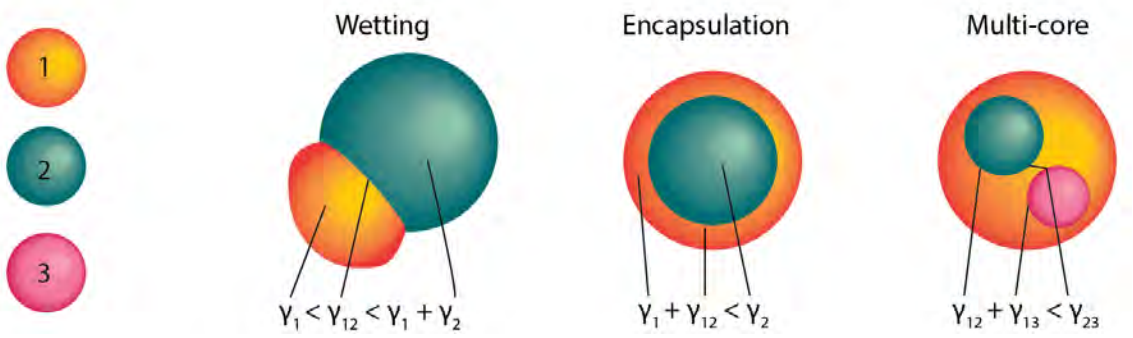

Figure 1.5: Schematic illustrations of the architectures formed in this work and the related interfacial tensions predicted from the literature, based on [97] and [95].

In order to affect control over the micro-architectures developed in this thesis, the relative strengths of the interfacial interactions may be leveraged. This will be attempted through the use of DNA nanotechnology, whereby control of nucleic acid sequences allows for tuning of inter-sequence attraction, in a method not achievable for traditional polymers or biomolecules. Additionally, as interfacial tensions do not necessarily relate to the physical properties of each individual phase, the design of

the DNA nanostructures will be varied to independently control the phase state of each coacervate region. This may allow control of the degree of fluidity or gelation in each phase, imparting upon each phase distinct physical properties that may assist in the production of synthetic cells or micro-reactors. For instance, fluid regions suspended in a gelated medium could allow for high localised reaction rates, with slow diffusion of products between regions, thereby controlling the overall reaction rate.

1.5 Nucleic acid nanotechnology

Historical accounts suggest that little attention was paid to Friedrich Miescher's 1869 isolation of a novel compound from the nuclei of leukocytes. Although Miescher spent years dedicated to the characterisation of the newly-termed nuclein, he continued to believe that proteins were responsible for the transfer of hereditary traits, nuclein having too little chemical diversity to be responsible for the vast array of transmissible information [98]. It was only in 1952 that Alfred Hershey and Martha Chase demonstrated that the nuclein particle, since renamed deoxyribonucleic acid, was the source of genetic transmission [99]. Soon after, work by Franklin and Wilkins, and Watson and Crick determined the structure of DNA to be a regularly repeating helix, with paired strands connected by matching bases [100] [101].

1.5.1 The structure and synthesis of DNA

The physical and chemical structure of DNA is now well established (figure 1.6). Cyclic ribose sugars are connected at their 3- and 5-carbons by phosphate groups, creating a polymer chain termed the 'backbone'. To the 1-carbon of each ribose is attached a base, one of either adenine, guanine, cytosine, or thymine. Where one chain is oriented in a 5' to 3' direction, a paired chain binds in the opposite orientation, 3' to 5'. This is termed 'anti-parallel' directionality. The paired backbone is comprised of matching bases: where one backbone contains adenine, the other will have thymine, and similarly cytosine will match guanine. Guanine and adenine are both purine bases, consisting of joint six- and five-member aromatic rings, while the pyrimidines cytosine and thymine are six-member rings. Pairing of purine-pyrimidine in base-pairs ensures the distance between each backbone is regular, equal to the distance of a double-ring paired to a single ring. Cytosine and guanine are bound by three hydrogen bonds, forming a stronger interaction than

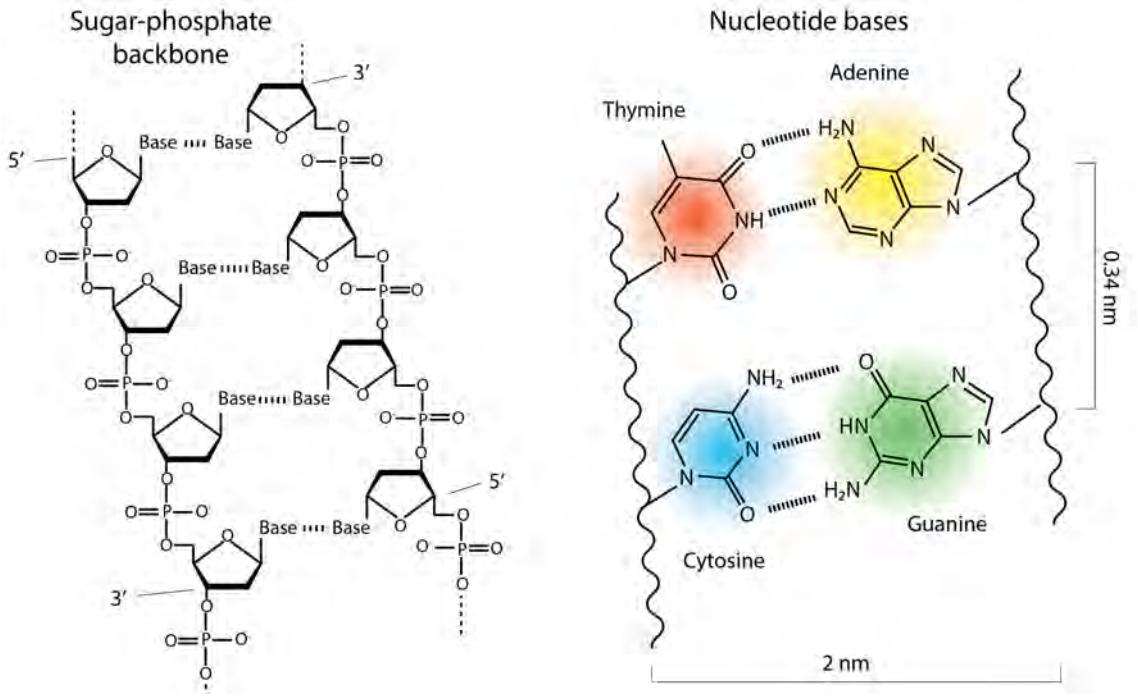

Figure 1.6: The chemical structure of the DNA polymer. Two dexoyribose-phosphate chains align in an anti-parallel fashion to form the backbone of the double helix. The backbone sugars are each bound to one of four nucleotide bases: thymine, adenine, cytosine, or guanine. The nucleotides most commonly hybridise via Watson-Crick base pair rules: thymine-adenine and cytosine-guanine. Adapted from [102].

the two hydrogen bonds connecting adenine and thymine.

The stability of DNA double helices is further increased by base stacking, a name given to the attraction experienced between overlapping π orbitals of the aromatic rings of nucleotide bases [103]. A series of A-T or G-C nucleotide pairs connected via the phosphate backbone will have a greater binding energy than the same nucleotide pairs in isolation, with the vertical stacking of the bases stabilising the helical structure (figure 1.7). This effect varies by order of nucleotide pairs, with an AT/CG stack providing an enthalpy increase of 5.6 kcal/stack, while a CG/CG stack produces 11.9 kcal/stack [104].

When paired, the hydrophobic nucleotides form flat planes. In order to minimise their exposure to water, they stack closely atop each other. It is this stacking that causes the helical spiral of double-stranded DNA (dsDNA) [105]. These two

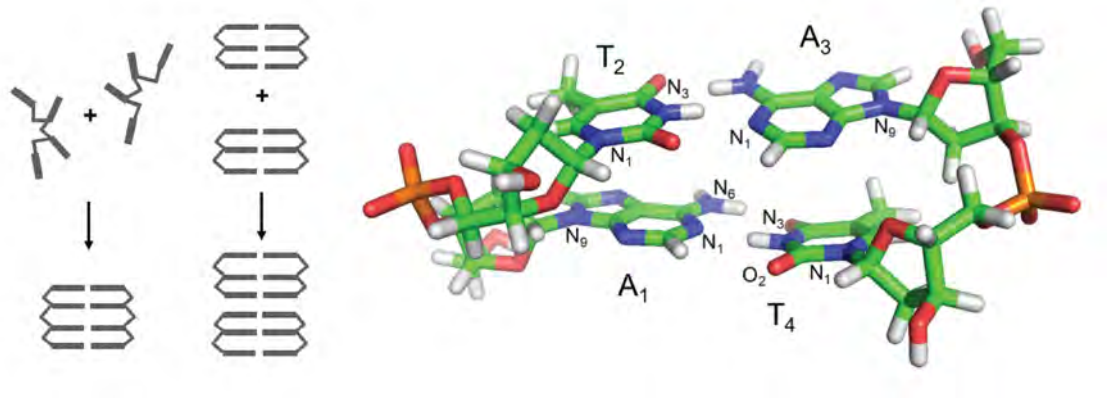

Figure 1.7: The adjacent aromatic rings of the nucleotide bases experience pi-pi stacking. This contributes to the hybridisation and stabilisation of complementary DNA sequences, and may cause two blunt-ended DNA helices to bind. The strength of this orbital interaction depends on the base pair sequence. Pi-pi stacking causes nucleotide bases to align closely together in flat planes, contributing to the helical shape of the DNA molecule. Figure adapted from [107]

interactions – hydrogen bonding between and pi-pi stacking of nucleotide bases – are credited with the stability of the DNA molecule. Through exposure to incompatible environments or extreme temperatures, these bonds may be disrupted, leading to the dehybridisation of the double helix into single stranded DNA (ssDNA) [106].

Single-stranded DNA is an extremely flexible polymer, having a persistence length of 2.2 nm [108]. When ssDNA hybridises to another ssDNA of matching bases, termed its complementary sequence, it forms a double stranded helix (dsDNA). The persistence length of dsDNA is 40 – 50 nm (∼150 bp), with a high stiffness afforded by base-stacking stabilisation effects [109] [110]. Orthogonal DNA motifs possess non-complementary nucleotide sequences. Without the attraction afforded by the hydrogen-bonding of aligned bases, the negatively charged strands electrostatically repel one another and will not interact. Therefore, even a short DNA sequence will only hybridise to form dsDNA when it encounters its complementary sequence.

Methods for DNA synthesis are well developed. Initially, modified sugar-bases were combined with phosphate groups via a condensation reaction in a step-wise manner,

with extensive purification required between each additional base [111]. For longer oligonucleotides, ligase enzymes were employed to join shorter sections. By 1977 a 42 bp synthetic somatostatin gene was produced using this method and inserted into the plasmid of *Escherichia coli* [112]. Development of solid-substrate methods and discovery of more efficient reactants reduced the synthesis time per base from hours to minutes [113] [114]. Further refinements to these techniques have since led to the modern solid-phase methods [115] [116] [117]. These modern techniques are high-throughput and low cost, with easy automation and error rates as low as 0.5% [118] [119]. Thus, DNA offers a further advantage over traditional polymers in designing nanostructures, with the method of synthesis allowing nucleotide-level precision in its structure and high homogeneity in its length.

Current commercial synthesis costs are low, $<$ \$1 AUD per nucleotide, but the scales available for production only range between 25 nmole - 10 μmole. Error rates are low but accumulate over the length of the oligonucleotide, such that sequences over 60 nt in length will have a significant amount of truncation defects that would require purification. Practically, commercial synthetic oligonucleotides are only possible for lengths less than 100-200 nt. Additionally, the solid-phase method initiates synthesis at the 3' end of the sequence. Any truncation defects will occur at the 5' end of the strand, which is an important consideration when designing DNA sequences.

1.5.2 DNA nanostructures

With the ability to synthesise custom oligonucleotides, use of the molecule beyond a genetic information carrier began to be considered. Robin Holliday in 1964 first described naturally occurring, non-linear forms of DNA, wherein two identical double helices would swap one of their backbones at a crossover-point, forming what would come to be known as a Holliday Junction [120] (figure 1.8). This initial discussion was in the context of gene conversion in fungi, a transient form of DNA during

meiosis. Decades later, Nadrian Seeman would use this Holliday Junction (HJ) to propose creating two- and three-dimensional structures out of DNA [121]. By rationally designing the nucleotide sequence of four short oligomers, a cross-shaped tile of DNA could be produced. In lengthening these oligomers and increasing the complexity of their design, three-dimensional crystal networks of DNA could be formed [9]. The key change from the biological Holliday Junction to the synthetic structure was the immobilisation of the cross-over site. While HJ arms each have the same nucleotide sequence, allowing movement of the cross-over site, Seeman ensured each arm in his structure was unique. Thus began the field of DNA nanotechnology, the creation of nanoscale structures using the highly predictable folding and base pairing of DNA.

DNA nanotechnology has since built upon this basis, creating repeating crystals, wireframe structures, and complex three-dimensional objects termed DNA origami (figure 1.9). DNA crystals consist of simple, nanoscale motifs designed to bind to themselves in a repeating fashion. This has been achieved through a variety of design methods, including a single 13-nucleotide sequence that self-pairs to create a continuous lattice structure [122], a seven-stranded triangular motif that binds via base-pairing to create the repeating unit of the crystal [123], or cholesterol-modified Holliday junctions [124]. These crystal structures are an example of synthetic SA systems, with simple molecular subunits combining via non-covalent hydrogen bonds or hydrophobic interactions to create large assemblies. Wireframe structures create two-dimensional tiles that tessellate across a plane, resulting in micron-scale arrays [125] [126], or discrete three-dimensional polyhedra [127].

Crystal and wireframe structures tend to use short DNA motifs computationally designed to have partially complementary nucleotide sequences. As all strands in these techniques must be individually synthesised, the size and complexity of the desired structures are limited by DNA synthesis capabilities. Shih *et al.* synthesized

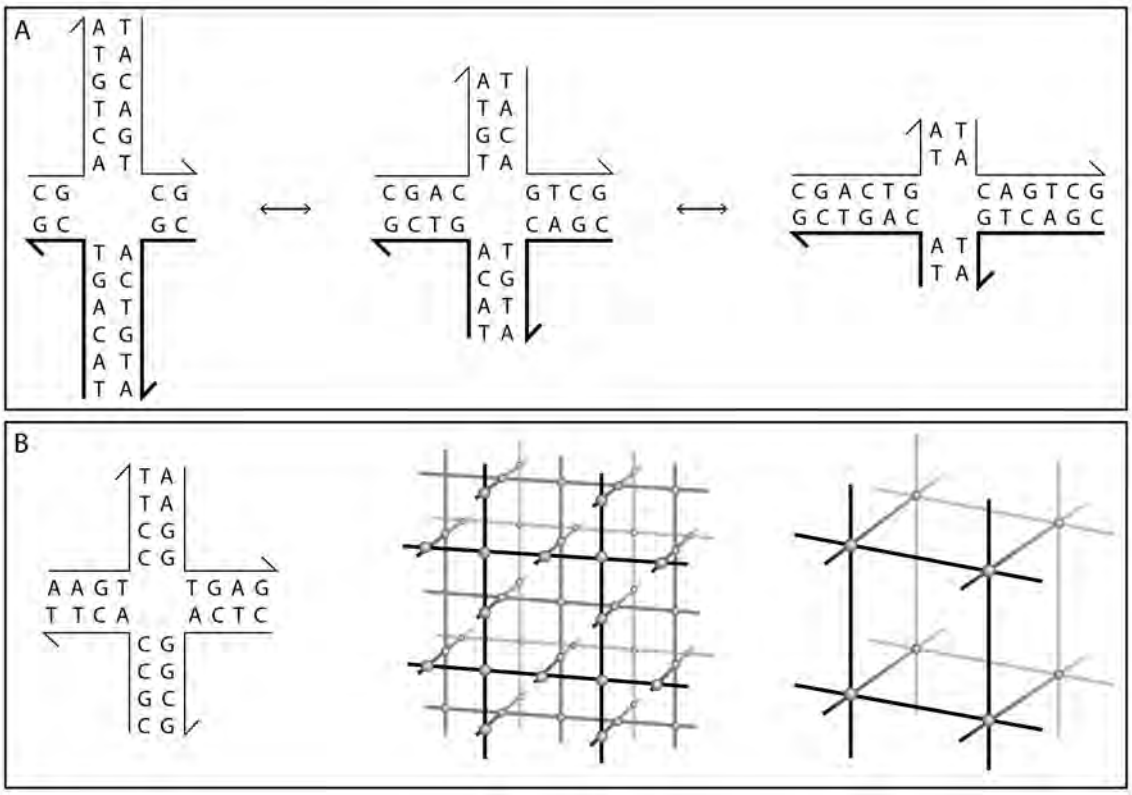

Figure 1.8: A comparison of Holliday junctions and Seeman lattices. **A**: Two identical DNA sequences cross-hybridise and form a junction. The symmetry of opposite arms allows the position of the cross-over to migrate in either direction. **B**: An immobile junction formed of four partially-complementary ssDNA strands. The junctions may vary in valency by changing the number of constituent strands. Extending the arms of the junctions allows for the creation of crystal structures; networks with four and six vertices per intersection shown. Figure adapted from [121].

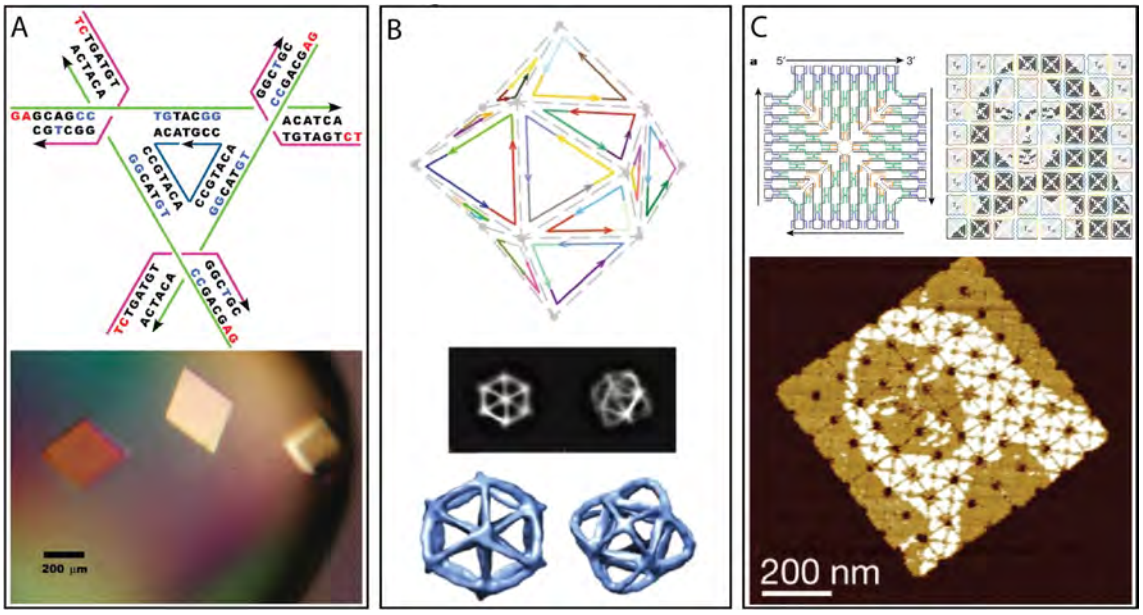

Figure 1.9: Examples of the products of DNA nanotechnology. **A** A nanoscale triangular motif with self-recognising sticky ends creates a micro-scale crystal. Adapted from [123]. **B** A wireframe polyhedron formed of discrete strands. Structural design is compared to averaged cryoEM micrographs and reconstructed three-dimensional maps. Adapted from [125]. **C** Scaffolded DNA origami is used to create a two-dimensional tile. Selective edge toehold placement arranges sixty four tiles in a desired pattern. Functionalisation of the surface of different tiles through protein adhesion creates a binary image. Adapted from [129].

a 1.7k base ssDNA strand that would fold into a wireframe octogon, nearing the limit of this technology [128]. Rothemund later developed DNA origami, the folding of 7k nt viral genomes into dense, complex three-dimensional structures [10]. This requires knowledge of the full nucleotide sequence of the circular ssDNA genome. Short (50-200 nt) DNA 'staples' are designed with complementarity to different portions of the genomic sequence. When annealed, the genome may be folded into a large variety of three-dimensional structures [129] [130] [131]. These techniques are only made possible through the base-pairing specificity of DNA.

1.5.3 Prediction of the melting temperature of DNA

For the rational design of DNA nanostructures, the ability to accurately predict the thermodynamic properties of the structure is required. Early methods of calculat-

ing the melting temperature of DNA sequences relied on simple arithmetic. For a given concentration of sodium cations, the T_M of a sequence was estimated as being linearly related to the sequence's GC content [132]. The higher number of hydrogen bonds between the guanine and cytosine was said to confer greater stability to the DNA helix [106]. However, it is base stacking, rather than base pairing, that contributes most significantly to the thermal stability of dsDNA [105]. Furthermore, the strength of base stacking is not uniform across a length of DNA. It is dependent on nucleotide sequence and proximity to an end pair [133] [134]. Finally, base stacking is further affected by environmental conditions, including DNA concentration, pH, cation charge and concentration. Thus, although the earliest methods of calculating the melting temperature of DNA relied simply on its GC content, current methods are now based on an extensive set of thermodynamic parameters found through experimental analyses of known samples [135] [134].

A great deal of effort has been put towards creating a model for the thermal stability of dsDNA. The latter decades of the twentieth century saw numerous groups investigating and publishing models of DNA denaturation. These were collectively termed "nearest neighbour" models, and based their estimation of system stability on pairs of adjacent hybridised nucleotides [135]. This method takes into account nucleotide order, position, proportion, and symmetry, and can be used to predict both free energy and melting temperature. The former is defined by the term:

$$\begin{aligned} \Delta G^o = & \sum_i n_i \Delta G^o(i) \\ & + \Delta G^o(initiates\ w/\ term\ G.C) \\ & + \Delta G^o(initiates\ w/\ term\ A.T) \\ & + \Delta G^o(symmetrical) \end{aligned} \tag{1.7}$$

finding the sum of the energy in each occurrence of every possible Watson-Crick base pair, plus modifiers based on if the first nucleotide pair in the sequence is a GC or AT, and if the sequence is symmetrical. The latter prediction, melting temperature, is found through the equation:

$$T_M = \Delta H^o / (\Delta S^o + RlnC_T) \tag{1.8}$$

with variations in the constant C_T depending on the symmetry and relative concentrations of nucleotides in the system. Each set of parameters, ΔG^o, ΔH^o, and ΔS^o, have been found through extensive study of oligonucleotide binding for different DNA sequences, creating tables of experimental values. This experimental characterisation was generally conducted through melt curve analysis (MCA). A range of DNA sequences were produced, varying by a single base-pair between sequences. The melting temperatures were compared, and the contributions of each base-pair and bp sequence towards the thermodynamic parameters thus calculated [136] [137]. Widely varying parameters, from a range of experimental studies of DNA polymers, oligonucleotides, hairpins, and dumbbells, were unified by SantaLucia in 1998 to create the commonly used Unified Nearest Neighbour (NN) model [135].

Progressions in the field have since further refined these parameters, improving the predictive capabilities of the NN model for large DNA molecules. The model has been additionally developed through understanding the transition of the polymer from a duplex to single stranded state, wherein melting is non-homogenous – distinct regions may form single-stranded loops, interspersed by hybridised sections [134].

Given these and the above insights, the Nearest Neighbour model provides a useful tool to predict the free energy and T_M of DNA phase transitions. However, the improved model does not align with experimental results for shorter DNA sequences,

less than 100 bases in length. These remain best described by GC content calculations, while still seeing significant variance between prediction and experimental values. The reasons for these discrepancies are unclear, with proposed explanations ranging from greater external contributions (DNA concentration, cation contributions) to AT base pairs being the major drivers of DNA duplex stabilisation [138]. Hence, predictive capabilities for short DNA sequences are lacking. This is relevant to this thesis, as this work involves DNA strand binding for strands typically < 100 nt, and is discussed further in section 2.6.

The NUPACK software suite is an online platform intended for the analysis and design of nucleic acids. The program is equipped with the ability to analyse multiple DNA sequences to determine the most probable equilibrium binding interactions. This tool can be used to predict, for a given set of DNA sequences, if desired on and off-target binding will occur at equilibrium to match design motifs. It can also be used to check for unintended secondary structures of single-stranded components that might slow the rate at which the equilibrium condition is reached [139]. Additionally, NUPACK hosts the ability to input a desired origami motif, with the program then generating nucleotide sequences that are predicted to result in the specified structure [140].

NUPACK makes use of a number of models in order to formulate its predictions. Initially it follows the SantaLucia NN model of base pair thermodynamics, recognising the fact that binding strength is reliant not only on the Watson-Crick base pair in question, but the adjacent and surrounding base pairs as well [135]. The program then lists all possible base-pairings between the strands present, and algorithmically determines which combinations allow for the lowest energy structure, the one most stable in the given set of conditions.

The hybridisation or melting of a DNA duplex may be experimentally monitored

using Fluorescence Resonance Energy Transfer. FRET is a mechanism by which energy is transferred from an excited fluorophore to a non-excited fluorophore, causing it to fluoresce [141]. This effect occurs when the emission spectrum of the excited fluorophore (the donor) overlaps with the excitation spectrum of the secondary fluorophore (the acceptor). This energy transfer is made possible by long-range dipole-dipole coupling of the fluorophores, wherein a positively charged region of one molecule aligns with a negatively charged region in the other.

In a typical FRET reaction, the system is irradiated in the excitation spectrum of the donor molecule. If the donor fluorophore is physically isolated, emitted photons will be detected in the emission spectrum of the donor. If the donor fluorophore is within a small distance (1 - 10 nm) of an acceptor, the emitted energy will excite the acceptor through dipole coupling [142]. This results in a decrease in detected fluorescence of the donor, and an increase in acceptor fluorescence. The efficiency of FRET depends on the probability of the energy emitted by the donor interacting with and exciting the acceptor. It is determined both by the degree of overlap between the spectra of the fluorophores and the physical distance between the fluorophores, R_{DA}. The distance between fluorophores whereupon FRET efficiency is 50% is termed the Förster distance, R_0, and is related to energy transfer efficiency through the equation [143]

$$E = \frac{(R_0/R_{DA})^6}{1 + R_0/R_{DA})^6} \tag{1.9}$$

As R_{DA} increases beyond R_0, transfer efficiency rapidly approaches zero. Measurement of acceptor fluorescence thus provides indication of the distance between the two fluorophores. If two complementary DNA sequences were functionalised with a donor and acceptor, the FRET efficiency could be used to monitor the hybridisation or melting of the duplex.

1.6 Phase-separated nucleic acid coacervates

In this thesis, we aim to use phase-separating DNA nanostructures to create synthetic cells. The thesis focuses on the creation of phase-separated DNA coacervates that include structurally distinct cores and shells, mimicking the cytoplasm and membrane of cells. In this section we describe the different approaches to DNA coacervates, their strengths and weaknesses, and different approaches to forming core-shell DNA coacervates.

1.6.1 Overview of synthetic nucleic acid coacervates

Nucleic acid coacervates have been formed using a variety of methods, combining different nanostructures and chemical interactions.

Single-stranded DNA sequences, containing multiple self-recognising domains, were shown to phase separate into micro-scale droplets [123]. Droplet formation was heavily dependent on the concentration of ssDNA and magnesium cations. Droplet size increased with DNA concentration, while droplet yield increased with $[Mg^{2+}]$ from 3 - 12.5 mM. At 22.5 mM $[Mg^{2+}]$, droplets instead fused into large amorphous aggregates.

Sequence-defined functionalised nucleic acid polymers (SfNAPs) were produced, polymeric dsDNA formed of a single continuous strand hybridised to multiple shorter complementary sequences [18]. Each of the short strands was appended with a binding sequence. A SfNAP was thus multivalent, and phase separation and droplet formation was observed between SfNAPs with complementary binding sequences. Individual SfNAP segments with only a single binding site did not undergo phase separation.

Multiblock co-polymers [144] were produced using ssDNA, containing repeating

stretches of a single base separated by a binding sequence [17] [145]. When the ssDNA was of sufficient length, brief incubation at elevated temperatures would initiate phase separation of the ssDNA, forming hydrogel droplets. For instance, a polymer containing repeating stretches of 20 adenine nucleotides and a 21 nucleotide barcode sequence to create a 1000 nt oligonucleotide would undergo phase separation when the temperature was increased from 25 - 45 ^{o}C, and return to a linear state once cooled [17]. The inclusion of a second ssDNA oligonucleotide, containing 20 thymine bases and a barcode sequence, allowed for interaction between the poly-A and poly-T stretches. The structure of these droplets depended heavily on the cations used, mixing in the presence of Ca^{2+} and forming core-shell structures when combined with Mg^{2+} [145]. Additionally, while droplet formation was reversible in the presence of magnesium cations, calcium cations caused irreversible phase separation.

Coacervates have also been formed from discrete DNA structures, termed nanostars [29] [146] [30] [24] [147] [27] [148] [19] [149] [150] [28] [23]. These are formed of multiple partially-complementary ssDNA strands that hybridise to form multivalent nanoscale motifs. Self-recognising ssDNA binding sequences on each nanostar allow for inter-star binding and phase separation. The design and formation of these structures is comprehensively detailed in section 1.6.2.

DNA nanostar motifs have also been functionalised with cholesterol moieties in place of their binding sequences [124] [151]. In such systems, a solution containing ssDNA and cholesterol-functionalised ssDNA strands are heated and slowly cooled. The cholesterol-modified strands initially form micelles through hydrophobic interactions. As the temperature decreases, nanostars form, and each arm hybridises with a cholesterol-ssDNA, forming a crystal network. The resulting phase-separated structures are crystalline, with the crystal structure depending on the number of arms in the nanostars [124]. These crystals were combined with DNA-only nanostars

[151]. The addition of ssDNA binding sequences allowed recognition between the cholesterol-DNA crystal and the DNA nanostars, forming a core-shell structure.

Finally, liquid-liquid phase separated droplets have been produced using *in situ* translated RNA nanostructures. These are formed from a single RNA oligomer, which duplexes via hairpin loops and self-binding to form a cross-shaped motif akin to a Holliday junction or DNA nanostar [152] [153]. The RNA motifs experience inter-molecular binding through kissing loops present at the end of each arm. When orthogonal droplets were confined inside water-in-oil droplets, the inclusion of surfactant RNA motifs allowed interaction, including the formation of a core-shell structure at a particular surfactant ratio [153].

1.6.2 DNA nanostar coacervates

Holliday Junctions were first described as a mechanism in meiosis; even Seeman's later proposal was only concerned with joints in large crystal structures. In the years following, the structures were investigated in isolation [154] [155] [156]. Later, DNA constructs consisting purely of such junctions were proposed and examined [29] [157] [158] [15]. Common nomenclature developed referring to them simply as DNA junctions or nanostars, and research focused on the potential for self-interaction. ssDNA binding sites, termed "sticky ends" (SE), were added to each arm of the star to facilitate binding between the motifs. It was found that such structures could form hydrogels, large-scale soft-matter structures, either spontaneously or via ligase catalysis [15] [16]. Next, more dynamic structures were investigated to achieve complex functions, for example systems that are reversible and reactive to their environments. Thus, the field began to focus on the creation of liquid droplets of DNA, spheres of nanostars suspended in solution [29] [146]. These self-assembled micro-droplets were produced using a mechanism newly discovered in the biological context, liquid-liquid phase separation (section 1.4).

An overview of star parameters

DNA droplets, formed of DNA nanostars via LLPS, have been produced for two decades, with research accelerating in the early 2010s. In that time, the structure of nanostars has undergone significant modification from the canonical Holliday Junction, based on experimental evidence and preferred properties (figure 1.10). Generally speaking, a nanostar consists of a small number of partially complementary strands which form about a central junction. Unlike a HJ, each arm of the nanostar consists of a unique nucleotide sequence, locking the star into a single junction location. Each arm is terminated with a short ssDNA motif, the *sticky end*, a palindromic sequence that is able to recognise and bind to copies of itself. This allows two adjacent nanostars to bind via their sticky ends, providing multivalent binding sites to bias the system towards phase separation. The physical structure of the stars can be classified by a number of parameters: the number of arms, the arm length, the presence and location of any unpaired bases, and the length and sequence-dependent binding strength of the sticky ends.

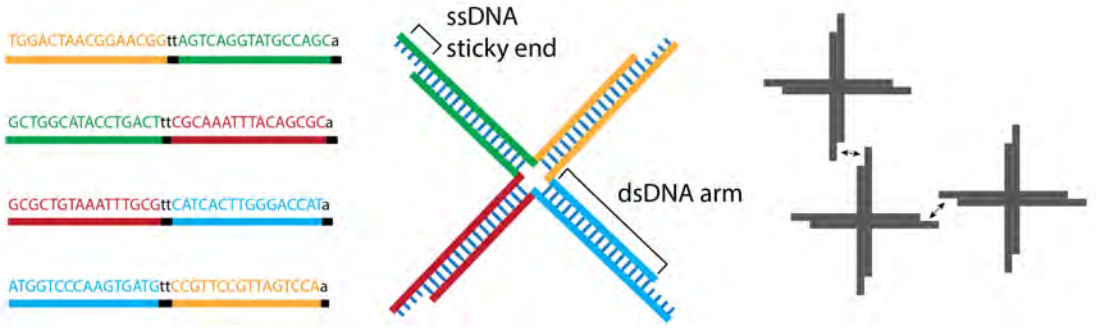

Figure 1.10: The basic structure of a DNA nanostar. Partially complementary strands will hybridise about a central junction to form a star-shaped structure. Complementary sequences highlighted in matching colours. ssDNA unpaired bases shown in lowercase black letters. Each dsDNA arm is terminated with a ssDNA sticky end. Adjacent nanostars bind via their sticky ends to form an extended disordered network. Adapted from [24].

In order to produce the nanostars and LLPS droplet systems, the DNA strands are typically annealed. This involves heating a solution of strands to above the melting

point of any sequences present. The solution is then gradually cooled, typically at a constant, controlled rate. Initially, individual strands will hybridise to form stars, their longer complementary sections ('arms') allowing for hybridisation at a relatively high temperature, T_{Hy}. Following this, weak attraction between SEs allows stars to begin interacting at lower temperatures, leading to the first stages of phase separation (figure 1.11). These initial interactions, leading to formation of liquid droplets, are observed to occur well above the algorithmically calculated melting temperature of the SE sequence [24]. The onset of LLPS is termed T_{PS}, the temperature of phase separation. The proposed mechanism for phase separation is weak, transitory binding between the palindromic sticky ends.

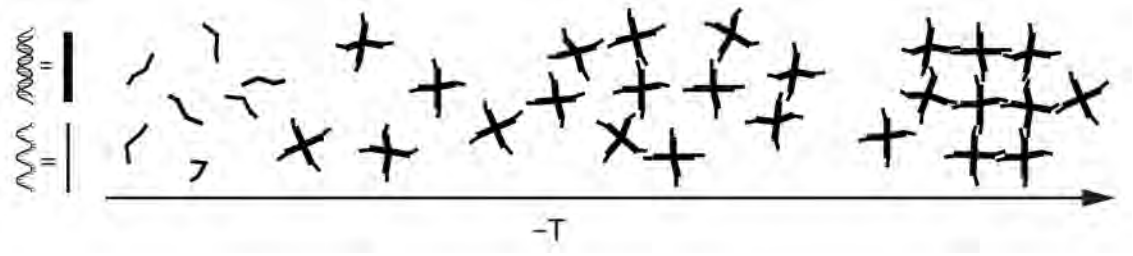

Figure 1.11: General process of nanostar phase separation: as system temperature decreases, individual strands hybridise into nanostars at T_{Hy}; sticky ends begin to transiently interact, initiating phase separation (T_{PS}); coacervate growth continues through coarsening and fusion during the active range until sticky ends stabilise and droplet forms a hydrogel (T_g).

As the system temperature cools further, the SE interactions grow increasingly more stable, eventually resulting in full hybridisation of SEs, forming hydrogel droplets at T_g. Notably, computational simulations indicate that no further decrease in temperature will ever lead to a crystallisation of the system, as the DNA nanostars achieve a lower energy state as a gel than they could as a solid crystal [159]. The temperature range between T_{PS} and T_g is here termed the active range, during which nanostar droplets are liquid and able to actively grow through coarsening and fusion (section 1.4). Changing star and system parameters can increase the time a system spends in the active range, leading to changes in the size and polydispersity of the

resulting droplets [29] [27].

Valency

Most commonly used are tri- and tetravalent stars, consisting of three to four unique DNA arms that form around a central junction. Discussed below, the valency of the stars affects the system's density, dissociation and melting temperatures, and tendency to crystallise. Typically, publications compare only a single form of star, either three armed (trivalent, Y-motif) or four armed (tetravalent, X-motif). A limited number of studies have compared the two in order to observes the effects of changing valency under the same conditions [16] [159] [147], or produced systems combining both Y- and X-motifs [24]. In the latter case, stars of differing valencies do not show inherent separation from one another. They readily form into mixed droplets, indicating that in these cases, phase separation is modulated most by particle interactions – sticky end complementarity – rather than physical structure.

Arm length

Many nanostars described in the literature use a twenty base pair (bp) arm length, following the example of an early paper by Biffi *et al.* [16] [25] [160]. Earlier stars were significantly smaller, with only 10 bp per arm [29] [158]. A link has been found between arm length and mesh size of the nanostar network [160]. A measure of mesh size is the average diameter of particles that are able to infiltrate the DNA droplet. While Nguyen *et al.* have investigated mesh size via this method, they did so only using nanostars of a single arm length, meaning the precise relation between arm length and mesh size has not been quantified [160]. It is possible that mesh size would increase with arm length up to the persistence length of dsDNA, providing the greatest possible separation between nanostar cores. Thus, the arm length could directly influence the size of particles able to penetrate into or be encapsulated by DNA spheres. A system developed by Okamura *et al.*, in which hairpin loops in

nanostar arms allow for the swelling and shrinking of a hydrogel, would allow for a more detailed investigation of droplet mesh size [161].

Agarwal *et al.* investigated the effect of tetrahedral nanostar arm length on the formation and growth rate of DNA droplets [27]. It was found that average droplet size increased when increasing the size of the DNA nanostars, for arm lengths between 6 - 40 bp from central junction to ssDNA sticky end (SE).

Unpaired bases

A major factor in the behaviour of DNA nanostars is the presence of unpaired bases at strategic locations. Early papers used continuous complementary sequences [29] [158], but later studies indicated that the inclusion of non-complementary bases provides flexibility and release of angular tension [16] [146] [162]. Nguyen and Saleh created a tetravalent system in which unpaired adenine bases were placed at the central junction of nanostars and at the start of the SE regions [146]. They demonstrated that under the conditions of their system, SE unpaired bases were required for the formation of liquid droplets. Inflexible stars, and stars that contained unpaired bases only at the junction, formed continuous hydrogels. They attributed this difference to the unpaired SE base causing a reduction in stability of the system, preventing long-spanning networks. Indeed, the presence of even a single unpaired base increases the hybridisation free energy of a DNA helix [163].

Many papers investigating LLPS DNA systems follow the nanostar design motif of Biffi et al. [16], in which two unpaired bases are placed at the junction and one at the SE [146] [30] [160] [164]. This lent credence to Nguyen and Saleh's assertion that an paired base at the SE is required for droplet formation. However, Sato *et al.* demonstrated the production of DNA droplets using unpaired bases only at the junction, meaning the base-pair conditions which lead to LLPS are not as restrictive as previously thought [24] [165]. Tran *et al.* demonstrated a destabilisation of droplet

formation when adding an unpaired base to the SE [150].

Sticky ends

The length of the nanostar sticky ends is of vital importance in designing droplets and droplet systems. This strongly influences the binding between nanostars, such as the temperature dependency and strength, and can be used to create partitioned and dynamic chemical environments. While droplet formation has been demonstrated to be possible using SEs between 4 and 12 nucleotides (nt) in length [24] [165], most published systems use a six or eight nt palindromic sequence. The nt length of the SE affects the droplet formation temperature, with a longer SE tending to increase the temperature at which LLPS occurs. This is attributed to the greater stability and subsequent higher melting temperature afforded by the additional bases [165].

Aside from length, the SE base sequence also affects nanostar binding and droplet formation (section 1.5.3). Matsuura *et al.*, comparing sticky ends of A_5T_5 and C_5G_5, observed that the higher melting temperature of the stronger G-C bond resulted in smaller droplets, when formed in a spontaneously cooled system [158]. Droplet formation is dependent on the period of time spent in the active range of the system, and as a spontaneously cooled system loses heat rapidly at high temperatures and slowly at low, formation of lower T_M products was favoured. Later papers, perhaps noting this unintentional favouring of certain formations, would use a constant cooling rate (discussed in section 1.6.2).

It is in the active range that droplets may exhibit liquid-like properties, deforming and actively growing. The gelation temperature (T_g) of a nanostar droplet is thought to be determined by three nanostar features – valency, geometry, and sticky end binding strength. For a given SE sequence, the T_g of droplets was seen to increase with increasing valency at a faster rate than the phase separation temperature [24]. This means that nanostars of lower valency will have a broader active

range than their larger counterparts. Finally, the sticky end strength also effects droplet formation and gelation temperatures. Sato *et al.* demonstrated that droplet gelation temperature rose more rapidly than formation temperature with increasing sticky end enthalpy [24]. This leads to a decreasing active range with increasing SE stability.

Additionally, Sato *et al.* demonstrated a variation in coacervate internal motility and surface tension in trivalent nanostars of three different 6 nt SE sequences [165]. These sequences contained the same proportions of GC and AT base pairs, but varied in binding strength due to base stacking effects. Saleh *et al.* similarly compared three NS systems of varying valency and SE sequence [147], and found that while both affected droplet gel temperature, a greater impact was observed for valency.

Strand length

Typically speaking, the length of nanostar strands is between 40-60 base pairs in length. While much investigation has been conducted on the properties of the NS sticky ends, less work has been done on modifying the arms themselves. The logic behind this can perhaps be attributed to synthesis limitations. With the current technological capabilities of the field, synthesis of high yield and purity oligomers up to 150 bp is possible, with longer strands available at a significantly reduced yield [118].

Environmental conditions

Following the design of the nanostar structure, the experimental conditions must be defined. A multitude of experimental parameters have been identified as crucial in the phase separation of DNA droplets, such as nanostar concentration, ionic concentration and identity, temperature control, and ageing process. A slight modification of these factors may result in large variation in the resulting structures, affecting

the size, density, and physical state of the droplets.

Nanostar concentration

As with any phase-separating system, DNA nanostars exist within a phase diagram. At low concentrations (the precise limit defined by environmental conditions), nanostars remain diffuse. At extremely high concentrations, the entire solution will form an extended hydrogel network [16]. It is only within the binodal curve that phase separation to form dense droplets may occur. Inside the binodal curve – in this system defined by DNA nanostar concentration and temperature – variances in DNA concentration ought to further affect droplet characteristics. Jeon *et al.* demonstrated that the concentration of nanostars in the low-density bulk phase in a droplet solution remains constant, regardless of the total DNA concentration [30]. This aligns with the expected behaviour of a system undergoing LLPS (section 1.4.1).

Nanostar phase separation can occur over a rather large range of DNA concentrations. Biffi *et al.* demonstrated phase separation occurring for trivalent stars at concentrations between 1 and 9 mg/mL, while tetravalent systems could stabilise from 1 to 17 mg/mL [16]. Conrad *et al.* further expanded upon these results, showing a broadening in the phase separation concentration range for nanostars of increasing valency [148] (figure 1.12). These values are likely additionally dependent on star size, base pair sequence, and salt content, among a range of other factors [148] [149].

Ionic conditions

The attraction of any available sticky ends is outweighed by the repulsion of the backbones. Discrete stars may bind via sticky ends, but they will repel one another on a broader scale. In order to achieve true phase separation, with the high density

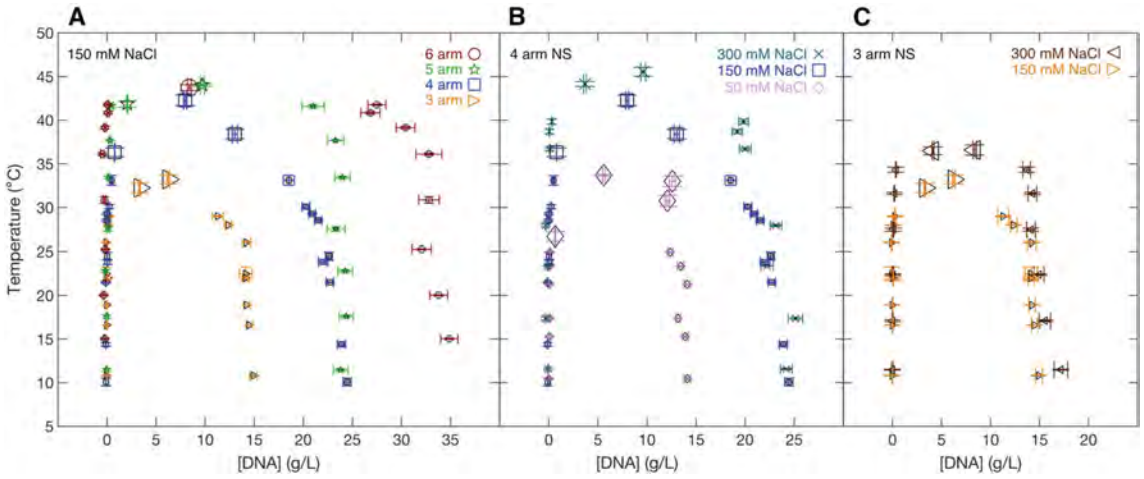

Figure 1.12: Phase diagrams of nanostars with 3-6 arms, comparing DNA concentration and temperature. Heightened nanostar valency increases the range of the phase-separating region; so too does an increase in NaCl concentration. Figure adapted from [148].

of DNA this entails, greater concentrations of cations than typically seen in DNA nanotechnologies are required [146]. Complex three-dimensional DNA origamis tend to use 12.5 – 30 mM magnesium cations, while hollow or planar structures use as little as 5 mM Mg^{2+} [166] [167] [168].

While individual nanostars form in the presence of a low concentration of cations, phase separation is not observed to occur until a great deal more shielding is present. Biffi *et al.* saw individual star formation at 48 mM NaCl, while in a phase diagram produced by Do *et al.*, phase separation of 5 µM nanostars was not seen below 200 mM NaCl [149]. Conrad *et al.* demonstrated an increase in the UCST of nanostar phase diagrams when increasing the concentration of NaCl (figure 1.12) [148]. In the case of the higher shielding potential of the divalent magnesium cation, Kengmana *et al.* annealed nanostars in isolation at 1.33 mM MgOAc, subsequently initiating droplet formation by increasing magnesium concentration to 27.5 mM at 37 ^{o}C [22].

At a given ionic concentration, an increase in DNA concentration effectively reduces the number of cations per molecule, weakening the shielding effects and all associated dependencies. This results in increased coarsening over time – at set

environmental conditions of ionic concentration and temperature, given the latter is above gel temperature, droplets will grow in diameter at a rate proportional to nanostar concentration [27].

In DNA nanostar systems, increasing [Na^+] has been found to decrease internal diffusivity while increasing star density, droplet viscosity, and surface tension at room temperature [30]. The authors suggested that this may be due to an increase in the strength of SE interactions, thereby increasing the energy requirement for initiating nanostar movement and decreasing the rate of its occurrence. They calculated the binding probabilities of their sticky end sequence at varying sodium cation concentrations, using experimentally determined nanostar concentrations. An increase in binding probability from 98.7% at 0.25 M [Na^+] to 99.5% at 1 M [Na^+] was found.

The dependence of fusion behaviour on [Na^+] is unclear. Do *et al.* explored systems of trivalent nanostars at room temperature. Fusion was seen to occur over a period of thirty minutes in 0.2 M NaCl, but did not occur at 0.5 M [149]. They proposed that the increase in [Na^+] increased the stability of inter-star bonds, thereby moving the droplet into a gel-like state. Conversely, Jeon *et al.* demonstrated that tetravalent NS droplet surface tension increased with increasing [Na^+], from 0.25 M - 1 M NaCl at 20^o [30], which would imply an increased drive towards droplet fusion (discussed below in section 1.6.2). However, the effect on droplet fusion rate was not explored in their work. We suggest the possibility that the two works describe different extremes of a system. An initial increase in [Na^+] could promote SE hybridisation, allowing for droplet formation and fusion through the shielding of backbone charges. As [Na^+] continues to increase, hybridisation could be stabilised enough that T_g moves below the system temperature, decreasing the rate of fusion. However, it is possible that droplet formation temperature would be similarly affected by a changing cation concentration. Further exploration of this effect is warranted in future works.

The effects of [Na^+] on the rate of duplexation of short DNA sequences (< 10 bp) were studied by Dupuis *et al.* [169]. They demonstrated a four-fold decrease in the dissociation constant of 8 bp duplexes when increasing [Na^+] from 25 mM to 1 M, and a forty-fold increase in the association constant, resulting in a 160-fold increase in the equilibrium constant (k_{eq}). This suggests that an increase in sodium cation concentration leads to a significant increase in the duplexation rate of short DNA sequences at a given temperature.

Processing conditions

The process of forming the DNA droplets is relatively straightforward. Typically, equimolar solutions of the various DNA strands are combined in an aqueous solution [24] [27] [149]. This solution is heated to denature any inter-strand bonds, resulting in high energy single strands. The temperature is gradually lowered, first allowing star formation as the longer sections of complementary DNA bind. As temperature decreases further, the shorter sticky ends hybridise, gradually seeing the formation of larger networks. The initial denaturation temperature is typically 90 – 95 ^oC, a point at which all secondary structures of component strands are expected to be melted. As the system is cooled, it passes through a relatively limited temperature range in which hybridisation of sticky ends occurs yet is transitory. It is within this active range that the formation of liquid droplets is possible. With further energy loss, the hybridised bases stabilise, and a hydrogel state is reached.

A two-step method of nanostar droplet formation has also been explored in the literature. In this method, nanostars are annealed under low ionic concentrations [25] [147] [22]. These conditions allow for the formation of individual nanostars, but the degree of ionic shielding is not high enough to allow for the formation of concentrated droplets. The cation concentration is then increased, triggering the isothermal formation of droplets. Droplet formation is typically conducted at an

elevated temperature to promote dynamic sticky end rearrangement. Incubation was conducted for one hour at 37 ^{o}C in the work of Kengmana *et al.*, or thirty minutes at 50 ^{o}C in Jeon *et al.* and Gao *et al.* [22] [25] [164].

Matsuura *et al.* first demonstrated that the rate of cooling in a DNA LLPS system affects the final droplet size, with a slower temperature change resulting in a larger droplet radius [158]. They saw up to a three-fold increase in droplet diameter when decreasing the rate of temperature change. Effectively, the slower rate of change allows the system more time within the active temperature range, allowing for the formation of larger spheres before being arrested in the gel state.

While earlier papers allowed spontaneous or unmonitored cooling of their systems [29] [158], more recent publications tend to maintain temperature decrease at 1 ^{o}C/min or less, maximising droplet size [24][27][149]. Furthermore, it was found that maintaining system temperature within the active range for an extended period saw larger droplets again, leading Matsuura *et al.* to attribute the droplet growth an Ostwald ripening mechanism in a shear-free system [29].

Incubation

During the system formation process, methods differ in whether the droplets are analysed immediately following temperature stabilisation, or if they are allowed to incubate for a period of time. Consider the earlier discussion of coacervate growth via Ostwald ripening or fusion (section 1.4). If nanostar droplets grow through either method, allowing the solution to stabilise prior to analysis may be of benefit.

Agarwal *et al.* demonstrated droplet growth following formation when aged at room temperature for an hour [27]. They further showed that the rate of droplet growth depended on the size of the constituent nanostars, with larger stars resulting in a higher rate of growth. Analysis of the rates of growth with respect to subunit size

and time suggested a combination of fusion and ripening mechanisms. It is noted that these experiments were performed at room temperature using nanostars of 4-nt SE, a sticky end length that produces droplets with high rates of fusion [165]. It is suspected that these structures were within the active range of the droplets, the temperature range between T_{PS} and T_g. It is within this range that sticky ends are not fully hybridised, allowing the internal movement of nanostars and the fusion of droplets. Below the gel temperature (T_g) of a droplet, growth rate is likely to decrease.

Arrangement of nanostars

There is little widespread agreement as the to the physical arrangement of nanostars in a phase separated droplet. Some assume a tetrahedral arrangement of the arms [170]; Nguyen *et al.* and Jeon *et al.*'s evidence suggests a planar configuration [146] [30]; and Rovigatti *et al.*'s computational simulations indicate an open cross structure with out-of-plane bending [170]. Early works demonstrated that droplets are able to form from a range of DNA densities, including those which correspond to a tetrahedral arrangement of stars. Biifi *et al.* thus concluded that the nanostars in phase separated droplets must be present in a tetrahedral arrangement, with a small degree of flexibility [16]. However, computational simulations of identical systems indicated that the structures were not tetrahedral, but rather held an X-shaped arrangement. Furthermore, a decrease in the system temperature contributed towards a closed-cross structure [170].

Holliday Junctions are known to form either an open cross structure, or a closed linear one, largely depending on the relative concentrations of the DNA motif and cations [155]. The negative charge of the DNA backbone typically causes a spreading of the arms, remaining in a planar structure to minimise deformation of the junction, while a sufficient ionic concentration will shield the electrostatic repulsion of the

nucleic acid backbone, allowing a closed configuration [156]. This repulsion shielding effect is known to be carried out by divalent metal cations, the most extensively studied being magnesium and calcium. Nguyen and Saleh demonstrated that this closing of a nanostar occurred in the presence of $MgCl_2$, but not in a NaCl solution, through the contraction of NS hydrogels [146]. However, when nanostars are present in a highly concentrated LLPS environment, the physical arrangement may change. Out-of-plane deformation in an open cross structure, if present, could be due to bonds between adjacent nanostars, and would potentially be aided by the presence of unpaired bases. The truth of this arrangement may not be a single structure, but a range of structures depending on the environmental conditions discussed above.

Characterisation methods for quantifying DNA coacervates

Most frequently, DNA coacervates are visualised using widefield or confocal microscopy. This allows observation of their appearance, structure, and behaviour. A common differentiator between liquid and gel states is the fusion of droplets whilst in solution, which can be readily observed via time-lapse microscopy. Further methods of defining a liquid state, or determining the liquid's properties, include microrheology and fluorescence recovery after photobleaching, both of which are indicators of internal mobility. Dynamic light scattering is additionally used to measure gel and liquid properties [16] [171].

When imaged via confocal microscopy, the contact angle of droplets against a solid substrate was found to vary with the chemical nature of the surface. DNA droplets were found to have low internal contact angles on hydrophobic glass surfaces, and high contact angles on hydrophilic glass (figure 1.13) [147]. The adsorption of BSA proteins to the hydrophobic surface of glass coverslips increased the contact angles of adhered droplets. Saleh *et al.* explained this as a reduction in the attraction between glass and droplet, increasing the interfacial tension. The adhesion to a

hydrophobic surface has also been observed to be reduced through the addition of long DNA strands to the surface of the NS droplets [164]. This was interpreted by Gao *et al.* as the polymeric surfactants passivating NS-droplet/surface interactions.

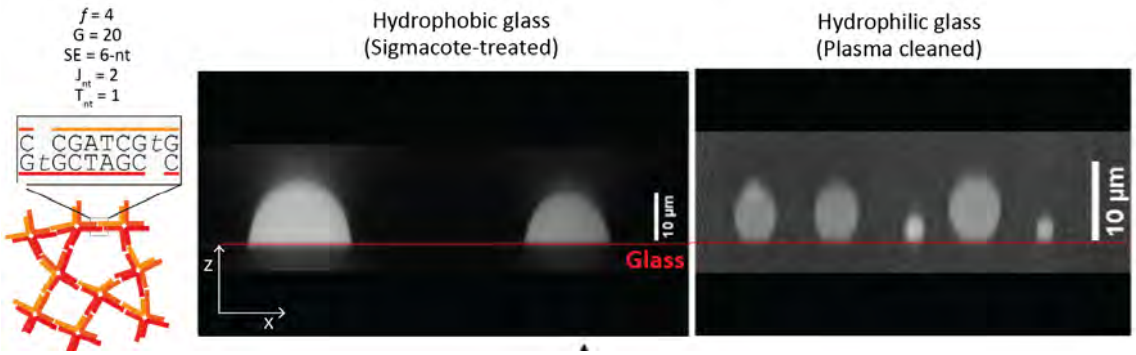

Figure 1.13: Droplet contact angle varies with surface treatment. NS droplets show a low contact angle ($\sim 70^o$) on a hydrophobic glass surface, and a high contact angle ($\sim 130^o$) on a hydrophilic glass surface. With a constant droplet surface tension, this indicates changing interfacial tension between droplet and substrate. Figure adapted from [147].

Control of droplet size

The ability to control the size of nanostar droplets is important when considering potential applications. Nanostar droplets are thought to initially form via nucleation, with further growth being the result of combined coalescence and coarsening mechanisms [27]. Coalescence is the fusion of droplets whilst in a liquid-like state. Through confocal observation on a heated stage, Sato *et al.* demonstrated droplet fusion when the solution temperature neared the phase separation temperature of the system [24]. The time required for complete droplet fusion at T_{PS} was seen to increase with sticky end stability [165]. They found that as SE length or binding strength increased, surface tension decreased. This was theorised to be caused by increasing SE hairpin formation and decreasing concentration of NSs in the droplet (figure 1.14). Simultaneously, internal droplet viscosity did not appear to be directly impacted by SE length. This led the authors to conclude that surface tension had an inverse relationship with fusion time, with a high surface tension leading to rapid

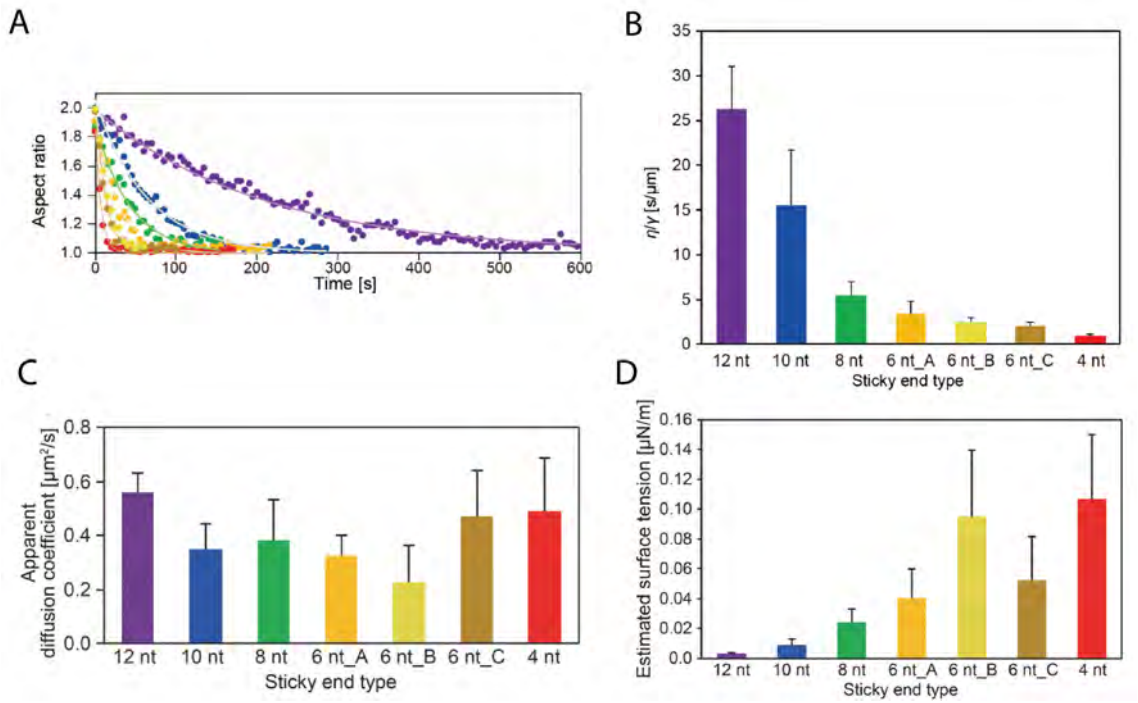

Figure 1.14: A rapid rate of droplet fusion appears to be driven by a high surface tension, and unaffected by internal viscosity. **A** The aspect ratio of droplets of different SEs undergoing fusion at T_{PS}, showing an increase with SE length (red = 6 nt to purple = 12 nt). **B** Droplet fusion rate allows calculation of inverse capillary velocities, showing an increase with sticky end length. **C** FRAP produces the apparent diffusion coefficient of nanostars, giving estimated viscosity, showing no relationship with sticky end length. **D** Inverse capillary velocity and viscosity allow estimation of surface tension, showing a decrease with sticky end length. Figure adapted from[165]

fusion. Therefore, we hypothesise that the rate of droplet fusion in solution - and thus droplet size and distribution - can be controlled using droplet surface tension.

Coarsening is the growth of large particles at the expense of smaller ones. Agarwal *et al.* demonstrated that the rate of NS droplet growth over time could not be attributed only to random fusion events, but also coarsening. The rate of growth scaled both with subunit geometry and subunit concentration [27]. This was seen to occur in samples held at a set incubation temperature, under conditions at which the nanostar sticky ends were known to result in a liquid-like droplet. The coarsening mechanism requires the active evaporation and condensation of nanostars at the surfaces of droplets. Prior coarse-grain simulations have indicated that DNA

nanostar networks never fully crystallise, but rather remain in a gel-like state [159]. It is hypothesised here that coarsening will occur over increasingly long periods of time with decreasing temperature.

1.6.3 Determining droplet formation temperature

Recent investigations have compared the melting point of the SEs to the droplet formation temperatures of LLPS systems. Such studies monitor the onset of phase separation through microscopic imaging. DNA nanostar solutions are sealed inside a viewing chamber and placed on a heated viewing stage. The stage's temperature is slowly decreased to anneal the sample. The T_{PS} is determined as the temperature at which droplet nuclei can be viewed (figure 1.15). While this technique allows for very precise identification of T_{PS}, it is inherently a low-throughput method. In a series of tetravalent nanostars of increasing SE length, droplet formation was consistently seen to occur well above the melting point of the sticky ends [24]. The mechanism behind this phenomenon is not immediately obvious – how can expanded networks form when the system is too dynamic for interstar bonds to stablise? As Sato *et al.* explain it, this behaviour can be attributed to weak interactions between the SEs. Transitory binding between even a portion of the SE base pairs would allow for dynamic hybridisation. When summed over a large population of individual nanostars, this would lead to the formation of fluid networks.

Early work also showed a marked difference in droplet formation temperature between valencies, with tetravalent stars undergoing phase separation more than fifteen degrees above trivalent stars [16]. Similar results were later observed when working with valencies of up to six arms, with a continually increasing phase separation temperature [24]. Notably, it was found that gel temperature also increased with valency, often to well above the predicted melting temperature of the SEs.

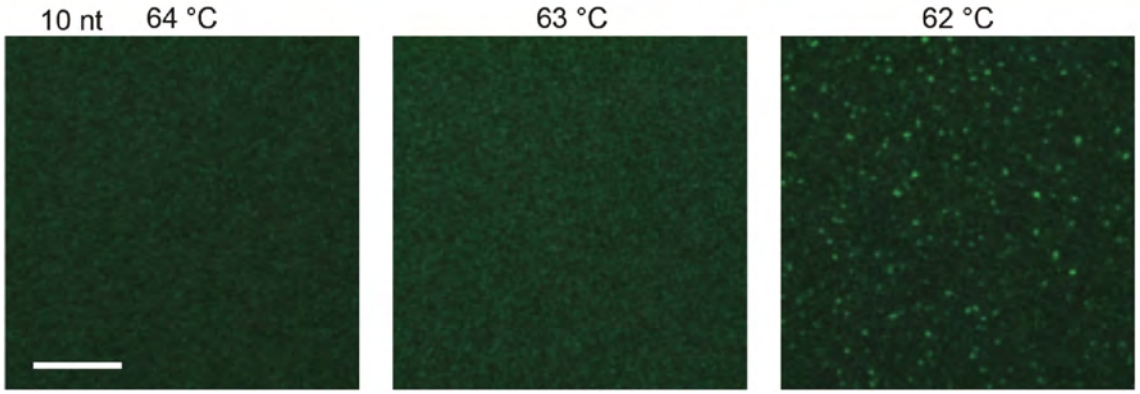

Figure 1.15: Identification of phase separation temperature through confocal microscopy. Bright nuclei become visible upon the transition from 63 - 62 ^{o}C, indicating the onset of coacervation. Figure adapted from [24].

Xing *et al.* noted that a decrease in the flexibility of the system drove the change from a liquid to gel state at a given temperature [172]. While Xing *et al.*'s modification in flexibility was performed through the removal of unpaired bases from key joints, Sato *et al.*'s increase in valency effectively achieved the same result. The greater number of bonds that are present between nanostars, which scales with the number of arms, the greater number of bonds are required to dehybridise before the nanostar can move through the system. This would increase the energy requirement for the system to remain in a liquid state, and, when combined with the previously discussed transitory binding, provides explanation for liquid and gel structure formation occurring above the SE melting temperature. By taking advantage of these two mechanisms, LLPS systems may be designed with a high degree of tunability, allowing for a range of applications.

1.6.4 Multi-phase DNA condensates

Recent papers have focused on the production of immiscible, controllable multi-droplet systems. These consist of multiple sets of nanostars with orthogonal SE sequences, creating environments of distinct, separated droplets. The inclusion of surfactant stars, containing both sets of SEs, allows for the interaction and eventual

merging of these distinct chemical environments. [25]. The interaction of these systems via surfactant is reversible upon degradation of the surfactants, allowing for the triggerable combination and separation of orthogonal droplets [24] [150].

The multi-star systems of Sato *et al.* and Jeon *et al.* combined structurally identical orthogonal-sequence nanostars with surfactant nanostars to create surface adhered droplets or lensed particles (figure 1.16) [24] [25]. In their methods, the co-annealing of fully orthogonal systems produced two distinct populations of droplets, which were shown to selectively partition ssDNA-functionalised biomolecules.

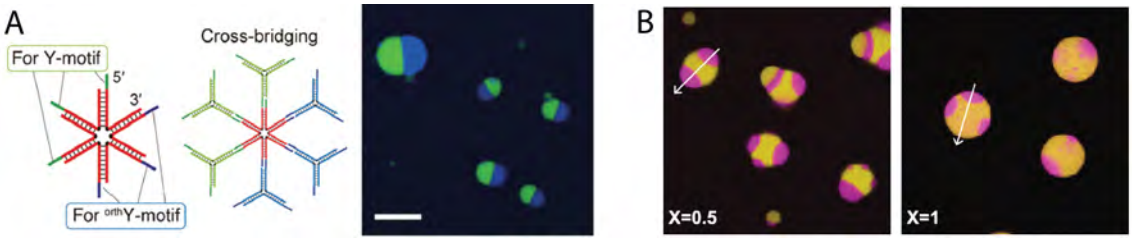

Figure 1.16: Multi-phase DNA-only droplet architectures produced in the literature. **A** Surfactant star structure and bifacial particles [24]. **B** Surface-adhered and lensed particles produced at increasing ratios of pink to yellow to surfactant stars [25].

Surfactant stars (s-Stars) in Sato *et al.* were a six-armed structure, with symmetrical SE placement that gave them complementarity to two different trimer star populations (figure 1.17) [24]. Jeon *et al.* used s-Stars of the same valency and geometry as their main phase-separating four-armed stars [25]. The cholesterol-DNA coacervate of Walczak *et al.*'s work used tetravalent cholesterol-modified core stars, six-armed s-Stars with one core-complementary sticky end and five shell-complementary SEs, and six-armed shell stars with only a single available sticky end [151].

Sato *et al.* used a Star-1:Star-2:s-Star ratio of 1:1:1 to create co-localised droplets. RNase digestion of s-Stars reduced this to 1:1:0.1, and resulted in a shift to bifacial particles. Walczak *et al.* used a Core:s-Star:Shell ratio of 1:2:10, designed to allow all s-Star and Shell SEs to be hybridised. Jeon *et al.* explored a range of Star-1:Star-2:s-Star ratios, and observed changing micro-architectures when increasing

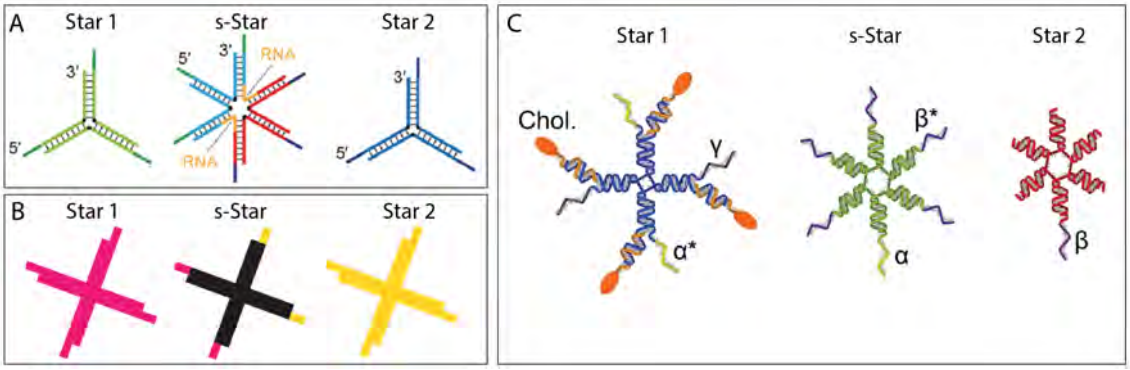

Figure 1.17: Structures of droplet stars and s-Star used in the literature. Figures adapted from **A** Sato *et al.* 2020 [24], **B** Jeon *et al.* 2020 [25], and **C** Walczak *et al.* 2021 [151].

the ratio of s-Stars to droplet stars (figure 1.18). When increasing S1:S2:sS from 1:1:0.1 to 1:1:1.5, the resulting architectures ranged from surface adhered to bi-facial to co-localised. These results show a relationship between the s-Star ratio and the resulting droplet morphology. Additionally, Walczak's work suggests a method for shell formation through the use of core and shell stars of differing droplet formation temperatures in a hybrid cholesterol-DNA NS system.

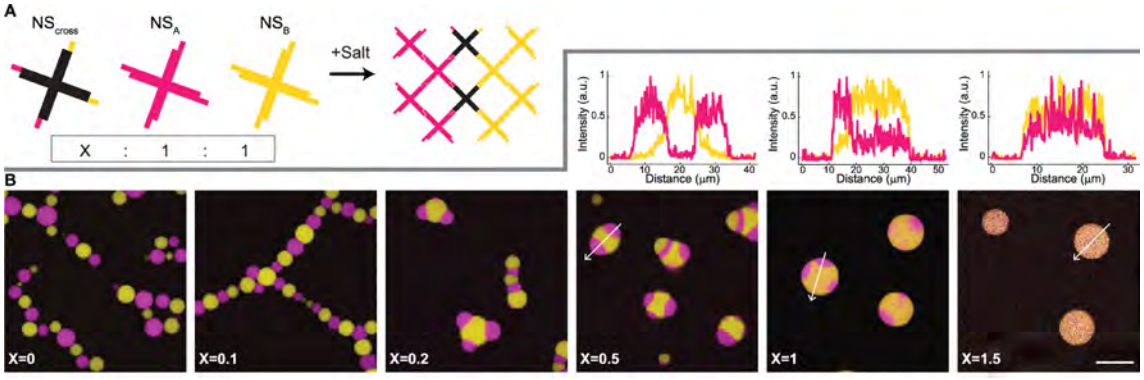

Figure 1.18: When orthogonal stars undergo LLPS, they form two distinct populations of droplets. The introduction of a surfactant star allows interaction between the two populations. With increasing surfactant star ratio, the system moves from discrete uniform droplets to alternating droplets arranged in chains, to increasing degrees of surface adhesion. At equal concentrations of nanostars and surfactant, lensed droplets form. When the surfactant is in excess, the system mixes into co-localised droplets. Figure adapted from [25].

1.6.5 Functional multi-phase coacervates

Multi-phase coacervate systems can be used to demonstrate functional behaviours (figure 1.19). Gong *et al.* used surfactant behaviour to perform computational pattern recognition [173]. Surfactant-mixed orthogonal droplets were encoded to perform AND and NOT commands, recognising the presence of miRNA inputs and producing varying droplet demixing outputs. Kengmana *et al.* and Bucci *et al.* demonstrated spatial control of RNA transcription reactions in DNA coacervates [22] [23], while Do *et al.* and Leathers *et al.* created localised strand-displacement reactions [149] [19]. Do *et al.* demonstrated that the physical proximity of nanostar droplets enhanced the rates of strand displacement reactions, even when the reaction itself was not localised in a condensate. This may be attributed to sub-micron scale clusters of nanostars, or physical crowding effects.

Okumura *et al.* used a system of nanostars which form an extended hydrogel network, instead of phase separating into concentrated droplets. They then used microfluidic devices to produce gel beads of roughly 30-60 μm size [161]. They designed a multi-star system in which droplets consisted of either (+) or (-) stars. The introduction of one star's constituent strands to the other's beads would initiate a displacement reaction and dissolve the bead. By modifying the ratio of (+) and (-) beads in solution, they could induce the selective dissolution of one population and retention of the other through temperature changes. A similar design principle could be applied to phase-separating droplets, allowing interaction or competition between orthogonal droplets.

In their work on nanostar droplet functionalisation, Sato *et al.* produced co-localised droplets through the inclusion of equimolar surfactant stars [24]. The surfactant stars were modified to contain RNA sequences at their central junction; addition of RNase A digestive enzymes split the surfactant stars and induced separation

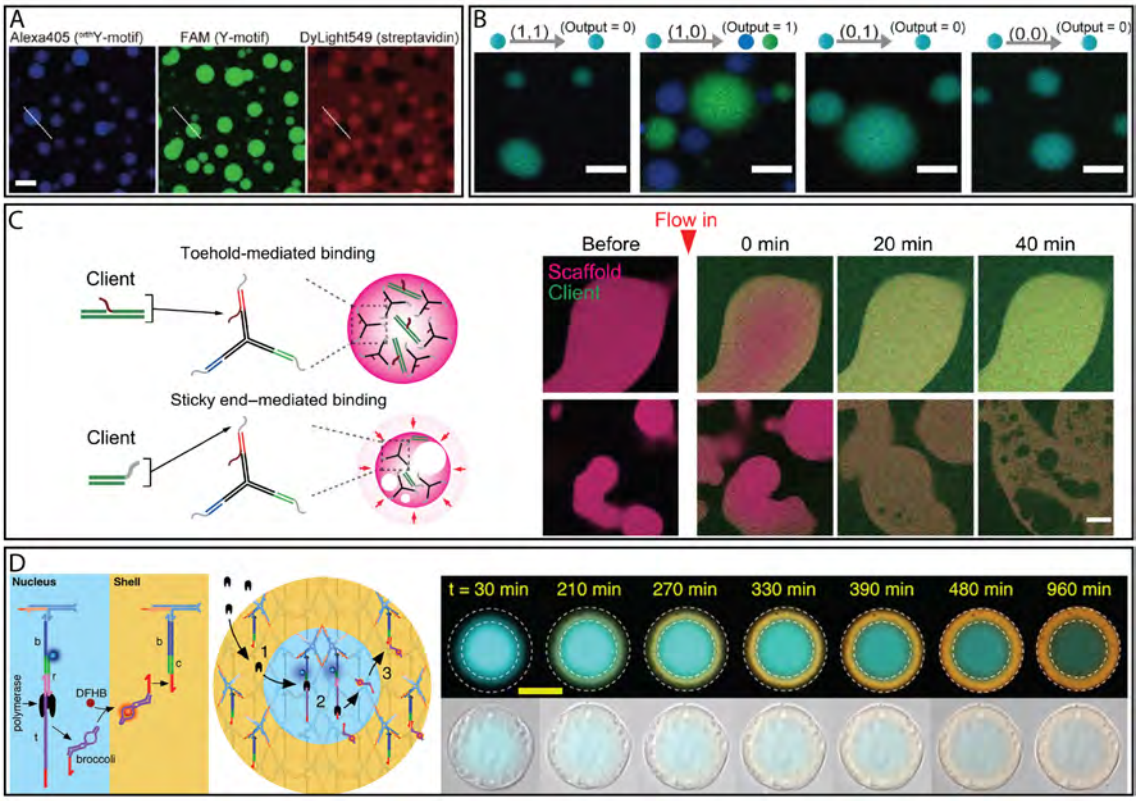

Figure 1.19: Examples of functional, multi-star coacervate systems. **A**: In a solution of two orthogonal droplet populations, one species of nanostar can be modified to possess a unique barcode ssDNA sequence. A biomolecule functionalised with the complementary barcode will compartmentalise within the selected population [24]. **B**: A mixed droplet system encoded with a $\wedge\neg$ logical operation; the surfactant will dissolve and the droplets will separate only if input A is present AND input B is NOT present [173]. **C**: Droplets formed of nanostars with two distinct toeholds. One allows non-destructive infiltration of an additive; the second causes dissolution of the droplet [149]. **D**: A phase separated droplet localises RNA transcription to create a reaction-diffusion wave [19].

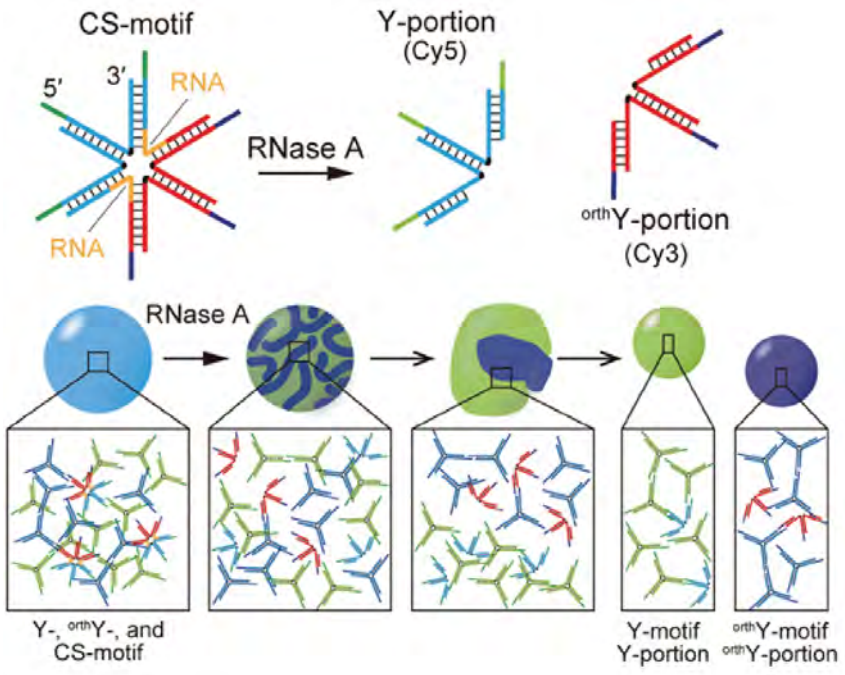

Figure 1.20: A surfactant nanostar with RNA sequences in its central junction may be digestied by RNase A. This results in the separation of a co-localised droplet into two distinct droplets. . Figure adapted from [24].

of the co-localised droplets (figure 1.20). By modulating the ratio of DNA-only and DNA-RNA surfactant stars, they created separate uniform, co-continuous, or bifacial droplets.

1.6.6 Core-shell DNA condensates

Core-shell DNA coacervates have been produced using a variety of techniques (figure 1.21). These include polymer-length DNA (∼1000 nt) phase separating through the entanglement of repeating sequences [17] [145], or droplets of flexible cholesterol-modified Holliday junctions surrounded by a corona of DNA-only HJs [151]. Droplets have also been formed of DNA nanostars, with shells formed either of sticky-ended polymer DNA [160] [164] or DNA origami tiles [28].

Depending on environmental conditions, the same polymer may form either a homogeneous solution or a phase separated system (section 1.4, figure 1.12). Tran *et*

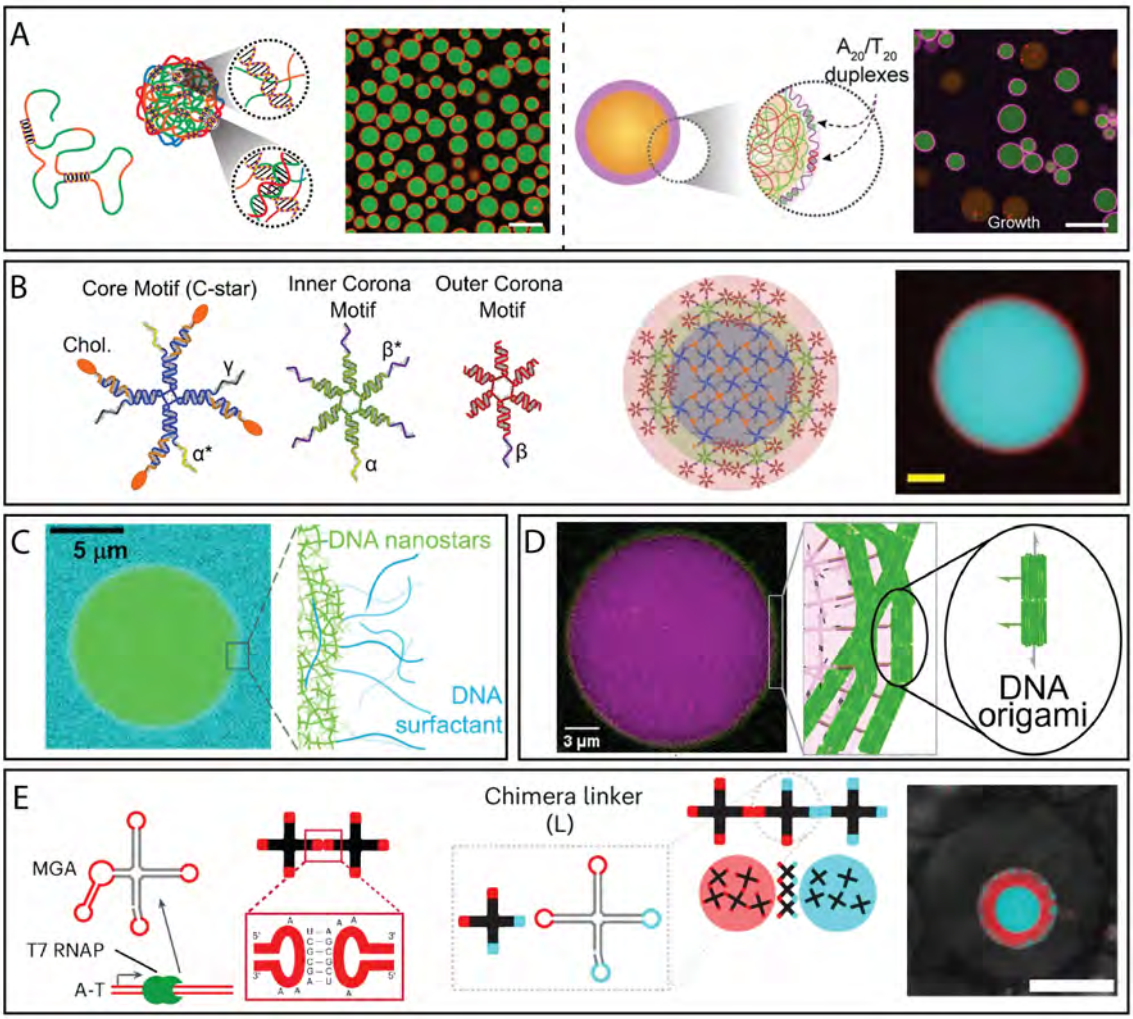

Figure 1.21: Examples of nucleic acid-based core-shell synthetic cells produced in the literature. **A**: Polymeric DNA with repeating sequences [17] [67]. **B**: DNA nanostars with cholesterol termini form coacervates through lipid interactions. Additional toeholds allow for an inner and outer corona of DNA-only nanostars [151]. **C**: LLPS DNA nanostar droplet coated with complementary polymeric DNA. The surfactant DNA is double stranded, with one or both ends possessing a short toehold to allow for interaction with the core. The polymers are too long to penetrate the core [164]. **D**: LLPS DNA nanostar droplet coated with DNA origami tiles [28]. **E**: RNA is transcribed *in situ* and forms nanostar-eqsue cross structures. Hairpin loops at the terminus of each arm allows for kissing loop interactions and phase separation. When confined inside W/O droplets, the addition of a surfactant star allows two orthogonal stars to form a core-shell structure [153].

al. demonstrated that the UCST of a nanostar system increases when confining the system within vesicles or W/O droplets, due to the reduced length scales of movement and relaxation [150]. Fabrini *et al.* expanded upon this when demonstrating *in situ* RNA transcription and nanostar droplet formation [153]. A disperse solution in the bulk phase, RNA nanostars formed phase-separated droplets when confined within W/O droplets. Combining this concept with orthogonal and surfactant RNA stars produced multi-droplet clusters, bifacial particles, and core-shell structures, depending on s-Star ratio. These systems were investigated in the context of creating organelles within synthetic cells, the DNA/RNA coacervates representing the membraneless organelle and the W/O droplet the cell. To our knowledge, the creation of bulk-phase core-shell nanostar droplets has yet to be achieved.

Alternatively, the Di Michele group synthesised DNA nanostar coacervates using cholesterol interactions in place of sticky ends [124]. In these nanomesh platforms, Leathers *et al.* established internal domains of differing functionalisation through the size-mediated infiltration of DNA invader strands [19]. The homogeneous cholesterol-DNA droplets possessed a toehold overhang. Numerous invader strands of varying lengths were simultaneously introduced to the solution. Shorter strands were able to rapidly infiltrate the dense nanostar mesh, binding to the overhangs as they did. The slower-moving longer strands possessed greater complementarity to the overhangs and displaced the short strands, creating a propagating front (figure 1.19 D). This method offers the ability to functionalise DNA coacervates after phase separation in an area-specific manner. This design principle could be leveraged for the control of DNA nanostar synthetic cells.

A factor linking most of these prior works is their use of homogeneous stars. Within each given work, each region is formed of structurally identical orthogonal nanostars linked by surfactant stars [24] [25] [153] or of a fully homogeneous droplet with different regions defined by single-stranded invaders [19]. An exception lies in the

work of Walczak *et al.*, wherein a core of cholesterol-DNA nanostars was surrounded by a shell of DNA-only nanostars [151]. This system was produced in a staggered annealing process, with initial heating to 95 ^{o}C, rapid cooling to 65 ^{o}C whereupon cholesterol-DNA cores would nucleate and grow, and a second rapid cooling to 35 ^{o}C, allowing for the formation and hybridisation of shell nanostars. While this process was successful in producing a core-shell structure, it relies upon cholesterol-cholesterol interactions for the bulk of the core. This results in limited control over and switching of droplet properties. Additionally, the high concentration of cholesterol within the core may disturb the partitioning or reactivity of encapsulated biomolecules. However, this work does take advantage of a vital concept: the control of phase separation temperature of nanostars based on physical aspects of their design.

1.6.7 Future work in DNA coacervates

A nascent field, phase separated DNA nanostars promise great potential. Claims have been made as to their possible use in drug delivery, as highly programmable biological structures [147][24][30][161]. To this end, recent studies have demonstrated their abilities in the capture and release of specific biomolecules, whether a passive collection or a targeted localisation [158][160][24][25]. Their use in biological computing has similarly been demonstrated, with proposed applications in disease detection and diagnosis [173][22]. Further applications of this technique include *in vitro* modelling of biological LLPS systems, to achieve a greater understanding of these cellular components; the study of protocellular structures and their interactions with other biomolecules; and providing a simple, controllable model in understanding complex valence- and binding strength-dependent systems [16][147][18].

1.7 Thesis aims and structure

This chapter provided an overview of the current state of research into synthetic cells, concerning their use as both artificial cells and practical reaction vessels (section 1.3). It then discussed self-assembly, a collection of biologically-inspired techniques that have been used in the creation of materials ranging from photovoltaic cells to surface coatings (section 1.4). Phase separation was focused on as a method of self-assembly, first understood in polymer science as a method of creating concentrated polymer coacervates (section 1.4.1). Liquid-liquid phase separation was then considered from a biological perspective, and shown to be a method used in the formation of membraneless synthetic cells (section 1.4.2). DNA nanotechnology was introduced as a technique for the creation of two- and three-dimensional nanoscale structures from nucleic acid polymers (section 1.5).

These concepts were then followed by a more detailed literature review of the formation of synthetic cells through the liquid-liquid phase separation of DNA nanostructures (section 1.6). It was noted that although synthetic cells with core-shell architectures have previously been produced using nucleic acid nanotechnologies, these tend to require complex, multi-step reaction pathways or combine proteins, lipids, and polymers with synthetic DNA constructs. Simple, one-pot formation of LLPS DNA coacervates is possible using DNA nanostars, and will form concentrated liquid droplets in a dilute solution. These have been extensively studied and have been shown to be able to selectively localise or exclude biomolecules; combine or split upon receiving a signal particle; and form distinct coacervates when mixed with orthogonal DNA.

However, gaps in the literature were found in that a comprehensive investigation of the physical characteristics of nanostars was needed. Additionally, a more thorough understanding of the thermodynamics of such systems must be sought, in order to

more effectively design and utilise nanostar coacervates. This is particularly necessary when using short SE sequences, due to the limitations of the NN model. Finally, although multi-star coacervate solutions have been investigated, stable DNA-only nanostar core-shell structures had yet to be achieved and investigated.

In this thesis, we aim to build upon earlier works to create phase-separating DNA nanostar droplets with a core shell-structure. This overall goal is divided into three research aims, which are used to define the structure of the following chapters:

Aim 1: Develop understanding of DNA NS droplets by systematically varying the physical characteristics of nanostars

Chapter 2 of this work concerns a detailed investigation of single nanostar droplets, particularly the interrelated effects of nanostar valency, size, SE binding strength, and environmental conditions on droplet formation. A new method for the high-throughput identification of droplet formation temperatures is developed and validated to facilitate this screening study.

Aim 2: Investigate the formation of micro-scale architectures in nanostar droplets

Chapter 3 details the production of two-star systems, expanding upon earlier works in the field to create core-shell structures. The droplet formation temperatures and the degree of complementarity between two droplet populations are explored for their effects on the resulting architectures. Core-shell structures of varying phase densities and fluidities are examined. Chapter 4 continues investigation into three-star systems.

Aim 3: Demonstrate system stability, chemical addressability, and dynamic functionalities in core-shell droplets

In Chapter 3, the ability to impart temporal stability and size control upon NS coacervate systems using a core-shell structure is demonstrated. In Chapter 4, the utility of the core-shell architecture in acting as a membrane-bound synthetic cell is demonstrated. The production of distinct, addressable chemical environments in the various droplet regions is shown, along with the passive or active exclusion of infiltrates.

A method for the identification of droplet gel temperature and droplet mixing is tested in Chapter 4, with proposals for modifications to this system in Chapter 5. Finally, Chapters 4 and 5 propose designs for dynamic structures, such as the switching of the physical characteristics of core-shell droplets or a shifting in chemical behaviour in response to an external signal.

Chapter 2

Single Star Droplets

2.1 Introduction

DNA nanostars provide a method for the development of model systems to study the formation of biological liquid-liquid phase separated droplets. The proteins and biomolecules that are typically involved in the formation of biological coacervates are highly complex (section 1.4.2). Differences in component size, shape, types of intermolecular forces present, and strength of intermolecular binding all affect the formation of membraneless liquid droplets [1] [20]. Coacervate complexity may be simplified and modelled through the use of DNA nanostars (section 1.6.2, fig. 2.1). The size and shape of DNA nanostars can be modified through their geometry. The strength of inter-star binding may be modulated through the presence of metal cations; the number of intermolecular bonds present per molecule (the valency of the star); and the strength of the sticky end bonds. Taking inspiration from biological droplets and utilising this simplified nanostar model, artificial phase separated droplets may be developed both for technological applications and to help understand this phenomenon.

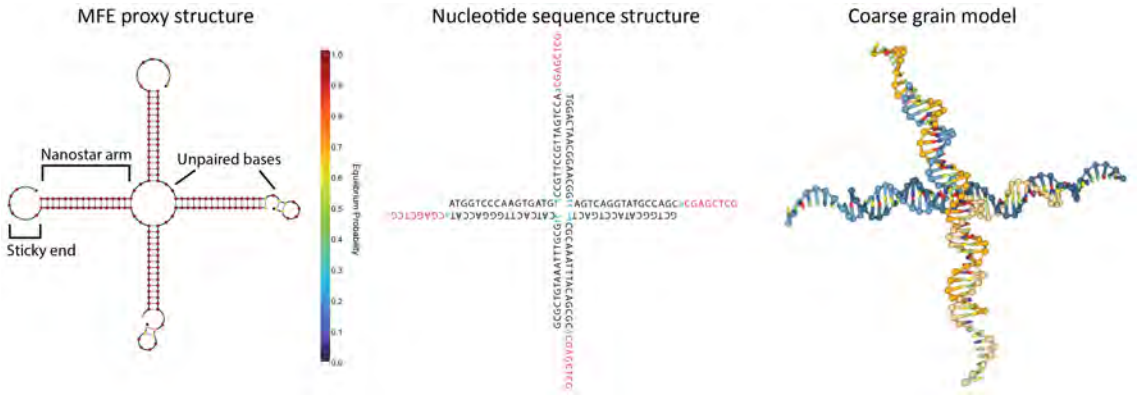

Figure 2.1: Construction of a four-armed nanostar ($f = 4$) with 8-nt sticky ends (SE). Minimum free energy structure prediction (NUPACK 2024) with sticky end, arms, and unpaired bases highlighted. Base-pair sequence of the structure (black = dsDNA arm, blue = ssDNA unpaired nt, pink = ssDNA sticky end). Coarse grain model structure prediction (oxDNA 2024).

This thesis aims to produce DNA droplets with predictable and controllable properties through the manipulation of the variables detailed above. We are motivated to create micro structures with well-defined material properties that are stable over time, in which programmable change may be induced.

This chapter addresses **Aim 1** of this thesis, intending to understand which nanostar parameters – including geometry, valency, and binding strength – provide the best control for desired droplet properties, such as size, distribution, density, and viscosity. This chapter quantifies single-star droplet populations to gain an understanding of each individual aspect as they relate to potential applications. The following sections characterise experimentally and technologically useful combinations of droplet properties. In later chapters this will be extended by investigations of multi-star systems, in order to produce LLPS droplets of greater complexity and technological applicability.

2.2 Selection of star and environmental parameters

As described in section 1.6.2, DNA nanostars take advantage of Watson-Crick-Franklin base-pairing to create non-linear structures. Nanostars (NS) consist of a small number (f) of partially complementary DNA oligomers. When annealed under appropriate conditions, the oligomers self-assemble about a central junction, forming a multi-armed structure with f arms. In addition to the number of arms, NSs vary in the length of the arms from central junction to terminus; in flexibility through the addition of unpaired bases at critical junctions; and in the inter-star binding strength through sticky end sequence design. Together, these create a large number of nanostar parameter combinations, each potentially resulting in unique droplet properties. The interrelated effects of valency, geometry, and binding strength are quantified in this section (table 2.1).

Parameter	Description	Values	References
f	Valency; number of arms	3, 4	[16] [174] [24]
G	Geometry; number of bases from centre to terminus	16 (S), 23 (L) bp	[27]
SE_L	Sticky end length	6, 8, 10 nt	[24] [165]
SE_{GC}	Sticky end GC content	50 - 75%	[160]
$SE_{\Delta G}$	Sticky end binding strength, entropy	6.6 - 12.3 kcal/mol	[30] [165]
J_{nt}	Unpaired bases at central junction	0, 2 nt	[146] [162]
R_{nt}	Unpaired bases at arm terminus	1, 3 nt	[146] [24] [175]

Table 2.1: Nanostar design parameters explored in this work. $-\Delta G$ calculated at 10 μM strand concentration, 0.5 M NaCl, and 25 ^oC.

A seminal work in the field of DNA nanostars was the 2013 examination of phase behaviour by Silvia Biffi *et al.*, which established nanostar sequence and phase separation methods [16]. A commonly used design in the literature is trivalent and tetravalent nanostars, with stress-relieving unpaired bases at the central junction (J_{nt}) and terminal joint (R_{nt}), annealed at a 0.5 ^{o}C/min ramp in a magnesium or sodium solution [30] [160] [146] [170] [159].

Building upon earlier works, we developed new variations of nanostar designs. The geometry of nanostars was expanded – smaller stars of 16 bp from terminus to centre, or larger stars at 23 bp. In conjunction, valency was varied, creating shorter-length trivalent and tetravalent stars, and longer-length tetravalent stars. Finally, sticky ends were explored in both their length and sequence design – ranging from 0 to 10 nt in length, and varying the binding strength for SEs of the same length by changing CG content and sequence. All corresponding DNA nucleotide sequences were designed using the cloud-based NUPACK software [176]. The presence of unpaired bases at the centre and termini was maintained. Together, this created a set of eighteen different nanostars, the investigation of which is detailed below.

Droplet appearance and behaviour are also affected by ionic conditions (section 1.6.2) [171] [149] [30]. DNA stars require a high concentration of environmental cations in order to phase separate. As a negatively charged particle, ssDNA will readily dissolve in water, but requires shielding of its phosphate backbone to overcome electrostatic repulsion and hybridise [177]. Investigations of nanostar droplets typically utilise sodium cations at concentrations between 0.35 – 0.5 M [24] [25]. Above the minimum cation concentration required for phase separation, further increases have been shown to affect the concentration of stars within a droplet, internal droplet viscosity, and interfacial tension, due to the heightened shielding allowing for denser packing of nanostars [30]. Considering the intended technological applications of this work and the need for stable droplets, the higher sodium concentration

of 0.5 M was generally used. Coacervate formation in the presence of magnesium ions is explored in sections 2.5.3 and A.17.

Under appropriate environmental conditions, DNA nanostars have been shown to form phase separated droplets when annealed. Of the various processes studied in the literature for the formation of DNA droplets (section 1.6.2), the one-pot process was chosen for this thesis. In this method, DNA strands and cations are mixed in solution at their final intended concentration, and annealed at a constant rate. Varying the parameters of this technique and analysing the resulting products allows for identification of key transitions in the system during annealing. T_{Hy}, T_{PS}, and T_g represent the temperatures of star formation, onset of phase separation, and gelation of the system, respectively. Knowledge of these transition points is key in later chapters of this work as it allows for quantitative comparisons of different nanostar formation processes.

Together, these varied parameters create a large phase-space of potential designs. These parameters were computationally and experimentally investigated to create a library of known, well characterised DNA nanostar droplets that may be further modified to create controllable architectures and dynamic systems.

2.3 Nanostar design

All experimental methods used in this thesis are detailed in Appendix A.

Nanostar sequences were produced using the Utilities and Design functions of the NUPACK software. Each strand was designed to be complementary to two others, with each distinct region separated by two non-pairing bases. These geometrical design constraints were input into the software, which then generated optimised DNA sequences with the corresponding secondary structure to match input geometry (table A.1). Many sequences can produce the same secondary structure, and to some extent these results are expected to be independent of sequence. The nanostar sequences produced for this work are shown in table 2.2, with complementary regions indicated by matching colours, and ssDNA shown as lower-case letters.

In comparison to the many-fold more complex structures of DNA origami, containing thousands of base pairs, nanostars are of a relatively simple design. Despite this, the base pairing specificity of DNA creates a theoretical 1.28×10^{10} different combinations of base pair sequences that may create the same physical structure of even the smallest 3S star. These theoretical sequences are limited by sequence constraints preventing, for instance, patterns of repeating bases [140].

Strand	Sequence (5' - 3')
3S-1	CCA CGC TAC GAT GCT GttTGA AGG CAG GAG TGA Ca
3S-2	GTC ACT CCT GCC TTC AttACC TGT CCG CAC CAA Ca
3S-3	GTT GGT GCG GAC AGG TttCAG CAT CGT AGC GTG Ga
Star T_M (^oC)	79.3
ΔG (kcal/mol)	-66.25
4S-1	TGG ACT AAC GGA ACG Gtt AGT CAG GTA TGC CAG Ca
4S-2	GCT GGC ATA CCT GAC Ttt CGC AAA TTT ACA GCG Ca
4S-3	GCG CTG TAA ATT TGC GttCAT CAC TTG GGA CCA Ta
4S-4	ATG GTC CCA AGT GAT Gtt CCG TTC CGT TAG TCC Aa
Star T_M (^oC)	72.5
ΔG (kcal/mol)	-85.32
4L-1	CAG CCG GTT GCC CTT AAG CTG CGa a GC ATC GGC ACA AAC GAC TGC ATC a
4L-2	GAT GCA GTC GTT TGT GCC GAT GCa aGG CTT CGC CTA CAG TCC GGC TCC a
4L-3	GGA GCC GGA CTG TAG GCG AAG CCa aCG CTC GGA GAC ACG ATT GGG CTG a
4L-4	CAG CCC AAT CGT GTC TCC GAG CGa aCG CAG CTT AAG GGC AAC CGG CTG a
Star T_M (^oC)	86.2
ΔG (kcal/mol)	-137.53

Table 2.2: Nanostar arm sequences developed in NUPACK, with the predicted T_M and Gibbs free energy of the full nanostar structure. ΔG calculated at 10 μM strand concentration, 0.5 M NaCl, and 25 ^oC.

In this work, nanostars are named for their valency, geometry, and SE sequence (figure 2.2). For example, a four stranded nanostar of the shorter strand length would be termed a 4S star. If appended with 6 nt SEs, the star is named 4S6. This design approach is modular. The same sticky end sequences are appended to every nanostar design, allowing for SE-mediated interaction between two nanostar shapes (e.g. 4L8 and 3S8) or the creation of a single star with multiple sticky ends (such as a 4L star with equal numbers of 8A and 8B SEs). Thus, this modular design allowed for greater complexity in the design of a star system than has previously been seen in the literature.

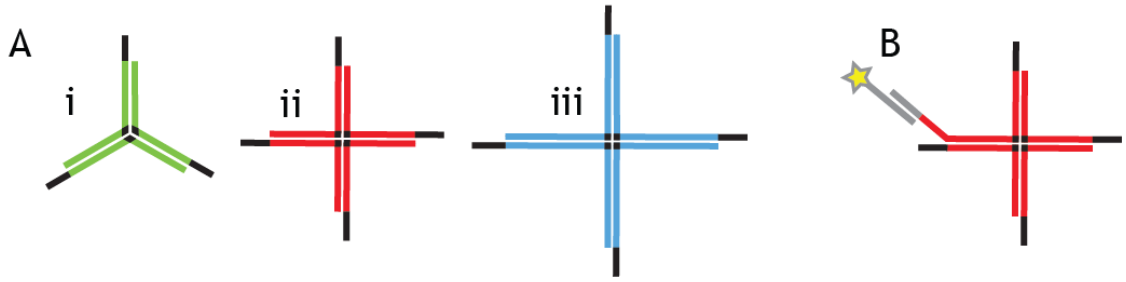

Figure 2.2: **A** General structures of 3S, 4S, and 4L nanostars (i-iii), showing increasing valency and arm length. **B** In order to visualise droplets, fluorophores are attached to nanostars.

Three basic nanostar designs were produced for this work – 3S, 4S, and 4L. In these designs, each of the f arms is complementary to two other arms, creating a star-shaped array about a central junction. The 3S and 4S stars have arms of the same length from central junction to terminus (16 bp), differing only in valency. This allowed investigation of the effect of the number of arms in nanostar behaviour. Conversely, nanostars 4S and 4L differ in geometry, with the latter having seven additional bases in its arm length. Each nanostar is of a unique sequence, here termed orthogonal stars, designed via NUPACK such that no significant hybridisation between different body designs was predicted to occur. The nanostar designs follow those of earlier works, drawing from the f, G, J_{nt}, and R_{nt} combinations seen in the literature (table 2.3). However, the sequences used here are different to those

of prior works. Multiple iterations of sequence redesign were required to produce sets of orthogonal stars.

	3S	4S	4L
Experimental designs in this thesis	$f = 3$ $G = 16$ $J_{nt} = 2$ $R_{nt} = 1$ $SE = 3$'	$f = 4$ $G = 16$ $J_{nt} = 2$ $R_{nt} = 1$ $SE = 3$'	$f = 4$ $G = 23$ $J_{nt} = 2$ $R_{nt} = 1$ $SE = 3$'
Biffi *et al.* [16]			$f = 4$ $G = 20$ $J_{nt} = 2$ $R_{nt} = 1$ $SE = 3$'
Sato *et al.* [24]	$f = 3$ $G = 16$ $J_{nt} = 2$ $R_{nt} = 0$ $SE = 5$'	$f = 4$ $G = 18$ $J_{nt} = 2$ $R_{nt} = 0$ $SE = 3$'	
Jeon *et al.* [25]			$f = 4$ $G = 21$ $J_{nt} = 0$ $R_{nt} = 1$ $SE = 5$'
Agarwal *et al.* [27]	$f = 3$ $G = 16$ $J_{nt} = 2$ $R_{nt} = 0$ $SE = 5$'		

Table 2.3: Comparison of experimental and literature DNA-only nanostar designs

For each of the three nanostar body designs used in this work, five sticky end (SE) variations were produced. These SEs were palindromic in sequence, allowing for self-recognition and binding (table 2.4). In order to prioritise SE synthesis and avoid truncation defects, sticky end sequences were appended to the 3' end of each nanostar arm (section 1.5.1). Select nanostar arm strands were modified to include a 5' extension (table A.2). These unique binding sequences allowed for the hybridisation of secondary strands to the nanostar. The secondary strands were functionalised

with fluorophores, thereby allowing visualisation of nanostar droplets.

Strand	Sequence (5' - 3')
6 nt SE	–CGA TCG
8 nt SE	–CGA GCT CG
8-A nt SE	–GCG ATC GC
8-B nt SE	–GCT ATA GC
10 nt SE	–CTG AGC TCA G

Table 2.4: Nanostar sticky end sequences

2.4 Verification of nanostar assembly

Assembly of nanostars was confirmed through Poly Acrylamide Gel Electrophoresis, and analysed using Dynamic Light Scattering and computational simulations.

Shown in figure 2.3 are the results of PAGE analysis conducted on nanostar 4L0. This star type lacks sticky ends, and was not expected to undergo multi-star hybridisation. Sharp bands in PAGE indicate a well-formed DNA product, with smears indicating truncated strands or aggregates. All samples were annealed under standard conditions (section A.3). Lane 1 contained a full nanostar, possessing strands 1-4. Lane 2 contained only three of the four strands. Lane 3 contained two orthogonal strands, which according to their nucleotide sequences should not hybridise; lane 4 contained two adjacent strands, which were designed to hybridise along half of their length. Lane 5 contained a single strand. Lane 1 was observed to contain a single sharp, high intensity band, which moved the slowest of all lanes; this band was taken to have a relative intensity of 1.0. Lane 2 contained a slightly faster band at a relative intensity of 0.85. Lanes 3 and 5 contained the fastest-moving bands, with two bands visible in lane 3. These had relative intensities of 0.24, 0.2, and 0.19,

respectively. Finally, lane 4 has a band of intensity 0.42 midway between the bands of lanes 2 and 3.

As expected, Lanes 3 and 5 appeared to show bands containing single-stranded DNA: the single strand added to lane 5, and the two non-hybridising strands of lane 3. The two strands in lane 4 hybridised to form a larger product, slowing movement through the gel. The same holds true for lane 2 and lane 1, with each containing a respectively increasing product size. This increase in apparent mass was in-line with expectations, considering each lane contained an increasing number of strands designed to be complementary. This similarly accounted for the increase in band intensity, from a minimum of 0.19 in single-stranded lane 5 to a maximum of 1.0 in the full structure of lane 1.

Each lane also contained indications of secondary products. General smearing of the band is indicative of truncated solid-phase synthesis products generating lower-mass strands. Lower mass bands of lower intensity in lanes 1 and 2 aligned with bands of lanes 3-5. These suggested a non-stoichiometric combination of strands and therefore the presence of incomplete stars. Finally, lane 1 also contained higher-mass bands above the full 4L0 structure, possibly indicative of a star dimer, as suggested by Jeon *et al.* [25]. These results supported the NUPACK predictions and design results. They are additionally in-line with the results of Biffi *et al.* and Nguyen *et al.*, who see increasing band mass when combining additional sequences of the structure, and non-stoichiometric low-mass products and dimerised high-mass products, respectively [16] [146].

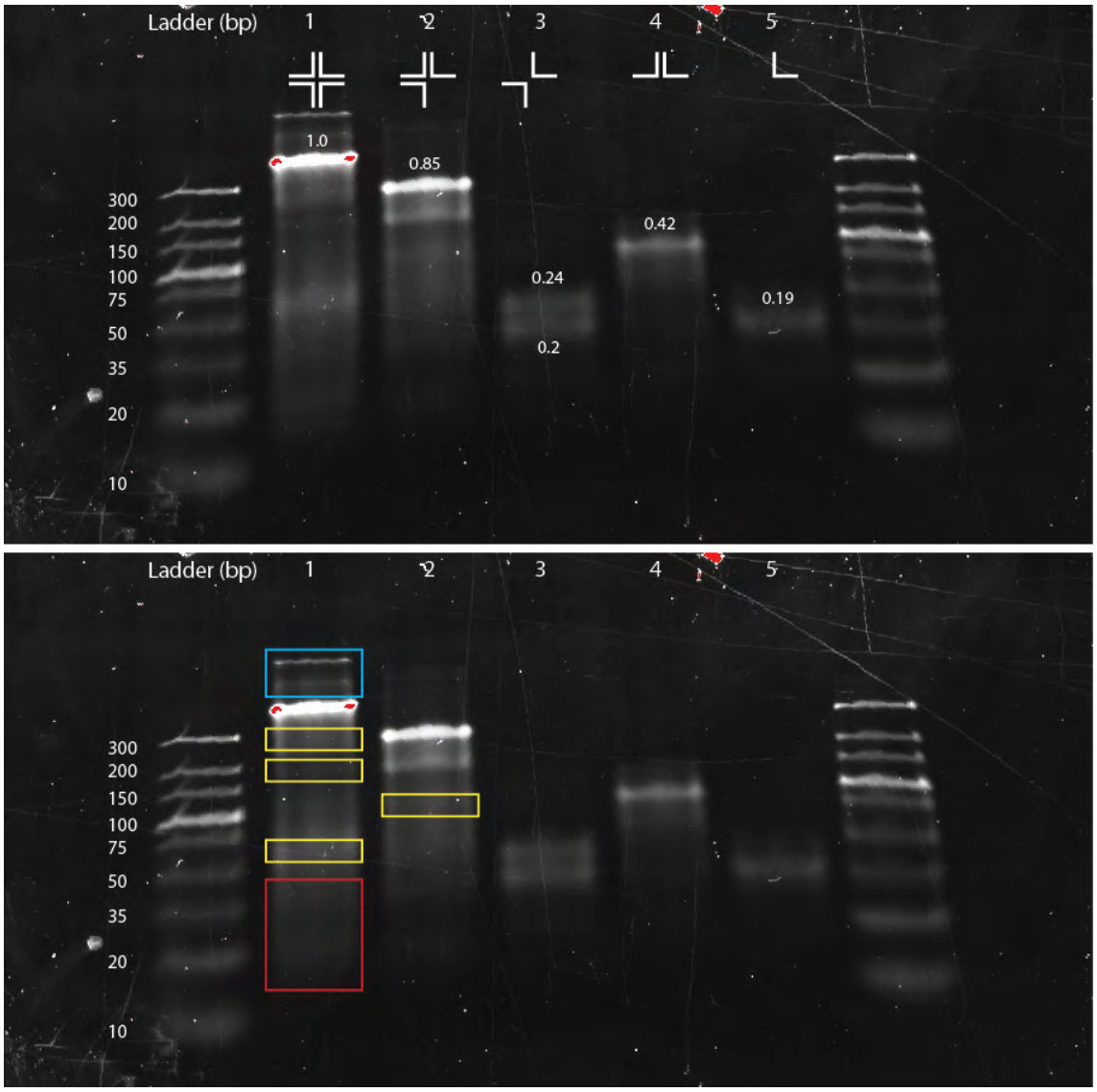

Figure 2.3: Polyacrylamide gel of 4L0 nanostar and components. Strands hybridised at 10 μM per strand, 0.5 M NaCl from 95 – 5 ^{o}C at 0.5 ^{o}C/min, and diluted 1:200 prior to loading. Conducted in Bio-Rad 10% Mini-PROTEAN TGX Precast Gel at 180 V for 40 minutes. **Upper panel**: designed structure, relative band intensity. Lane 0: DNA Ladder. Lane 1: full nanostar. Lane 2: three of four nanostar arms. Lane 3: two non-pairing arms. Lane 4: two paired arms. Lane 5: single arm. **Lower panel**: same gel, with annotated secondary products. Blue: dimerised nanostars of higher mass. Yellow: lower mass products aligned with later lanes indicating incomplete products. Red: smear of truncated DNA.

Three methods were used to estimate the size of the three 0-nt SE nanostars. The first was dynamic light scattering, a method used to measure the size distribution of particles in suspension (section A.5). This was applied to solutions of 3S0, 4S0, and 4L0 nanostars. This produced measurements of hydrodynamic size quantified by portion of the total particle population. The measured D_h of the three nanostars were fit to Gaussian functions, excluding measurements above 100 nm, averaged across three replicates. This analysis produced narrowly distributed hydrodynamic sizes for each nanostar, of 6.7 ± 0.3 nm, 7.4 ± 0.1 nm, and 8.5 ± 0.7 nm for 3S, 4S, and 4L, respectively (figure 2.4). ANOVA indicated a significant difference between each measured size (p <0.0001), aligning with the expected increase in nanostar size based on valency and arm length.

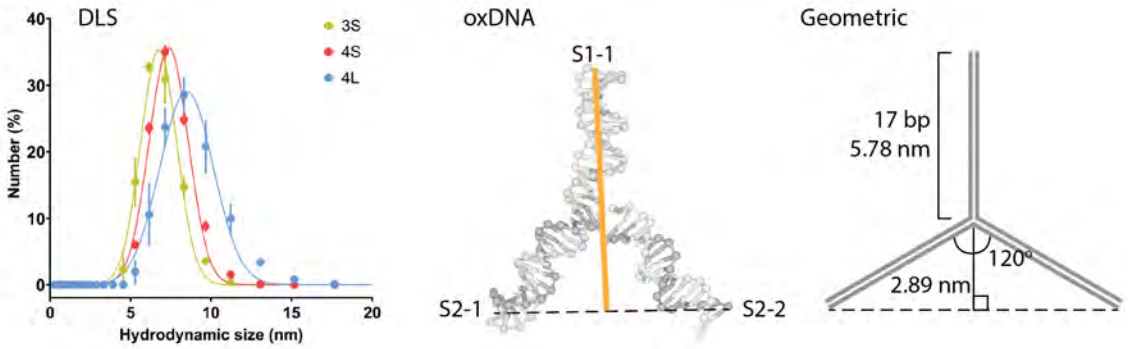

Figure 2.4: Methods of determining nanostar size. **Dynamic light scattering** results of 3S0, 4S0, and 4L0 represented as size by number (%). Nanostars annealed at standard conditions and analysed using a refractive index of 1.5826 and an extinction coefficient of 0.00; averaged across three replicates. Error bars indicate standard error about the mean. Curves are Gaussian fit models; R^2 of 0.95, 9.98, 0.91 for 3S, 4S, and 4L, respectively. **oxDNA** trimer size measurement calculation method. **Geometric** trimer size calculation method, given 1 bp = 0.34 nm.

In comparison to other polymers, double stranded DNA is inflexible, displaying a persistence length of 40 – 50 nm (∼150 bp) [109] [110]. Meanwhile, ssDNA has a much lower persistence length, at approximately 2 nm [108] [178]. Nanostar arms in this work are well within the persistence length of dsDNA, and are thus expected to behave as stiff rods. However, the ssDNA hinges at the central junction of each star allow for heightened flexibility in the nanostar structure, permitting independent

movement of each arm. This is expected to result in varied nanostar conformations, resulting in the observed variability in measured nanostar size. Given the high concentration of cations in use, the charge of the phosphate backbones would likely be sufficiently shielded to allow a linear conformation, while the flexibility of the central junction could allow the arms to bend out-of-plane into a tetrahedral arrangement [146] [179].

Nanostar sizes were also estimated using Virtual Move Monte Carlo (VMMC) simulations and simple geometric modelling. The former was achieved using the coarse-grained oxDNA simulation tool, replicating the ionic concentration and temperature of the experimental system [180]. A VMMC method is a simulation in which a series of input parameters are defined, alongside a possible range for each parameter. The simulation is repeatedly run, with each iteration of the simulation randomly generating each input from within the possible range. Nanostars 3S0, 4S0, and 4L0 were modelled in a VMMC, producing a series of physical nanostar orientations based on the randomly selected input parameters. A minimum of 150 frames were produced for each nanostar. The oxDNA program provides three-dimensional location data for every nucleotide in the simulated object. At every time-frame, the three-dimensional position of the first and last nucleotide of each strand was calculated. The dimensions of tetrameric nanostars were calculated as the average of the four end-to-end distances at every time frame. For trimer nanostars, Heron's formula was applied, as the ends of each arm could be considered the vertices of a triangle. Given that the distances between these points were known, the height of the resulting triangle in all three directions could be calculated. The average of these across all time-frames was taken as the size of the trimer nanostar.

Similar logic was followed in modelling the theoretical maximum size of nanostars through geometry, by taking the length between two base pairs in a strand of DNA to be 0.34 nm [108]. In the case of a tetrameter nanostar, the largest possible

configuration would be an cross-shaped planar conformation. The dimensions of this are taken as a square, defined by the end-to-end distance of each strand. For trimer nanostars, the maximum possible extension of all three arms would create an equilateral triangle, the height of which was similarly calculated.

The results of the VMMC simulations put the size of 3S0, 4S0, and 4L0 nanostars at 7.9 ± 1.6 nm, 9.9 ± 1.5 nm, and 13.2 ± 2.6 nm, respectively (table 2.5). The theoretical geometric sizes are 8.67 nm, 11.56 nm, and 16.32 nm. This indicated an increase in mean nanostar size with geometry and valency, with an additional increase in distribution with increasing geometry. Analysis of variance showed a significant difference between each of the VMMC-derived measurements, with P values of less than 0.0001. These results are in-line with expectations, as discussed above.

While the three measurement techniques – DLS, oxDNA, and geometric modelling – provide similar trends in their results, both theoretical models indicate a larger mean size and SD for each of the three nanostars, in comparison to the experimental results. The narrower distribution may be attributed to the bulk nature of DLS, which simultaneously measures all NS configurations and averages out the variance in the population. The increased mean nanostar size, as calculated via VMMC, suggests that the oxDNA model may underestimate the degree of bending and packing of DNA strands, thereby overestimating the size of simulated particles. Further VMMC simulations, discussed in section A.6, were used to study the physical conformations of nanostars. Altogether, this work provides the basis for the later discussion of relative nanostar sizes.

	DLS (nm ± SD) ($n = 3$)	oxDNA (nm ± SD) ($n = 150$ – 500)	Geometric (nm)
3S0	6.7 ± 0.3	7.9 ± 1.6	8.67
4S0	7.4 ± 0.1	9.9 ± 1.5	11.56
4L0	8.5 ± 0.7	13.2 ± 2.6	16.32

Table 2.5: Experimental, simulated, and theoretical nanostar sizes, including standard deviation of n repeats of measured values.

2.5 Characterisation of nanostar droplets

This section describes the formation and investigation of nanostar coacervates. The understanding and regulation of the physical characteristics of droplets is essential in later sections of this thesis, wherein complex assemblies of controllable architectures and dynamic properties are studied. In this section the characterisation of nanostar droplets is described, including size, distribution, and appearance; analysis of internal viscosity and degree of infiltration; and variations in droplet formation rate and cation concentrations.

2.5.1 Macroscale properties

Here, the factors affecting droplet shape and contact angle are considered. Following annealing (section A.3), nanostars were immediately observed by fluorescence microscopy. Further discussion of computational image analysis for droplet detection and sizing is detailed in section A.7.

In addition to the chemical conditions of annealing, the size and shape of the resulting droplets may also be affected by the physical shape and material of the chamber in which they are annealed. In this work, condensate solutions were annealed in conical 0.2 mL tubes and immediately transferred to rectangular glass viewing chambers. If condensate phase separation is initiated at physical nucleation sites, the relative smoothness of the container may affect the population size and distribution. Furthermore, the shape and aspect ratio of the container would impact the sedimentation of droplets. If annealed in a cylindrical tube, sedimentation would have a lessened impact on droplet size; however, a conical tube would concentrate together sedimenting droplets, possibly resulting in increased incidences of fusion and a larger or more polydisperse droplet size.

Most nanostars were observed to form discrete, spherical droplets. Exceptions to

this observation were 6 nt SE and 8B nt SE stars, which formed large, irregular structures instead of discrete spheres (figure 2.5). Analysis of droplet appearance and size gives insight into the physical properties and formation mechanics of nanostars. For example, irregular shapes can result either from deformation at a solid interface or an incomplete relaxation from partially-fused to spherical states [181].

When imaged, nanostar droplets were not homogeneously distributed through the solution. There was a tendency for droplets to aggregate together in chains or three-dimensional superstructures. However, three-dimensional confocal imaging made clear that these consisted of discrete droplets undergoing surface interactions, having come into contact in solution without fusing. This is in contrast to the 8B nt SE irregular structures, which saw no delineation between possible spheres, but rather continuous structures.

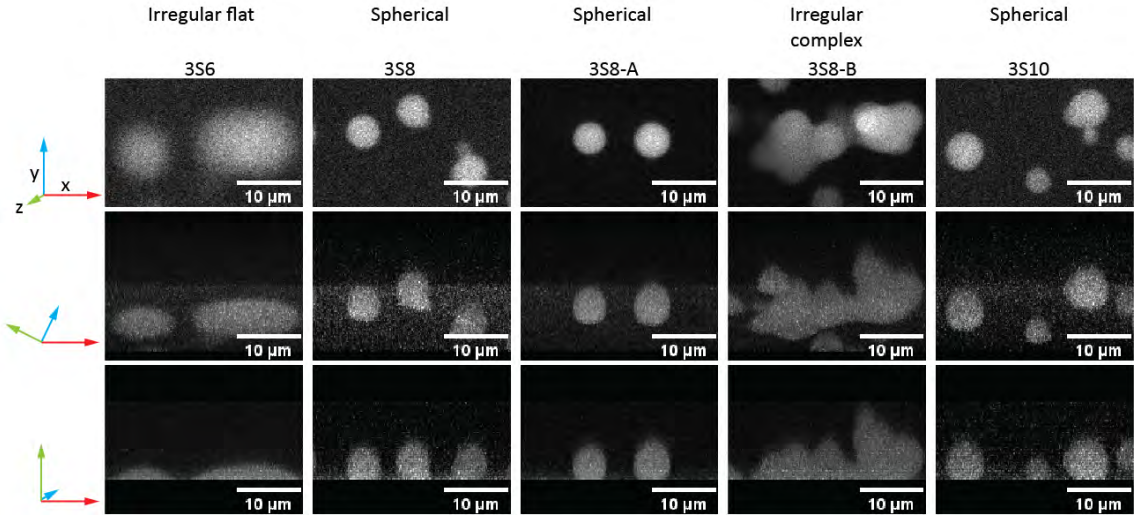

Figure 2.5: Three dimensional projections of 3S nanostar droplets, from top-down, isometric, and side-on views. Images captured at the solution/glass slide interface of the viewing chamber, with the uncoated glass creating an attractive surface for the DNA droplets. Spherical droplets are seen for 3S8, 3S8-A, and 3S10 nanostars, with a low degree of deformation against the base of the viewing chamber. 3S6 nanostars show a very high degree of wetting and deformation. 3S8-B nanostars form complex multi-core irregular structures – spheres partially fuse to create irregular objects 2-10x larger than gelated spheres. Scale bars 10 μm.

Given that all other forces remain constant, the contact angle between a liquid

droplet and a solid substrate will increase with an increasing droplet-substrate interfacial tension. High interfacial tension occurs when the attractive forces between a droplet's surface particles are greater than the attraction between the surface particles and the substrate. Thus, comparison of the contact angle of different droplets to the same surface can give indication of the relative interfacial tensions of these droplets. Variation in interfacial tension may be caused by the strength of the inter-particle bonds, or the number of bonds present between particles.

Contact angle can also be affected by the chemical nature of the surface and any surfactants present in the system (section 1.6.2). In the absence of surfactants or a changing substrate, changes in contact angle between a droplet and substrate can be a useful way to characterise a changing interfacial tension.

Higher valency stars are expected to form more bonds between stars, thereby increasing the number of transitory interactions that drive phase separation and droplet stabilisation. When quantifying droplet formation temperature, Sato *et al.* saw an increase in T_{PS} with nanostar valency. They attributed this to an increase in the number of binding points between nanostars increasing the stability of the structure [24]. Conrad *et al.* demonstrated increased droplet stability with increasing valency by showing a rise in the plateau modulus – a measure of droplet stiffness – indicting a greater number of inter-particle bonds [174]. Therefore, the increase in valency from 3S to 4S stars in the system studied in this thesis is expected to increase the average number of inter-star bonds and the droplet interfacial tension, thereby increasing the contact angle.

In this thesis, droplet contact angle on a hydrophilic glass surface was used to compare different valency droplets (figure 2.6). The low resolution of images limited precision to $\pm$ 10 ^{o}. Droplets formed of 3S6 nanostars showed a high degree of wetting against the glass substrate, with a contact angle of approximately 20^o. Stars

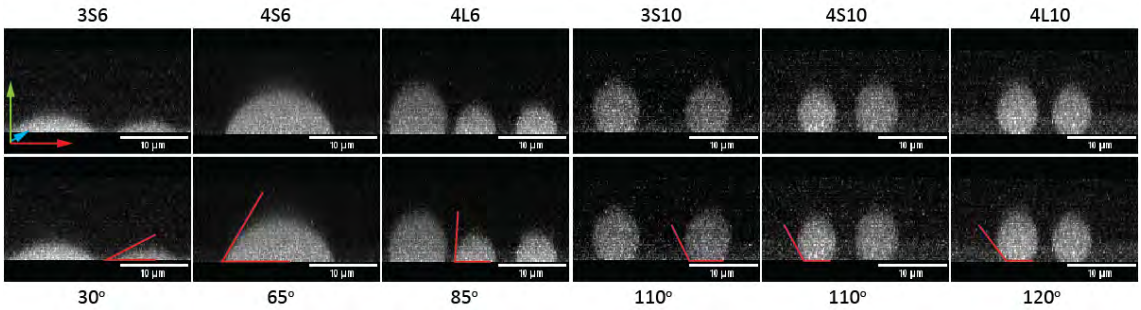

Figure 2.6: 3D projections of exemplar droplets showing three dimensional structures. In contrast to the spherical 10-nt SE droplets, 3S6, 4S6, and 4L6 droplets have decreased internal contact angles indicating lower relative interfacial tension. Scale bars 10 μm.

of increased valency, 4S6, had a higher contact angle at approximately 60^o. This agrees with the expected increase in inter-particle binding strength predicted by Sato *et al.* and Conrad *et al.* leading to an increase in interfacial tension [24] [174].

It was also observed that larger tetravalent stars displayed higher contact angles than their shorter-armed counterparts. 4L6 nanostar droplets had a contact angle of approximately 80^o, in comparison to the 60^o of 4S6 nanostars. This suggests an increase in interfacial tension with longer nanostar arms. This difference may be attributed to the body of the star, consisting of 23 bp arms in an L star versus 16 bp in an S, with ssDNA nicks at every junction and terminus (figure 2.7). Consider a sequence of nanostars in a droplet creating a continuous chain 1000 bp long. This would contain 24.4 4S6 length nanostars, or 18.2 4L6. Each additional nanostar in the chain introduces a crossover site at the central junction of the star structure, as well as two nicks in the chain at the unpaired base hinges at each terminus. Thus, the shorter stars would result in a higher density of nicks and crossovers, both of which are known to increase stretching in DNA structures [182]. This increased stretching of the 4S6 nanostar mesh could reduce the interfacial tension of the droplets in comparison to 4L6 droplets, leading to the lower contact angle measured for 4S6 droplets.

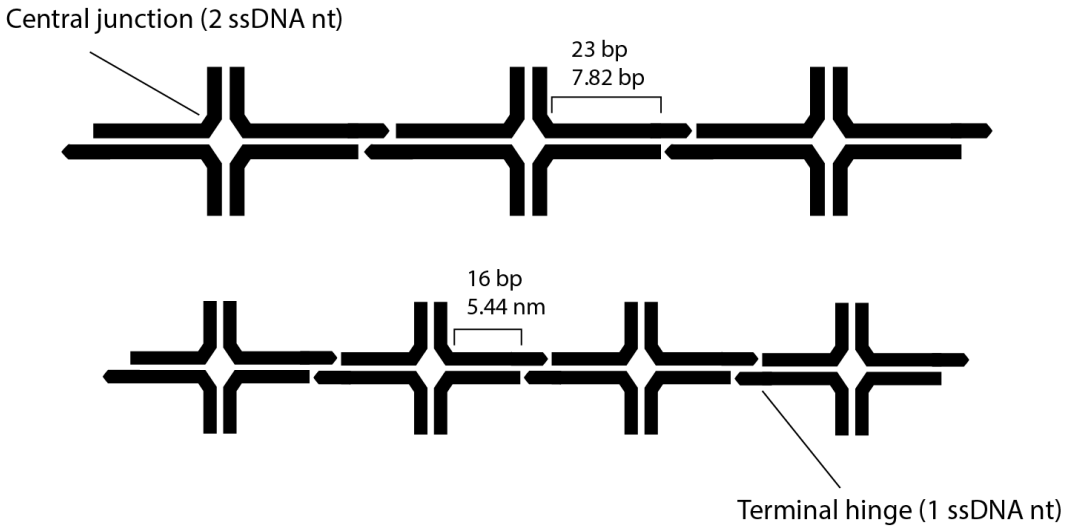

Figure 2.7: Representation of density of nicks and ssDNA over a given length for nanostars of varying arm length.

Alternatively, the interfacial tension may be considered from the perspective of free energy costs. When a nanostar moves from the bulk of a droplet to the surface, its number of available configurations becomes limited, with all arms having to face towards the centre of the droplet. It is this entropic cost which creates the interfacial tension of the condensate. When increasing the valency of the star, the limitation in arm configuration is heightened, causing greater free energy cost and thus resulting in a heightened interfacial tension. Additionally, per unit volume, a droplet consisting of S stars has a greater number of arms and sticky ends. If nanostars at the droplet were were to possess unbound sticky ends, a free energy cost would be imparted upon the system.

In droplets of higher strength SEs, droplet contact angles were uniformly high. This is potentially attributed to the higher binding strength between nanostars leading to an increase in interfacial tension. However, Sato *et al.* estimated interfacial tension through the observed fusion rate of droplets and found a decrease in interfacial tension with increasing SE length at different temperatures [165]. Additional interactions may affect these observations. For instance, it was noted earlier that

the contact angles of different droplets may be compared if all other forces remain constant. However, if the strength of NS-substrate bonds is affected by the length or sequence of the ssDNA sticky ends, then the contact angles of different droplets may not be quantitatively compared. Therefore, the above results can only lead to the qualitative interpretation that increasing valency, arm length, and SE length appear to increase droplet interfacial tension.

Trends observed in droplet size

Previously in section 1.6.2, the concept of an active range of T was introduced as the period between droplet formation and gelation, during which the droplet exists in a liquid-like state. A range of NS parameters have been proposed or observed to effect the active range (section 1.6.2, table 2.6). The strength of these competing parameters upon the active range of a nanostar droplet have not yet been determined and will be examined here.

System parameter	Hypothesised effect on active range	Hypothesised effect on growth rate	Observed effect on droplet size	Reference
Sticky end binding strength	$\Delta T_g > \Delta T_{PS}$	Decreasing interfacial tension decreases fusion rate	Smaller droplets	[24] [165]
NS valency	$\Delta T_g > \Delta T_{PS}$	Unknown	Smaller droplets	[24]
NS arm length	*Increase mesh flexibility* *Decrease* T_g *or* T_{PS}	Increase initial droplet size and coalescence in incubation	Larger droplets	[27]
NS concentration	Unknown	Increase initial droplet size and coalescence in incubation	Larger droplets	[27]
$[Na^+]$	Decreases T_g and T_{PS}	Unknown	Unknown	[149] [30]

Table 2.6: Effects of increasing nanostar production parameters on droplet size.

The ability to control the size of nanostar droplets is important when considering potential applications. Based in previous literature results, our current hypothesis is that the rate of droplet fusion in solution - and thus droplet size and distribution - can be controlled using droplet interfacial tension.

The interplay between multiple system parameters and the resulting droplet size was examined. Nanostar droplets were formed under standard conditions (section A.3) and the size of the resulting droplets was quantified (section A.7). Droplets formed of nanostars 3S6 and 4S6 ($SE_{\Delta G}$ -6.6) were found to have significantly greater mean sizes and distributions than any other droplet (figure 2.9). Nanostars of the slightly stronger 8B SE ($SE_{\Delta G}$ -8.1 kcal/mol) resulted in multi-core irregular structures with undefined size, rather than spherical droplets. Of the remaining SEs (8, 8-A, & 10 nt), there was a trend of increasing droplet size with both valency and arm length.

The large measured droplet sizes of 6-nt SE nanostars are likely partially due to the high degree of wetting experienced by these droplets. As these structures flattened across the solid substrate, their apparent radii would have significantly increased in comparison to droplets which retained their spherical shape. As such, the low temperature of gelation ($< T_R$) of these nanostars leads to an overestimation of the measured droplet size when measured at the viewing chamber interface.

No significant difference was detected between the droplet radii of 3S6 and 4S6 nanostars. However, 3S6 droplets experienced a higher degree of wetting ($\sim$30 ^{o}) against the glass substrate than 4S6 droplets ($\sim$65 ^{o}). This suggests that 4S6 droplets – in solution – are larger than their 3S6 counterparts. The size of these droplets in solution could perhaps be determined using dynamic light scattering, which can detect particles up to 10 μm in size. These results are in contrast to the results of Sato *et al.* [24]. They showed that an increase in valency decreased the active range of the system, which would suggest a decreased droplet size through

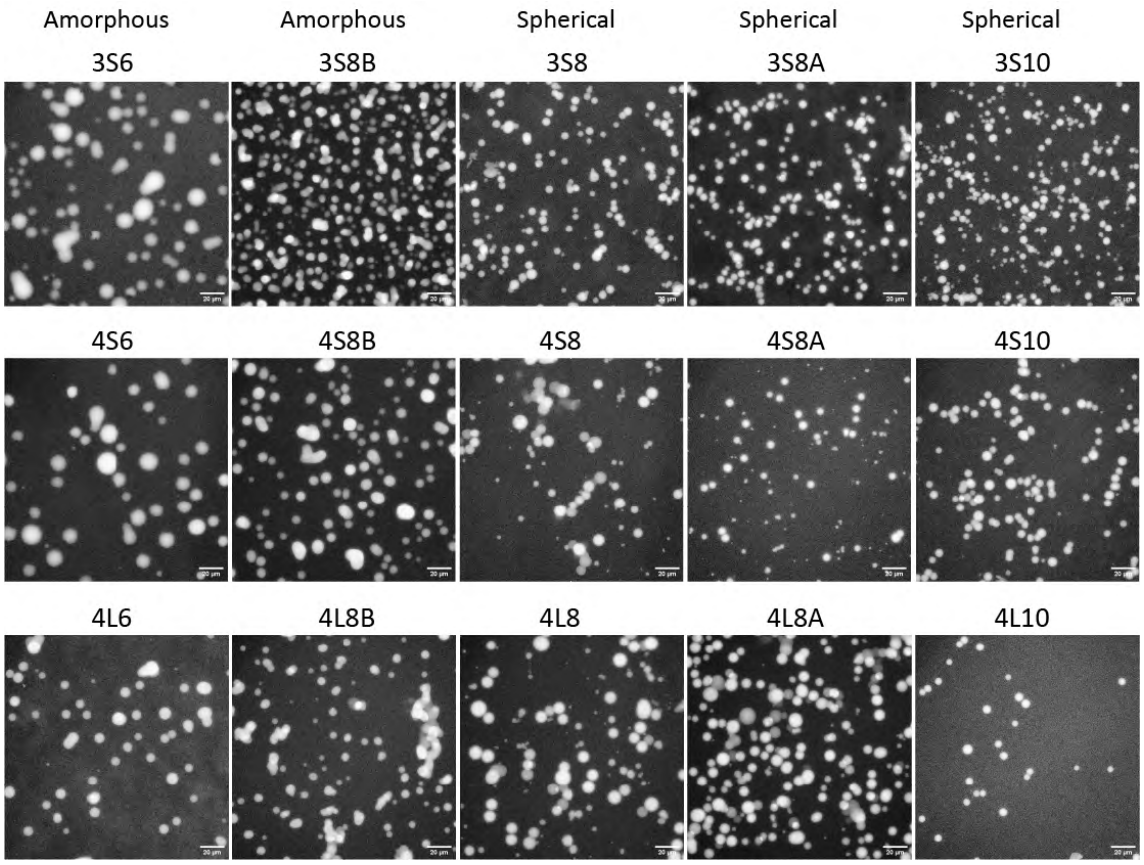

Figure 2.8: Example micrographs of phase separating DNA nanostar droplets, prepared at standard conditions of 10 μM nanostars and 0.5 M NaCl, annealed at 0.5 ^{o}C/min. Scale bars 20 μm.

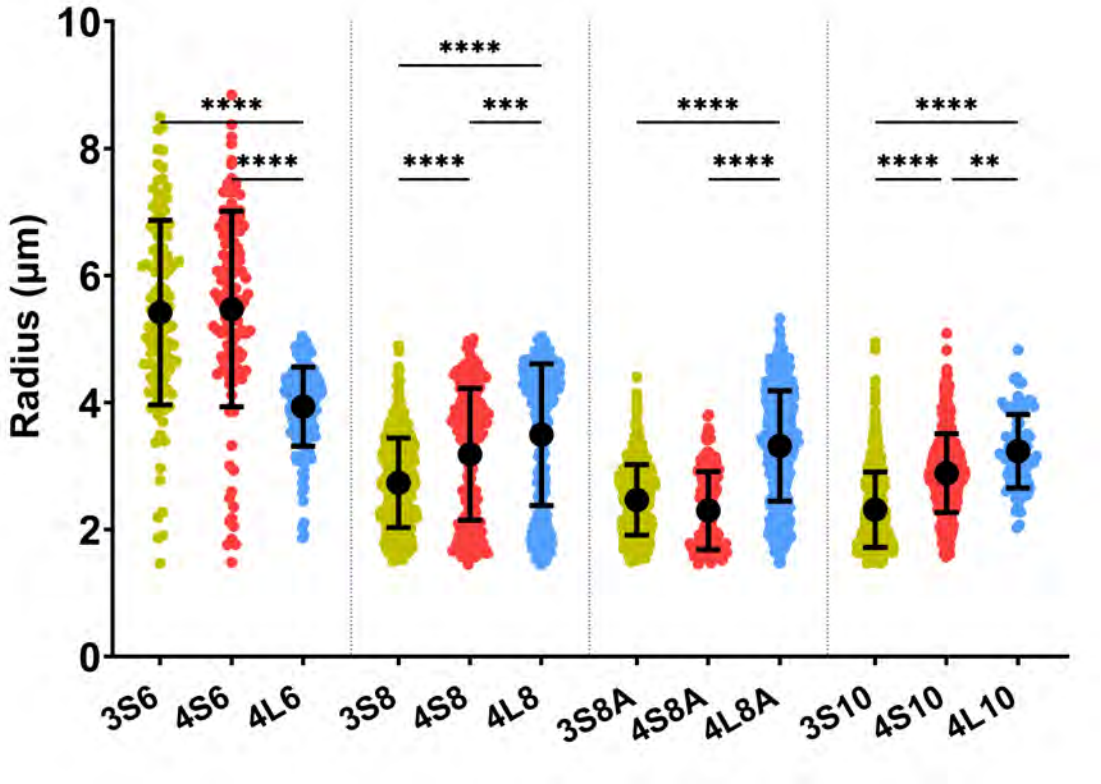

Figure 2.9: Droplet radii produced under standard conditions, shown as individual values and mean with SD. Prepared at standard conditions of 10 μM per DNA strand, 0.5 M NaCl, and 0.5 ^{o}C/min. 8-B nt SE nanostars did not form spherical droplets.

lessened opportunity for droplet growth.

Under standard conditions, stars with sticky ends of higher binding strength (8, 8-A, & 10 nt) formed spherical droplets of a lower polydispersity. Stronger binding strengths are hypothesised to increase the time required for fusion events to occur [165]. Here, a constant period of incubation was used for all samples, which may have reduced the number of fusion events for stronger SEs. At T_R, these droplets retain their spherical appearance at the coverslip interface, suggesting they are beneath their respective temperatures of gelation. The observed increase in droplet size with nanostar arm length for a given SE is in line with literature predictions, based on increased rates of fusion and coarsening [27].

Droplet size does not appear to be affected by nanostar valency, with mean size decreasing with 8A-nt SEs but increasing with others. This contradicts expectations put forth by Sato *et al.*, who show a decreasing active range with increasing valency [24]. Similarly, Sato *et al.* describe a slower rate of droplet fusion with increasing sticky end strength, which would result in a reduced droplet size [165]. However, no such trend was seen in the results of this thesis.

To summarise, the varied droplet systems studied here - considering nanostar valency, arm length, and sticky end strength - do not provide control over coacervate droplet size. Polydispersity was high across all samples. While some system parameters appear to align with mechanisms described in the literature, no consistent trends in droplet size could be identified. Nanostar sticky end strength appears to allow a level of control over droplet fluidity, with distinctions being drawn between gel-like and liquid-like droplets. Therefore, alternate methods of controlling droplet size must be sought. For instance, inspiration may be drawn from the work of Gao *et al.*, who incubated nanostar droplets alongside linear surfactant dsDNA, and saw a homogenisation of droplet sizes with increasing concentrations of surfactant [164].

2.5.2 Molecular scale properties of droplets

Internal mobility of nanostars

Droplet fluidity depends on inter-star forces, which are related to star valency and sticky end binding strength. In order to measure dynamic fluid behaviour, Fluorescence Recovery After Photobleaching was employed (section A.9).

Example fluorescence recovery traces are shown in figure 2.10, with summary data shown in figure 2.11. Data analysis and fitting are detailed in section A.9. Upon conducting FRAP analysis, droplets containing 8, 8A, and 10-nt SEs saw little to no fluorescence recovery over the five-minute capture period. This suggests a very

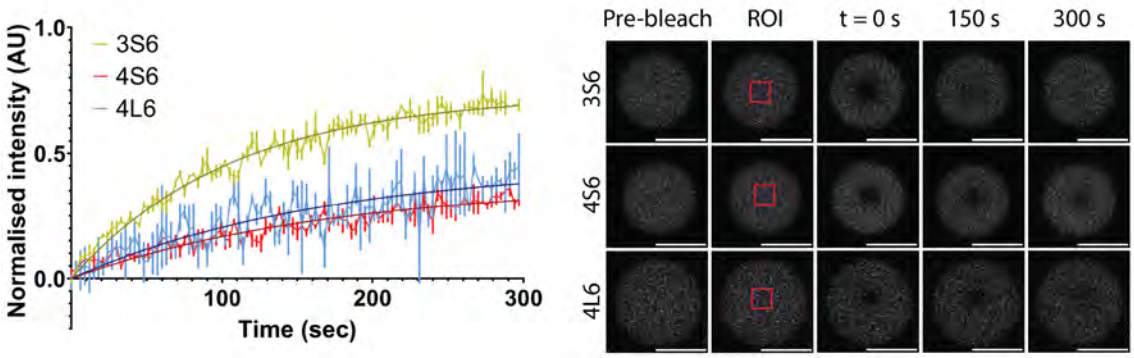

Figure 2.10: Example curves for fluorescence recovery after photobleaching for 3S6, 4S6, and 4L6 droplets prepared under standard conditions. FRAP conducted at 28 ^{o}C. Trendline showing fitted data of $n = 3$ measurements. Error bars showing standard deviation. Example images of pre- and post-bleach droplets with ROI highlighted. Scale bars 5 μm.

low mobile fraction of nanostars under testing conditions [183]. Droplets with 6 and 8B-nt SEs each saw partial recovery. 3S stars tended to have the greatest degree of internal diffusion, with mean recovery values of 73% and 76% for SEs 6-nt and 8B-nt, respectively. This confirmed the systems were above their T_g at 25 ^{o}C. Meanwhile, 4S and 4L droplets saw a lower partial mobility. At the maximum timepoint of 300 s, 4S droplets had recoveries of 38% and 31%, while 4L had 46% and 44%, for 6-nt and 8B-nt, respectively.

In the tested systems, fluorophores were appended to 5' non-SE ends of NS arms via a 22-23 nt barcode extension and a partially complementary 45 nt fluorophore strand. Nanostar populations were prepared to contain 1% fluorophore-modified stars. This extension, appended opposite to the arm's SE, may have impacted the sticky-end binding rate of the nanostar arm. If the presence of the fluorophore extension were to act as a steric block to SE-SE binding, fluorophore stars may be more mobile in the nanostar mesh when compared to non-modified stars. This effect would have been additionally prevalent when considering trimer stars as compared to tetramer. Thus, FRAP measurements may be more representative of the movement of fluorophore nanostars specifically, rather than unmodified stars in general.

The internal diffusion and mobility of nanostars was used here as a measure of droplet fluidity. Mobility contributes to the overall deformation of droplets against a solid substrate, alongside the interfacial tension of the droplet at the droplet-water interface. Droplets of higher nanostar valency had lower degrees of fluorescence recovery, even with weaker 6-nt and 8B-nt SEs. This is attributed to the greater number of inter-star bonds requiring greater energy input for star movement, resulting in lessened rotation or translation. 4L droplets had a slightly higher mobile fraction than 4S droplets. It is hypothesised that the larger distance between nanostars decreases the k_{on} of SEs, allowing slightly higher mobility at a given temperature.

Lower valency 3S nanostars have fewer bonds needing to be broken to allow nanostar movement, in comparison to tetravalent stars. This was seen to result in a high majority of droplet nanostars being part of the mobile phase, and thus a high degree of fluorescence recovery. Thus, in agreement with earlier results [24], the increased valency of 4S and 4L nanostars contributed towards decreased mobility, and suggest increased temperatures of gelation.

Fluorescence recovery after photobleaching can give qualitative indication of coacervate fluidity. If employed at a range of temperatures, it can be used to identify the gelation temperature of a droplet as the point at which fluorescence recovery begins to occur [24]. In order to obtain such data, a confocal microscope with a controllable temperature stage and enclosed system is required. If a heated stage or objective heating collar are used in a general atmosphere, the body of the microscope will act as a heat sink and prevent the accurate heating of the sample. Therefore, the entire microscope must be encased in a temperature-controlled enclosure. Alternate methods of T_g identification are discussed in Chapter 4.

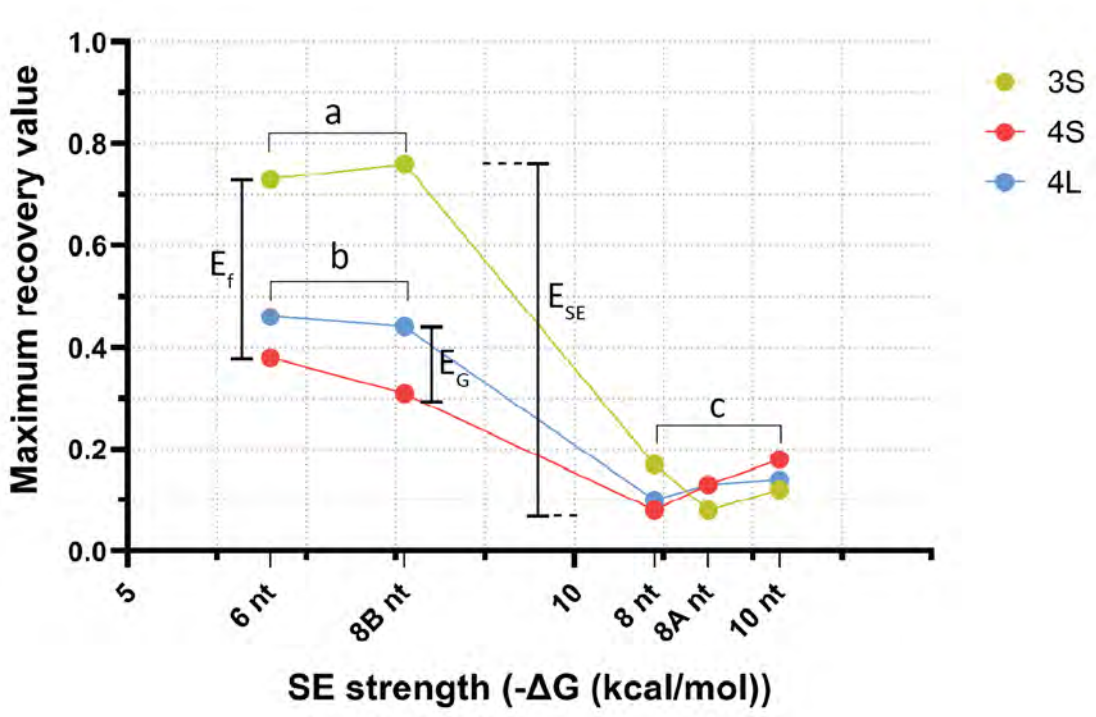

Figure 2.11: Maximum fluorescence recovery values of fit of average FRAP recovery curves at $t = 300$ *s*. **A**: High recovery = high fraction mobile phase; $T >> T_g$. **B**: Moderate recovery = low fraction mobile phase; $T > T_g$. **C**: No recovery = gelated droplet; $T < T_g$. E_f Effect of valency on fluorescence recovery. E_G Effect of arm length. E_{SE} Effect of sticky end sequence.

Nanostar mesh size

When considering potential technological applications, the mesh size of NS droplets deserves consideration. The average space between nanostars determines the maximum size of objects which may infiltrate or be captured by droplets. It is thought to be determined by arm length, number of bonds between stars, and the on vs off rate of sticky end binding. A commonly used method to determine mesh size is the passive infiltration of biomolecules of increasing size [160]. Dextran is a polysaccharide made of covalently linked chains of glucose molecules. A series of dextran particles between 4 – 70 kD in mass were combined in solution with nanostar droplets (section A.10). The degree of infiltration of each dextran gives indication of the mesh size of each droplet, with a low partition coefficient indicating a low degree of infiltration. In order to ensure homogeneous infiltration, solutions were incubated for 10 hours at 4 ^{o}C. Samples of 6 and 8B-nt SE NSs merged into extremely large irregular structures during incubation. Therefore, only 8, 8A, and 10-nt SE droplets were imaged.

Dextran infiltration was measured as the partition coefficient, the fluorescence intensity of dextran within a droplet in comparison to the dilute background. In all studied droplets, the partition coefficient was found to decrease with increasing dextran mass (figure 2.12). No significant variances in distribution of FTIC-dextran were seen across the width of droplets, indicating homogenous infiltration after ten hours. The partition coefficients of the largest studied infiltrate, 70 kD dextran, were compared between samples. For all tested SEs, 4S droplets had markedly lower rates of partitioning than 3S and 4L stars for all dextran sizes (Tukey multiple comparisons test, $p < 0.0001$) (figure 2.13 A). For both 4S and 4L stars, no significant difference in the degree of partitioning was seen between sticky ends (Tukey multiple comparisons test, ns). 3S stars had an increase in infiltration with increasing SE binding strength (0.60 $\pm$ 0.02, 0.61 $\pm$ 0.02, 0.64 $\pm$ 0.02 for 8, 8A, and 10-nt SEs)

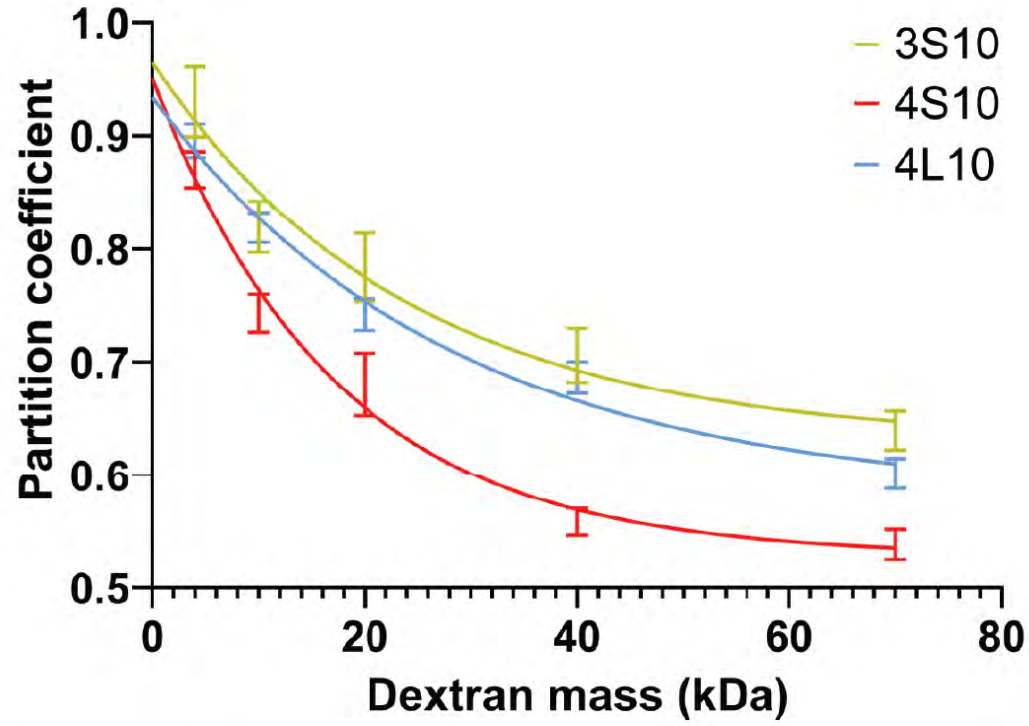

Mass (kDa)	4	10	20	40	70
R_{min} (nm)	10.58	14.36	18.09	22.80	27.47
P ± SD	0.869 ± 0.016	0.743 ±0.017	0.681 ±0.028	0.558 ±0.012	0.538 ±0.013

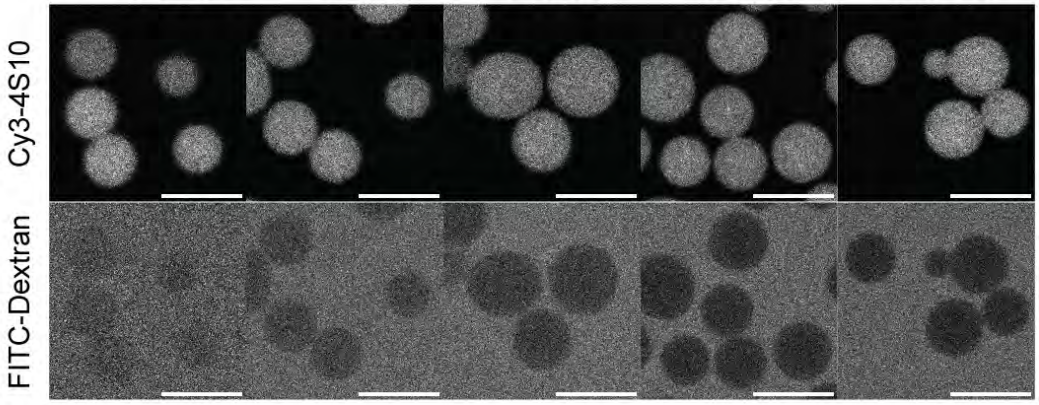

Figure 2.12: Top: Dextran infiltration in 3S10, 4S10, and 4L10 droplets, measured as ratio of fluorescence intensity of dextran inside and outside of droplets. Average of $n = 10$ droplets. Curve showing one-phase exponential decay, $R^2 > 0.91$. Error bars showing standard deviation. **Bottom**: Example micrographs of dextran infiltration in 4S10 droplets. Scale bars 10 μm.

(figure 2.13 B). This suggests that 4S nanostars form a denser mesh network than 3S or 4L.

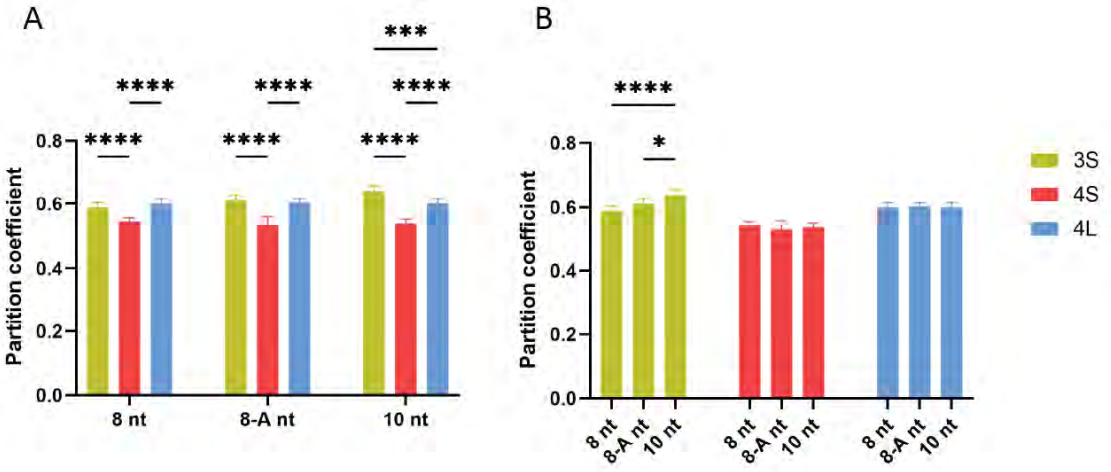

Figure 2.13: Experimentally determined partition coefficients of 70 kD dextran in nanostar droplets. **A**: When comparing droplets by nanostar sticky end, the partition coefficient in 4S nanostars is significantly lower than in 3S or 4L. **B**: When comparing droplets by nanostar valency and arm length, no difference is seen between sticky ends for 4S or 4L nanostars, while partitioning in 3S nanostars increases with SE binding strength. Data shown as mean ± SD, with results of Tukey multiple comparisons test statistical analysis, $n = 9$.

A possible explanation for the difference in partitioning is a higher packing density of 4S nanostars in comparison to 4L. Additionally, the higher valency compared to the trivalent 3S would cause a higher average number of inter-particle bonds between adjacent stars. The increased infiltration in 3S10 droplets in comparison to 3S8 or 3S8-A may be the result of the increased inter-particle distance afforded by the lengthier sticky end. The reason this effect is not seen in tetravalent stars is unclear. Perhaps the slight increase in mesh size afforded by the 2 nt increase in SE length is outweighed by the increased inter-particle binding of the higher valency stars. The inter-star distance of various nanostars was further studied using VMMC simulations (section A.11).

The method of dextran infiltration to establish the mesh size of droplets was previously used by Nguyen *et al.* in studying nanostars of [$f = 4$, $G = 20$ bp, $SE_L = 6$

nt] [160]. They were able to establish a numerical estimation of the mesh size, using the dextran mass at which partitioning was beneath 0.5. They found a partition coefficient of 0.52 ± 0.03 at a dextran mass of 40 kD, which has an equivalent hydrodynamic diameter of 9 nm. Thus, the mesh size of the droplet was estimated to be approximately 9 nm. However, this method of estimation cannot be applied to the results of this thesis, as no nanostar achieved partitioning beneath 0.5. In the work of Nguyen *et al.,* a concentration of 1.0 M NaCl was used, in comparison to the 0.5 M here [160]. As previously established, an increase in $[Na^+]$ tends to move droplets towards a gel-like state [149]. The lower $[Na^+]$ used in this thesis may thus result in droplets with higher permeability. Therefore, in order to quantitatively establish mesh size of the droplets in this work, a higher cation concentration or larger dextran infiltrates would be required. However, here we have quantified the relative behaviour of nanostar droplets.

2.5.3 Effects of assembly conditions

DNA nanostar phase separation is a dynamic, cooperative process – it does not occur instantaneously, but rather progresses slowly over time. Following the onset of phase separation, when the reaction temperature moves below T_{PS} into the active range, droplet formation is initiated through nucleation and progresses through coarsening and fusion. These growth mechanisms continue throughout the active phase until the gelation temperature is reached, whereupon sticky end on-rates increase beyond off-rates, halting overall change in the system. As both growth mechanisms are time-based, relying on chance meetings of nanostars and droplets in solution, the extent of droplet growth may be controlled through modulation of the annealing rate [29].

System annealing rate

The rate at which nanostar systems are annealed directly affects the temporal length of the active range. An exemplar nanostar, 4S10, was chosen for the homogeneous size and high density of its droplets under standard conditions, and annealed at rates between 0.1 – 5 ^{o}C/min (figure 2.14). Slow annealing rates, 0.1 and 0.2 ^{o}C/min, resulted in the formation of extremely large irregular super-structures up to 50 μm in size. As the annealing rate of the system was increased, mean droplet size and size distribution grew progressively smaller, from 3.04 $\pm$ 0.76 μm SD at 0.5 ^{o}C/min to 1.5 $\pm$ 0.16 μm SD at 5 ^{o}C/min.

At slower rates of cooling, fusion between droplets proceeds over a longer period of time. Conversely, reducing the period of time during which sticky ends are able to actively hybridise reduces the number opportunities for droplet fusion, thereby resulting in a reduced droplet size. Furthermore, droplet populations appeared to increase in homogeneity with an increase in annealing rate. Nucleating as spontaneously annealing clusters of nanostars, DNA droplets grow through fusion and coarsening of these clusters. Any minor non-homogeneities in the initial system would be compounded the longer the random incidences of fusion are allowed to continue. Given a shorter period of time in which fusion may occur, fewer inhomogeneities in droplet size may result. Thus, 0.5 ^{o}C/min was determined to be the slowest possible rate for spherical droplet formation under the conditions of this study, and control over droplet size through annealing rate was demonstrated.

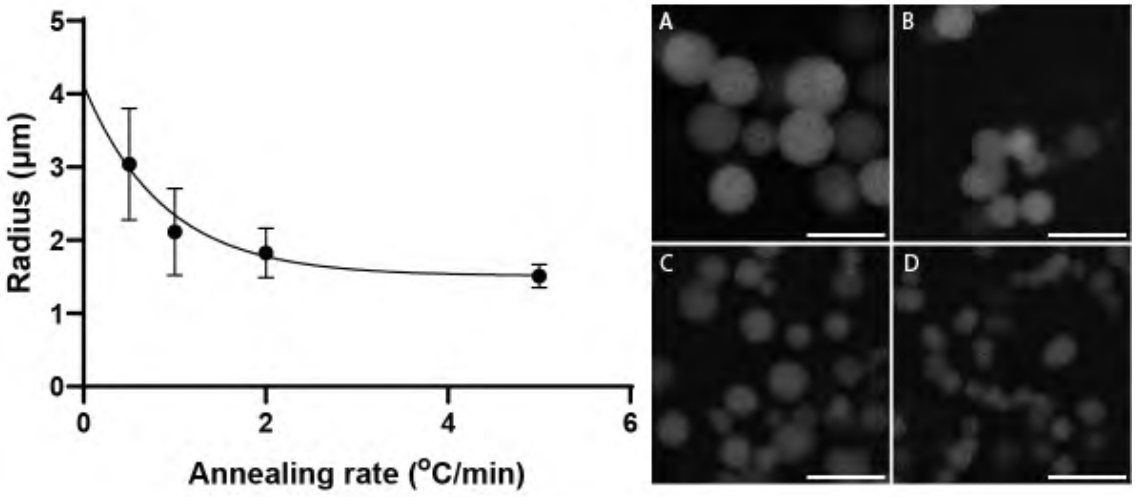

Figure 2.14: Decreasing radii of 4S10 nanostar droplets produced at increasing annealing rates; line drawn as visual guide. Error bars showing standard deviation; n = 68-612. Example images of (A-D) 0.5, 1, 2, and 5 ^{o}C/min annealing rates. Scale bars 10 μm.

Nanostar and sodium concentrations

The respective concentrations of DNA and cations in a system have inverse effects (section 1.6.2). Increasing the concentration of oligomers in solution while maintaining constant [Na^+] decreases the number of cations per strand, while increasing [Na^+] with constant DNA concentration will increase this ratio. Due to the inherent repulsion of the phosphate backbone, the shielding afforded by cation complexation is required for DNA hybridisation and nanostar phase separation [184]. As the ratio between cation and DNA concentration increases, so too does the potential for stronger binding between and closer packing of DNA strands.

Analysis of the sticky end binding sequence in NUPACK was conducted here, simulating 1 μM SE strands at 25 ^{o}C at varying NaCl concentrations. In increasing [Na^+] from 0.25 M to 1 M, a corresponding decrease in Gibbs free energy of the SE-SE duplex was seen, from -10.577 kcal/mol to -11.484 kcal/mol. This indicates an increasing bond strength between sticky ends with an increased sodium concentration, aligning with the predictions of Jeon *et al.* [30]. Thus, we hypothesise that for a given nanostar, the temperature of gelation will increase with increasing sodium cation concentration.

Four condition variations were explored to investigate the above effects on this system (figure 2.15). Standard droplet production conditions see DNA combined at 10 μM per strand and [Na^+] at 0.5 M. New samples were prepared containing a lower total DNA concentration; an increased concentration of sodium cations; a lower per-nanostar DNA concentration; and a switch to the divalent magnesium chloride in place of the monovalent sodium.

Firstly, we compared a system with a decreased per-strand concentration of DNA. An NS concentration of 5 μM and maximum total concentration of DNA 20 μM, was compared to the 10/40 μM of the standard system. Here, the effective num-

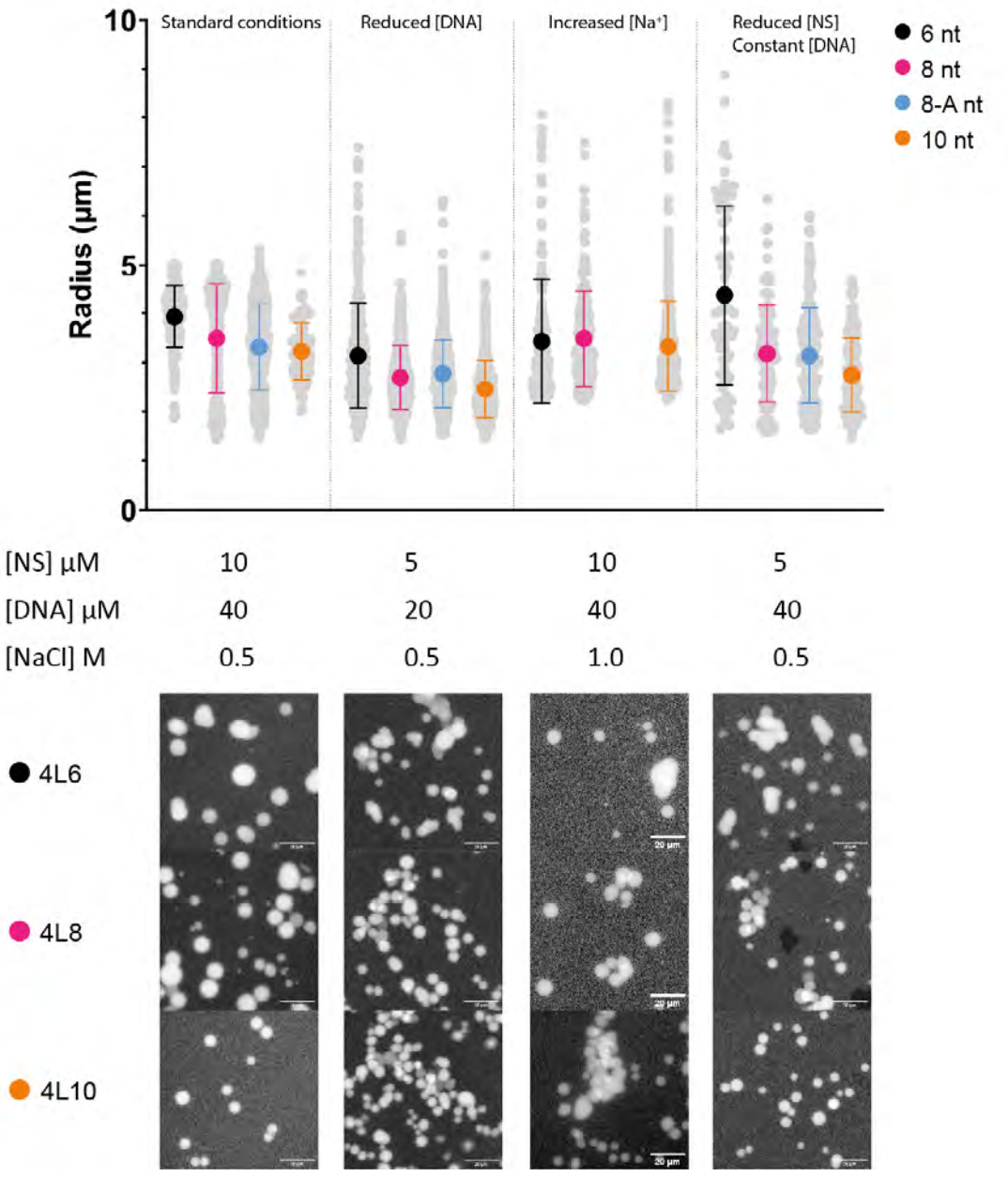

Figure 2.15: Radii of droplets formed under varying production conditions, showing mean and standard deviation. Scale bars 20 μm.

ber of cations available per DNA strand increased 2-fold. Under these conditions, the mean droplet radii decreased while the observed number of droplets tended to increase (table 2.7). The droplets were also observed to have a greater tendency to stick together in multi-droplet aggregates, particularly 6-nt SE droplets. The observed increase in population distribution was the result of multi-droplet aggregates; while these can visually be identified as individual droplets, the automated droplet detection algorithms (as discussed in section A.7) struggled to distinguish between closely packed droplets. Dupuis *et al.* studied the effects of [Na^+] on the binding rates of short DNA sequences [169] (section 1.6.2). The lengths studied are comparable to the sticky ends used in this work (6 - 10 nt). Therefore, their observations are possibly applicable to this system. It is hypothesised that an increase in the cation:DNA ratio will increase the T_g, due to the increase in k_{eq} predicted by Dupuis *et al.*. This may lead to a decrease in the number of fusion events, resulting in a reduced droplet size.

Nanostar concentration has previously been shown to directly affect droplet size, with droplet size scaling linearly with nanostar concentration [27]. Agarwal *et al.* saw a similar effect when increasing nanostar arm length at constant [NS] and [Na^+]. Both experimental variations result in a decrease in number of cations available per strand. Therefore, the decrease in droplet size with reduced DNA concentration observed here is in line with previously observed trends.

Following this, we considered the effects of an increase in sodium concentration. When maintaining standard DNA concentration and increasing [Na^+] to 1.0 M, a decrease in mean droplet size and increase in distribution were again observed. Simultaneously, an increase in the internal contact angle of 6-nt SE droplets was noted, suggesting an increase in droplet interfacial tension. Additionally, significantly larger droplets than the standard mean were occasionally noted, distinct from multi-droplet aggregates in their homogeneous appearance.

Nanostar	4L6	4L8	4L8A	4L10
Radius ± SD (μm)				
10/40 μM	3.93 ± 0.62	3.49 ± 1.12	3.32 ± 0.87	3.23 0.58±
5/20 μM	3.14 ± 1.06	2.70 ± 0.65	2.78 ± 0.69	2.46 ± 0.58
Average count per 10 μm^2				
10/40 μM	0.156	0.273	0.577	0.089
5/20 μM	0.290	0.461	0.516	0.622

Table 2.7: Mean droplet sizes and densities when decreasing total DNA concentration at a constant cation concentration. The mean number of detected droplets across three sample images was found; each image had dimensions of 184.7 μm^2. The mean droplet count was divided by $(18.47)^2$ to estimate the number of droplets per 10 μm^2.

The decrease in droplet size followed the same trend as when decreasing [DNA], and was here attributed to the same causes: the increased cation:DNA ratio was suspected to increase the droplet gelation temperature, reducing opportunities for droplet fusion or coarsening. The cause of the larger droplets was uncertain. Do *et al.* link increasing [Na^+] to an enhanced SE-SE binding stability, slowing the rate of fusion between droplets [149]. Similarly, the work of Dupuis *et al.* suggests an increase in SE-SE bond stability with increasing sodium cation concentration [169]. This may provide an explanation for an increase in observed incidences of aggregates, but does not account for the larger spherical droplets seen.

As discussed below in section 2.6.2, the temperature of phase separation of DNA nanostars does not appear to significantly vary when increasing [Na^+] from 0.5 M to 1 M NaCl. Therefore, an increase in [Na^+] is hypothesised to increase the temperature of gelation of droplets and thus decrease their active range. This reduced period of time during which droplet growth may occur, given a constant rate of annealing, is thereby expected to result in a reduced overall droplet size.

The system parameters were further varied by decreasing DNA nanostar concentration while maintaining total DNA concentration, through the addition of non-reacting DNA dimers as bulking strands. This decreased the nanostar concentration while maintaining effective [Na^+]:[DNA], allowing interrogation of the effect of DNA nanostar concentration in isolation. Under these conditions, nanostar radii decreased in comparison to the standard condition, but not to the degree seen when the total DNA concentration was reduced. Under these conditions, 6-SE droplets showed a similar contact angle at the glass interface to the standard condition. In this experiment, the presence of the bulking strands ensured the per-strand concentration of sodium cations remained constant with the standard. This supports the hypothesis that an increase in droplet interfacial tension is linked to an increase in the [Na^+]:[DNA] ratio. If droplets prepared under these conditions had a similar gelation temperature to the standard, and thus a similar active range, then the reduced droplet size was likely the result of the reduced concentration of DNA nanostars available for phase separation.

Although the effects of [Na^+] and nanostar concentration appear to have predictable effects on the size of the resulting droplets, it does allow predictive control of droplet size or homogeneity. Broad variations in droplet size are still common, as are the formation of multi-droplet aggregates. Thus, a different method of control is required to modulate droplet size, homogeneity, and separation. Efforts to this effect are discussed in Chapter 3.

Droplet formation using magnesium cations

The formation of nanostar droplets using magnesium cations in place of sodium cations was attempted, using concentrations between 0.01 – 0.5 M $MgCl_2$ (figure 2.16). No condition was found wherein all nanostars could form distinct droplets. In all tested conditions, the majority of nanostars formed irregular particles beneath

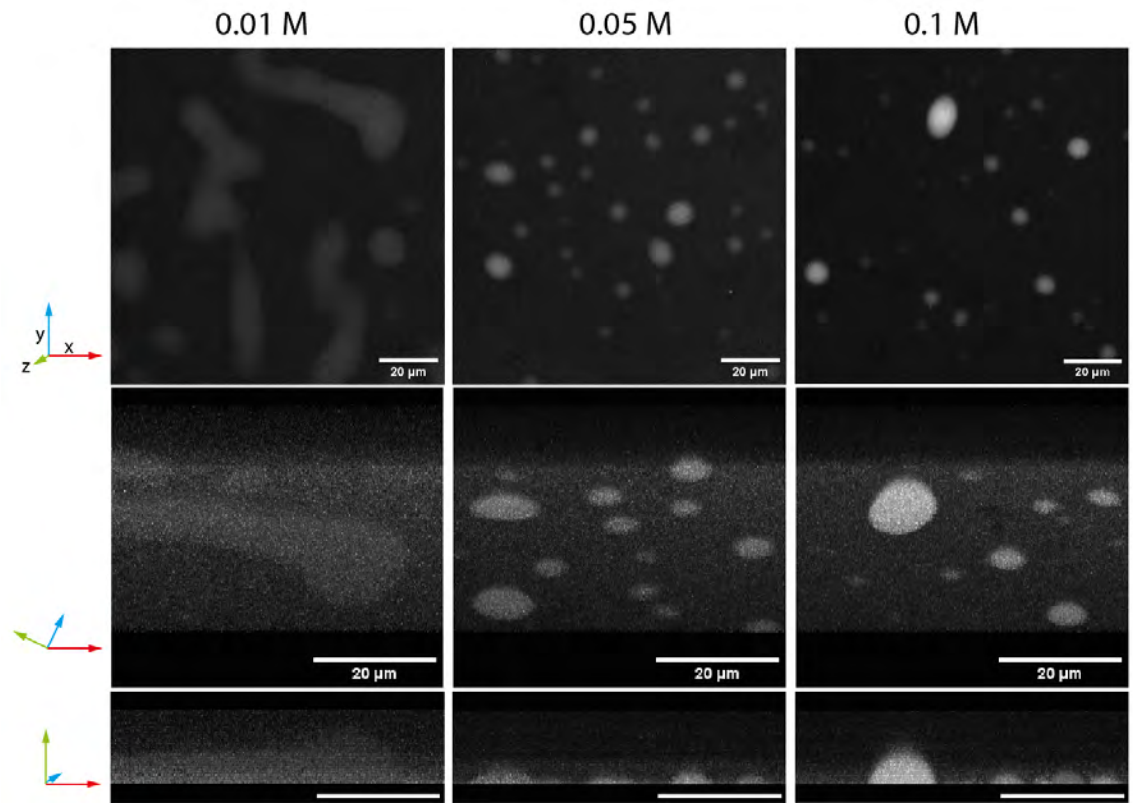

Figure 2.16: 4L6 droplets annealed in varying concentrations of $MgCl_2$. All concentrations see high degrees of deformation against the glass substrate. An Mg^{2+} concentration of 0.01 M results in the formation of extended irregular structures, instead of distinct droplets.

1 μm in size, or did not form any visible construct. Those that did phase separate did not form spherical droplets. 4L6 nanostars formed extended aggregates at 0.01 M and droplets at 0.05 – 0.1 M. These droplets showed extremely low contact angles, with near complete wetting of the droplets. Using the pixel intensity of each coacervate as a qualitative estimation of droplet density, droplets appeared to increase in concentration with increasing $[Mg^{2+}]$, but this could not be quantified.

Previous works have formed DNA nanostar condensates in low concentrations of divalent cations, when investigating enzymatic activity in such systems (table 2.8) [147] [185] [22] [23]. DNA nanostructure formation requires 10-100 fold lower Mg^{2+} divalent cation concentration than Na^{+} [168] [150]. This effect is not solely reliant on the charge of each cation [186]. The efficiency of DNA origami folding at a

given cation concentration is dependent on the specific identity of the salt, with Bednarz *et al.* attributing this difference to the binding modes of the cations [187]. Binding modes differ between ions, with lower mass salts preferentially binding to DNA phosphate groups, while heavier ions complex with nucleic acid bases [188].

Reference	Buffer conditions	Enzymes
[147]	50 mM K-Ace 10 mM Mg-Ace	Sma 1
[185]	50 mM K-Ace	Sma 1
[22]	27.5 mM Mg-Ace	YIPP RNase A RNase H
[23]	10 mM MgCl2 0.05 M NaCl	RNase-H UGD

Table 2.8: Cation concentrations used in DNA condensate systems with enzymatic reactions in the literature.

This indicates that phase separation of discrete droplets using low concentrations of divalent cations is possible, but is improved by the inclusion of additional monovalent cations. Alternatively, in the work of Kengmana *et al.*, the exclusion of unpaired base hinges at the termini of each arm [22]. It is suggested that the high flexibility of nanostars used in this thesis disallows the close packing required for phase separation when using a lower concentration of cations, despite the higher charge shielding of divalent cations. Tran et al. report phase separation of nanostars at either 0.1 M NaCl or 0.01 M $MgCl_2$, when segregated within a GUV [150]. Confinement in this manner is reported to increase the local concentration of nanostars, which would promote the closer packing required for phase separation.

2.6 Temperature dependence of DNA nanostars and droplets

Discussed in section 1.5.3, the native form of DNA is a tightly wound helix, consisting of two strands of nucleotides paired through hydrogen bonding. In a solution of DNA, dehybridisation of strands occurs over a range of temperatures. The midpoint of this transition, where exactly half of the nucleotide population is denatured, is termed the melting temperature. The temperature at which the denaturation of DNA occurs is a key value in understanding any given oligonucleotide. This is particularly true in the field of nanotechnology, where it relates to the temperature where nanostructures will begin to form through DNA hybridisation. However, calculating the denaturation temperature of any given sequence is a complex process, particularly when considering sequences beneath 100 bp in length. The hybridisation temperatures of the short oligonucleotides used in this work were thus experimentally determined.

Intercalating dyes are fluorescent molecules which insert between the stacked bases of a double-stranded oligonucleotide, or become attached to the minor groove of the double helix. When bound to an oligonucleotide in this manner, their fluorescence can increase up to a thousand-fold [189]. This selective fluorescence can be used to quantify the amount of dsDNA in a solution at any given point in a reaction. By heating and cooling DNA in the presence of an intercalator, and monitoring its emission, the temperatures at which the DNA melts or rehybridises can be identified. This process is known as DNA hybridisation curve analysis (HCA), and was first tested on linear dsDNA to confirm its veracity for this system (section A.12).

2.6.1 Hybridisation of 0 SE nanostars

The kinetics of nanostar folding were investigated using HCA, with blunt-ended stars first analysed to assess star formation independent of phase separation (section A.13). Calculating the melting temperatures of each individual arm as linear sequences can provide an estimate of star formation temperature range. Temperatures of 68.8 ± 2.2 ^{o}C, 66.0 ± 1.0 ^{o}C, and 80.1 ± 1.7 ^{o}C for 3S, 4S, and 4L stars, respectively, were found using the Two State Melting Hybridisation function of DINAMelt at 0.5 M [Na^{+}] and 10 μM [DNA]. These are markedly lower than the estimated hybridisation temperatures of the full structures found using the Analysis function of NUPACK, under the same model conditions, which are 79.3 ^{o}C, 72.5 ^{o}C, and 86.2 ^{o}C, respectively.

When considering the formation of a full nanostar, rather than each arm in isolation, an increased temperature of hybridisation is expected due to cooperation between each arm. DNA hybridisation is a dynamic process, with base pairs constantly hybridising and melting. Structure formation and stabilisation occurs when the rate of hybridisation (k_{on}) is greater than the dehybridisation (k_{off}). In the formation of nanostars, the local concentration of strands is higher than that of the bulk solution, as each arm is connected to two others. The strands of a nanostar may transiently or partially bind at a temperature above the formation temperature of a single arm. As the strands separate, the heightened local concentration promotes the hybridisation of further complementary sequences, thereby increasing the k_{on} of the system as a whole. Therefore, the multivalent nature of nanostars means their formation is a cooperative process, and the hybridiation temperature of a nanostar is expected to be affected by both arm length and valency [16] [24].

Hybridisation and melt curves were produced in order to assess the kinetics of nanostar formation during annealing. At experimental conditions of 10 μM [NS], 0.5 M

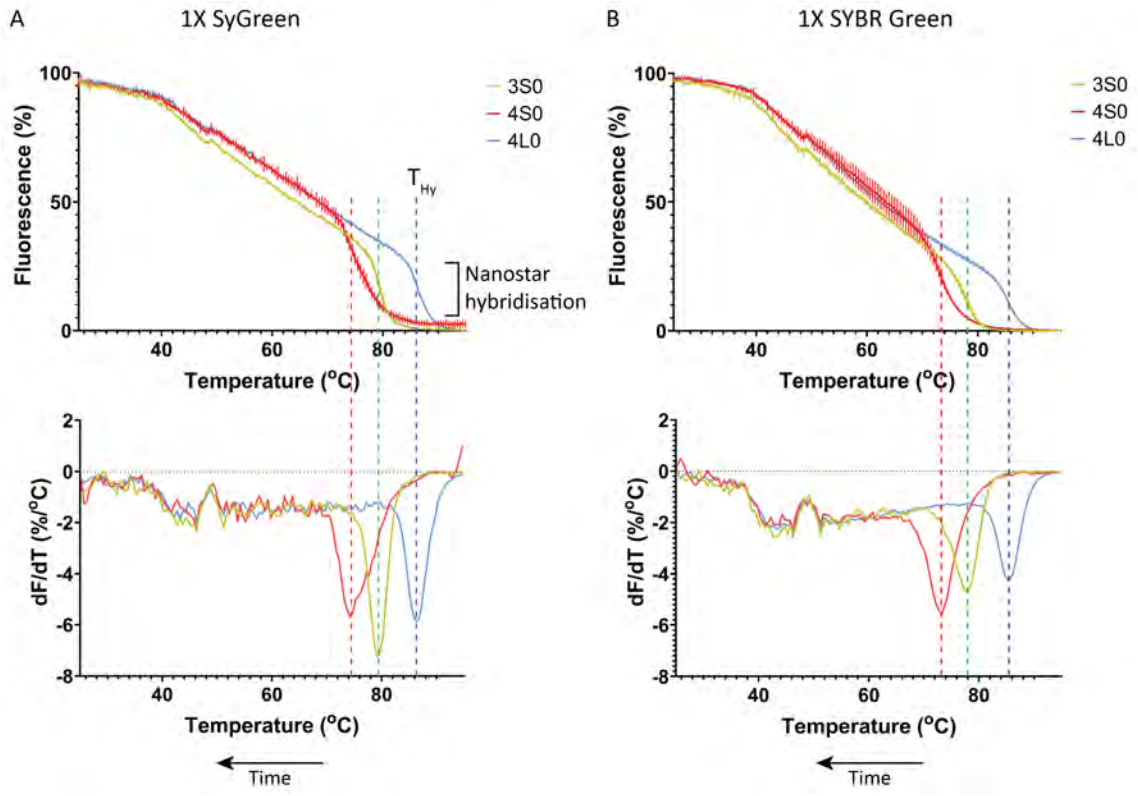

Figure 2.17: Normalised hybridisation curves and associated derivative curves of 3S0, 4S0, and 4L0 nanostars at 10 μM in 0.5 M NaCl; conducted in RotorGene Q qPCR system. Mean of $n = 4$ with error bars as standard deviation. Comparing **A**: 1X SyGreen and **B**: 1X SYBR Green intercalating fluorophores.

NaCl, and a temperature ramp of 0.5 ^{o}C/min, nanostars were annealed from 95 to 25 ^{o}C in the RotorGene Q using 1X SyGreen and 1X SYBR Green. Described below, analysis was simultaneously conducted in a plate-reader based qPCR system. In this method, samples containing 0.5X SYBR Green produced a low signal:noise ratio. Therefore, this lower concentration of SYBR Green was excluded from ongoing plate-reader experiments.

In nanostars lacking a sticky end, HC traces followed the same pattern as sticky end duplexes (figure 2.17). These saw an initial rapid rise in fluorescence intensity from right to left, at different temperature ranges for each star structure. Following this initial rapid growth, a steady increase in fluorescence was seen until an eventual plateau at 40 ^{o}C. Of note is the smooth increase in fluorescence in these systems upon

initial hybridisation. This indicates a spontaneous or simultaneous folding of stars, rather than a stepwise process, which would present as a shouldered fluorescence curve. The gradual increase in trace fluorescence following the initial star formation is an artefact of the instrument used, which sees a rise in fluorescence detection with temperature in empty sample chambers (figure C.1).

The initial rapid rises in fluorescence correspond to the formation of each respective nanostar. The long sequences and high valency of the nanostar bodies stabilise the structures and allow hybridisation at high temperatures. The hybridisation temperature of each structure was determined to be the peak of its derivative curve, aligning with the midpoint of the period of fluorescence rise. For 3S0, 4S0, and 4L0 nanostars, formation temperatures (T_{hy}) were found to be 79.25, 74.25, and 86.25 ^{o}C using 1X SyGreen, or 77.75, 73.25, and 85.25 ^{o}C using 1X SYBR Green. These are in close agreement with the NUPACK values of 79.3 ^{o}C, 72.5 ^{o}C, and 86.2 ^{o}C. Having 48, 64, and 92 hybridised base pairs in every structure, their energies of hybridisation are thus found to be more accurately predicted by NN models than the shorter sticky ends in section A.12.

Analysis was also conducted using the CFX Opus Real-Time PCR, a plate-reader system. Nanostar formation temperatures were determined to be 79.25, 74.25, and 85.75 ^{o}C using 1X SyGreen, and 79.75, 74.25, and 85.75 ^{o}C using 1X SYBR Green for 3S0, 4S0, and 4L0 nanostars, respectively (figure 2.18). These values were in close agreement with both RotorGene measurements and computational predictions, validating both methods (figure 2.19).

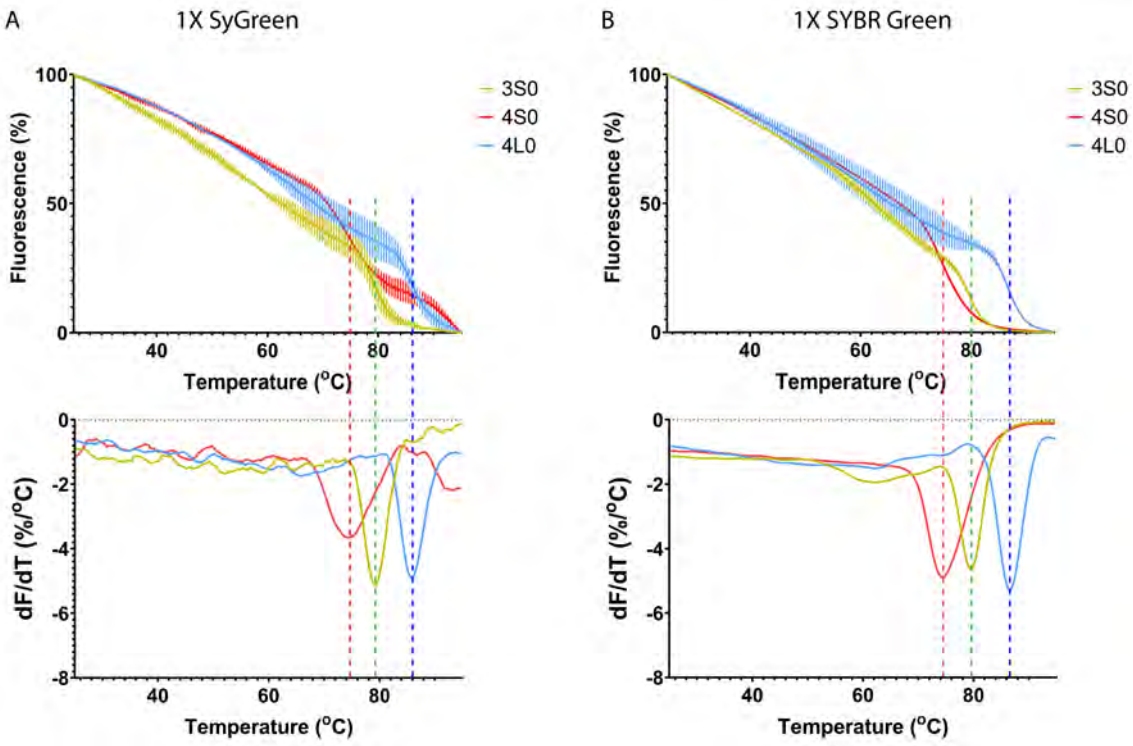

Figure 2.18: Normalised hybridisation curves and associated derivative curves of 3S0, 4S0, and 4L0 nanostars at 10 μM in 0.5 M NaCl; conducted in Opus CFX qPCR system. Mean of $n = 3$ with error bars as standard deviation. Comparing A) 1X SyGreen and B) 1X SYBR Green intercalating fluorophores.

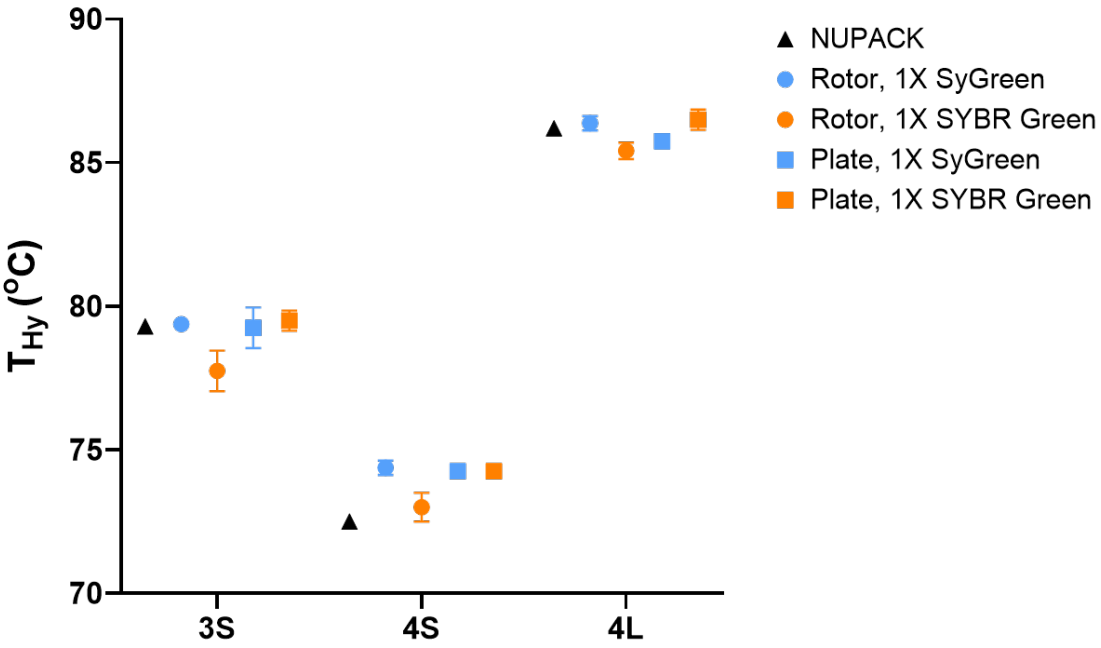

Figure 2.19: Estimated hybridisation temperatures of 0-nt SE nanostars. The first derivatives were calculated for the hybridisation curves of 0-nt SE nanostars, using different intercalating dyes and different fluorophores. The means of four repeats were calculated to estimate the hybridisation temperatures of different nanostars, and compared to calculated values (NUPACK).

2.6.2 Hybridisation of phase separating nanostars

Upon confirming the utility of hybridisation curve analysis for the study of nanostar formation kinetics, the method was applied to phase separating nanostars. Analysis was conducted using 10 μM nanostars prepared at 0.5 M NaCl. SyGreen fluorophores were used at 1X concentration, while SYBR Green was used at 0.5X in the RotorGene Q and 1X in the CFX Opus, due to oversaturation of detection intensity in the former.

Hybridisation profiles of phase separating nanostars produced using the CFX Opus show a shouldered or two-step curve (figure 2.20). An initial peak in hybridisation was seen as the formation of nanostars, followed by a second, broader rise in fluorescence upon the onset of sticky end hybridisation.

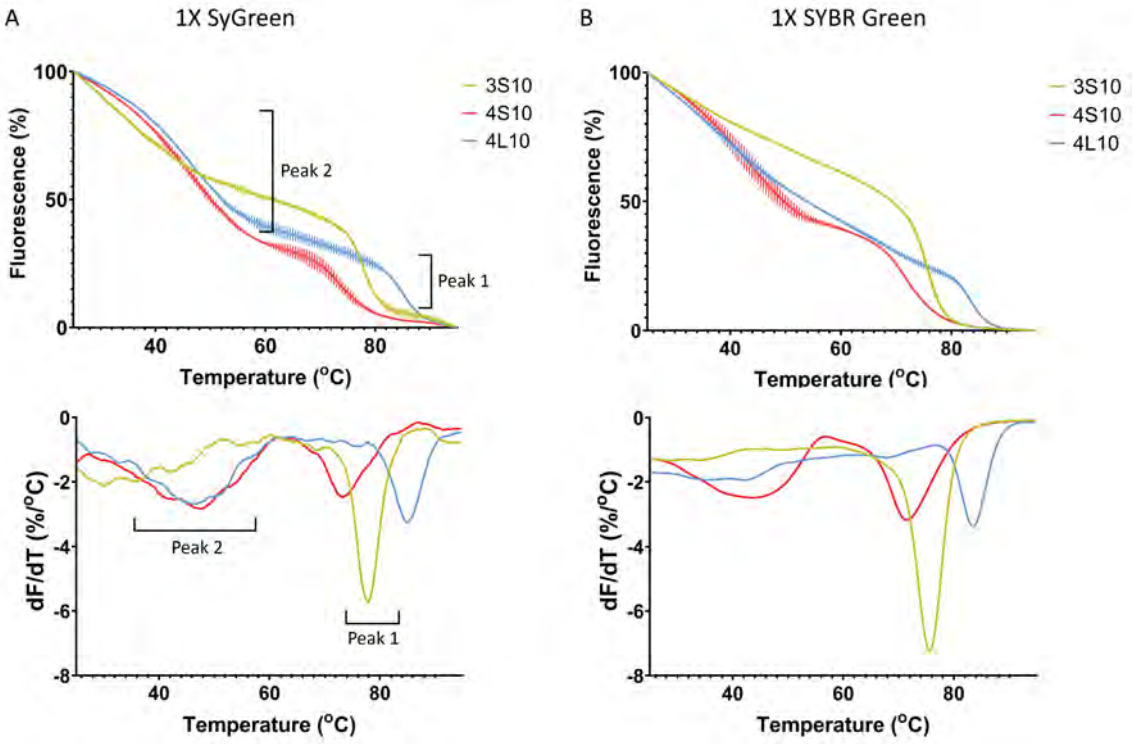

Figure 2.20: Normalised hybridisation curves and associated derivative curves of 3S10, 4S10, and 4L10 nanostars at 10 μM in 0.5 M NaCl; conducting in Opus CFX qPCR system. Mean of $n = 3$ with error bars as standard deviation. Comparing A) 1X SyGreen and B) 1X SYBR Green fluorophores.

Whilst this second stage of hybridisation occurs for every star in solution, it is expected to be a transient process, with sticky ends constantly hybridising and dehybridising in liquid droplets. The rises in detected signal seen are thus shallow and broad, representing the dynamic process gradually increasing in net fluorescence. Therefore, while this technique may give indication of the onset of phase separation, it is limited in its specificity.

In contrast to the Opus CFX, droplets analysed under identical conditions in the RotorGene Q see sharp, specific reductions in fluorescence intensity in the region of expected phase separation (figure 2.21). The RotorGene Q is a centrifuge-based system – samples are continuously spun in a uniformly heated chamber. In contrast, the plate-reader system places samples in a heated block, under a heated lid; the block changes in temperature according to the annealing profile, while the lid remains at 105 ^{o}C to prevent condensation of the sample. The centrifugation system has dual benefit in our application – the uniform heating of the chamber is expected to provide a more homogeneous temperature gradient during annealing, and the low-speed centrifugation concentrates the nanostar droplets as they phase separate.

Phase separation results in the formation of densely packed nanostars – Jeon *et al.* indicate densities of 35.1 mg/mL at comparable experimental conditions [25]. Cyanine dyes such as those in the SYBR family experience self-quenching effects at high concentrations or when in close proximity. Fluorescence of SYBR Green decreased at $\sim 1.25 \times 10^{-5}$ in a dispersed state, or at $\sim 0.6 \times 10^{-5}$ M with an inter-fluorophore distance of 3.4 nm [190]. The high packing density of nanostars in a phase-separated droplets may be sufficient to induce these same self-quenching effects, leading to the observed decrease in fluorescence intensity. Alternatively, the centrifugation of the developing droplets may cause them to sediment towards the base of the container, as the phase separated droplets have a greater density than the bulk phase. If this were to cause the majority of the droplets to fall beneath

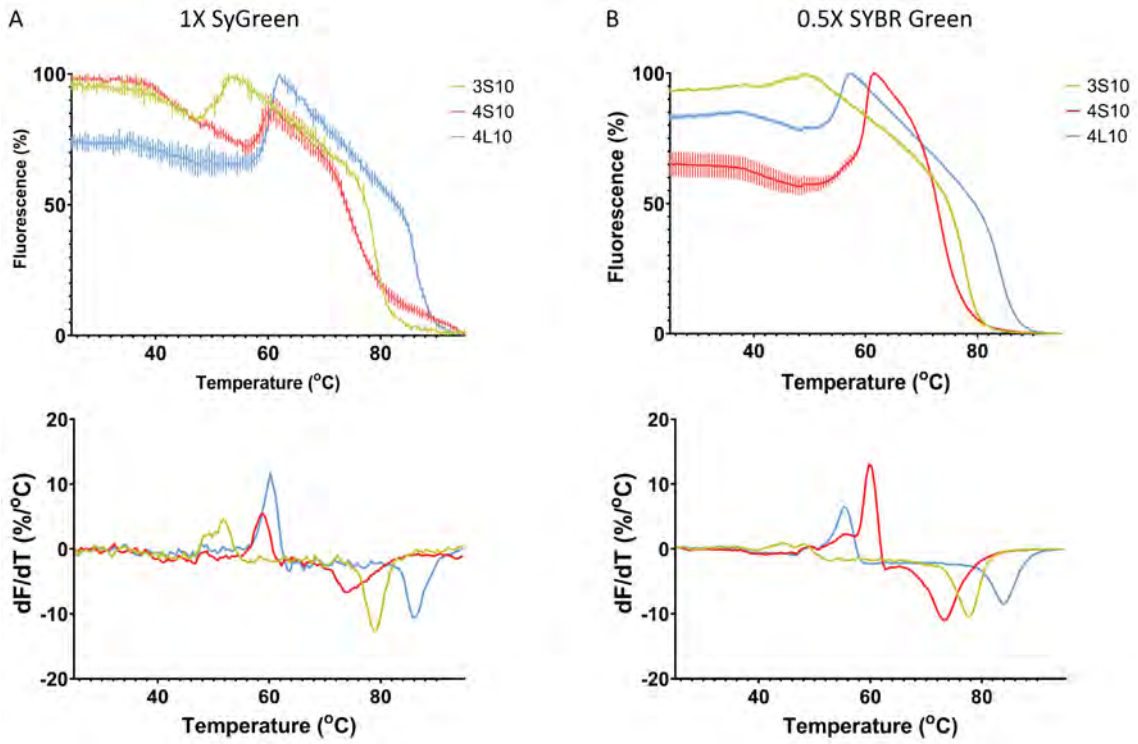

Figure 2.21: Normalised hybridisation curves and associated derivative curves of 3S10, 4S10, and 4L10 nanostars at 10 μM in 0.5 M NaCl; conducting in RotorGene Q qPCR system. Mean of $n = 4$ with error bars as standard deviation. Comparing A) 1X SyGreen and B) 0.5X SYBR Green fluorophores.

the height of the thermocycler detector, the detected fluorescence would sharply fall. Either mechanism - self-quenching or sedimentation - attributes the measured decrease in fluorescence intensity to the onset of phase separation.

The decreases in fluorescence intensity seen in figure 2.21 can be used to estimate phase separation temperature, measured as the temperature of inflection in the Fluorescence vs Temperature curve. A custom MATLAB script was used to analyse normalised fluorescence data and extract local peak maxima, which were then used to identify the phase separation temperature (T_{PS}) (section A.13, script B.5).

The experimentally determined phase separation temperatures of each nanostar were plotted against the calculated free energy of its respective sticky end and computationally derived SE melting temperatures (figure 2.22). T_{PS} is seen to follow a

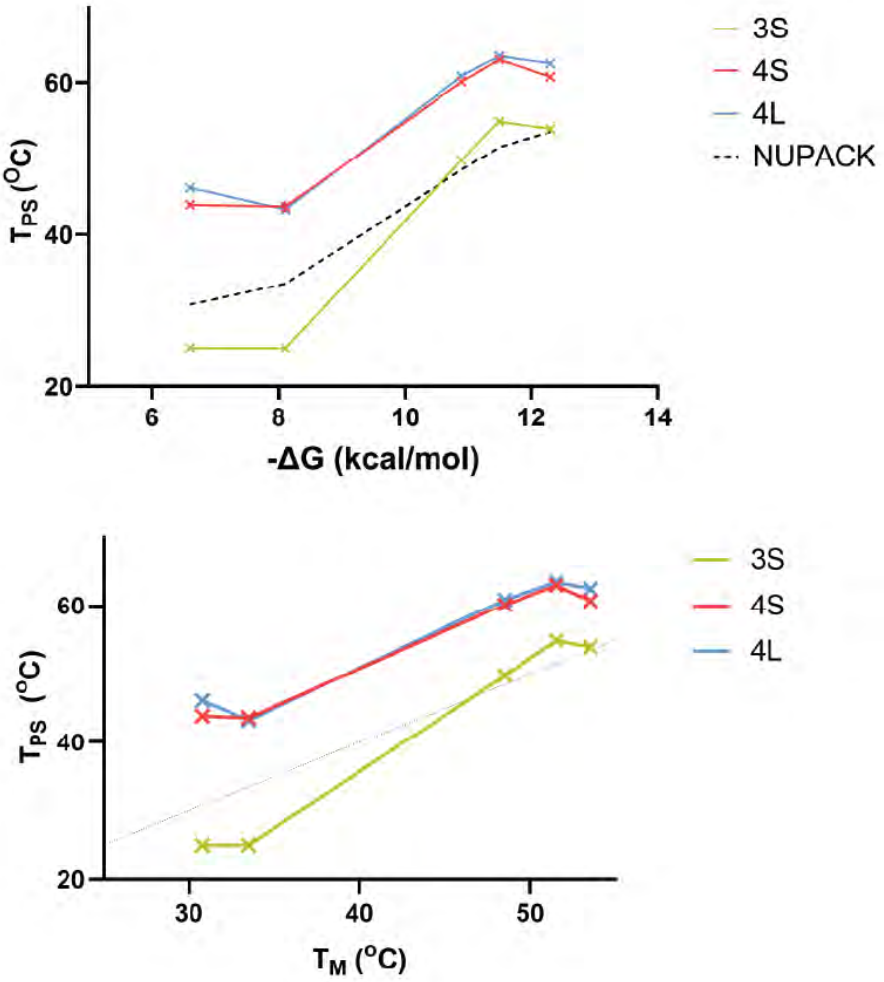

Figure 2.22: Experimentally derived phase separation temperatures of all nanostars at 10 μM in 0.5 M NaCl, extracted from hybridisation curves produced in Rotor-Gene Q qPCR system. Showing mean with error bars as standard deviation, $n = 4$. Comparing 1X SyGreen T_{PS} against the predicted free energy and the computationally calculated T_M values of each sticky end dimer. Note: systems with a recorded phase separation temperature of 25 ^{o}C did not present a T_{PS} inflection point in their hybridisation curves (figure A.15). Therefore, T_{PS} is recorded as the lowest system temperature.

general trend of T_M against ΔG, but at differing intensities of temperature depending on star structure. Tetravalent 4S and 4L nanostars tend to have elevated T_{PS} in comparison to T_M, while trivalent 3S stars have reduced or equivalent T_{PS}.

An increase in phase separation temperature with valency was observed by Sato *et al.* when increasing nanostar valency from f = 3 - 6 [24]. They suggested that additional stabilisation was afforded by greater star valency of four-armed stars, accounting for the increased T_{PS}. Phase separation is initiated by transitory binding of sticky ends in solution. A single pair of SEs binding, even temporarily, increases the local concentration of sticky ends via the arms of the connected nanostars, pushing the local system towards hybridisation. Once droplets have nucleated, the multiple crossovers in the nanostar mesh stabilise the structure, with more crossovers creating a denser mesh and more stable structure. The increase of phase separation temperature with increasing valency is also similar to the work of Conrad *et al.*, who saw an increase in the upper critical solution temperatures of nanostar phase diagrams with increasing valency [148]. Their work estimated phase transition temperatures through direct viewing of droplet formation via fluorescence microscope. Agreement with the trends seen in the literature helps validate the interpretation of hybridisation curve analysis.

2.6.3 Nanostar droplet melting

Further details of nanostar kinetics were investigated using melt curve analysis, studying the dehybridisation of systems with heat. Samples were annealed from 95 – 25 ^{o}C at 0.5 ^{o}C/min, held at 25 ^{o}C for 15 minutes, and then heated to 95 ^{o}C at the same rate.

A hybridisation curve of 3S10 nanostars was produced under standard conditions (figure 2.23). An initial rapid rise in fluorescence intensity (F%) was seen at approx-

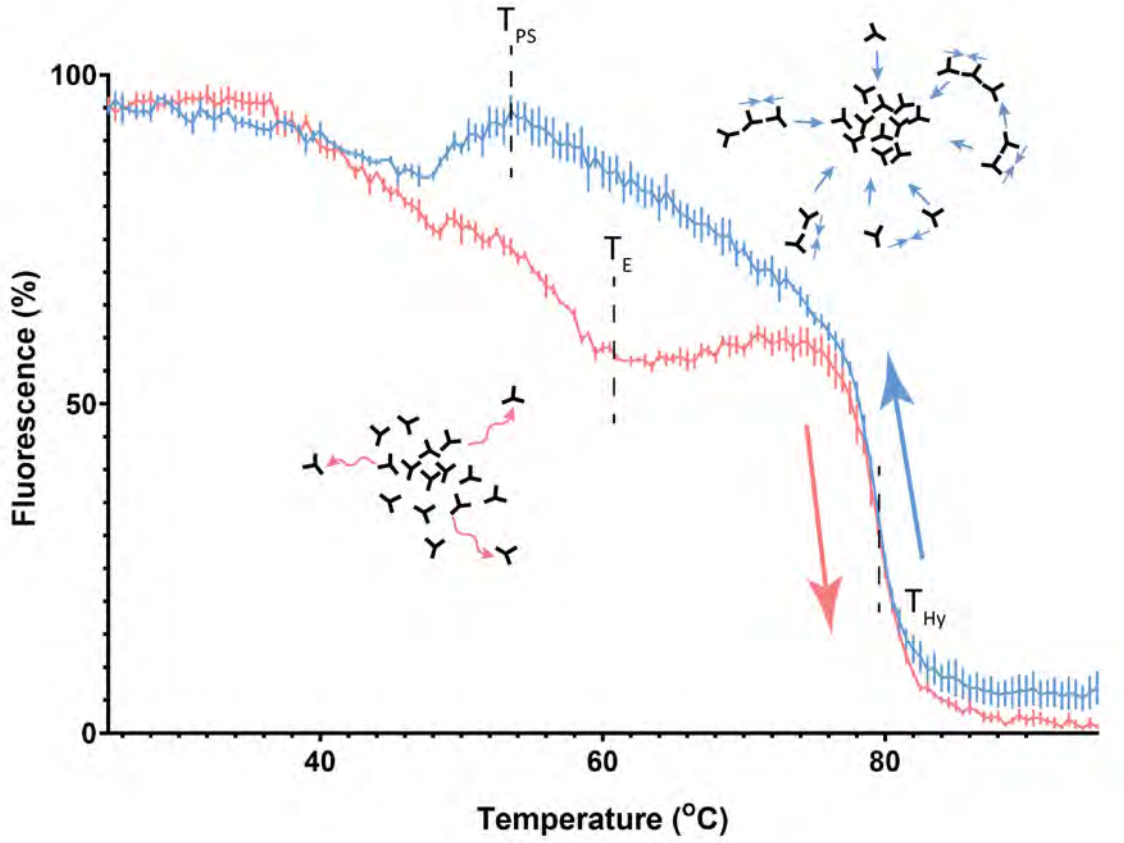

Figure 2.23: Fluorescence intensity curves of a 3S10 nanostar droplet when cooled (blue) and heated (red). Starting from 95 ^{o}C, the system was cooled at 0.5 ^{o}C/min to 25 ^{o}C to produce a hybridisation curve, and then heated at the same rate to investigate melting. Key temperatures are identified in the curves. T_{Hy}: Nanostar hybridisation and melting. T_{PS}: Sticky end hybridisation and phase separation. T_E: Sticky end melting and droplet evaporation.

imately 80 ^{o}C, indicating the onset of nanostar hybridisation. The first derivative of this peak was used to define T_{Hy}. The rate of fluorescence intensity growth then decreased, with F% growing linearly until approximately 53 ^{o}C, whereupon a sharp decrease in F% was seen. This inflection point is hypothesised to indicate the onset of phase separation, and defines T_{PS}. Droplet phase separation is expected to be a cooperative process, with an initial nucleation site promoting the further binding of adjacent nanostars.

After reaching 25 ^{o}C, the system was heated to produce a melt curve. As the system temperature increased, fluorescence intensity gradually decreased. Ethidium

bromide intercalating dye, to which SyGreen is related, demonstrates an increase in quantum yield with increasing temperature [191].The observed decrease in fluorescence intensity is an artefact of the instrument used, which sees an inverse linear relationship between temperature and detected intensity (figure C.1). Upon a inflection point (T_E), fluorescence intensity stabilised, where it remained until T_{Hy} was reached. Fluorescence then rapidly fell, indicating dehybridisation of the nanostar body. This inflection point during melting tended to occur at a higher temperature than the phase separation temperature during hybridisation. As the hybridisation of sticky ends is a cooperative process, with the binding of one pair of stars promoting association with others, droplet formation is expected to rapidly occur upon onset of the phase separation temperature. This is seen in the rapid decrease in fluorescence intensity upon hybridisation (T_{PS}).

When heating droplets, we propose that the extended mesh network of nanostars acts as a single structure and stabilises sticky ends above their individual melting temperatures, through the above discussed concept of cooperative binding. Additionally, the dissociation of droplets is a slow process, with nanostars gradually dispersing through simple Brownian motion (in contrast to the cooperative association and centrifugation promoting droplet formation). This would act to explain the elevated temperature at which droplet dissociation and evaporation appears to occur, in comparison to measured T_{PS}. Finally, nanostar hybridisation and melting occurs at the same temperature (T_{Hy}). Above T_E, sticky end interaction is not expected. Therefore, nanostars act as independent structures, with no additional stabilisation.

2.6.4 Validation against known systems

The accuracy of this technique in measuring the phase separation temperature of nanostars was further tested by applying it to structures of known T_{PS}. The stan-

dard method of identifying droplet formation is the visualisation of nanostars on a heated stage in a confocal microscope (section 1.6.3). They are gradually cooled under the same conditions as typical annealing, and the field of view is monitored for nascent droplets (figure 1.15). Sato *et al.* determined the droplet formation temperatures (T_d) of stars varying in sticky end length and valency using this technique [24]. Stars of the same sequence were ordered and prepared according to their conditions – 15 μM nanostars and 0.35 M NaCl – and analysed using the RotorGene Q, annealing from 95 – 25 oC at 1 ^{o}C/min in the presence of 1X SyGreen or 1X SYBR Green.

Sato *et al.* compared trivalent stars with sticky ends between 6 – 12 nt in length, and tetra- and hexavalent stars of 8 nt SEs, in order to study the effects of valency and sticky end length [24]. They found that an increase in valency increased T_d, attributed to entanglement of the nanostars, while the increasing binding strengths of the SEs similarly raised droplet formation temperature. The T_d were compared to $T_{M-motif}$, a value calculated from the computationally predicted hybridisation temperature of each sticky end. While T_M is generally calculated as the temperature at which 50% of bases will be hybridised, Sato *et al.* argue a lower portion of SEs require hybridisation to connect two nanostars. They calculate this portion as:

$$1 - (1 - X(T))^k = 0.5 \tag{2.1}$$

Wherein k is the number of arms in a nanostar and *X(T)* the hybridisation probability at temperature *T*. Solving for $k = 3$, 4, and 6 gives values of 21, 16, and 11% respectively. These hybridisation probabilities were used to calculate $T_{M-motif}$ from the fitted hybridisation curves of each sticky end sequence. While $T_{M-motif}$ aligned closely with the experimentally determined T_d for nanostars with lengthy sticky ends ($>=$ 10 nt), they increasingly differed for shorter or weaker SEs. For shorter SEs,

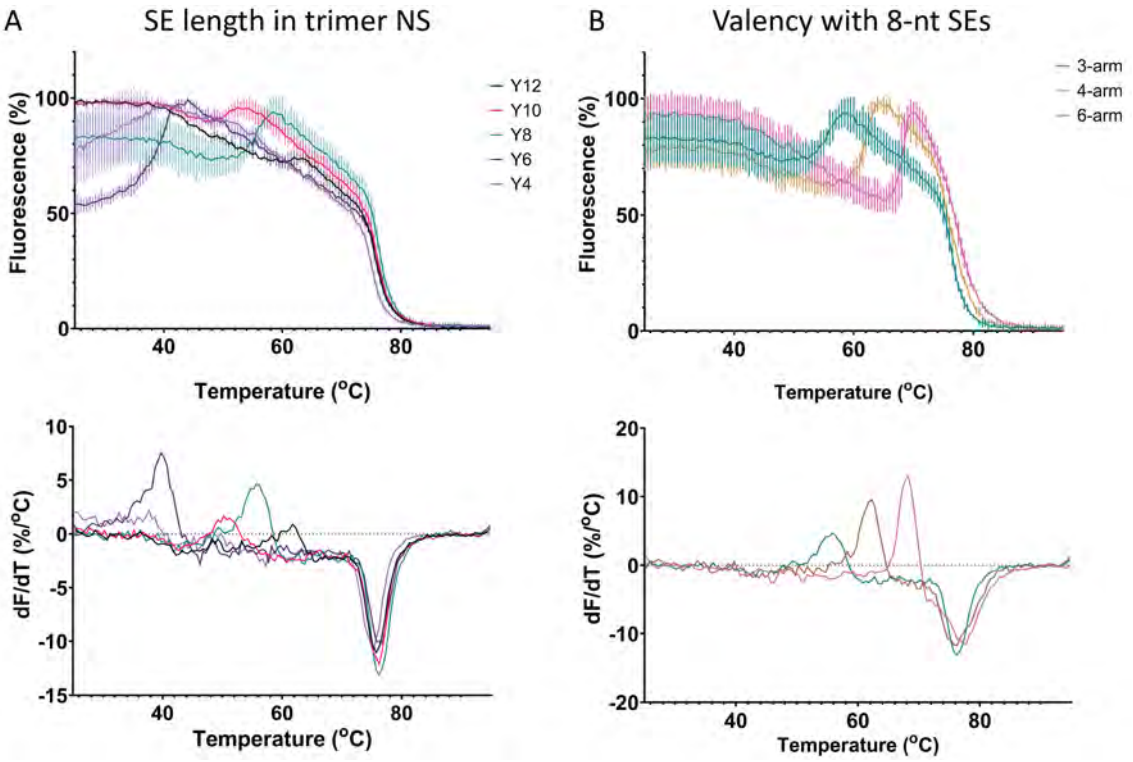

Figure 2.24: Hybridisation curves and associated derivatives for **A**: varying sticky end lengths on a three-armed nanostar (Y motif) and **B**: nanostars of increasing number of arms with 8 nt SEs.

$T_{M-motif}$ remains ineffective at predicting T_d even with increasing nanostar valency. In this thesis, hybridisation curves were produced for each nanostar studied in Sato *et al.* and from these determined the T_{PS} (figure 2.24).

When measured using HCA, the phase separation temperatures of these systems increased with sticky end strength and valency, in line with the trend noted by Sato *et al* (figure 2.25). The HCA-determined T_{PS} remained within 3-14% of the recorded droplet formation temperature. Thus, hybridisation curve-based T_{PS} estimations tend to align closely with temperatures of droplet formation.

Across all samples, the HCA-derived T_{PS} was systematically less than the visually determined T_d. In their work, the droplet systems prepared by Sato *et al.* contained 20 mM Tris-HCl (pH 8.0). This aspect of the solvent was not replicated in this thesis; it is possible that the difference in solution conditions affected droplet

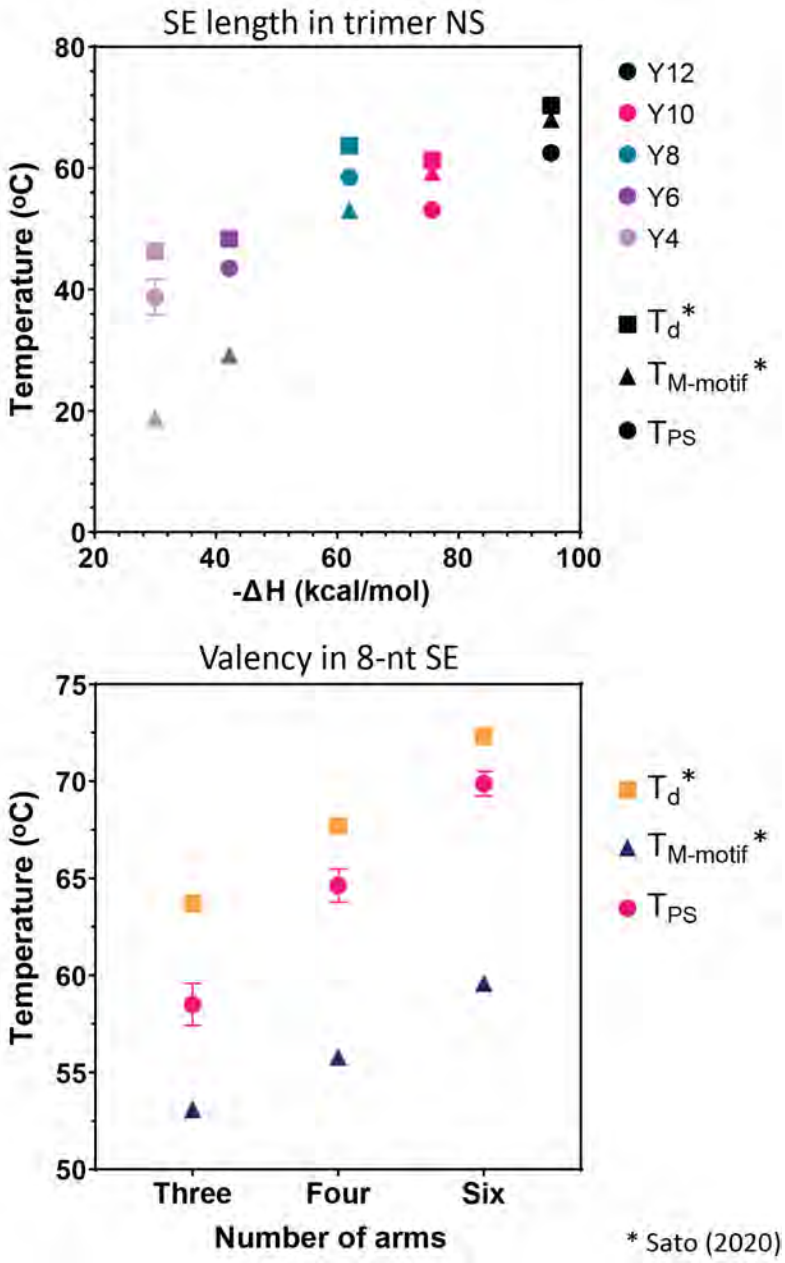

Figure 2.25: Comparison of experimental T_{PS} measurements with T_d and $T_{M-motif}$ values from [24] for **Top**: three-armed nanostars with sticky ends between 4 – 12 nt, and **Bottom**: three, four, and six-armed nanostars with 8 nt SEs.

formation, resulting in a reduced phase separation temperature. Alternatively, in the HCA method the peak in fluorescence intensity, attributed to the onset of phase separation, was caused by self-quenching of tightly packed fluorophores. It is possible that a delay exists between the onset of phase separation, visually found as T_d, and the growth of droplets to a size where total fluorescence is diminished, T_{PS}. Additionally, HCA was here performed in a centrifuge system, while T_d was found on a heated microscope stage. This physical difference between the systems may also contribute towards the observed systematic difference in T_d and T_{PS}.

Both the droplet visualisation and HCA techniques produced phase separation temperatures in close agreement. In HCA, the repeatability of the method was high, with low variation between repeated measures. Additionally, the throughput of the HCA technique is significantly faster, allowing simultaneous analysis of seventy two different samples.

2.7 Summary and Conclusion

In this chapter, phase separating nanostars were successfully designed and produced, in line with Aim 1 of this thesis (section 1.7). Variations upon the structural design were investigated and tested for their effects on droplet properties of size, fluidity, and density (figure 2.26).

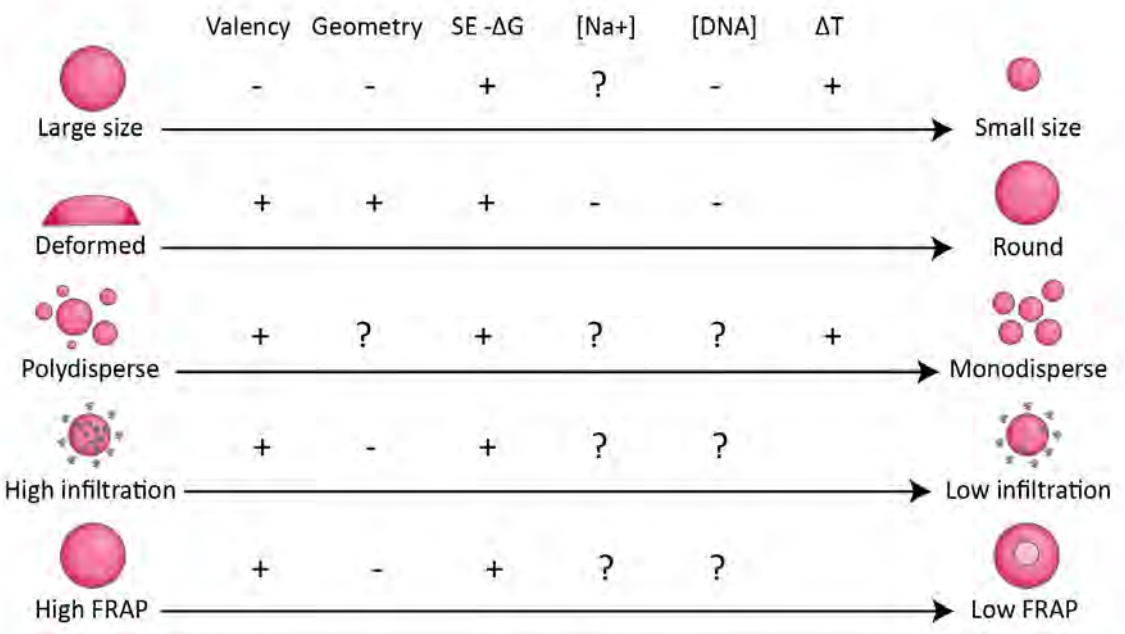

Figure 2.26: Summary of observed effects of nanostar system design on coacervate properties.

It was found that nanostar arm geometry and valency both have effects upon droplet infiltration and fluidity. With increasing length or decreasing number of arms, infiltration increased, while increases in either arm length or number decreased droplet deformation at a solid surface (section 2.5.2, 2.5.1). Molecular subunit mobility was investigated through FRAP, and it was found that the degree of fluorescence recovery strongly strongly increased with decreasing subunit binding strength and valency (section 2.5.2). Inter-star connections were investigated on the basis of their binding strength, and their effects on droplet size and distribution quantified. A link was found between binding strength and droplet size, with an increase in the former

leading to a decrease in the latter (section 2.5.1). This was tied to strong nanostar sticky ends resulting in a low droplet interfacial tension, impeding droplet fusion and resulting in a smaller mean size. However, a direct method of controlling droplet size through nanostar parameters could not be identified. Investigations were conducted on droplet production conditions. Future works should more systematically investigate [Na^+] and concentration effects.

A method of quantifying droplet formation temperature was developed and evaluated for consistency and reliability (section 2.6). The determination of phase separation temperature through hybridisation curve analysis was compared to literature values of temperature-ramped confocal imaging and $T_{M-motif}$ [24]. As the HCA method described here allows for the simultaneous processing of up to 72 samples, it is of significantly higher throughput than confocal imaging, in which only one sample may be imaged at a time, and which requires a specialised heat stage. The HCA method was also found to produce T_{PS} values of much higher correlation to confocal T_d, in comparison to the accuracy of $T_{M-motif}$.

The droplets studied in this chapter were poly-disperse in size, and control of the physical structure of nanostars did not allow for programmable macro-scale droplet properties. In Chapter 3, these nanostars will be combined into binary droplet systems, in attempt to create synthetic cells from DNA nanostar droplets.

Chapter 3

Form and function of two-star droplets

3.1 Introduction

Synthetic cells are an area of much active exploration, investigating areas from abiotic synthesis to materials production and drug delivery (section 1.3). In this thesis, we are interested in the development of synthetic cells for two distinct applications: the creation of a microreactor vessel and the creation of a model leukocyte. A DNA nanostar microreactor vessel would allow for a selectively permeable region in which biomolecules could concentrate. The dense mesh network would disallow passive infiltration of enzymes or proteins, while the tagging of selected molecules with appropriate DNA barcode sequences would allow active capture in or exclusion from the droplet. The inclusion of micro-architectures, creating distinct regions of different nanostars in a single droplet, could then allow for sequential or stepwise reactions. Enclosing a reaction space within an impermeable or semi-permeable membrane would impart stability upon the system. While such properties have pre-

viously been achieved in liposome-based synthetic cells, the ease of synthesis and addressability of DNA droplets makes them an attractive area of exploration.

Leukocytes are a key component of vertebrates' immune system, aiding in the detection of and response to disease (section 1.2, figure 1.1). In creating a model leukocyte, we intend to replicate its physical characteristics in order to better understand its abilities and function. Leukocytes undergo significant physical changes during their life-cycle. If such properties were synthetically replicated - controlled adhesion strength, site recognition, modulation of body shape and fluid properties, self-directed movement - the behaviour of leukocytes could be better understood. This could allow for greater understanding of how they function in the immune system. Additionally, artificial structures replicating these physical properties could in the future be adapted for medical or pharmacological purposes.

In this thesis, the approach to creating a synthetic leukocyte makes use of a core and shell to mimic the cytoplasm and membrane of a cell. It is thought that this will allow for a transition between stable sphere and dynamic states. The stable structure consists of a gelated droplet, while the dynamic state could be achieved by a deformable liquid core within a thin gelated shell. As individual nanostar droplets encompass such a spectrum of stabilities (section 2.5.2), the creation of multi-star core-shell structures may result in synthetic cells of these desired physical characteristics. Incorporation of nucleic acid displacement reactions could then allow switching between designated physical states through the modification of inter-star binding strength or valency, replicating the sphere-to-dynamic transition of leukocyte cells. This chapter develops a method to predict and synthesise DNA artificial cells formed of two distinct nanostar regions, and discusses the control of micro-scale architecture that this enables.

Methods explored in the literature for the produced of two-star droplet architectures

are summarised in section 1.6.6 and table 3.1. When creating synthetic cells or microreactors from nucleic acid nanostars, a number of gaps in the literature have been identified. These questions are used in guiding the implementation of Aim 2, the formation of two-star nanoscale structures (section 1.7).

- **Question 2.1** Moving beyond bifacial particles, what micro-architectures can be formed using multi-phase DNA nanostar coacervates?
- **Question 2.2** Is it possible to produce core-shell coacervates using structurally distinct nanostars, without the use of RNA or cholesterol moeties?
- **Question 2.3** Can DNA NS core-shell structures be formed in a bulk solution?
- **Question 2.4** Can a system be designed in such a way to have areas of both distinct physical properties and independent chemical addressability?

Reference	**Nanostar**	**Development**	Chemical addressability?	Physical distinction?	Core-shell structure?	Dynamic system?
Sato [24]	f = 3 G = 16-bp SE = 8-nt	Bifacial droplets. Protein partitioning.	Yes	No	No	Yes
Jeon [25]	f = 4 G = 21-bp SE = 6-nt	Surfactant ratio effects	Yes	No	No	No
Tran [150]	f = 3 G = 18-bp SE = 8-nt	Confinement effects.	No	No	No	Yes
Fabrini [153]	f = 4 G = 25-bp SE = 6-nt	Surfactant effects in confinement.	Yes	No	Yes	Yes
Leathers [19]	f = 4 G = 35-bp SE = cholesterol	Post-production functionalisation.	Yes	No	Yes	Yes
Walczak [151]	f = 4,6,6 G = 35,26,18-bp SE = cholesterol,13,13-nt	Cholesterol core, DNA shell. Staggered formation through $T_P S$ design.	No	Yes	Yes	Yes

Table 3.1: Two-star architectures explored in the literature.

Drawing inspiration from the work of Jeon *et al.* and Walczak *et al.*, the approach of forming core-shell coacervates with a staggered phase separation process is taken [25] [151]. The method for determining the phase separation temperatures of nanostars (section 2.6.2) is used to guide the development of staggered systems. In this thesis, we aim to investigate more deeply how DNA-DNA interactions can drive patterning. To do so, the orthogonality of each droplet system is d emonstrated in the absence of surfactant stars, followed by a systematic investigation of mixed systems. The morphologies of two-star systems are characterised, determining trends in micro-architecture formation; the effects of star configuration and energetics; and the limits of these proposed trends. The resulting core-shell systems are tested for temporal stability, demonstrating long-term encapsulation and prevention of fusion of cores, an essential property for the development of synthetic cells.

3.2 Phase separation in two-star systems

The phase separation temperatures of fifteen variations of nanostars – five sticky ends, two valencies, two lengths – were measured by HCA in Chapter 2. The T_{PS} of nanostars with a series of sticky ends were found to generally follow the same trend as the calculated hybridisation temperatures of the sticky ends. Increasing the valency of nanostars (f = 3, 4) was observed to increase T_{PS}, but arm length (G = 16 and 23 bp) had no significant effect.

In a solution containing a combination of two different nanostars, it is predicted that two distinct droplet populations will form. This assertion is based on the orthogonality of the stars as computed by NUPACK software, and on results shown in the literature, where orthogonal droplet populations did not interact [24] [25] [22]. The arm sequences of 3S, 4S, and 4L stars were all designed to be non-complementary between NS types, while SE sequences are shared. This means that

4S8 and 3S10 nanostars were designed to possess non-complementary sequences in both their arms and sticky ends, while 4S8 and 3S8 nanostars have orthogonal arms but complementary sticky ends. Therefore, 4S8 and 3S10 NSs are predicted not to interact, while 4S8 and 3S8 stars are expected to mix (figure 3.1). This presumption was tested on solutions containing various combinations of droplets – 4S8 with 4L8A, 4L6, 3S10, or 3S8, with methods described in section A.14.

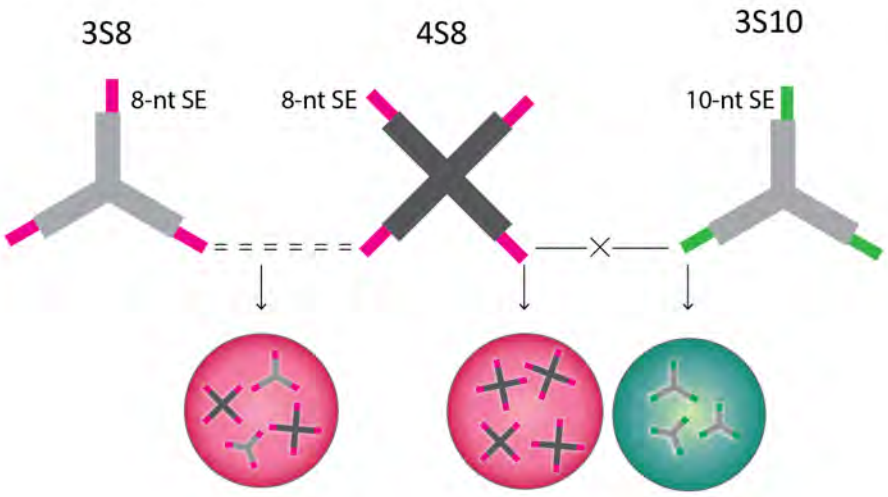

Figure 3.1: Predicted function of sticky end specificity in forming separate or co-localised droplets in multi-star systems.

As predicted, the first three solutions formed distinct populations of droplets, while the combination of 4S8 and 3S8 nanostars formed co-localised droplets. Regions were distinguished in confocal microscopy through the use of different fluorophore labels in different nanostars. NS 4S8 has a phase separation temperature (T_{PS}) of 60.4 ^{o}C, in comparison to 4L8A at T_{PS} = 63.1 ^{o}C. When co-annealed in solution, both stars formed distinct populations of droplets. 4S8 nanostars in combination with 4L6 (T_{PS} = 46.1 ^{o}C) or 3S10 (T_{PS} = 53.5 ^{o}C) also formed multiple droplet populations (figure 3.2). The use of orthogonal nanostars with complementary sticky ends – 4S8 and 3S8 (T_{PS} = 49.4 ^{o}C) – created co-localised droplets. These results are line with systems described in the literature, of fully orthogonal stars remaining distinct but complementary sticky ends allowing for mixing. The observed interactions

are hypothesized to be the result of DNA sequence complementarity versus orthogonality. The stars in systems A - C were designed to be entirely orthogonal, which would disallow hybridisation or mixing. This prediction was substantiated by the observed separation of droplet populations, indicating orthogonality in the designed sequences. Conversely, sample D consisted of orthogonal stars with complementary sticky ends, which mixed to form co-localised droplets.

Non-complementary DNA strands repel one another, with no base-pairing to compensate for the electrostatic phosphate backbone repulsion. Independent separation of the two droplet phases maximises NS-NS interactions for stars with complementary SEs, and minimises electrostatic repulsion between stars with non-complementary SEs.

This shows that two star types possessing non-complementary arms can be induced to form a single coacervate droplet through the inclusion of complementary sticky ends. Additionally, the first pair of nanostars confirms that possessing similar phase separation temperatures does not provide sufficient drive to induce the mixing of orthogonal droplets. The second and third combinations further demonstrate this species exclusion occurring over a broad range of ΔT_{PS} and relative fluidities. Finally, the combination of 4S8 and 3S8 droplets, although possessing a broad ΔT_{PS} = 11 ^{o}C, experience complete homogeneous mixing. This can be taken to mean that the lower T_{PS} 3S8 nanostars are either co-separating with the higher valency 4S8 stars, or are able to infiltrate the extant droplets upon the onset of their phase separation. The difference in valencies or arm lengths between nanostars did not appear to affect the formation of mixed droplets. Altogether, these results show that stars with orthogonal arms and orthogonal SEs form two droplet populations, while stars with orthogonal arms and complementary SEs form mixed droplets.

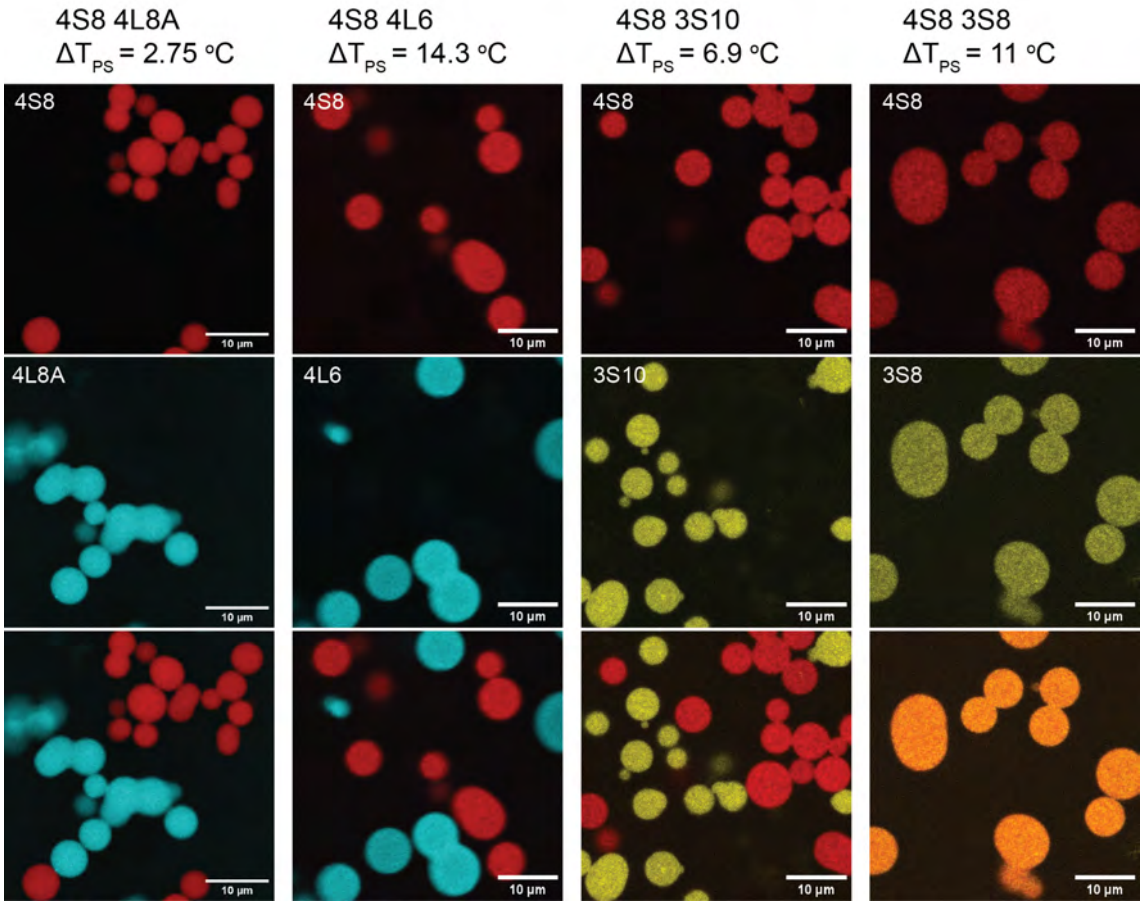

Figure 3.2: Confocal micrographs of four pairs of DNA nanostar droplets – 4S8 NSs combined with 4L10, 4L6, 3S10, or 3S8. All 4S droplets are false-coloured red; 4L droplets are coloured cyan; and 3S droplets are coloured yellow. Homogenously mixed droplets combine red and yellow to appear orange. Scale bars 10 μm.

3.3 Surfactant induced mixing in two-star systems

In comparison to the surfactant designs discussed in section 1.6.4, this thesis develops a different approach. Instead of creating a third star species of unique arm sequence and design, one of two stars is modified in its "degree of complementarity" (%C) to the other. This is achieved through the replacement of a select portion of sticky ends in a nanostar population (figure 3.3). The replacement of sticky ends is possible due to the modular design of the nanostars in this work. All NSs of a single star type have the same arm sequences, varying only in their attached sticky end. Therefore, through appropriate selection of NS strands, a single star could be made to possess four distinct sticky end sequences, if required. For instance, if half of "strand 1" in a 4L8 star solution were replaced with strand 1 from a 4L10 star, the resulting structure would contain 12.5% 10-nt SEs. The resulting 4L8 droplets are thus described as having 12.5 % complementarity to 4S10 or 3S10 droplets. This allows for the creation of multi-star systems with a controlled degree of complementarity between the two populations from a minimum number of NS component strands.

As described above, the co-annealing of fully orthogonal nanostars will result in distinct droplet populations, while orthogonal stars with complete SE complementarity will create co-localised droplets. In a solution containing a single type of NS, droplet formation has only been shown to occur when the nanostars possess self-recognising sticky ends. Matsuura *et al.* demonstrated that trivalent nanostars without sticky ends would not form coacervate droplets [29]. In this work, combining two nanostars of a single complementary SE sequence always formed co-localised droplets (figure 3.2). Mixing occurred regardless of differences in valency or size of the two nanostars. This observed behaviour is hypothesised to occur because of the predicted

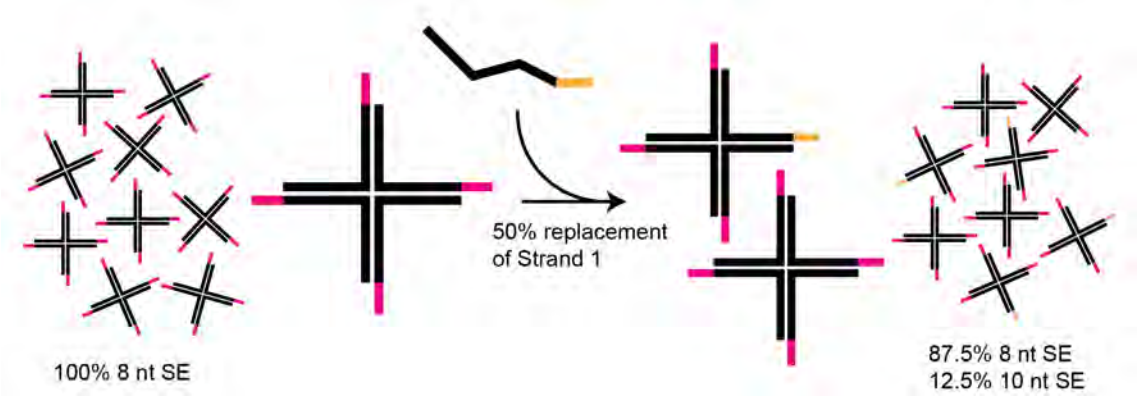

Figure 3.3: Definition of sticky end replacement used in this thesis. Nanostar systems were designed to be modular, with each nanostar body possessing one of five possible sticky ends. Arm sequences in a nanostar system can be used with any sticky end variant. The degree of complementarity can be tuned by varying the number and proportion of replaced strands. The illustrated system possesses 12.5 %C to 10-nt SE nanostars (yellow SE).

droplet formation mechanism discussed in Chapter 1 (figure 1.11). Star formation is mediated by arm sequence, while phase separation occurs only through interactions of sticky ends. Therefore, it is proposed that under the appropriate environmental conditions, any combination of stars will co-localise into mixed droplets, given that they possess the same sticky end (100 %C).

A question then arises, concerning mixed star populations of limited degrees of complementarity. Motivated by the works of Jeon *et al.* and Fabrini *et al.*, different combinations of nanostars were prepared here, from 0 - 50 %C [25] [153]. In a system containing 4S8 and 4L8A nanostars, with a ΔT_{PS} of 2.75 ^{o}C, 4L8A nanostars were modified to have a progressively greater %C to the 4S8 droplets. This was performed by replacing an increasing portion of 4L8A strands with the appropriate 4L8 strands, with details shown in table A.6. When increasing the %C of 4L8A to 4S8, confocal images show surface adhesion at 6.25 and 12.5 %C, lensed droplets at 25 %C, and co-localisation above 50 %C (figure 3.4). This aligns with the results of Jeon *et al.*, who saw similar lensed droplets at 1:1:1 star-surfactant ratios, with surface adhesion at lower s-Star ratio and co-localisation at higher ratios (figure 1.18).

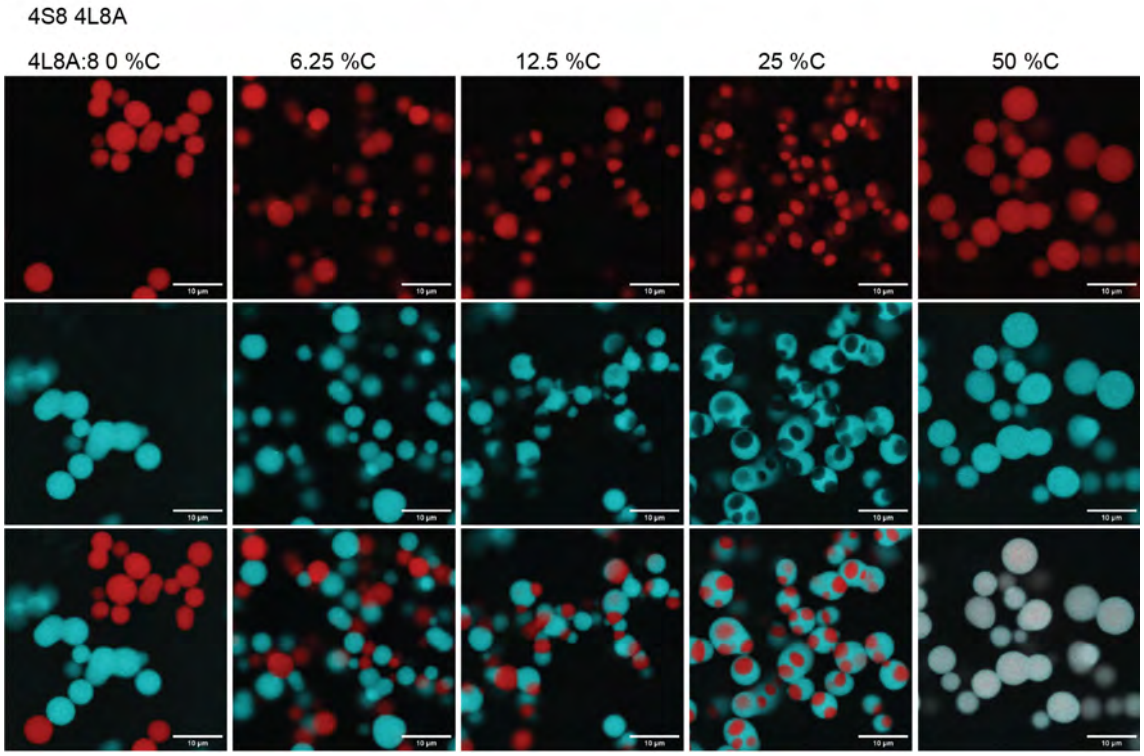

Figure 3.4: Microscale architectures upon increasing complementarity of low ΔT_{PS} nanostars, 2.75 ^{o}C, 4S8 and 4L8A, false-coloured red and cyan respectively. At 0 %C, complete separation is seen between populations. At 6.25 and 12.5 %C, an increasing degree of wetting of 4S8 against 4L8A occurs, conferred by the low level of attraction of 4L8A to 4S8. Patchy droplets form at 25 %C, with multiple cores of 4S8 suspended within spheres of 4L8A. At 50 %C, the degree of attraction between nanostar populations leads to co-localisation of droplet phases. Scale bars 10 μm.

This observed trend in droplet morphology was expected. At low degrees of complementarity, 4L8A droplets experience a small number of possible interactions with 4S8 droplets. We propose that the small proportion of s-Stars in 4L8A droplets are unable to disrupt the surface tension of the droplet. As such, it remains largely spherical, experiencing only slight deformation at the interface with 4S8 droplet phase regions. According to HCA measurements, both droplet populations form near-simultaneously. This could allow adhesion when they come into contact, but not fusion. The orthogonality of the majority of the SEs appears to outweigh the limited attraction experienced by the complementary SEs. At 25 %C, instead of surface-adhered but still distinctly separate droplets, discrete spherical objects were formed. These consisted of lensed 4S8 regions within a larger 4L8A droplet (figure 1.4). Finally, with a further increase in the attraction between droplets at 50 %C, the two populations of nanostars resulted in mixed droplets.

These observations potentially provide insight into the formation of microscale architectures. According to the phase-separation model discussed in chapter 2, 4L8A NSs form droplets at 63.1 ^{o}C, while 4S8 droplets form at 60.4 ^{o}C. If this is accurate, shortly following the formation of 4L8A droplets, when they are small and densely populated, 4S8 nanostars would also initiate phase separation. The complementary sticky ends might allow attachment of the forming 4S8 droplets to the extant 4L10 droplets, while the majority-orthogonal SEs would ensure they could not fully intermix. Due to the low ΔT_{PS} of the system, this process would occur within a short period of time, as droplet formation follows a linear folding ramp of 0.5 ^{o}C/min, and $\Delta T = 2.75$ ^{o}C occurs in 5.5 minutes. As both regions in the structures would be above their gelation temperature, patchy particles could fuse and be driven by surface tension to produce spherical structures. This proposed mechanism aligns with observations in the work of Fabrini *et al.*, who transcribed RNA nanostars in W/O droplets and allowed them to ripen at 37 ^{o}C [153]. Initially, dense multi-droplet

clusters are seen, containing regions of both nanostars. Gradually, the clusters came into contact and deformed, with complementary regions fusing and forming spherical structures. If the above model is correct, lensed particles form when two stars with limited %C phase separate in close succession.

To further explore the range of two-phase morphologies, pairs of nanostars with a broader ΔT_{PS} were then mixed (figure 3.5). A combination of 4S8 and 4L6 droplets at 25 %C resulted in core-shell structures, with a tendency towards the formation of partially-fused shells. Similarly, 4S8 and 3S10 NSs formed core-shell droplets, but with a lower complementarity (16 %C). The 3S10 shells also showed a lower tendency towards fusion than 4L6 shells. These combinations reveal two factors of consideration: alongside an appropriate ΔT_{PS}, the degree of complementarity between two stars required for shell formation appears to depend star valency. Additionally, shell formation is not affected by star size, only T_{PS}, with a 4S core being able to form with a shell of either the larger 4L or the smaller 3S nanostars.

Comparison may be drawn to the work of Nguyen *et al.*, who showed size-based partitioning of longer dsDNA rods to the surface of a nanostar droplet [160]. Their study used straight rods of dsDNA 131 - 426 bp (44.54 - 144.84 nm) in length, and compared infiltrate length with the number of complementary SEs (0 - 2). The minimum rod length required for droplet exclusion was 202 bp with one SE, and the required length increased to 278 when adding a second complementary SE. In contrast, the largest nanostar in this system (4L10) is only 59 bp (20.06 nm) in width, well within the range for infiltration according to Nguyen *et al.*'s results. Therefore, while size-based shell formation may be possible in our system, it is not observed for the parameter range explored here.

Imaging of core-shell systems using brightfield microscopy provides further insight into the droplet morphology. BF microscopy distinguishes between regions of vary-

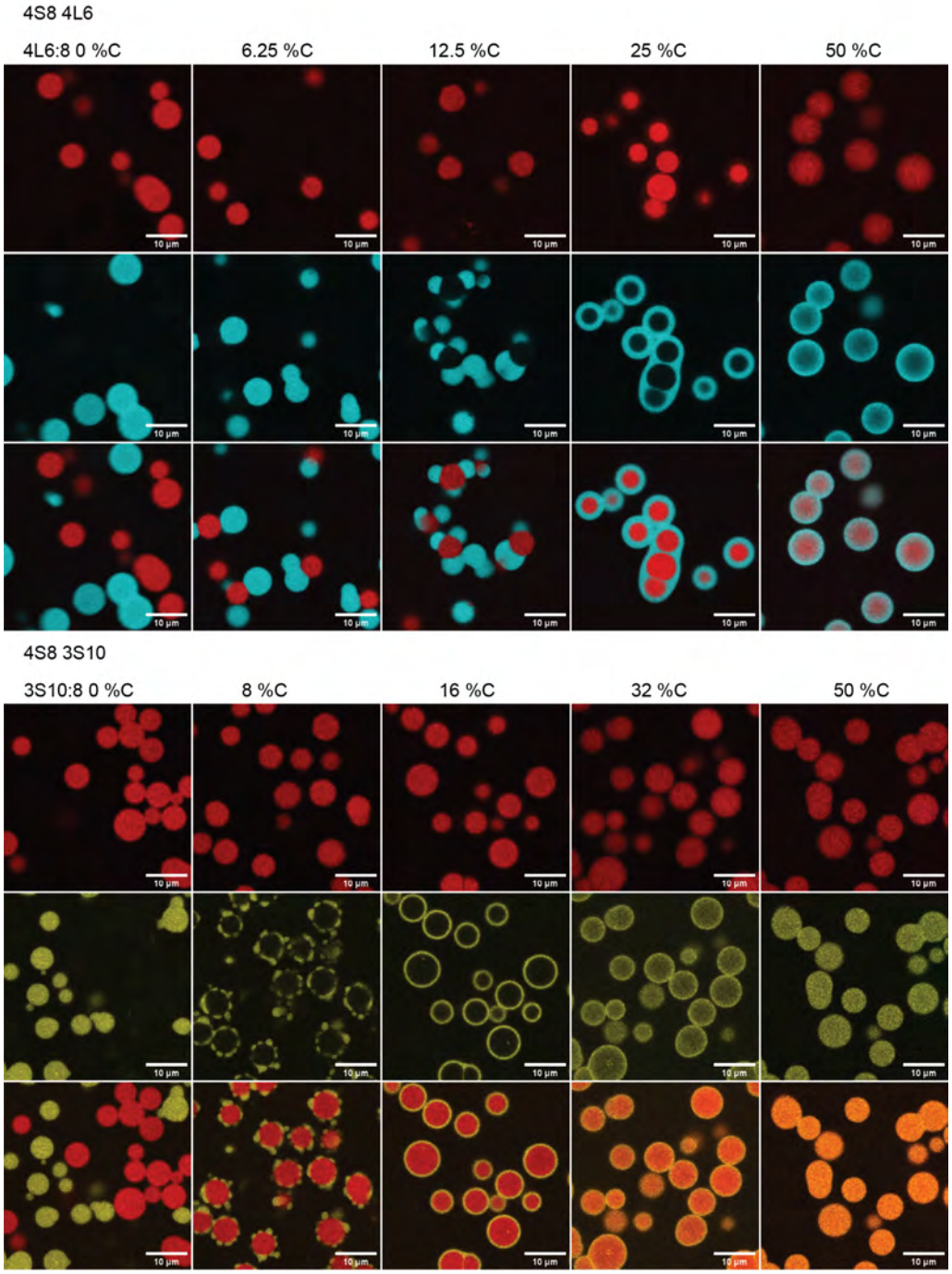

Figure 3.5: Microscale architectures upon increasing complementarity of high ΔT_{PS} nanostars pairs, comparing the same core star with two different shell stars, 4S8 4L6 (14.3 ^{o}C) and 4S8 3S10 (6.88 ^{o}C). Droplets are false coloured red for 4S8, cyan for 4L6, and yellow for 3S10. At 0 %C, there is complete separation between populations. At low degrees of complementarity, wetting of the lower T_{PS} star occurs against the high T_{PS} core. At 25 %C and 16 %C respectively, core-shell structures form. At 50 %C, mixing of phases is observed, and is more homogeneous for the 3S10 shell. Scale bars 10 μm.

ing density in a sample. Differences in refractive index between regions causes bending of the absorbed light, creating contrast at region boundaries that allows visualisation of different structures. Core-shell droplets were simultaneously imaged using this technique and confocal microscopy (figure 3.6). The core-shell regions, seen in confocal images as areas of distinct fluorescence, have a sharp boundary in BF microscopy. This suggests that the core-shell structure is not a simple diffusion gradient of nanostars in the droplet, but rather supports the interpretation of them as distinct physical regions. Similar BF imaging by Leathers *et al.* in their diffusion-based shell structures demonstrated that no physical boundary existed between infiltration regions [19]. Meanwhile, distinct region separation has been visualised in BF imaging in core-shell and lensed polymeric coacervates [97] [96].

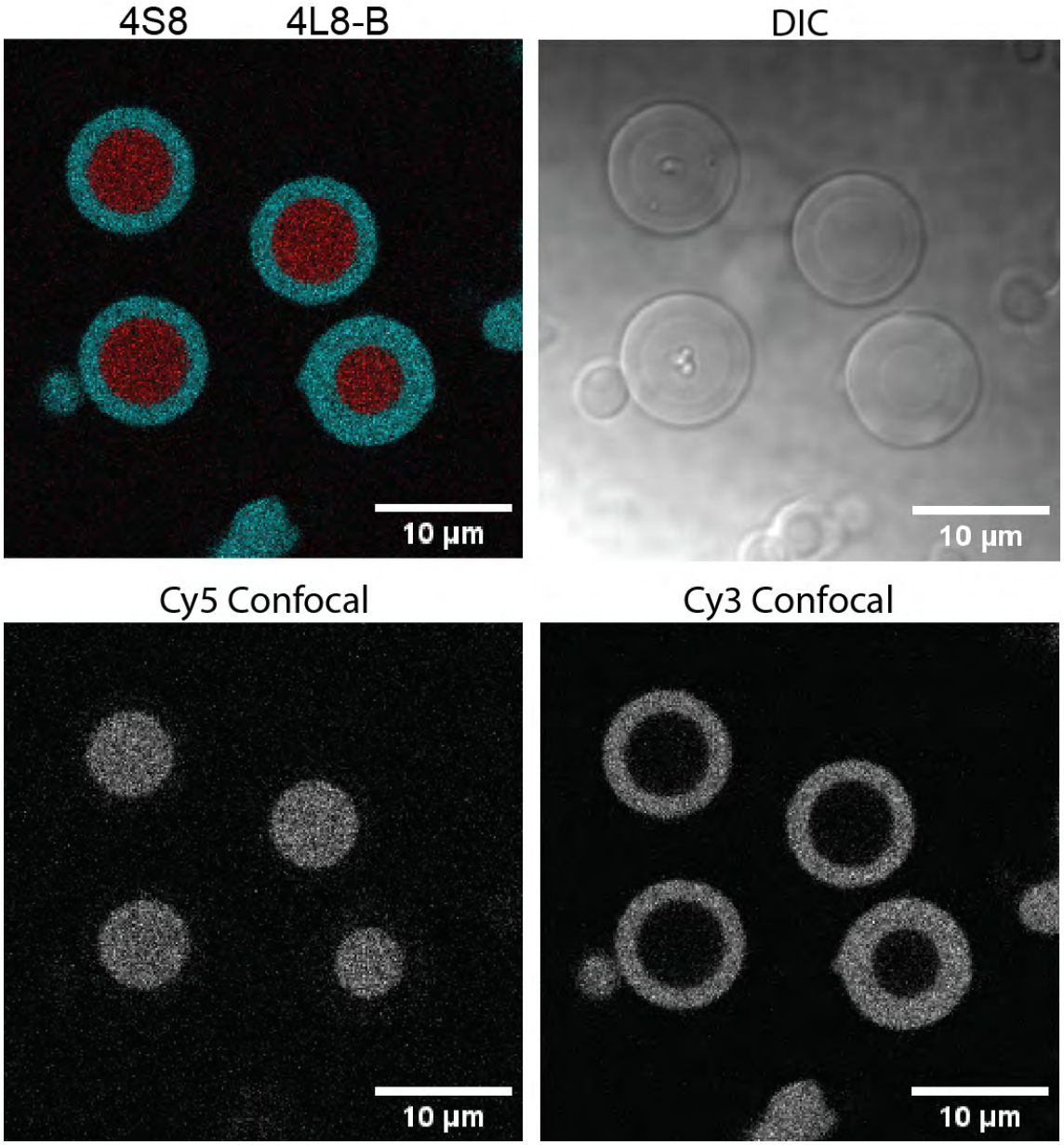

Figure 3.6: 4S8 4L8-B core-shell droplets. Individual channels of the core and shell fluorophores highlights the distinct separation of the two layers. A brightfield micrograph detects differences in the refractive index of the core and shell, creating a dark boundary between the layers, highlighting the distinct physical properties of the regions. Scale bars 10 μm.

The relative tendency towards phase separation of stars can be linked to the strength of sticky end binding as stabilised by increasing valency. The order of T_{PS} appears to determine core-shell positioning in this system. A possible mechanism for this is that on a molecular scale, stars of a higher binding strength undergo phase separation first, forming droplets (figure 3.7). The higher binding strength of the NS is influenced by both sticky end sequence and valency. As the system temperature continues to decrease, stars of lower T_{PS} would then initiate phase separation. Staggered phase separation may result in an initial nucleation and droplet formation of the "core" stars. At lower T, when the lower T_{PS} "shell" stars begin to phase separate, their partial complementarity to the extant droplets would allow them to nucleate upon the droplet surface, forming either surface patches or a shell [192] In contrast, in size-exclusion based layering, larger particles remain trapped on the outside of a droplet, forming the shell [28]. Alternatively, shell formation through spontaneous spinodal decomposition may be possible, but does not align with the gradual, fusion-based formation process seen in these systems. Direct visual observation of multi-phase droplet formation is required to elucidate the mechanism.

The proposed relationship between core-shell forming nanostars can be visualised using their respective hybridisation curves. For instance, figure 3.8 compares the hybridisation curves of 4S8 and 3S10 nanostars. The 3S10 nanostar, by virtue of its stronger arm binding sequence, hybridises at a higher temperature ($T_{Hy}1$) than the 4S8 nanostar ($T_{Hy}2$). As the system continues to cool, the valency of the 4S8 nanostar leads it to phase separate ($T_{PS}1$) at a higher temperature than the 3S10 nanostar ($T_{PS}2$). Given appropriate %C between the two stars, a core-shell droplet will form (figure 3.5).

Beyond phase separation, the physical states of two-phase droplet regions may be predicted by considering the relative strengths of the SE DNA sequences. The stronger binding energy of the 10-nt SE means the 3S10 droplet will likely stabilise

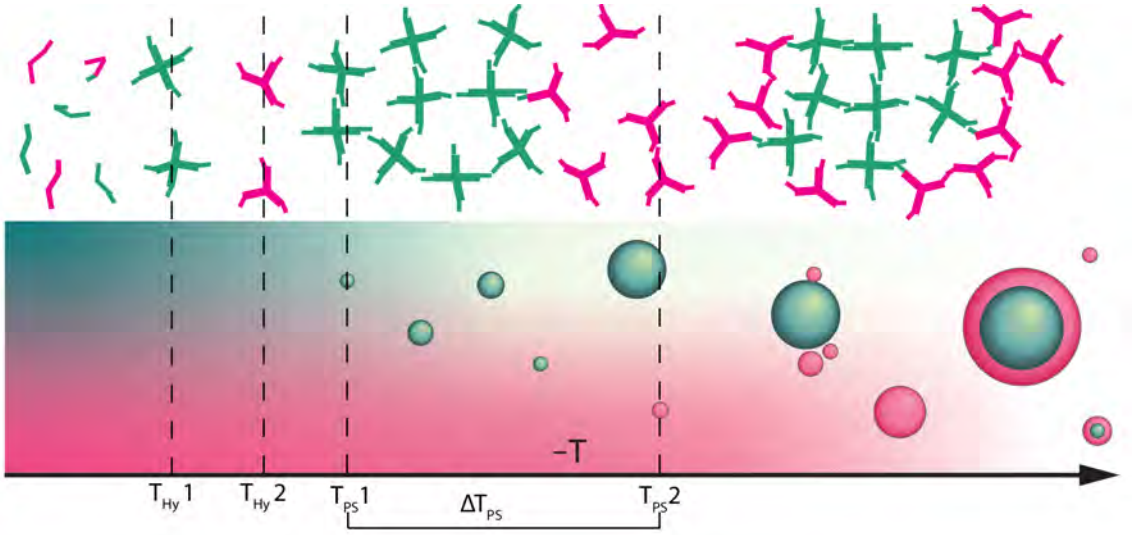

Figure 3.7: Schematic of proposed mechanism for two-phase droplet formation. At high temperatures, all strands are single stranded. On cooling, strands hybridise into nanostars; the tetravalent star hybridises first at $T_{Hy}1$, followed by the trivalent star at $T_{Hy}2$. The trivalent star has a limited degree of complementarity to the tetravalent. At lower temperatures, phase separation is initiated, with tetravalent stars forming droplets at $T_{PS}1$. These droplets grow via coarsening and fusion until $T_{PS}2$, at which point the trivalent stars initiate phase separation. The partial complementarity of the trivalent stars allows for nucleation upon the existing tetravalent droplet surfaces, leading to the formation of a core-shell structure. The formation of the shell prevents further growth of core droplets, acting as a kinetic trap and limiting the core size.

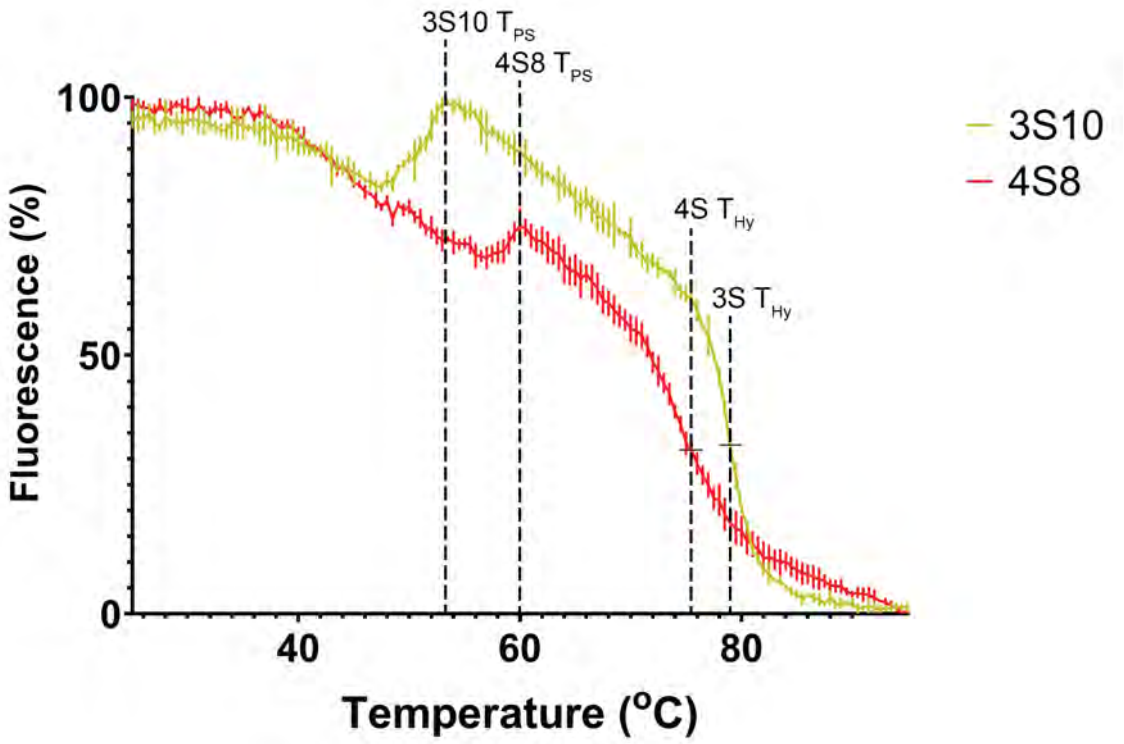

Figure 3.8: Overlaid melt curves of 4S8 and 3S10 nanostars at 10 μM in 0.5 M NaCl, measured in a Qiagen RotorGene Q. The process of formation by cooling runs from left to right. Temperatures of note are highlighted. 3S nanostars hybridise prior to 4S nanostars, due to higher arm stabilities. During cooling, the 4S8 nanostar phase separates into droplets (4S8 T_{PS}) before the 3S10 (3S10 T_{PS}).

and enter a hydrogel state at a higher temperature than the 4S8 nanostar. Thus, there may exist a temperature at which the 3S10 shell is a gel, while the 4S8 core is a liquid.

In this section, it was found that if one droplet population possesses a limited degree of complementarity to the other, unique architectures will result. The novelty of this work is seen when such systems are created using pairs of nanostars with a high ΔT_{PS}. The type of interaction between the two populations is predictable as a function of the difference in T_{PS} (ΔT_{PS}) and the degree of complementarity (%C).

3.4 Investigation of sticky end replacement

Examples of surfactant stars in the literature used a variety of star structures and SE placements (figure 1.17). This leads to uncertainty in whether it is the structure of surfactant stars that affects microstructure formation, surfactant concentration, or both. Variations in the pattern of strand replacement in shell nanostars were investigated in a dual tetravalent system. Earlier results indicated that complementarity of twenty-five percent of nanostar B SEs to nanostar A formed an A:B core-shell structure. Here, four forms of shell nanostar sticky end replacement were tested (figure 3.9), with calculations detailed in section A.15:

- Strand 1: The total replacement of one strand, leading to all nanostars in the system having a single core-complementary SE.
- Strand 1+2: Replacement of half of two different strands, adjacent in placement, creating a population of stars with a symmetric distribution between 0-50 %C.
- Strand 1+3: Replacement of half of two different strands, opposite in placement, creating a population of stars with a symmetric distribution between 0-50 %C.
- Strand 1-4: Replacement of one quarter of each strand, creating varieties with an asymmetric distribution of 0-100 %C.

Four solutions of 4S8 4L8-B 25 %C droplets were annealed. When imaging, Cy5 fluorophores were applied to the core nanostars and Cy3 to the shell. It was found that regardless of the pattern of sticky end replacement, core-shell structures formed (figure 3.10). This suggests that the degree of complementarity between nanostar populations and ΔT_{PS} are the key parameters in determining overall morphology. The case of the total replacement of strand 1, resulting in 100% of shell nanos-

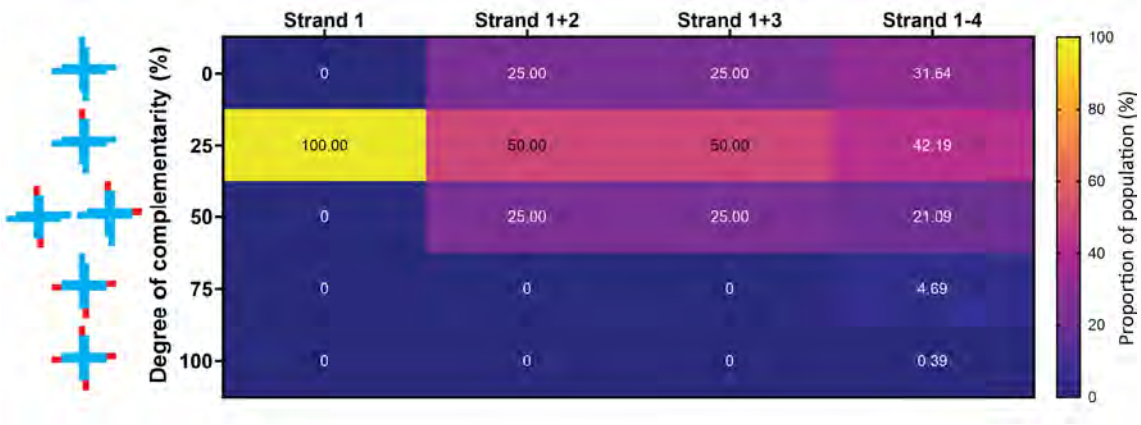

Figure 3.9: Probabilities of tetravalent star structures based on pattern of sticky end replacement, with all at 25 %C. Calculated as discrete probability distributions in section, assuming strand binding to NS events are independent of SE sequence A.15.

tars having 25% complementarity to the core, demonstrates that an independent surfactant species is not required to initiate this behaviour.

In the case of 25% S1-4 replacement, viewing the shell nanostar micrograph channel separately shows a higher degree of shell infiltration into the core region of the droplet, when compared to the three other replacement methods. The replacement of 25% of all strands results in a shell star population predicted to contain up to 0.4% 100% complementary stars, and 4.7% at 75 %C. As previous results have shown, shell populations with greater than 50% complementarity result in infiltration and mixing with the core droplet. This small portion of high %C shell nanostars could be the cause of an enhanced infiltration. However, ANOVA analysis of the central intensity of each replacement type shows no significant difference between groups.

The replacement of 50% of two strands, either the adjacent Strands 1 and 2 or the opposite S1 and S3, is expected to result in a nanostar population in which half will possess one core-complementary SE, while the remaining population is split between 0% and 50% complementarity. This assumes that the recruitment of different strands to a nanostar during formation occurs randomly, with the sticky end

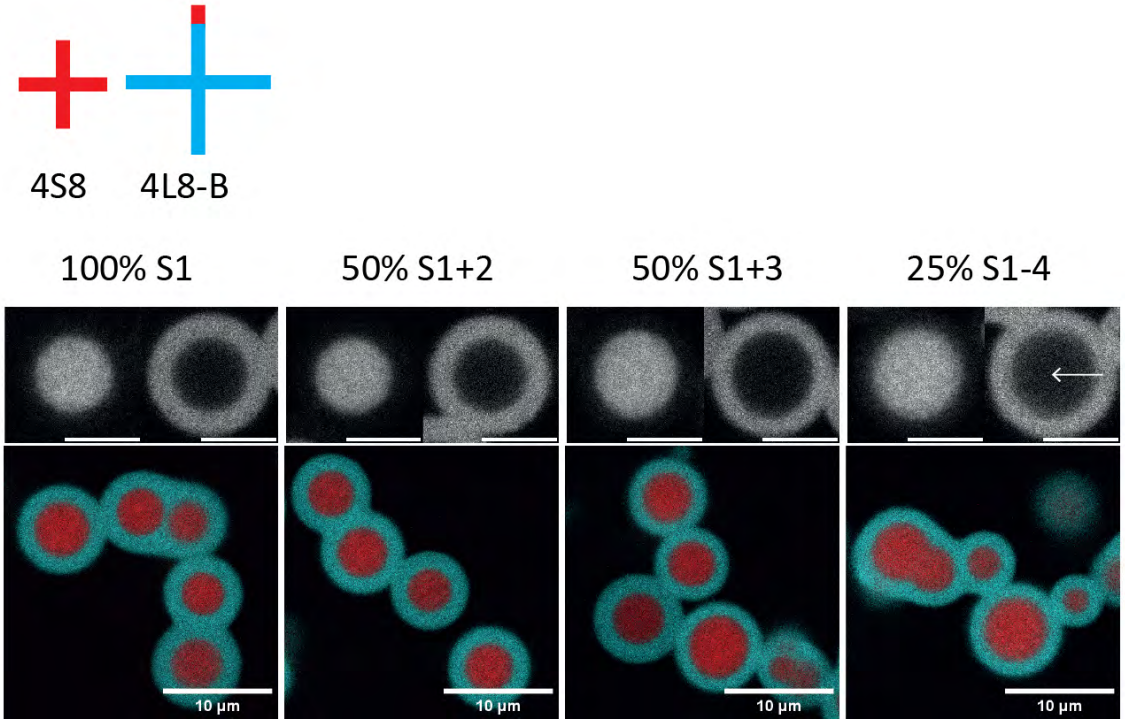

Figure 3.10: Four patterns of sticky end replacement in creating 4S8 4L8-B core-shell structures with 25 %C of shell to core. Complete replacement of one strand or 50% replacement of two strands results in homogenously thick, well separated shells. Replacement of one quarter of all strands appears to show a heightened degree of infiltration into the core (white arrow). Scale bars 10 μm.

of one arm being independent of the SEs of others. However, the thermodynamics of DNA duplexation are affected by the presence of ssDNA tails [163]. Dimer formation temperature is decreased through proximity to the repulsive ssDNA backbone, with the effect on T_M increasing with increased tail length. Therefore, it is possible that nanostar hybridisation is affected by SE replacement, rendering the duplexation of individual arms no longer independent events. If the effect of the ssDNA SE on nanostar hybridisation is dependent on the SE length or sequence, it is possible that the population distributions of surfactant stars vary with the type of SE replacement.

The nanostars in this work are highly flexible, afforded by the high cation concentration and the unpaired bases at the central junction and arm termini. According to the OxDNA simulations conducted in section 2.4, stars are able to adopt a broad number of physical conformations, from open planar to linear. Nanostars with flex-

ible central junctions were predicted to freely move between two variations of an open rotated structure (figure 3.11). Given that the majority of nanostars adopt a planar configuration in simulations (section A.6), the relative placements and positions of SEs in figure 3.11 would suggest that adjacent replaced nanostars are equally distributed in opposite and adjacent SE conformations, while opposite replacement tends only towards adjacent conformations.

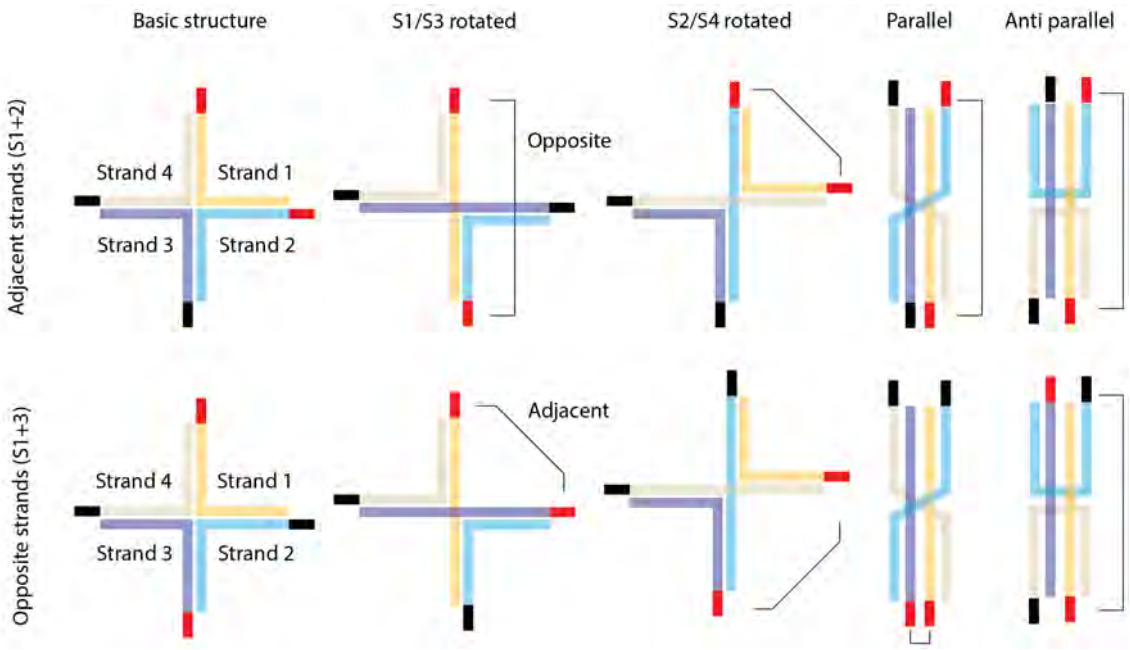

Figure 3.11: When replacing two strands of a tetravalent star, either opposite or adjacent strands may be chosen. Internal bending and rotation of arms about the central junction mans that the position of the resulting sticky ends may be either opposite or adjacent, irrespective of arm pattern.

The simulations in section A.6 were conducted on systems of single nanostars. The data may therefore imperfectly model the flexibility of nanostars when constrained in a three-dimensional mesh, as is the case in a stabilised droplet. However, when considering the moments at the onset of phase separation, which is when shell formation is initiated, stars are expected to exist in the bulk phase in isolation or in minimal clusters. Thus, while unable to model the system in its entirety, these simulations nevertheless have relevance to discussions of phase separation.

Altogether, it was demonstrated that core-shell structures may be produced from a set of two nanostars, using multiple different surfactant star configurations. This suggests that while the concentration of surfactant stars, or the relative %C, is important in producing known architectures, the structures are not impacted by the physical configuration of the surfactant star.

3.5 Prediction of two-star droplet architecture

Following the results from Section 3.3, we hypothesise that ΔT_{PS} can predict core-shell morphology. Specifically, the requirement is estimated to be $\Delta T_{PS} > 3^{o}$C. As shown in table 3.2, with the exception of pairs of nanostars with the same body type or sticky end, the majority of nanostar combinations are predicted to result in layered droplet conditions. The remaining pairs are expected to form patchy droplets, due to the similarities in their phase separation temperatures.

Star 2 \ Star 1	3S6	3S8-B	3S8	3S8-A	3S10	4S6	4S8-B	4S8	4S8-A	4S10	4L6	4L8-B	4L8	4L8-A	4L10
3S6							18.6	35.1	38.0	35.8		18.3	35.9	38.5	37.5
3S8-B						18.9		35.1	38.0	35.8	21.1		35.9	38.5	37.5
3S8						-5.9	-6.1		13.3	11.0	-3.6	-6.5		13.8	12.8
3S8-A						-11.0	-11.3	5.3		5.9	-8.8	-11.6	6.0		7.6
3S10						-10.0	-10.3	6.3	9.1		-7.8	-10.6	7.0	9.6	
4S6		-18.9	5.9	11.0	10.0							-0.6	17.0	19.6	18.6
4S8-B	-18.6		6.1	11.3	10.3						2.5		17.3	19.9	18.9
4S8	-35.1	-35.1		-5.3	-6.3						-14.0	-16.9		3.4	2.4
4S8-A	-38.0	-38.0	-13.3		-9.1						-16.9	-19.8	-2.1		-0.5
4S10	-35.8	-35.8	-11.0	-5.9							-14.6	-17.5	-0.1	2.8	
4L6		-21.1	3.6	8.8	7.8		-2.5	14.0	16.9	14.6					
4L8-B	-18.3		6.5	11.6	10.6	0.6		16.9	19.8	17.5					
4L8	-35.9	-35.9		-6.0	-7.0	-17.0	-17.3		2.1	-0.1					
4L8-A	-38.5	-38.5	-13.8		-9.6	-19.6	-19.9	-3.4		-2.8					
4L10	-37.5	-37.5	-12.8	-7.6		-18.6	-18.9	-2.4	0.5						

Table 3.2: ΔT_{PS} (^{o}C)for nanostar pairs and predicted architectures; star 1 (column) – star 2 (row). Green shading predicts S1:S2 core-shell pattern, $\Delta T_{PS} > 3$ ^{o}C; yellow shading predicts S2:S1 core-shell pattern, $\Delta T_{PS} <$ -3 ^{o}C; red shading predicts patchy droplets, -3 ^{o}C $< \Delta T_{PS} < 3$ ^{o}C. White regions predict mixed droplets, through matched SEs or arm sequences.

3.5.1 Screening of two-star morphologies

Several droplet configurations predicted in table 3.2 were experimentally investigated. Combinations of trivalent and tetravalent stars used 16 %C surfactants, while tetravalent and tetravalent stars used 25 %C. Representative confocal images are shown in figure 3.12. The majority of tested combinations aligned with predicted structures, forming core-shell or patchy droplets as indicated by ΔT_{PS}. Those samples which did not align with the above theory were investigated further.

Nanostar combinations with ΔT_{PS} below 3 ^{o}C tended to form patchy particles. Instead of the single, concentric regions of core-shell droplets, these possessed a higher morphological complexity [94]. In order of increasing intricacy, the structures include lensed particles, co-continuous regions, and hierarchically nested droplets (figure 3.13). These structures formed at the same degree of complementarity as core-shell droplets. This suggests the observed differences in morphology are not the result of differing degrees of interaction, as was the case in the works of Jeon *et al.* and Fabrini *et al.*, but rather the relative timing of the formation of each phase [25] [153].

We may compare these observations with the results of Malouf *et al* [193]. Expanding upon the work of Walczak *et al.* [151], they formed core-shell nanostar condensates, using cholesterol moeties in place of ssDNA sticky ends. They demonstrated that the formation of core-shell architectures was dependent on the size ratio of the two constituent nanostars, with such structures only forming at ratios above 1.2. Furthermore, their results indicated that larger nanostars were invariably confined to the surface of demixed droplets, forming the shell, as they were unable to penetrate the dense mesh of the smaller nanostar core. Additionally, Malouf *et al.* considered ΔT_M as an effector of core-shell formation and found it to be unrelated, leading them to conclude that their core-shell structures were the result of size-

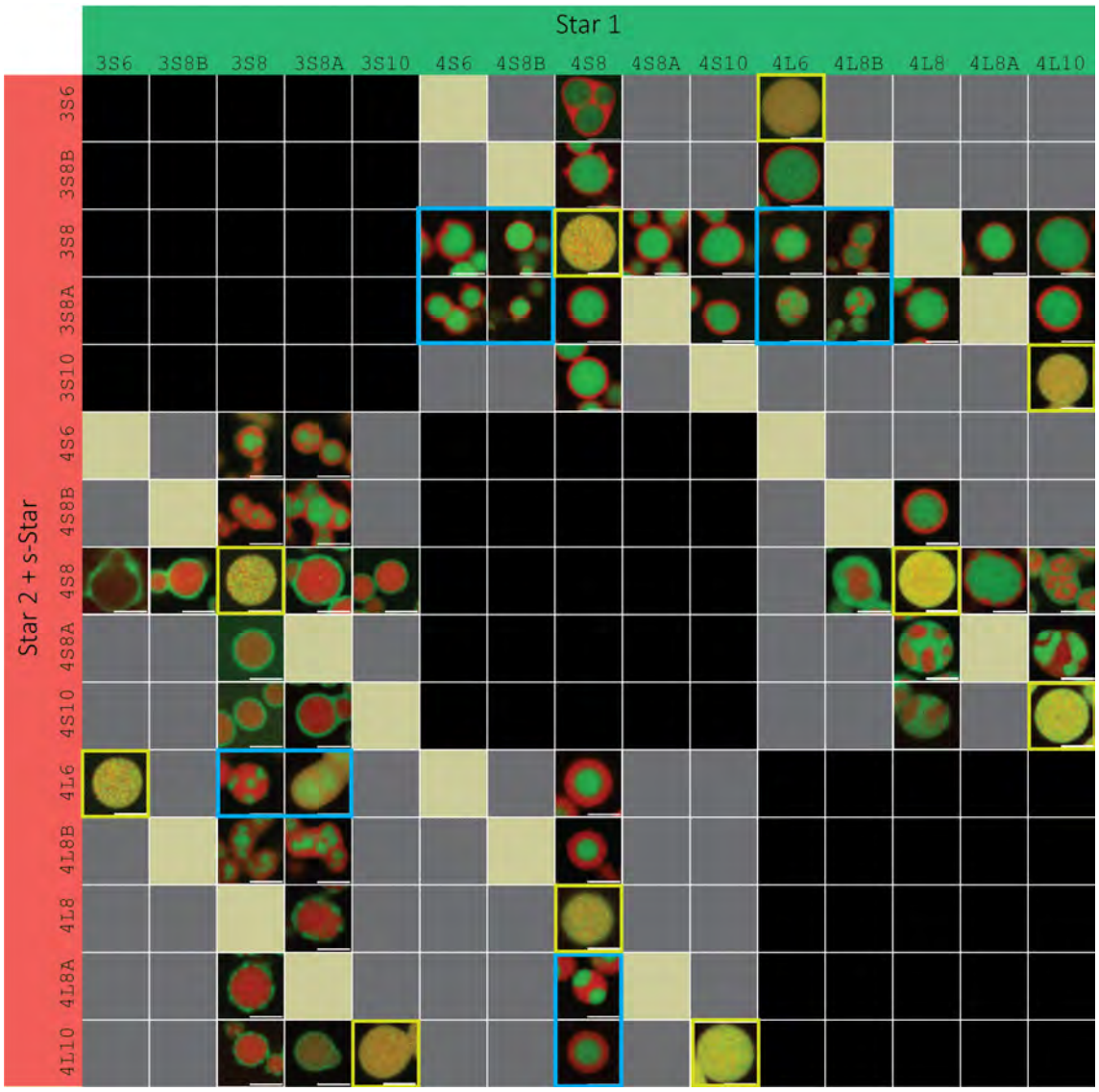

Figure 3.12: All core-shell systems produced in this thesis. Star 1 (green) was unmodified; star 2 (red) includes surfactant stars created by SE replacement, 16 %C for trivalent and 25 %C for tetravalent. **Black squares**: Nanostars of matching arm sequence - co-localised droplets predicted. **Yellow squares**: Nanostars of matching SE sequence - co-localised droplets predictd. **Grey squares**: Untested combinations. **Yellow outlines**: Co-localised droplets of matching SEs. **Blue outlines**: Droplet architecture that does not match the structure predicted in table 3.2. Scale bars 10 μm.

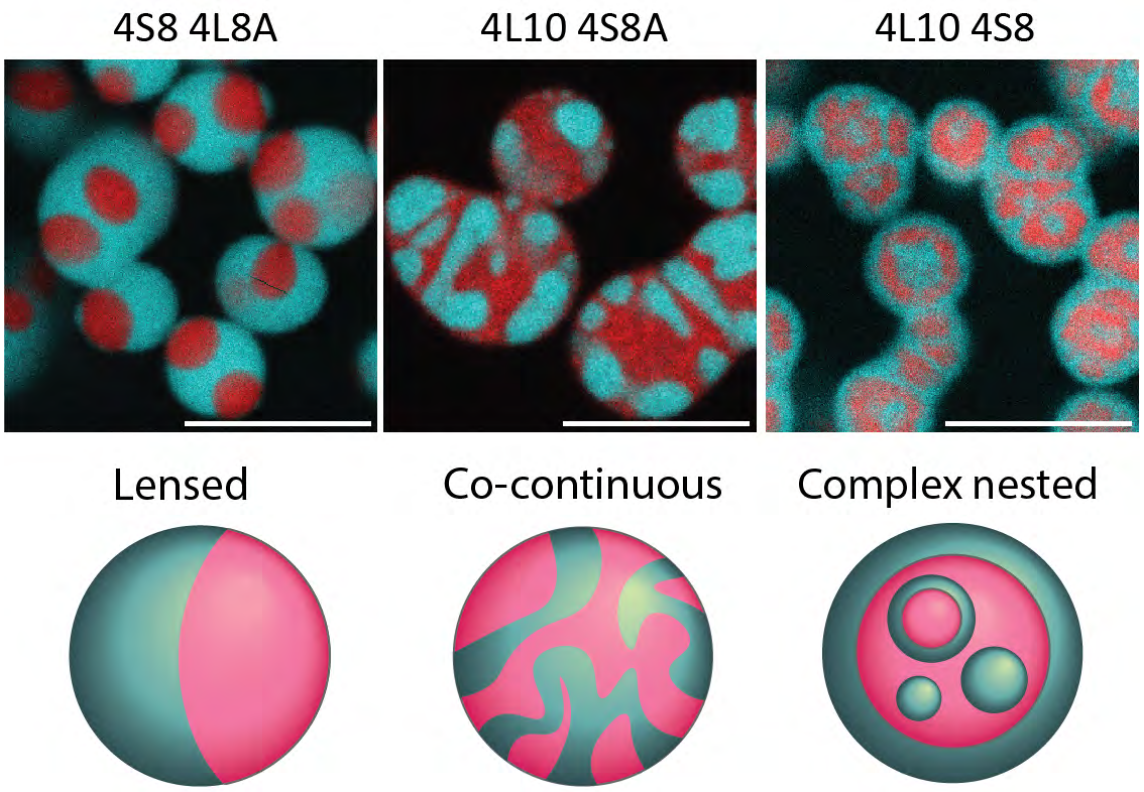

Figure 3.13: Morphologically complex droplets observed in this work. Scale bars 10 μm.

induced phase separation. These results lie in contrast to the structures observed here. In this work, it was found that core-shell microarchitectures formed at C/S NS size ratios between 0.6-1.7, with no indication of size-based NS partitioning within the studied range (figure 3.14). Additionally, 95% of core-shell droplets formed at $\Delta T_{PS} > 3\ ^oC$, while only 50% of complex structures were above this same threshold. These results thus suggest a kinetic drive towards core-shell formation based on the relative phase separation temperatures of the constituent nanostars, rather than a size-based separation. The difference between the two systems may be attributed to the different modes of nanostar interaction - cholesterol moeties, as compared to ssDNA sticky ends.

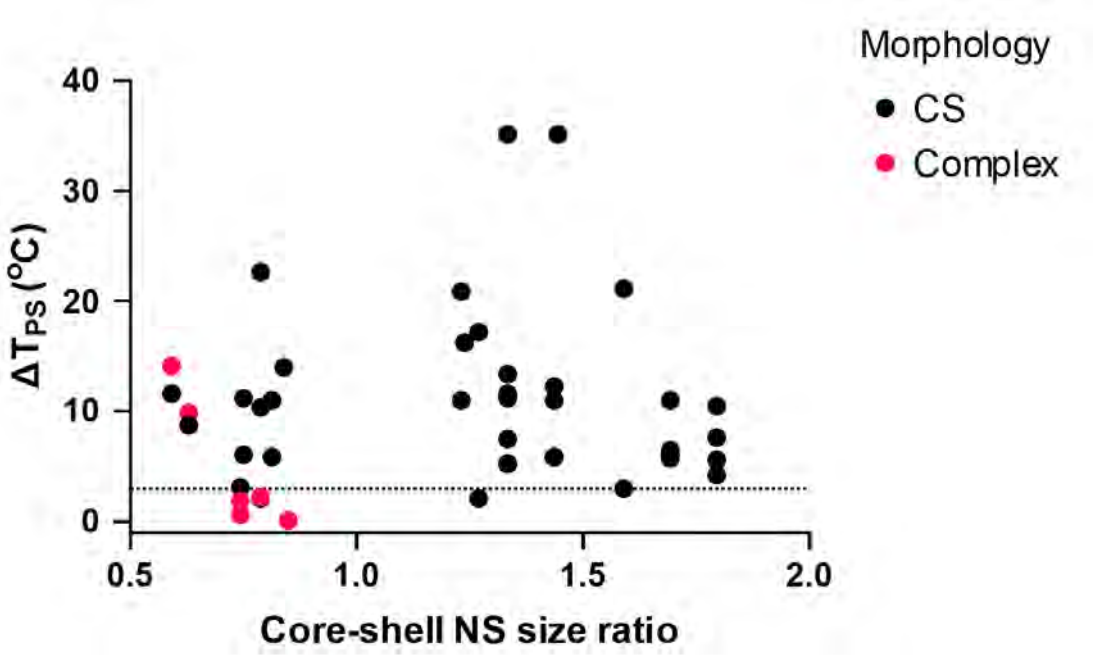

Figure 3.14: Comparison of the core-shell NS size ratio and measured ΔT_{PS} of core-shell and complex droplet microarchitectures. Horizontal line at 3 ^oC highlights the approximate boundary between core-shell and complex morphologies.

3.5.2 Droplets not matching prediction

As shown in figure 3.15, the T_{PS} of a surfactant star is shifted in the direction of the replaced sticky end. In investigating a 4S8 25% 6-nt system, 4S8 had a T_{PS} of 58.13 ^{o}C, 4S6 had 40.5 ^{o}C, and 4S8 25% 6-nt had 49.38 ^{o}C. The replacement of SEs with a less stable sequence may result in the surfactant star having a lower T_{PS} than either unmodified star. For instance, 4L10 nanostars typically phase separated at 59 ^{o}C, while 4L8 phase separation occurred at 57.38 ^{o}C. In a system containing 4L10 25% 8-nt surfactant stars, phase separation temperature was measured as 55.5 ^{o}C. The inclusion of lower T_{PS} 8-nt SEs appears to reduce the T_{PS} of the system as a whole, resulting in an increase in ΔT_{PS} and a shift from a patchy to a core-shell system (figure 3.16).

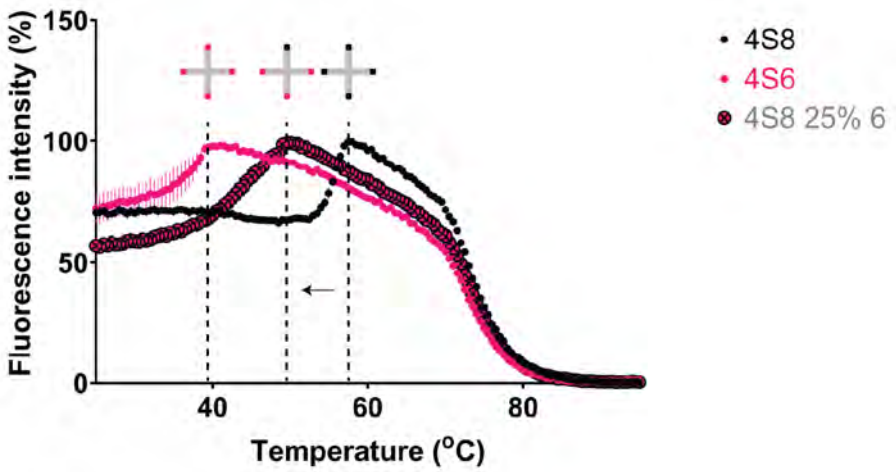

Figure 3.15: T_{PS} changes with SE replacement. Comparison of hybridisation curves of 4S8, 4S6, and 4S8 25 %C 6-nt nanostars. The hybridisation temperature of the chimeric nanostar shifts in the direction of the lower T_{PS} SE.

The combination of 4S8 and 4L10 nanostars have a ΔT_{PS} of 2.4 ^{o}C. As shown in figure 3.16, modifying the 4S8 nanostars to include 25 %C surfactant stars does indeed result in multi-core patchy droplets. However, modification of 4L10 nanostars to induce complementarity to 4S8 droplets instead results in a 4S8-core 4L10-shell structure. This suggests that the ΔT_{PS} of the system may vary depending on which

nanostar population is modified. Therefore, HCA was performed on surfactant stars, and their T_{PS} compared to an unmodified population.

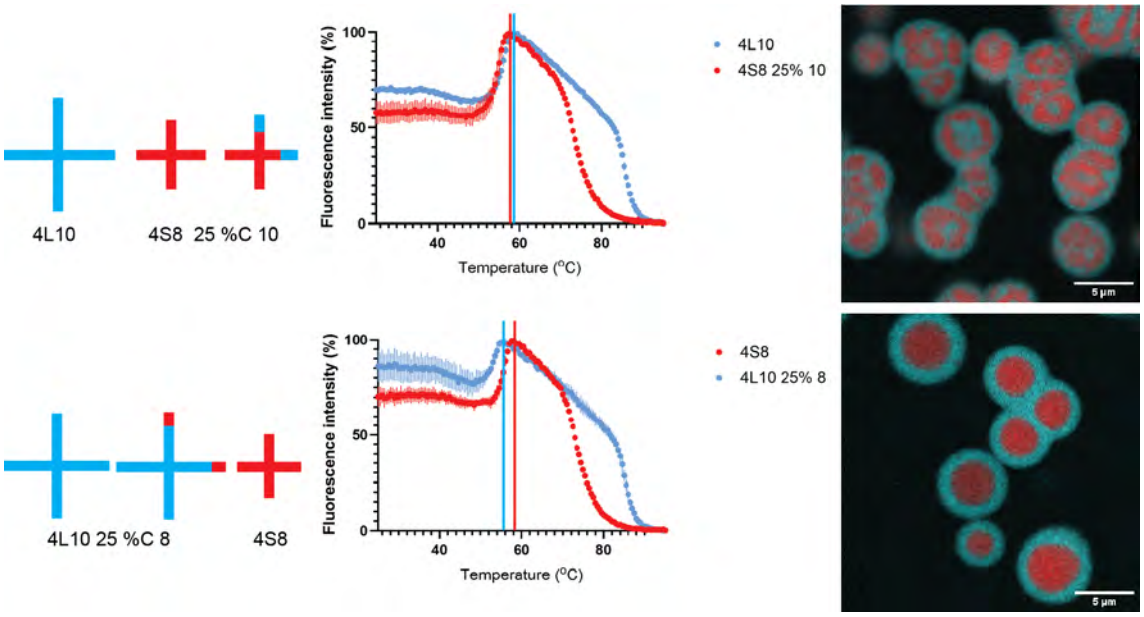

Figure 3.16: Hybridisation curves of 4S8 4L10 two-star solutions, comparing surfactant star choice on HC and resulting droplet structures. **Measured** T_{PS}: 4S8 = 58.13 °C. 4L10 = 59 °C. 4S8 25% 10-nt = 57.5 °C. 4L10 25% 8-nt = 55.5 °C. Scale bars 10 μm.

Discrepancies between predicted and actual structure were particularly prevalent in systems containing 6-nt or 8B-nt SEs. The markedly lower T_{PS} of these sticky ends significantly reduced the T_{PS} of higher -ΔH surfactant stars. Alternatively, stars possessing these SEs, when modified to act as surfactants to higher T_{PS} systems, saw a dramatic increase in ΔT_{PS}. These effects combined to result in micro-architectures contrary to predicted structures. Overall, of the fifty investigated star combinations, thirty eight aligned with initial predictions based on HCA-based ΔT_{PS}. While most of the irregularities could be explained by SE-modified HCA, certain combinations are still beyond the predictive capabilities of this system. Thus, basic nanostar HCA may be used to screen for potential micro-architecture formation. The resulting ΔT_{PS} may be indicative of core-shell or patchy droplet formation, with more precise prediction coming from HCA of surfactant stars.

3.5.3 Droplets matching prediction

Of the nanostar combinations which successfully formed core-shell structures, several were investigated in further detail. These samples continue to follow the method of forming core-shell structures at 16 %C in trimer-containing pairs, and 25 %C in tetramer-only pairs. The core-shell order of the structures similarly aligns with the ΔT_{PS} of the nanostars, with the higher T_{PS} star forming the core.

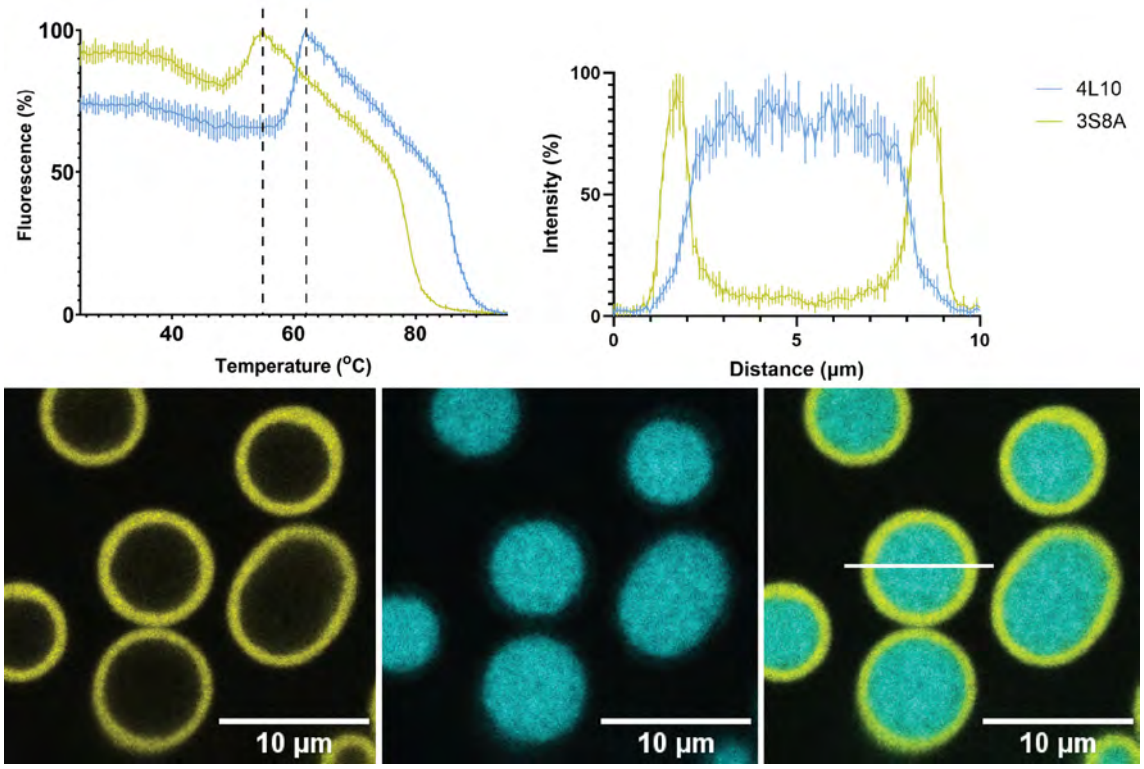

Figure 3.17: Core-shell structure of 4L10 3S8A, with hybridisation curves and representative pixel profile. Average shell width 0.84 ± 0.05 μm. Scale bars 10 μm.

Core-shell systems, shown in figure 3.17 and in Appendix C, produced homogeneous shells with distinct separation between internal and external regions. Dimer or aggregate structures were noted, with adjacent droplets exhibiting partially fused shells. In such structures, even when consisting of many multiple droplets, cores remained distinctly separate from each other. For any given combination of nanostars, the same physical appearance was repeatedly produced, showing high repeatability of this technique (figure 3.18).

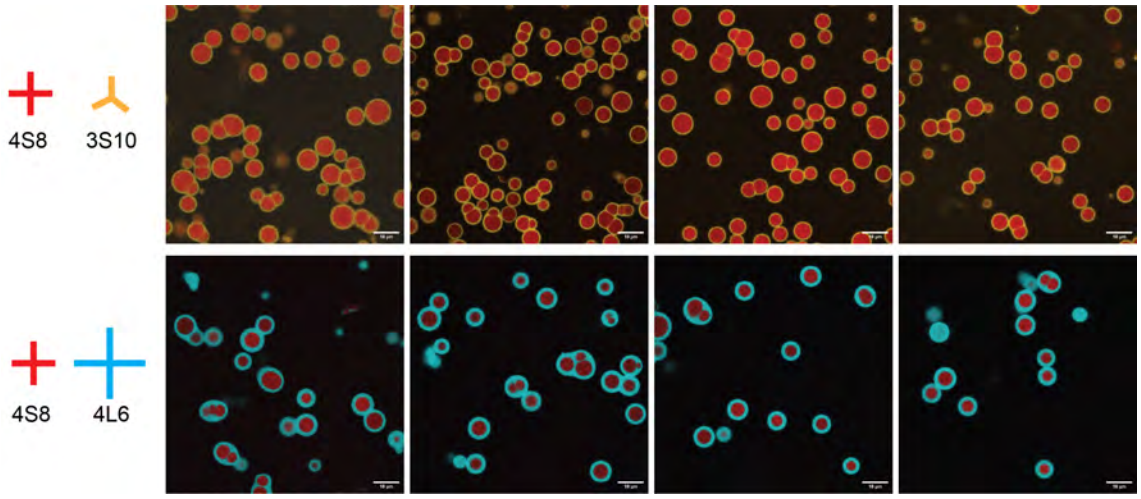

Figure 3.18: The same nanostar pairs always formed the same physical structures, including population density, core size, and shell width. Imaged solutions were prepared up to 1 year apart, from different DNA and cation stocks. Scale bars 10 μm.

3.5.4 Trends in shell width

Trends in the physical characteristics of core-shell structures were investigated. A Gaussian smoothing method applied to shell channel pixel profiles in order to measure shell width (section A.16). Within a given droplet population, shell thickness varied between 7.4-16.7%, with a larger shell star size tending to result in a higher standard deviation.

The thickness of droplet shells was compared to shell T_{PS}, system ΔT_{PS}, core identity, shell sticky end enthalpy (-ΔH), shell sticky end free energy (ΔG), and shell nanostar size (figure 3.19). Of these, shell NS size (figure C.14) was the only factor found to have a significant effect on shell width. Linear regression analysis produced an R^2 value of 0.75, indicating a moderate linearity of data, and a slope p-value $<$ 0.0001, indicating a statistically significant relationship between star size and shell width.

Systems with shells formed of 4L nanostars were significantly thicker than others. This may be due to the length of 4L arm. Given a constant number of nanostars, a crystal network formed of longer nanostars is expected to fill a larger volume than

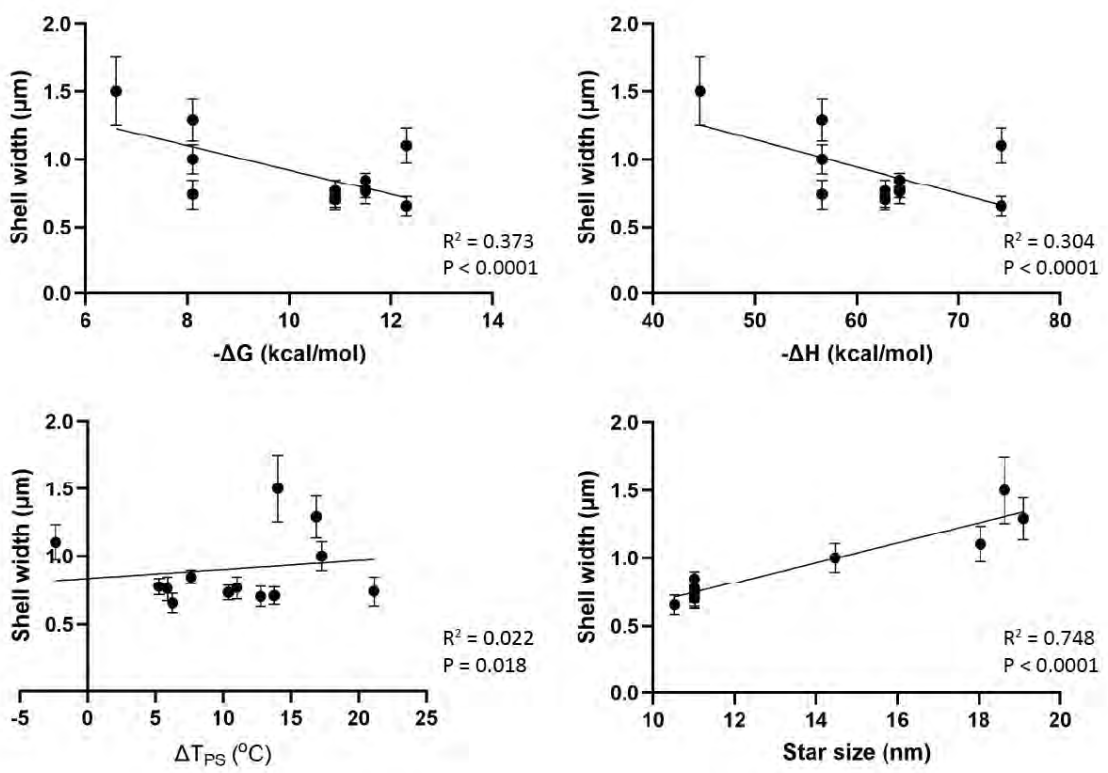

Figure 3.19: Comparison of measured shell width to shell SE $-\Delta H$, shell SE $-\Delta G$, core−shell T_{PS}, and shell star size. Error bars showing standard deviation of measured widths. Results of linear regression analysis shown as p-value of slope and R^2 value. No trend is evident between shell width and system formation temperature, shell SE bond enthalpy, or shell SE bond entropy. A trend was observed of shell thickness increasing with star size, of moderate confidence. Star size was found through oxDNA simulations (fig. C.14).

stars of shorter arm length. Alternatively, the time between shell formation and gelation may contribute towards shell width. However, these theories are not supported by the measurements of droplet size discussed in Chapter 2. While 4L droplets tended to be larger than others, the difference was not to the degree seen between shells. Further investigation of this phenomenon is required, via the production of further nanostar combinations.

3.5.5 Surfactant direction

In this work, core-shell nanostar combinations were typically produced such that the shell nanostar possessed complementarity to the core, through the creation of surfactant stars. Due to the stabilising effects of nanostar valency [24], trivalent nanostars were found to have lower phase separation temperatures than tetravalent stars (section 2.6). As discussed above, the order of core-shell formation is hypothesised to occur based on phase separation temperature. Therefore, due to tetravalent stars tending to phase separate at higher temperatures, and surfactant modification being applied to shell stars, trivalent-tetravalent NS pairs were always prepared with surfactant modification of the trivalent star. Above, it was asserted that tetravalent nanostars required 25 %C for the formation of core-shell structures, while trivalent-tetravalent pairs required 16 %C. However, it was unclear whether a trivalent-tetravalent system in which the tetravalent star was modified would require 16 %C or 25 %C of the tetravalent surfactant.

Multiple 4L8A 3S8 solutions were prepared, varying the direction and degree of complementarity between the two stars (figure 3.20). When the 3S10 stars were modified to have 16 %C, core-shell structures formed. When the 4L8A stars were produced using 16 %C, ringed structures formed; however, instead of a uniform shell, the outer layer had a bubbled appearance. It was hypothesised that during core-shell formation, core droplets initially form; as the temperature decreases, shell nanostars nucleate across the surface of the core droplets. As shell NS phase separation continues, these areas of nucleation grow until they meet and fuse, gradually forming a homogeneous shell. At lower degrees of complementarity, shell nanostars are unable to fully encapsulate the core, and instead form surface adhered droplets. In the case of 4L8A 3S8 droplets with 16 %C modified 4L8A stars, the bubbled shell appearance would seem to indicate the degree of complementarity between the two phases is insufficient to enable complete shell formation. It was thus hypothesised

that an increased %C between the phases would enable complete shell formation.

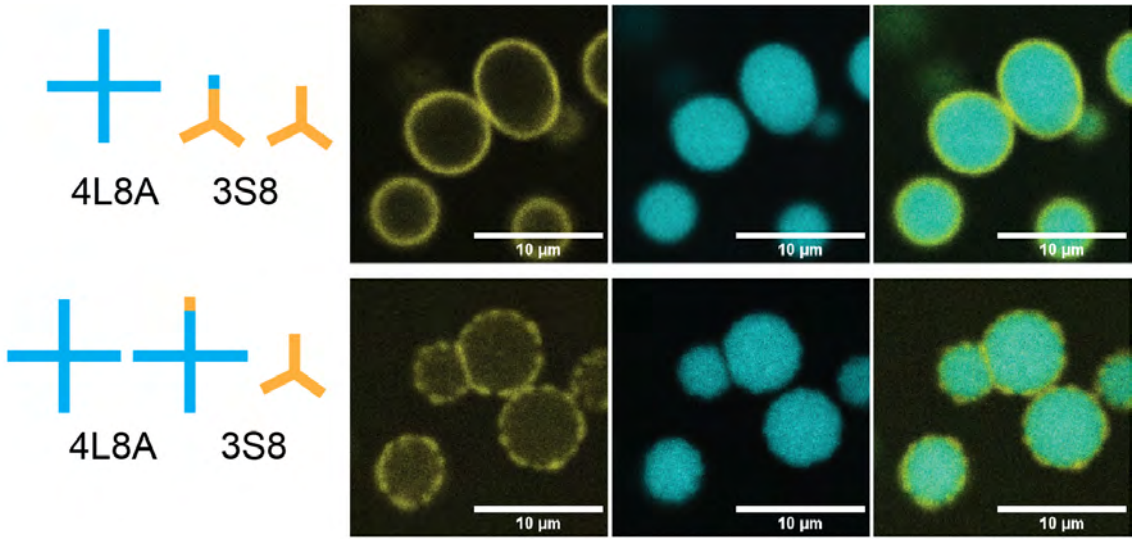

Figure 3.20: Comparing the morphologies of 4L8A 3S8 (16 %C) droplets with varying direction of surfactant modification. Scale bars 10 μm.

Solutions of 4L8A-modified 4L8A 3S8 nanostars were prepared with gradually increasing degrees of complementarity (figure 3.21). At 10 %C, surface adhesion of discrete 3S8 droplets was noted; at 20 %C and above, infiltration and mixing of the two phases was seen. It therefore appears as though the degree of complementarity required for core-shell formation depends on the valency of both stars in the system, not simply the surfactant-modified star. When combining a trivalent and tetravalent star, evidence indicates that surfactant-modification of trivalent stars requires 16 %C replacement of sticky ends, while modification of the tetravalent star requires a degree of complementarity between 16 - 20 %C. When similar tests were performed on tetravalent-tetravalent systems, in varying the direction of complementarity between core and shell, identical structures formed at 25 %C, regardless of region of modification.

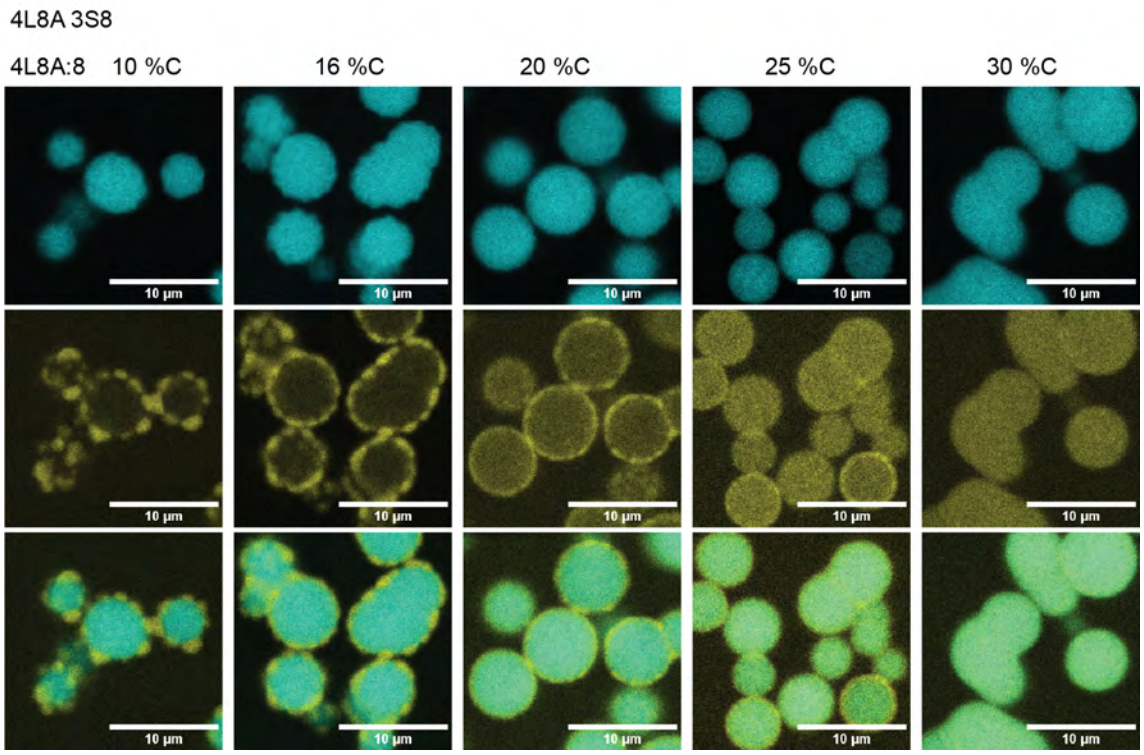

Figure 3.21: Comparing the morphologies of 4L8A 3S8 droplets when varying the degree of 4L8A surfactant modification. Scale bars 10 μm.

3.5.6 Summary of core-shell conditions

Aims of this thesis included the production of core-shell synthetic cells using only DNA nanostructures, without polymeric or lipid interactions, and the formation of these synthetic cells in a bulk phase. The above work demonstrates that the use of structurally and energetically diverse DNA nanostars allows for the prediction and formation of multiple core-shell droplets. This method relies on sequential phase separation of nanostars, with T_{PS} predictable as a function of nanostar valency and and SE sequence. In this system, core-shell droplet formation may be induced through the selective replacement of one star's sticky ends to allow limited complementarity to the other. In solutions containing trivalent and tetravalent stars, 16 %C of the trivalent star allows shell formation, while in systems containing only tetravalent stars, 25 %C induces shelling. This work aligns with systems explored in the literature, and expands upon them through investigation of the energetics of the involved nanostars.

3.6 Control of droplet size

As previously described, droplet growth in phase separated systems occurs through fusion, a random process that leads to a large variation in droplet diameters. Here, core sizes were compared to droplet radii of solutions of the same star (figure 3.22). In all systems studied, a significant reduction in core size was noted in comparison to the bare droplet. When creating a shelled system, an outer layer of stars encapsulates the initial droplets, creating a barrier between droplets of the same star. This may act as a kinetic trap in the system, reducing the time period during which fusions may occur, resulting in a more homogeneous population of droplets.

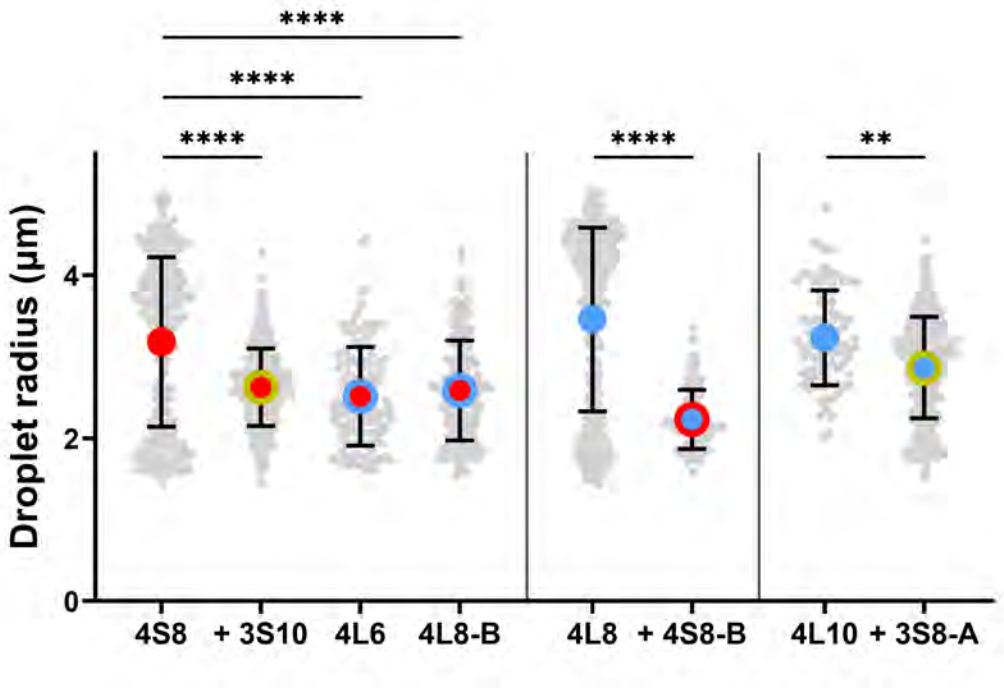

Figure 3.22: Measured droplet radii of bare and encapsulated droplets.

Thus far, all core-shell systems were produced at standard conditions – a total DNA concentration of 10 μm, Na^+ concentration of 0.5 M, and annealing between 95 – 5 ^{o}C at 0.5 ^{o}C/min. The proposed mechanism for the formation of these structures is partially time based, with the size of droplets being affected by the period spent in the active range and the likelihood of complex morphologies versus layering being

determined by the time between incidences of phase separation. Thus, the effect of annealing rate on layering was investigated.

Annealing rates between 0.5 – 5 ^{o}C were used in the formation of layered droplets. It was hypothesized that an increased annealing rate (ΔT) would reduce the period of time during which the system is in the active range of the droplets, resulting in reduced opportunities for growth via fusion. In addition to the work conducted here, an avenue of investigation that is of interest is non-homogenous annealing rates. As the temperatures of phase separation for each layer are known, it is possible to construct an annealing profile with varied ΔT during different periods. This could, for instance, selectively promote either core or shell growth.

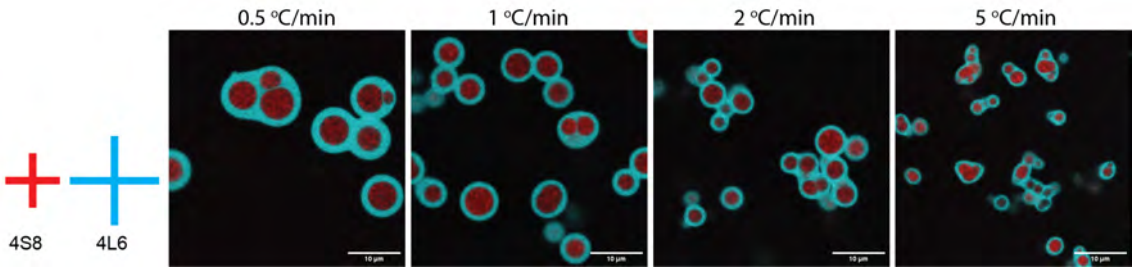

Figure 3.23: 4S8 4L6 droplets annealed at rates between 0.5 and 5 ^{o}C/min show an increase in size with a decreasing annealing rate. Scale bars 10 μm.

Annealing rates between 0.5 – 5 ^{o}C/min were studied for 4S8 4L6 25 %C droplets, as shown in figure 3.23. All investigated temperature ramps formed core-shell structures. The core and total droplet sizes were measured for each annealing rate to quantify the effect on structure formation. The core radii decreased with increasing ΔT, from 2.23 $\pm$ 0.55 μm to 0.88 $\pm$ 0.19 μm; so too did total droplet size, from 3.82 $\pm$ 0.41 μm to 1.33 $\pm$ 0.22 μm (figure 3.24). No marked difference was seen in the ratio of core to total size with ΔT. Together, this is taken to mean that under the given conditions, 4S8 and 4L6 nanostars phase separate at the same rate when in their active range. If one were to phase separate significantly faster than the other, it is hypothesised that this difference would manifest as a changing ratio of

sizes in comparison to the standard 0.5 ^{o}C/min. Samples of a lower ΔT appeared to increase the incidences of multiple core-shell structures sharing a partially fused shell. However, this observation may be biased by the fact that in any given field of view, a greater number of droplet structures are seen for lower annealing rates, thereby increasing the number of compound structures noted.

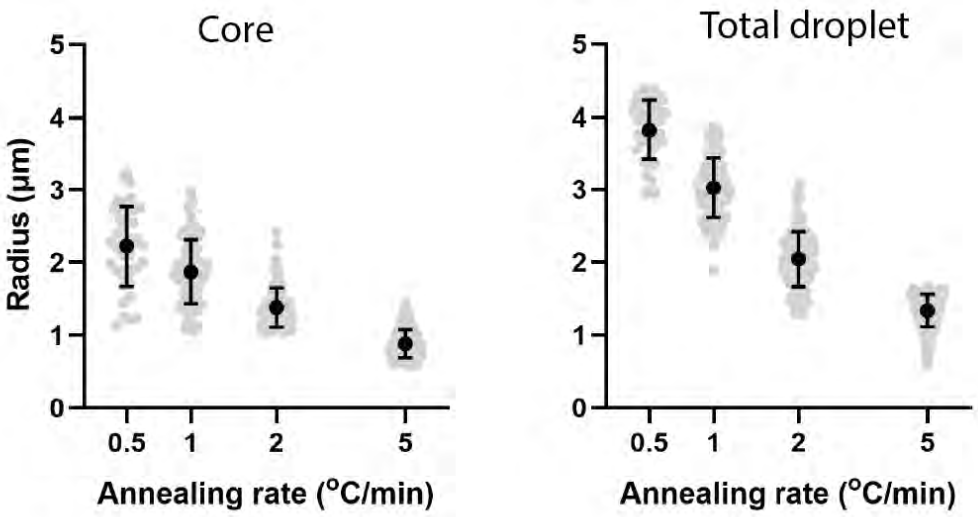

Figure 3.24: Core radius and total radius of 4S8 4L6 droplets with an increasing annealing rate.

Matsuura *et al.* conducted similar work on single-nanostar droplets, comparing variations in annealing rate [29]. The tested conditions included different ΔT (0.1 - 2 ^{o}C/min), spontaneous cooling (seeing a rapid temperature decrease at high temperatures and a slower rate of change at low temperatures), and pausing annealing for a period of time near the T_M of the droplet's sticky ends. As expected, a decreasing annealing rate led to a rise in droplet size; so too did holding the solution at 40 ^{o}C for a period of three hours. The effect of spontaneous (non-linear) cooling varied depending on the sticky end sequences of the nanostars. Thus, beyond what is studied here, further investigations in this area are warranted.

3.7 Stability of droplets over time

In investigating LLPS droplets with microscale architectures, the eventual goal is to create technologically-applicable structures. Whether this application is as microreactor vessels or artificial cells, long-term stability of the droplets is essential. The temperature at which nanostars form is determined by their valency and geometry, and droplet phase separation temperatures are largely a function of valency. In contrast, fluidity following droplet formation is primarily determined by sticky end strength, and only secondarily by valency. This fluidity can be measured as the degree of fusion over time, with more gelated or viscous droplets having significantly slower fusion.

3.7.1 Bare droplets

Unshelled 4S8 droplets were incubated between 28 - 37 ^{o}C (figure 3.25). At fifteen hours of incubation, images showed that droplets partially fused at 28 ^{o}C, with individual droplets still discernible. At 31 ^{o}C, droplets had fused into extended, irregular structures, while 37 ^{o}C saw the formation of spherical structures 2 – 5 times the size of initial droplets. Following forty-five hours of incubation, these trends continued, with 28 ^{o}C samples producing irregular networks and all higher temperatures forming spherical objects. These are in contrast to samples maintained at 4 ^{o}C, which saw no fusion even by t = 45 h.

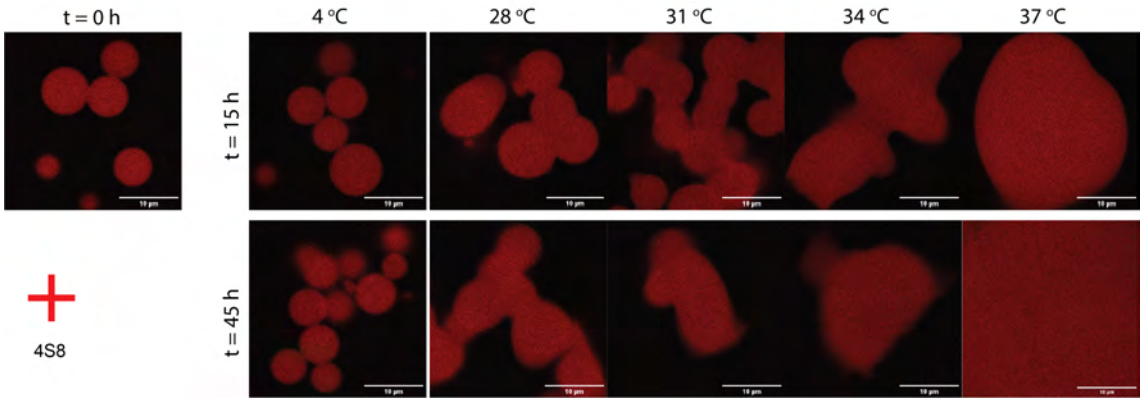

Figure 3.25: Bare 4S8 droplets, prepared at 10 μm and 0.5 M NaCl, were incubated at a range of temperatures for 45 hours. Fluidity in the system is defined as the propensity of droplets to fuse. Droplets at 4 ^{o}C show no difference to initial samples; from 28 ^{o}C onwards, droplets fuse into extended structures within 15 hours, and by 37 ^{o}C show complete fusion. Scale bars 10 μm.

3.7.2 Encapsulated droplets

The fusion of 4S8 3S10 core-shell droplets was similarly investigated (figure 3.26). At fifteen hours, samples incubated at 28 – 31 ^{o}C were visually indistinguishable from those held at 4 ^{o}C. They consisted of spherical core-shell architectures with distinct separation between layers. This separation between layers was maintained with increasing incubation temperature, with no increase in core/shell nanostar overlap (measured as the Pearson correlation between Cy3 and Cy5 fluorophore channels). As the environmental temperature increased, the 3S10 shell displayed partial deformation at 34 ^{o}C. Shells began to fuse, and the core was no longer spherical. At 37 ^{o}C, shells fully fused, resulting in multi-core objects. At 45 hours, 34 ^{o}C incubation similarly showed the formation of extended, multi-core structures, while 37 ^{o}C samples showed evidence of core fusion. These results suggest that the encapsulation of 4S8 droplets in a 3S10 shell enhances core stability over time, in a temperature dependent manner.

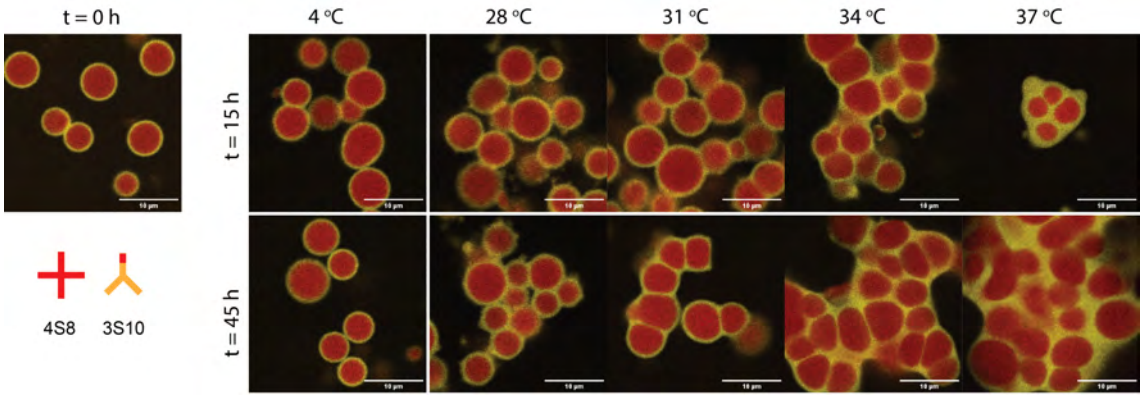

Figure 3.26: 4S8 3S10 droplets, prepared at 5 μm/nanostar and 0.5 M NaCl, were incubated at a range of temperatures for 45 hours. Investigating the fluidity of shells and the ability to stabilise liquid cores. Cores show little change up to 31 ^{o}C, indicating gelation. At 34 ^{o}C, shells fuse and allow deformation of their liquid cores. By 37 ^{o}C, fluidity in shells is seen, with the loss of any individual shell physicality and the fusion of core droplets at 45 h. Scale bars 10 μm.

The incubation of bare and shelled systems appears to show the partial fusion of 4S8 droplets at 28 ^{o}C, while 4S8 3S10 droplets do not see evidence of core fusion until

37 ^{o}C. Therefore, at conditions above the gelation temperature of 4S8 droplets and below the gelation temperature of 3S10 droplets, it is hypothesised that 4S8 3S10 core-shell structures would see greater long-term stability than bare 4S8 droplets.

This understanding of the relative behaviours of nanostars thereby allows the formation of liquid/gel, liquid/liquid, gel/liquid, or gel/gel droplet layer combinations, depending on the requirements of the eventual technological application.

Similar results have previously demonstrated the prevention of coacervate fusion through encapsulation [194] produced protamine/folic acid micro-scale droplets through liquid-liquid phase separation; when droplets came into contact in solution, they would readily fuse and grow. These droplets were encapsulated in membranes of dextran molecules of increasing molecular weight. Low mass, highly fluid membranes (MW $\leq 70kD$) were unable to prevent droplet fusion, while low fluidity membranes (MW $\geq 20kD$) were found to stabilise the coacervates. Similarly, Folkmann *et al.* produced liquid-like P granule protein (PGL) coacervates, which were shown to rapidly fuse upon contact [195]. The mean size and distribution of a population of coacervates was shown to increase over time, attributed to fusion and coarsening of droplets. When a MEG-3 protein coating was applied to the surface of the coacervates, the droplet surface tension decreased and the rate of droplet fusion was reduced. Additionally, the protein coating acted as a steric hindrance in preventing droplet coarsening, resulting in a stablisation of the mean size of the droplet population.

Deformation as a measure of fluidity

The degree of deformation of encapsulated droplets upon contact was quantified as a measure of fluidity. A script was written to outline circles around droplet shells (script B.6). At lower temperatures of incubation, the identified circles outlined the boundaries of phase separated droplet shells with a high degree of accuracy

(figure 3.27). At elevated temperatures, the fluid droplets deformed; when shells were outlined, the detection resulted in overlapping circles (figure 3.28). The area of intersection between circles was taken as a measure of the deformation experienced by the droplets, linked to the fluidity of the shells or core. This method could only be applied to encapsulated systems, as bare droplets did not retain the physical landmarks required for computer vision identification of individual structures. For every pair of overlapping circles identified, the area of intersection was calculated. It was hypothesised that deformation of droplets against one another would lead to an increase in the overlap of identifying circles, increasing the intersection area.

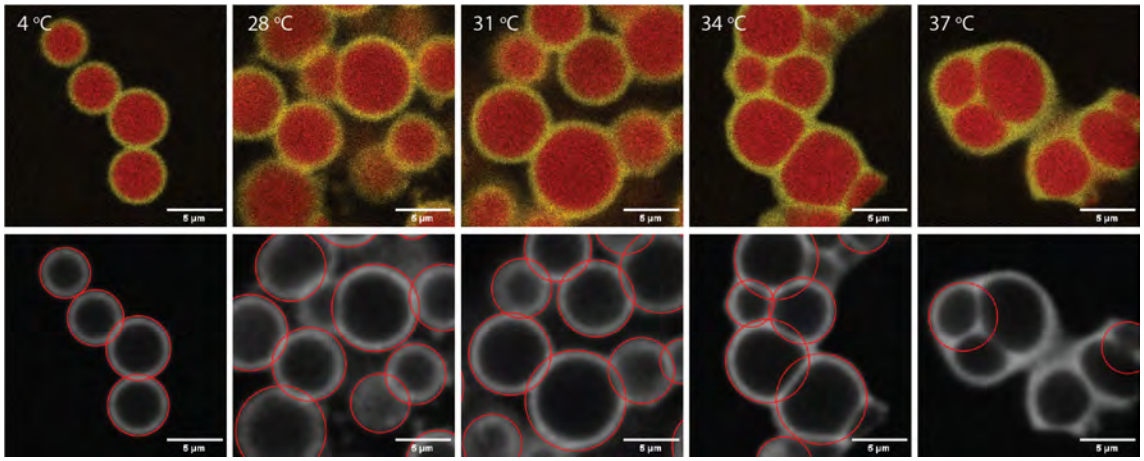

Figure 3.27: 4S8 3S10 droplets, incubated from 4 – 37 ^oC for fifteen hours, with circular structures identified by applying a Circle Hough Transform algorithm to the shell channel. Scale bars 5 μm.

This analysis initially resulted in a number of outlier measurements, identified using ROUT non-linear regression (Q = 1%) [196]. Visual analysis of the corresponding intersections revealed two types of droplet duplexation, here termed **active** and **passive** (figure 3.29). The former is hypothesised to occur during the active range of the shell. It is thought that collision of two shelled droplets will lead to deformation and fusion of the shells, driven by surface tension towards forming a single spherical object. This results in the flattening and thinning of the border between the two cores. The second form of duplexation occurs below the active range of the

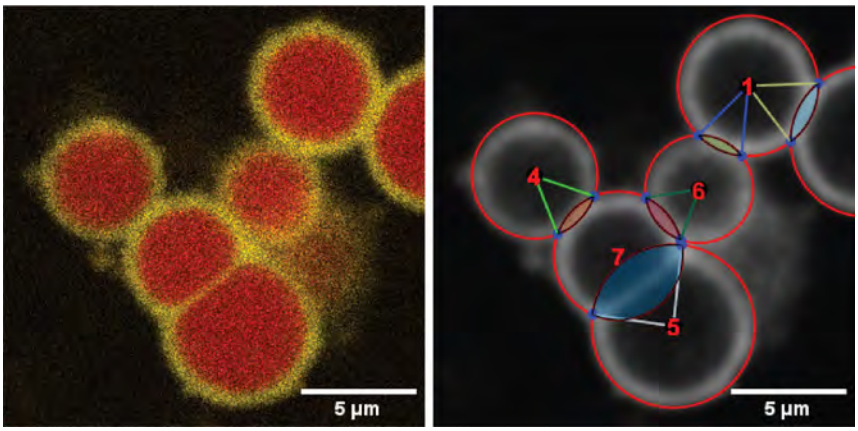

Figure 3.28: Example confocal image and detected areas of intersection in a sample incubated at 28 ^{o}C. Intersection between circles 5 and 7 display a large area of intersection and non-circular cores. Intersections between circles 1 & 7, 4 & 7, and 6 & 7 show smaller areas of intersection and lack core deformation. Scale bars 5 μm.

shell. While shells may "stick" to one another, indicating a small degree of nanostar interaction, the droplets maintain their individual spherical appearances.

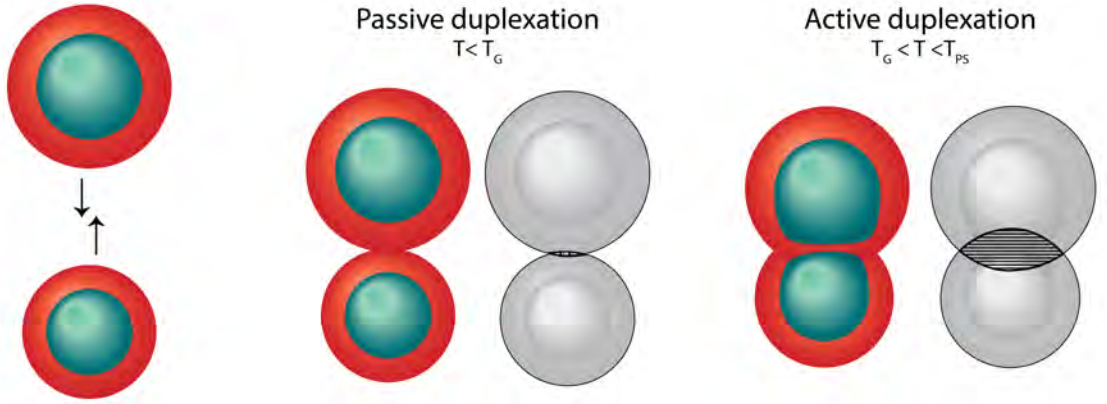

Figure 3.29: Illustration of the two hypothesised methods of core-shell droplet interaction. In the **passive** form of duplexation, the system is beneath the active range of the shell. Minimal interaction is seen between shells, leading to a limited degree of surface attachment and a small area of intersection. If two droplets meet whilst within the active range of the shell, **active** duplexation occurs. Non-circular droplets and a large area of intersection can be seen in this state.

When incubated beneath the gelation temperature of the shell, the majority of droplet duplexes would be expected to form through the passive method. If the incubation temperature were raised above T_G and the shells returned to a fluid state, active duplexation would become possible. It is expected that the number

of actively duplexed droplets would then increase over time. Datasets in which actively fused droplets were identified as outliers were considered to be stable, with the few incidences of active fusion hypothesised as having occurred during incubation (figure 3.30). Hence, these outliers were removed from consideration. Conversely, incubation at 34 ^{o}C saw a wide range of areas of intersection. None were identified as outliers, which was taken to mean that active fusion was actively occurring under this condition.

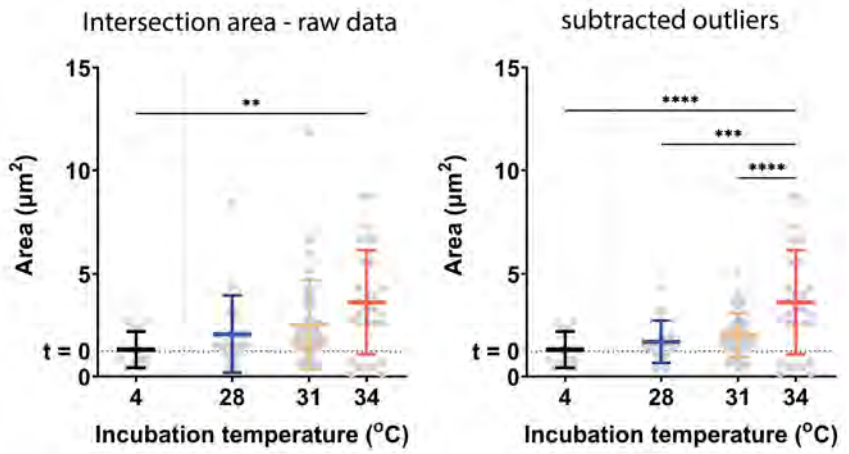

Figure 3.30: Areas of intersection for 4S8 3S10 droplets incubated at a range of temperatures for 15 h, before and after removal of outliers. Line at t = 0 indicates mean area of intersection in samples immediately following annealing. A significant increase in area mean and range is seen at 34 ^{o}C, indicating fluidity of shells.

This technique was used to quantify the approximate lower boundary of the active range of 3S10 shell nanostars. Incubation at and beneath 31 ^{o}C for fifteen hours showed no significant change in the area of intersection between droplets, as compared to samples imaged immediately following annealing. Incubation at 34 ^{o}C resulted in a significant increase in mean intersection area, suggesting the system experienced shell fluidity under these conditions. Samples held at 37 ^{o}C experienced such a degree of deformation that the computer vision algorithms could not reliably identify circular objects in micrographs; therefore, quantitative data is not available for this condition. However, visual analysis shows an enhanced degree of shell fusion at 37 ^{o}C as compared to 34 ^{o}C, with individual shells no longer discernible

and the formation of multi-core spherical objects (figure 3.27. Thus, this analysis leads to the conclusion that the shells of 4S8 3S10 systems approach their gelation temperature between 31 and 34 ^{o}C.

3.7.3 Comparison of shell stabilities

The 4S8 3S10 system was compared against one with a weaker SE shell, 4S8 4L6. Multi-star systems were prepared at a volume of 100 µL, split into 10 µL aliquots, and stored at either 4 ^{o}C or room temperature. These were imaged immediately upon production, at 24 hours of incubation, and every two days following. Under these conditions, the 3S10 shell appeared gelated, with no changes in the appearance of droplets, degree of fusion of shells, or degree of mixing between core and shell (figure 3.31).

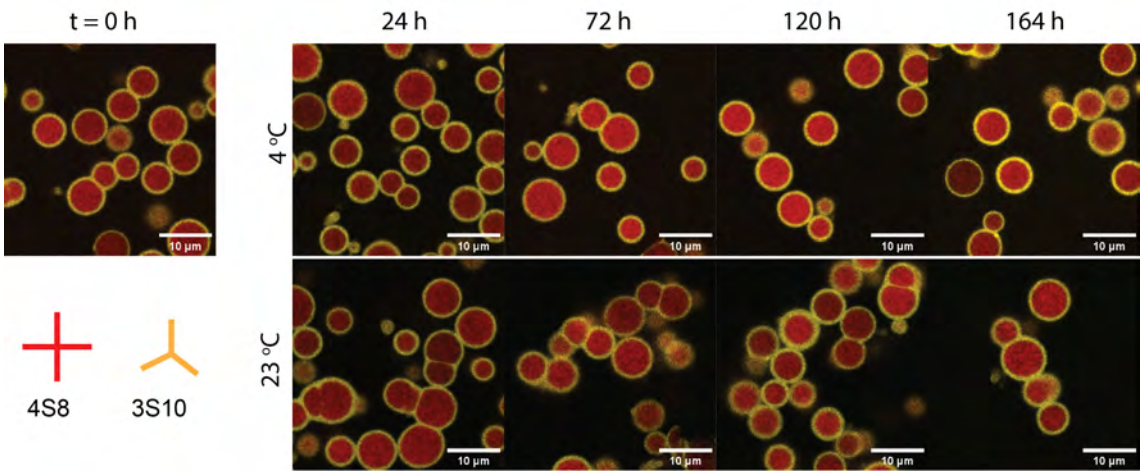

Figure 3.31: 4S8 3S10 droplets incubated at 4 ^{o}C and 23 ^{o}C for seven days. Under both conditions, droplets do not see a significant change in their appearance over time. Scale bars 10 μm.

At t = 0, 4S8 4L6 droplets tended to have thick, homogeneous shells, with these shells experiencing slight fusion into chained structures after 1 week at 4 ^{o}C (figure 3.32). When held at 23 ^{o}C, the 4L6 shells fused into extended, multi-core irregular objects within 24 h; it is noted that 4S8 3S10 droplets required 45 h at 34 ^{o}C to reach a similar state. As time progressed, 4S8 4L6 droplets held at 23 ^{o}C continued

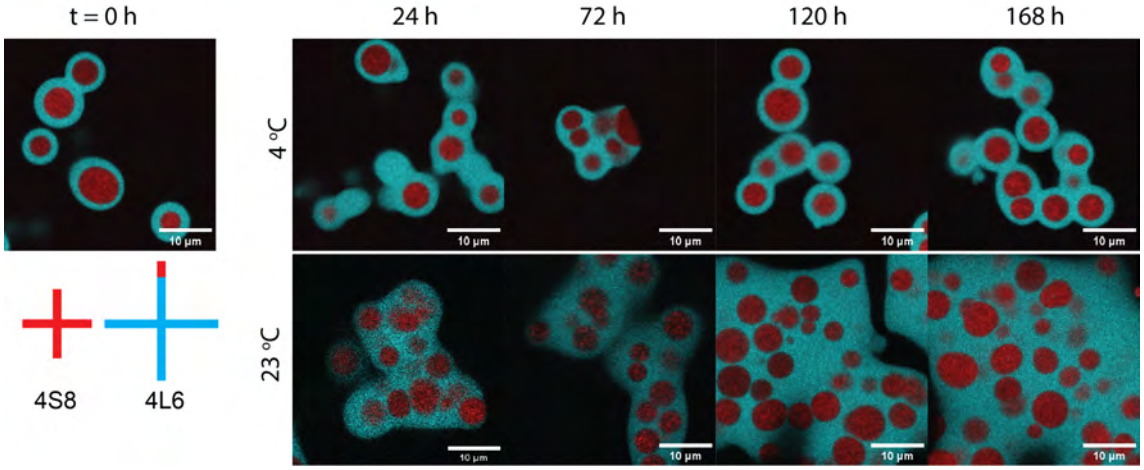

Figure 3.32: 4S8 4L6 droplets incubated at 4 ^{o}C and 23 ^{o}C for seven days. At 4 ^{o}C, droplets do not see a significant change in their appearance over time. At 23 ^{o}C, 4L6 shells show evidence of fusion after 24 h incubation. Shells continue to fuse with the passage of time, forming larger multi-core aggregates. Scale bars 10 μm.

to fuse into larger irregular structures. Despite the fluidity of the shell, no significant change in core size was noted, as 4S8 droplets are gelated at this temperature. These results indicate that the 4S8 4L6 system was more prone to fusion, hypothesised to be a function of the weaker 6-nt SE in the shell.

3.8 Movement of nanostars between droplets

In designing a microreactor system, a key aim is the implementation of selective transport. This can allow for control over the location of reactants, the rate of mixing, or the order of steps in a reaction pathway. Such a system was demonstrated by Elani *et al.*, who created multi-compartment lipid vesicles with distinct chemical contents in each compartment [46]. The compartmentalisation of select enzymes in distinct areas of the vesicle complex, and the inclusion of trans-membrane pores in the vesicle lipid bilayers, allowed for the creation of a multi-stage reaction pathway.

When considering the nanostar coacervates investigated in this thesis, a bare droplet would exhibit little selectivity over the capture or transport of its contents. Due to

the liquid-like nature of LLPS droplets, any compartmentalised cargo is able to freely diffuse out of the droplet. In order to effect control over such movement, the droplet must be encapsulated within a chemically distinct shell. If the compartmentalised cargo were physically or chemically incompatible with the shell, it could potentially remain within the encapsulated droplet. Modification of the cargo or the shell would be required to release the contents of the droplet.

This concept was investigated in systems of bare and encapsulated nanostar droplets. In any nanostar droplet solution, the system contains low- and high-density regions of nanostars. A defining characteristic of LLPS droplets is the ability of any given molecular subunit to diffuse between phases, moving between dense and dilute regions. It was hypothesised here that the presence of a shell would hinder the rate of diffusion of nanostars into and out of an encapsulated core, in comparison to movement through a bare droplet. Numerous solutions of bare and core-shell droplets were produced, each containing distinct fluorophores. Following annealing, these were combined and incubated; the rate of nanostar movement between the dilute phase and a droplet was measured as the degree of fluorescence co-localisation over time. This method was used to investigate the relative rates of infiltration between bare and encapsulated droplets, and between encapsulated droplets.

3.8.1 Movement between bare and encapsulated droplets

Solutions of 4S8 and 4S8 3S10 droplets were prepared in 0.5 M [Na^+]. The bare 4S8 droplets were functionalised with ATTO488 fluorophores, while the core-shell system was functionalised with Cy3 in the core and Cy5 in the shell. Following annealing, the two solutions were combined and incubated for 48 hours at 4 and 28 ^{o}C in a ProFlex Thermocycler System, with confocal imaging conducted at 0, 24, and 48 hours. Following mixing of the solutions, the dilute phase was expected to contain 3S10-Cy5, 4S8-Cy3, and 4S8-ATTO488 nanostars. It was expected that

4S8-Cy3 nanostars would infiltrate into the bare droplets at a higher rate than 4S8-ATTO488 into encapsulated droplets. This hypothesis was predicated upon the orthogonality of 4S8 and 3S10 nanostars; the assumption that the 3S10 shell would prevent movement of 4S8 nanostars; and that free fluorophore strands not bound to nanostars were negligible.

Confocal images of incubated samples are shown in figures 3.33 and C.15. When imaged immediately following annealing, both bare and encapsulated droplets exhibited spherical, homogeneous appearances. Each population is distinct, with no mixing of fluorophores evident. When incubated at 4 ^{o}C, samples retained the same appearance for up to 48 hours, indicating gelation of the system and a very low degree of nanostar mobility. When incubated at 28 ^{o}C, the two droplet populations appeared to undergo active duplexation, forming surface-adhered multi-droplet aggregates. These aggregates contained both bare and encapsulated droplets. Within 24 hours of incubation, a thin shell of 3S10 nanostars appeared on the surface of bare 4S8 droplets (figure C.16). This is hypothesised to be the result of dilute-phase 3S10 surfactant nanostars depositing on the bare droplets and initiating isothermal encapsulation.

During this same period, infiltration of 4S8-Cy3 nanostars into bare droplets and 4S8-ATTO488 nanostars into encapsulated droplets was seen. It was assumed that both droplet populations would contain a functionally constant concentration of their initial fluorophore. Infiltration was thus quantified as the fluorescence intensity of fluorophore B in fluorophore A droplets, in relation to the maximum channel intensity of fluorophore B. At 4 ^{o}C, no significant change was seen in the Cy3 infiltration fluorescence intensity in bare droplets (F% = 4.45% $\pm$ 0.48 at t = 0, 3.98% $\pm$ 0.95 at t = 48 h). In contrast, ATTO488 infiltration intensity rose from 6.45% $\pm$ 0.40 at t = 0 to 8.0% $\pm$ 0.45 at t = 48 h in shelled droplets (Tukey multiple comparisons test, P$<$ 0.0001). At 28 ^{o}C, the degree of infiltration was much higher

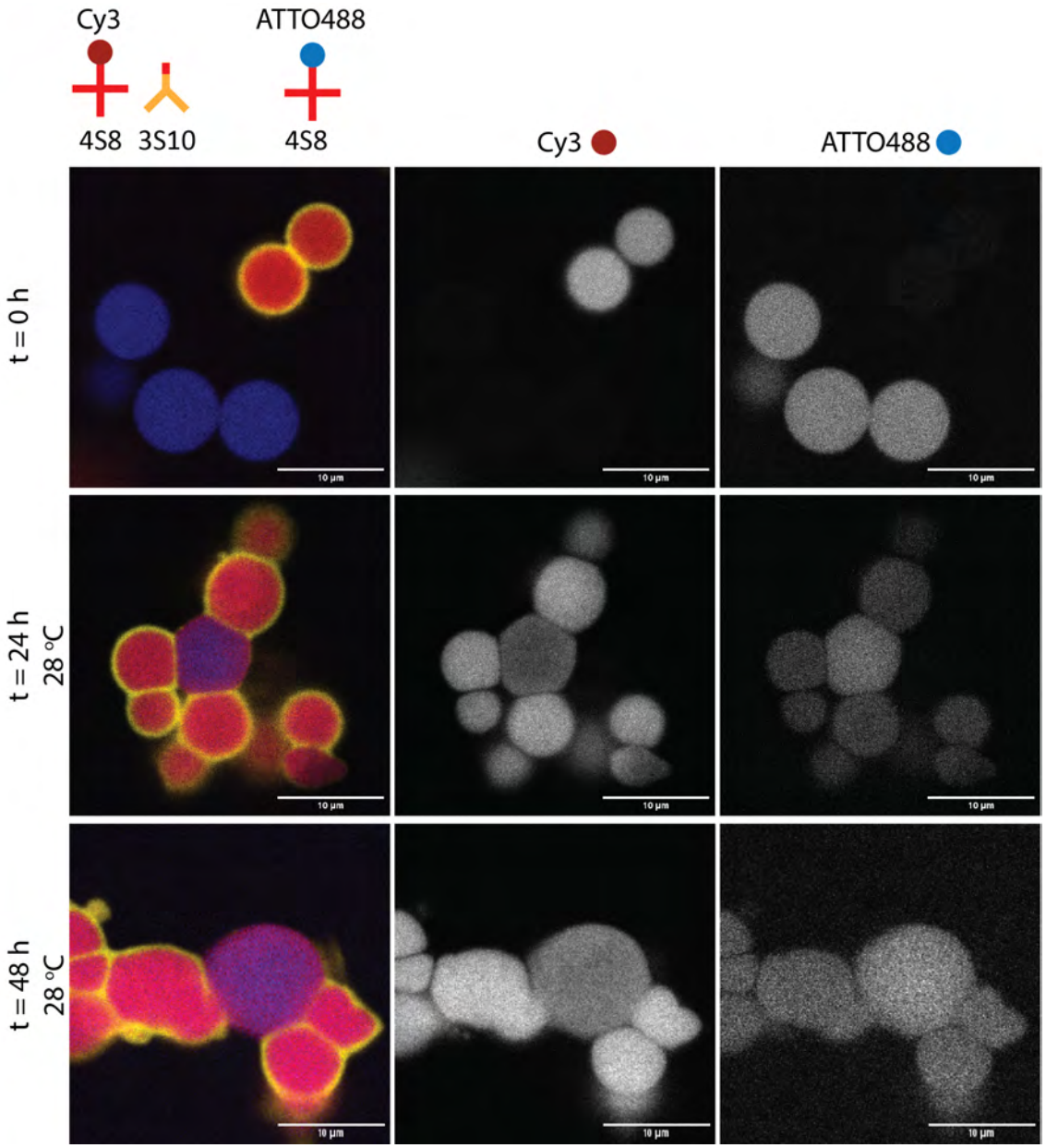

Figure 3.33: Bare 4S8-ATTO488 droplets were combined with core-shell 4S8-Cy3 3S10-Cy5 droplets and incubated at 28 ^{o}C for 48 hours. When 4S8 channels are viewed individually, infiltration of fluorescent nanostars into alternate droplets may be assessed. The ratio of the fluorescence intensity of Cy3 in bare droplet regions to the maximum channel intensity is 46.38% $\pm$ 2.07, while the ratio of ATTO488 in shelled droplets is 34.43% $\pm$ 2.21. This suggests a higher rate of infiltration of dilute phase 4S8-Cy3 into bare droplets than 4S8-ATTO488 into shelled droplets. Bare 4S8-ATTO488 droplets are coloured blue; core-shell 4S8-Cy3 3S10-Cy5 are coloured red and yellow, respectively. Scale bars 10 μm.

in both bare and shelled droplets, rising to 46.38% ± 2.07 and 34.43% ± 2.21, respectively. The increase in infiltration intensity was significantly higher in bare droplets than shelled droplets (Tukey multiple comparisons test, $P<0.0001$). This would suggest that infiltration of bulk nanostars from the dilute phase into bare droplets is favoured over shelled droplets.

This interpretation assumes the factors governing the rate of infiltration of nanostars are equal, and droplets differ only in the presence of a shell. However, the chemical structures of the relevant fluorophores must be taken into account. Cy3 is a hydrophobic cyanine dye, consisting of two nitrogen-containing aromatic groups connected by a hydrocarbon chain [197]. In contrast, ATTO488 is a hydrophilic molecule containing two amino groups and two sulphonic acid groups [198]. The distinct chemical structures of these fluorophores may result in differing behaviours when considering infiltration into the densely packed nanostar droplets. While the above results would appear to indicate favoured infiltration of nanostars into bare droplets over encapsulated droplets, this conclusion must be investigated for fluorophore effects. In order to more closely investigate the relative degrees of infiltration of nanostars into phase separated droplets, this experiment must be repeated with reversed placements of fluorophores, or with alternate fluorophore choices.

3.8.2 Movement between encapsulated droplets

Similar incubation studies were performed on combinations of encapsulated droplets. The ability of DNA NS shells to impart long-term stability on NS coacervates was tested. Two solutions of 4S8 droplets were prepared, functionalised with distinct fluorophores; these were combined and incubated at 25 and 28 ^{o}C for a period of seven days. The same incubation was conducted on combinations of 4S8 3S10 core-shell droplets. Earlier results in section 3.7 demonstrated the fusion of 4S8 droplets over time, and the ability of 3S10 shells to maintain distinction between cores. The

distinct fluorophore modifications of this experiment were intended to examine the degree of fusion or mixing between droplets.

Confocal images of bare 4S8 droplets incubated over time show a heightened degree of fusion at 28 ^{o}C as compared 25 ^{o}C (figure 3.34). When shelled droplets were incubated under the same conditions, samples held at 25 ^{o}C largely retained their spherical appearance, suggesting the 3S10 shell was in a gel-like state. However, when incubated at 28 ^{o}C, droplets formed multi-core aggregates with deformed shells, indicating a fluid-like state for both core and shell regions. Despite this fluidity of the shell, individual cores remained separated, instead of fusing as bare 4S8 droplets did. This further demonstrates the stabilising effects of nanostar shells in maintaining physical distinction between droplet cores.

The use of distinct fluorophores in the cores of 4S8 droplets allowed for visualisation of the movement of nanostars between the dilute and dense phases. In the iteration of this experiment conducted at 25 ^{o}C, the 4S8 nanostars were functionalised with either ATTO488 or Cy5 fluorophores. This pairing was chosen in order to minimise any possible overlap between fluorophore spectra, as ATTO488 has excitation/emission peaks at 502 and 522 nm, while Cy5 functions at 648 and 668 nm. However, when incubating these samples at 25 ^{o}C for an extended period of time, it was found that the Cy5 fluorophore lost a significant portion of its fluorescent intensity, rendering its movement into 4S8-Cy3 droplet regions undetectable. In order to avoid this bleaching effect, when conducting the incubation series at 28 ^{o}C, the 4S8 cores were functionalised with either ATTO488 or Cy3. However, the use of different fluorophores in these experiments has the potential to affect the chemical environment of the droplets in which they are sequestered, modulating the observed physical responses. Quantitative comparison of the experimental data is thus not possible, with modifications to the experimental design required for any future analyses. The results of these incubations may be qualitatively assessed to

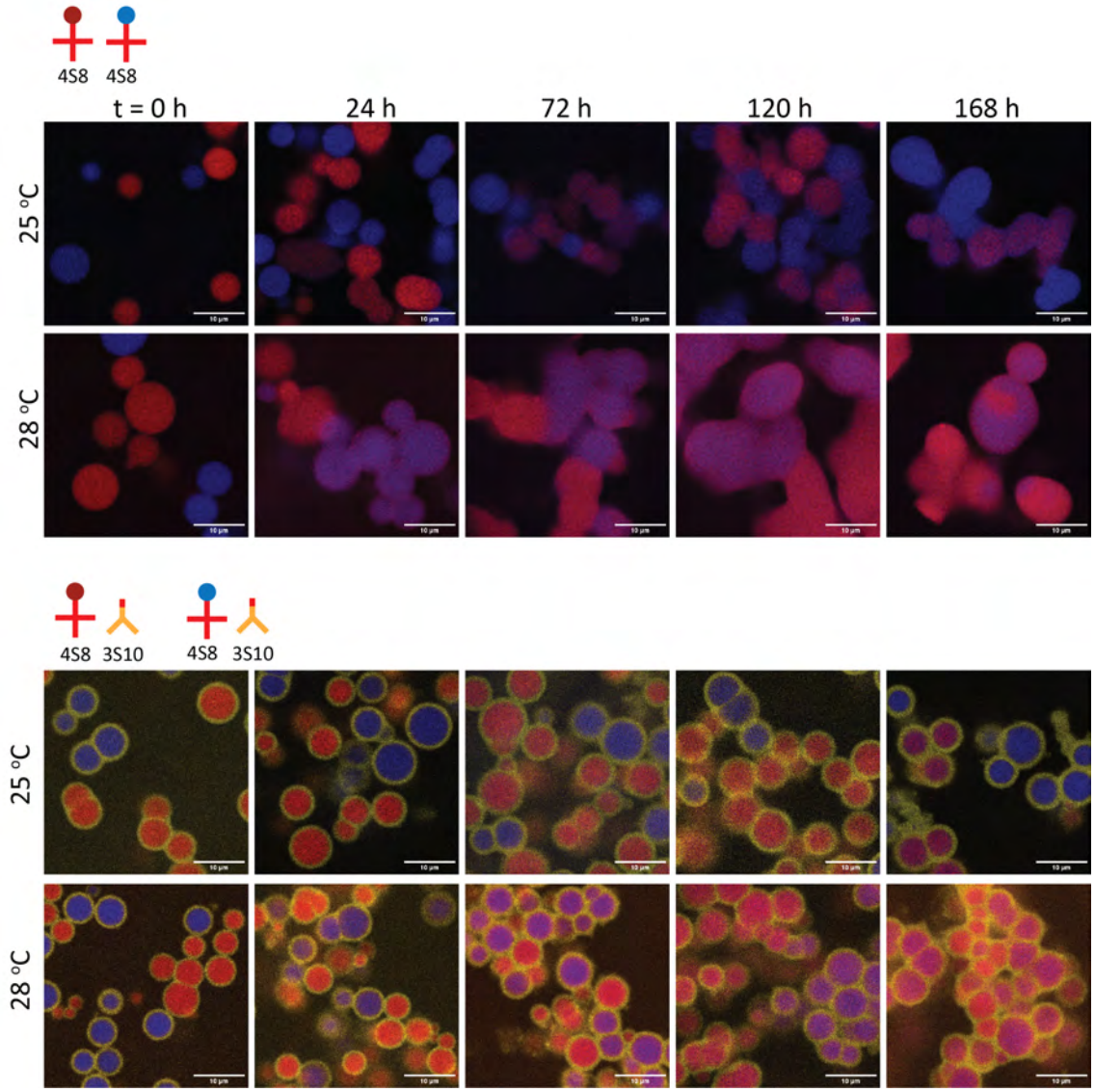

Figure 3.34: Solutions of droplets with distinct fluorophore modification were separately annealed and then mixed. Combined 4S8 or 4S8 3S10 droplet solutions were incubated at 25 or 28 ^{o}C for seven days. Droplets incubated at 25 ^{o}C were functionalised with Cy5 (red) or ATTO488 (blue) fluorophores, while 28 ^{o}C samples used Cy3 (red) and ATTO488 (blue). Fusion of bare 4S8 droplets into extended aggregates is seen at 25 ^{o}C. When encapsulated in a 3S10 shell, 4s8 3S10 retain a spherical appearance at 25 ^{o}C. At 28 ^{o}C, encapsulated droplets merge into extended structures, with individual core-shell regions deformed but distinguishable. Scale bars 10 μm.

draw inferences about these systems, but no definite conclusions can be made.

When bare droplets fused at 25 - 28 ^{o}C, the spherical coacervates merged into large, irregular structures. However, the irregular structures still contained distinct regions of discrete fluorophores. Although the droplets were driven by surface tension to fuse when meeting, they did not homogeneously mix their contents. This suggests that the bulk of the droplet mesh structure is in a flexible, gelated state - able to deform, but prone to retaining its original nanostar configuration.

The nanostars within the body of the mesh are likely stable in their placement - surrounded by complementary stars in all directions, they may adopt any energetically favourable physical conformation and will still be able to bind via their sticky ends to adjacent stars. However, nanostars at the surface of a droplet must align all of their arms inwards in order to achieve duplexation of their sticky ends. This physical restriction is likely unfavourable, and contributes to the surface tension experienced by the droplet. Surface nanostars therefore possess the drive to adjust their conformation and bind to adjacent droplets, while central nanostars are not driven to intermix. This explains the fusion and lack of mixing observed under the given experimental conditions. Any observed co-localisation of distinct fluorophores is hence attributed to the dynamic movement of dilute phase nanostars, rather than mixing of dense phase droplet meshes.

Encapsulated droplets incubated at 25 - 28 ^{o}C appeared to show intermixing of core 4S8 fluorophores between Cy5 or Cy3 and ATTO488 regions. The degree of intermixing cannot be qualitatively compared between conditions, due to the different bleaching rates of the fluorophores and the possible differences in their chemical behaviours. Co-localisation of 4S8 fluorophores is seen despite the physical separation between cores. This gives further credence to the hypothesis that this intermixing is due to movement between the dilute and dense phases, rather than

adjacent dense phases. It is thus concluded that the apparent fluidity of 4S8 cores at 28 ^{o}C is a result of the flexibility of the nanostar mesh, rather than an indication of liquidity or free movement of the individual nanostars.

While these results may be used to infer insights into the structure and behaviour of nanostar coacervates, the conclusions that may be drawn are limited. Further investigations into the motility of dense and dilute phase nanostars are warranted, concerning the deformation of droplets and the intermixing of their contents. Work to this effect is continued in Chapter 4.

3.9 Conceptual energy profile of a core-shell system

The formation of a core-shell structure in this system can be conceptualised by considering the qualitative energy profile of the reaction. In a single nanostar system, as the annealing of the reaction proceeds over time, there will exist a period in which nanostars are able to bind via their sticky ends. During this period, droplet nucleation and growth will occur, facilitated by the reduction in SE free energy with decreasing system temperature (figure 3.35 A). If the reaction proceeds unimpeded, the resulting coacervates will continue to grow throughout the active range of the system.

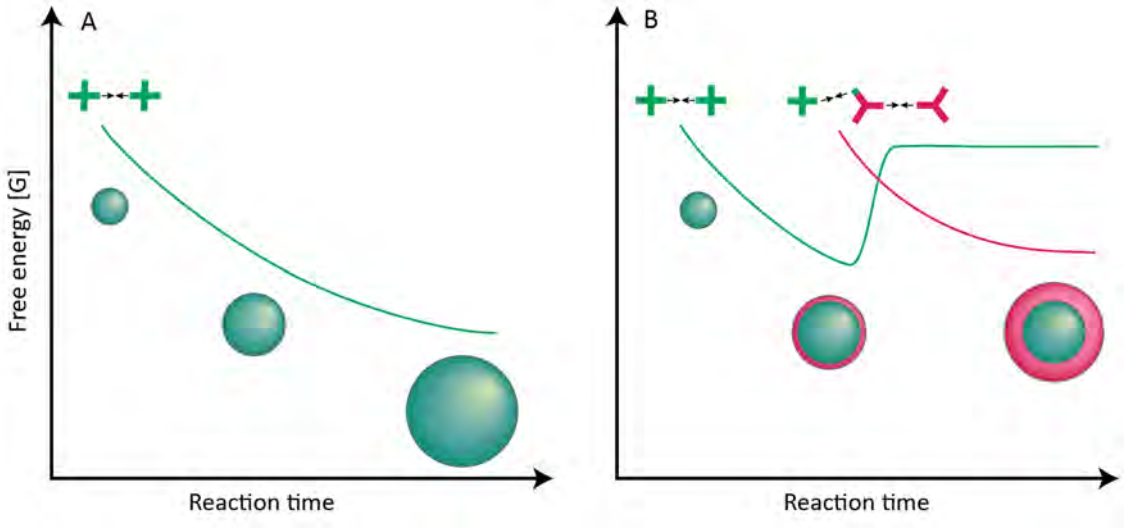

Figure 3.35: Conceptual energy profiles of **A**: phase separation and coacervate growth of a single nanostar system; **B**: phase separation, coacervate growth, and shell formation of a two-star core-shell system.

However, if a second nanostar is added to the system with an appropriate ΔT_{PS} and degree of complementarity, core-shell formation will occur (figure 3.35 B). Initially, coacervate formation will proceed as normal, with the high T_{PS} nanostar phase separating and forming droplets at a high temperature. This is later followed by the phase separation of the low T_{PS} nanostar, with complementarity to itself and

to the existing droplets. The second nanostar will nucleate upon the surface of the initial droplets, forming an outer shell. This will result in a significant increase in the energy required for fusion of two core droplets, as a physical barrier now exists between them. A kinetic trap thus slows the rate of fusion of the core droplets, and results in a smaller core droplet size.

Modulation of the time between the first and second incidences of phase separation in this system would theoretically provide a means of control over the droplet core size. If this reaction were to be conducted isothermally, or if a system were allowed to proceed to its energetic minimum over an indefinite period of time, it is unclear whether core-shell structures would remain, or if a complete separation of droplet phases would be seen.

3.10 Summary and conclusion

The work in this chapter was guided by Aim 2 of this thesis, concerning the formation of micro-scale architectures in nanostar droplets (section 1.7). The orthogonality of nanostar droplets with distinct sticky end and arm sequences was demonstrated through the co-annealing of different nanostar combinations (section 3.2). Nanostars with complete orthogonality were shown to form distinct droplet populations regardless of similarity or difference in phase separation temperature. Orthogonal nanostars with complementary sticky ends were shown to co-localise despite a phase separation difference of 10.4 ^{o}C, demonstrating that sticky end complementarity takes precedence over arm orthogonality in droplet mixing, and that phase separation does not need to occur simultaneously to produce mixed droplets.

Research question 2.1 asked what micro-architectures could be formed using DNA nanostars. Solutions of orthogonal nanostars were combined alongside surfactant nanostars, varying the degree of complementarity between the populations (section 3.3). It was found that core-shell droplet structures could be formed when inducing 16 %C in trivalent nanostars or 25 %C in tetravalent nanostars, in systems where ΔT_{PS} was greater than approximately 3 ^{o}C. When the difference in phase separation temperature was beneath this value, lensed, co-continuous, or nested complex structures resulted. The formation of core-shell structures was found to be dependent on the degree of complementarity between nanostar phases, but independent of the structure of the surfactant nanostar (section 3.5). These results additionally addressed research questions 2.2 and 2.3, which concerned gaps in the literature around forming core-shell structures using DNA nanostars in a bulk solution. The ability to predict nanostar droplet micro-architecture based on ΔT_{PS} was demonstrated, developing a rapid method of assessing and predicting droplet structures.

The encapsulation of fluid coacervates in a core-shell structure was shown to re-

duce the mean size and polydispersity of the core in comparison to bare droplets (section 3.6. This demonstrates control over droplet size, beyond that which could be achieved through modulation of individual star structures in Chapter 2 (section 2.5.1). Additionally, encapsulation was shown to induce stabilisation of the core region and prevent fusion at elevated temperatures, in comparison to bare droplets (section 3.7.2). Different combinations of nanostars in core-shell structures were shown to have different physical properties, offering control over the level of fluidity in either the core or shell of a droplet (section 3.7.3). This partially addressed research question 2.4, creating droplets with distinct physical properties and chemical addressability. Further exploration of question 2.4 is conducted in Chapter 4.

Many future avenues of investigation may follow the work conducted in this chapter. While the degrees of complementarity required for core-shell formation in tetravalent-tetravalent or tetravalent-trivalent nanostar systems were identified, no reason for these particular values was found. Expanding the valencies and combinations of nanostars studied may provide further insight into this area. Further experiments must also be conducted to explore the movements of nanostars within and between phases when isothermally aged over an extended period of time.

Chapter 4

Functional synthetic cells

4.1 Introduction

In accordance with Aims 1 and 2 of this thesis, the investigation of individual nanostars and the production of core-shell structures have been demonstrated. In this chapter, in line with Aim 3 and research question 2.4, distinct physical and chemical properties of nanostar droplet regions are investigated.

The work conducted in this thesis was largely driven by the motivation to create functional synthetic cells from nanostar coacervates. As discussed in section 1.3, a living synthetic cell possesses the ability to demonstrate internal organisation; control the exchange of its contents with the environment; produce and respond to messaging signals; demonstrate self-directed movement; and metabolise energy to grow. While this thesis does not aim to demonstrate abiogensis, it does intend to create cell-like properties in phase separated droplets. This chapter aims to demonstrate the first three functionalities of synthetic cells in layered DNA NS coacervates:

- **Aim 3.1**: Demonstrate internal organisation by creating organelles.
- **Aim 3.2**: Passively control the movement of cargo into the droplet core.
- **Aim 3.3**: Effect active control over cargo compartmentalisation.

A function of encapsulating nanostar coacervates in a core-shell micro-architecture was demonstrated in section 3.7, in preventing fusion of cores over time. In addition to physically stabilising the core, the shell is here investigated as a physical or chemical barrier to infiltration by cargo molecules.

Aim 3.1 involves the creation of sub-cellular compartments of distinct chemical or physical environments to allow for internal organisation within the DNA coacervate. This concept was briefly explored in Chapter 3, in the creation of morphologically complex droplets in two-star systems (figure 3.13). Such systems are investigated further in this chapter, in creating droplets of increased physical complexity in three-star systems.

Ji *et al.* investigated protein coacervates encapsulated in dextran shells of varying molecular weights [194]. They demonstrated that low molecular weight cargo molecules such as Hoechst dyes and BSA molecules were able to infiltrate through the shells and compartmentalise within the coacervate core. They also investigated the infiltration of *Escherichia coli* bacteria into the coacervates, and found that high density shells (dextran MW $\geq$ 250 kD) were able to prevent infiltration. Similar concepts are explored in this chapter, in accordance with Aim 3.2, demonstrating passive size-based exclusion through different nanostar shell densities.

Gao *et al.* produced PDDA/dextran polymer coacervates surrounded by a membrane formed of gold nanoparticles and thiotic acid-modified PEG [199]. The membrane-bound coacervate was initially impervious to infiltration by cargo molecules; upon radiation- or chemical-mediated disruption, the membrane structure was par-

tially disassociated, allowing uptake of BSA molecules and polymer coacervates. Selective cargo uptake was also demonstrated, by modulating the affinity of the cargo polymer to the coacervate. In a similar vein, this chapter addresses Aim 3.2 by investigating the selective compartmentalisation of cargo molecules, by modulating the chemical affinity of the cargo molecule to different regions of a DNA NS droplet. Following Aim 3.3, the concept of signalling-mediated control over infiltration is explored, by demonstrating the uptake and triggerable release of cargo.

This chapter expands upon earlier sections through the investigation of two- and three-star micro-architectures in the presence of different cations. This is followed by a demonstration of the passive control over infiltrate size, through the selection of shell nanostars with varying mesh densities. The active capture of DNA-functionalised streptavidin is then demonstrated in different regions of core-shell droplets, alongside control over the degree of capture. Toehold-mediated strand displacement reactions then allow for the signal-mediated release of captured cargo. Modification of the nanostar shell to act as an inhibitor to compartmentalisation is also shown. Finally, a method for the quantification of droplet mixing and cargo capture is discussed.

4.2 Multi-star droplets

Micro-structures formed when combining two distinct nanostars were explored in Chapter 3. Using ΔT_{PS} and %C, the droplet architecture may be predicted with a high degree of accuracy. Based on the developed theories, the formation of three-star systems was attempted. The work of Walczak *et al.* demonstrated the formation of core-shell structures using a third surfactant star (figure 1.17) [151]. This system effectively creates a three-layered structure, with a core, shell, and surfactant interface layer. A variation on this method was attempted in this thesis.

A solution containing 4S8, 3S8A, and 4L8B nanostars was prepared. As shown in the hybridisation curves in figure 4.1, each nanostar phase separates at distinct temperatures. If the appropriate degree of complementarity were applied to each nanostar, the formation of a three-layered structure would potentially be possible.

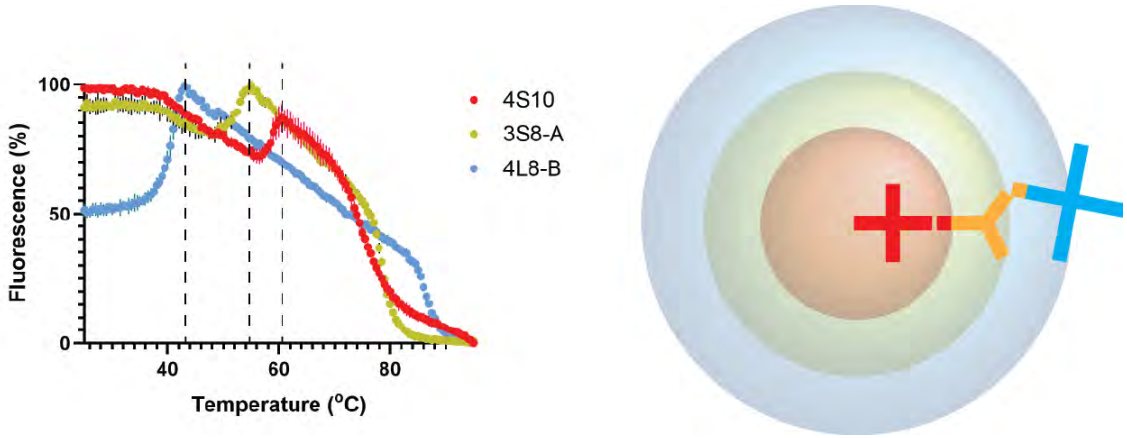

Figure 4.1: Hybridisation curves of 4S10, 3S8A, and 4L8B nanostars in 0.5 M [Na^+], showing high ΔT_{PS} between nanostars. Hypothesised three-layer droplet formation in a 4S10 3S8A (16 %C 10-nt) 4L8B (25 %C 8A-nt) system.

Of the three nanostars, 4S8 remained unmodified, 3S8A had 16 %C 8-nt, and 4L8B had 25 %C 8A-nt. Upon annealing, a core-shell structure formed, with a 4S8 core and a co-localised 3S8A and 4L8B shell (figure 4.2). The mixing of the shell nanostars, instead of concentric layer formation, is likely due to a combination of multiple factors. First, the replacement of a portion of 4L8B sticky ends with 8A SEs in-

creases the T_{PS} of the nanostar (figure 3.16), reducing the ΔT_{PS} between 3S8A and 4L8B. Second, the 4L8B nanostar was modified to have 25 %C to 3S8A; as previously discussed, a trivalent-tetravalent NS pair with above 20 %C leads to infiltration and co-localisation of stars, regardless of ΔT_{PS} (figure 3.21). Third, the required %C of 4L8B to 3S8A in this system is likely less than in a two-star solution containing these NSs, as the 3S8A nanostars themselves were modified, and thus had fewer 8A-nt SEs. Therefore, while the formation of a concentric three-star layered droplet may be possible, further development of this system would be required.

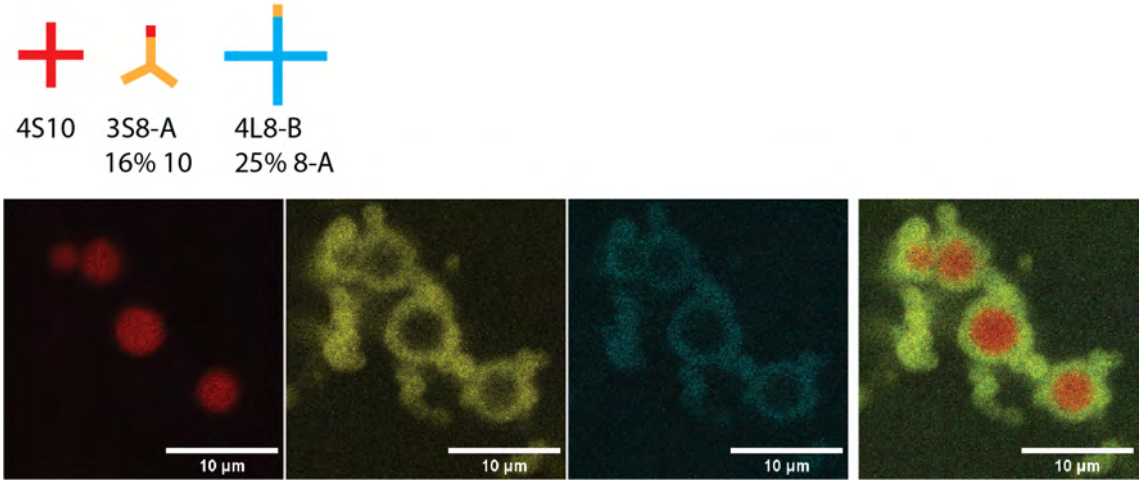

Figure 4.2: A 4S10 3S8A (16 %C 10-nt) 4L8B (25 %C 8A-nt) system in 0.5 M [Na^+] forms a 4S10 core and a co-localised 3S8A and 4L8B shell. Scale bars 10 μm.

Aim 3.1 directs the formation of distinct organelles within the core of a core-shell droplet, which would allow for the spatial localisation of reactions. The formation of a three-star droplet containing a co-continuous core and outer shell was thus attempted, henceforth termed nested co-continuous (figure 1.4). In this system, a 4L8 4S8A co-continuous droplet was combined with a 3S10 star (figure 4.3). Both the 4S8A and 3S10 nanostars were modified to induce complementarity towards 4L8 stars. The degrees of complementarity were varied, at 25-50 %C for 4S8A stars, and 8-16 %C for 3S10. As the target of the surfactant stars, 4L8, was unmodified, the degree of complementarity required for either co-continuous or core-shell formation was expected to remain unchanged. If this hypothesis was accurate, surfactant

modifications of 25 and 16 %C would result in a co-continuous core confined within an outer shell; an increase in 4L8 4S8A complementarity would create a co-localised core; and a decrease in 4L8 3S10 complementarity would form patchy surface adhesion.

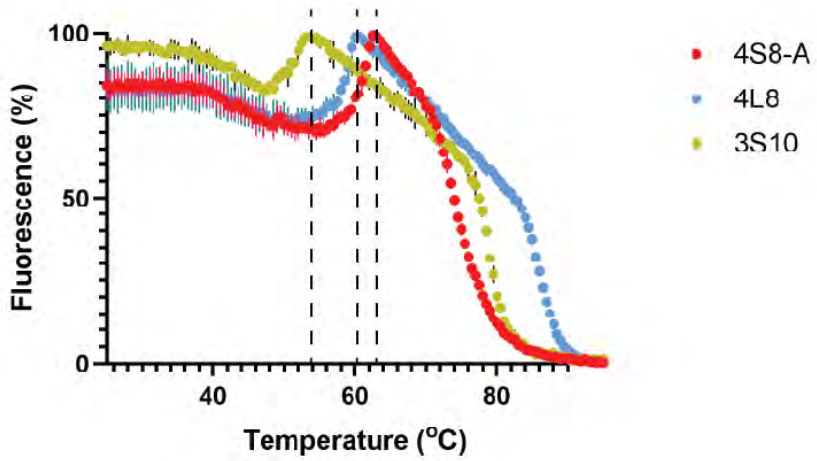

Figure 4.3: Hybridisation curves of 4S8A, 4L8, and 3S10 nanostars in 0.5 M [Na^+], showing high ΔT_{PS} between 3S10 (green) and tetravalent nanostars, and low ΔT_{PS} between 4L8 (blue) and 4S8A (red) nanostars.

The 4L8 4S8A 3S10 solutions were annealed under standard conditions. Shown in figure 4.4 are the results of varying the degrees of complementarity between stars. As hypothesised above, 25 %C of 4S8A to 4L8 created co-continuous cores, and 16 %C 3S10 to 4L8 formed a shell around the outside of the core (figure 4.5). Although this discussion describes the complementarity of 3S10 as only being directed towards 4L8 nanostars, 4S8A nanostars also possess 8-nt SEs. Therefore, the 3S10 shell fully encapsulated the 4L8 4S8A core, binding to both regions of nanostars and forming a nested co-continuous droplet.

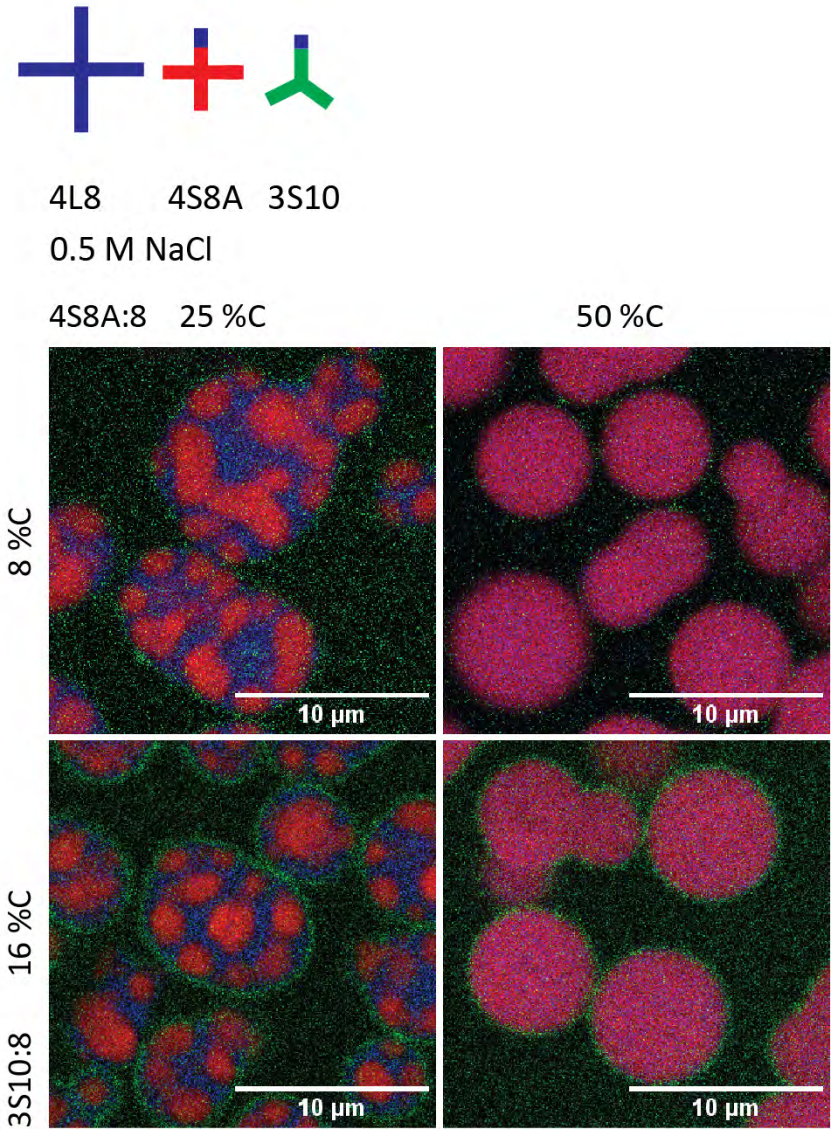

Figure 4.4: Droplet structure formation in a 4L8 4S8A 3S10 system in 0.5 M [Na^+], varying the degrees of complementarity between nanostars. 4L8 fluorescence is shown in blue, and 3S10 is shown in green. Phase separation of 3S10 nanostars was not seen at 8 %C. Scale bars 10 μm.

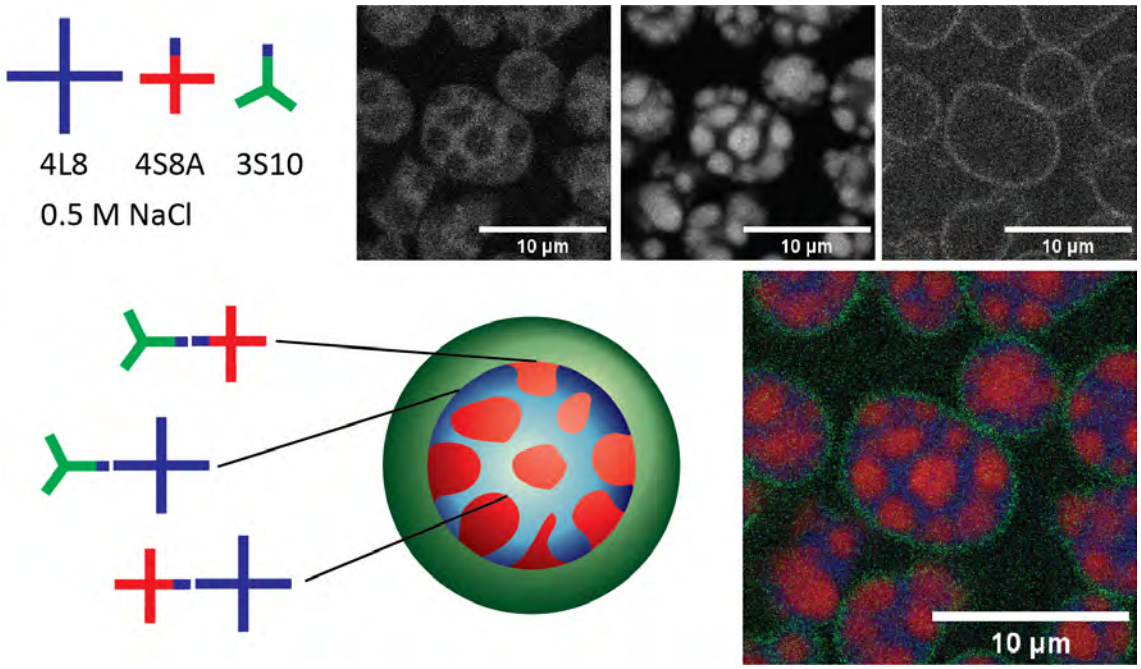

Figure 4.5: Droplets formed in a 4L8 4S8A (25 %C 8-nt) 3S10 (16 %C 8-nt) system in 0.5 M [Na^+], showing a nested co-continuous structure. Schematic of droplet structure shows predicted nanostar interactions at droplet region boundaries. 4L8 fluorescence is shown in blue, and 3S10 is shown in green. Scale bars 10 μm.

When increasing the degree of complementarity between the two interior nanostars, a mixed core and outer shell resulted. This creates a potential avenue for future explorations. For instance, Sato *et al.* induced the fission of mixed droplets through the digestion of surfactant stars (section 1.19) [24]. If a similar concept were applied here, a mixed-core/shell droplet could be triggered to form a nested co-continuous droplet, upon introduction of ribonuclease A. Alternatively, a strand-displacement reaction could take the place of the digestion reaction. This could allow for the production of core-shell synthetic cells that undergo phase separation and form interior organelles, upon receipt of an external signalling molecule. Designs to this effect are discussed in section 5.2.2.

In order to investigate the effects of varying cation valencies, the nested co-continuous system was prepared in 0.05 M $MgCl_2$ (section A.17). In a two-star system of 4L8 4S8A, multi-core droplets form in a magnesium ion solution, with 4S8A droplets suspended in a continuous 4L8 phase (figure A.22). Upon addition of 3S10 shell stars, the 4S8A regions migrated to the surface of the central core, giving the appearance a three-layered structure (figure 4.6).

Closer inspection of individual channels revealed that the 4S8A nanostars did not form a continuous layer between 4L8 and 3S10. Instead, 4S8A nanostars appeared to form distinct spheres which sat at the interface between inner and outer layers. Between these, small regions of the 4L8 core made contact with the 3S10 shell (figure 4.7). This extended across the volume of the droplet, creating a homogeneous core, a patchy inner shell, and a homogeneous outer shell, allowing interaction between all three types of nanostar.

In investigating these systems, 4L8 4S8A 25 %C droplets formed patchy structures in both 0.5 M [Na^+] and 0.05 M [Mg^{2+}] solutions. The addition of a 3S10 16 %C shell resulted in a nested co-continuous structure in a sodium chloride solution, and

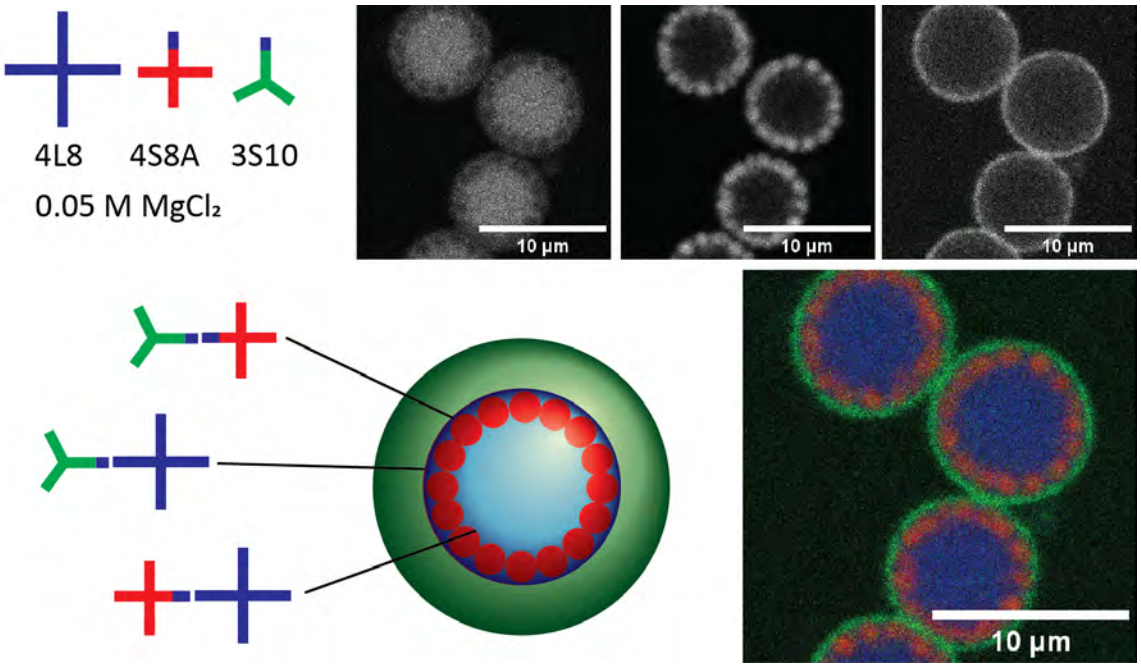

Figure 4.6: Droplets formed in a 4L8 4S8A (25 %C 8-nt) 3S10 (16 %C 8-nt) system in 0.05 M [Mg^{2+}], showing a three-layered structure. Schematic of droplet structure shows predicted nanostar interactions at droplet region boundaries. 4L8 fluorescence is shown in blue, and 3S10 is shown in green. Scale bars 10 μm.

a three-layer structure in magnesium chloride. It is hypothesised that the change in cation caused variation in the inter-star binding strengths, resulting in the differing structures [95]. In the sodium chloride solution, a high bond strength may exist between 4L8 and 4S8A, forming the co-continuous core, while the bonds between 3S10 and either core star are lower but equal, resulting in the homogeneous shell. Conversely, when in the presence of magnesium chloride, the bond strength between 4S8A and either other star may be equal. This would lead to the system maximising the area of contact between both 4L8 and 3S10 with 4L8A.

This three-star system was further investigated by modifying the complementarity of the 3S10 shell nanostar. In a solution of 0.05 M [Mg^{2+}], 3S10 surfactant stars were modified to possess either 16% 8-nt or 8A-nt SEs. These have binding free energies of -10.9 and -11.5 kcal/mol, respectively. In line with earlier results, the former case produced a three-layered droplet. When the system was modified to

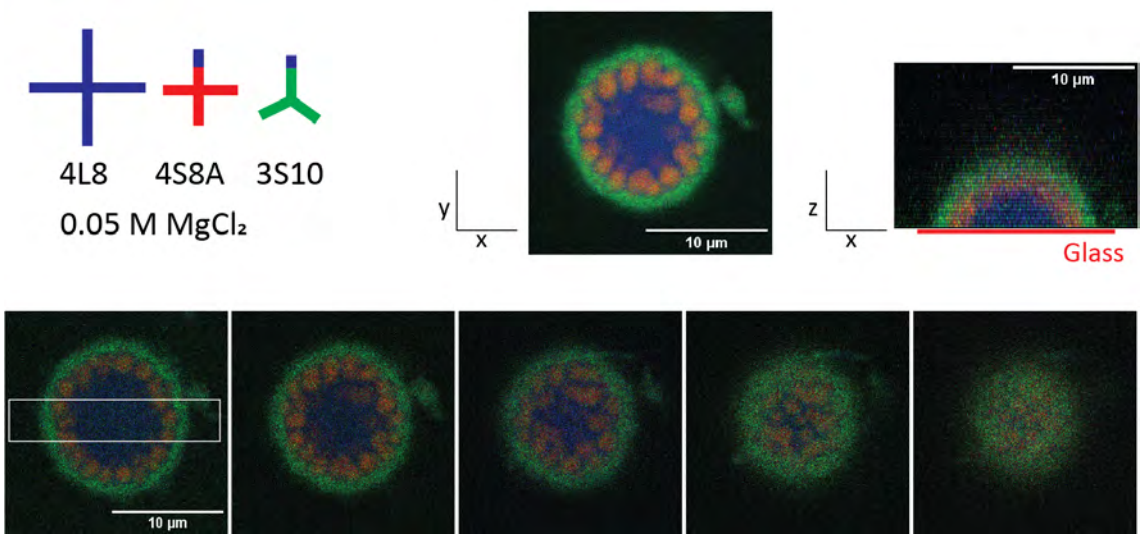

Figure 4.7: Confocal images of three-layer 4L8 4S8A 3S10 droplets. XY cross-section shows central 4L8 core, distinct 4S8A spheres at interfacial boundary, and 3S10 shell. XZ cross-section shows hemispherical structure of droplet against glass substrate. XY cross-sections rising through the Z axis show distinct 4S8A spheres arranged across the interfacial boundary, with regions of 4L8-3S10 contact. Highlighted area corresponds to XZ cross-section. 4L8 fluorescence is shown in blue, and 3S10 is shown in green. Scale bars 10 μm.

induce 8A complementarity in the 3S10 nanostar, the width of the 4S8A droplet layer reduced, and infiltration of the 3S10 nanostars through both 4S8A and 4L8 regions was seen (figure 4.8).

The formation of three-star micro-structured droplets was successful. However, further investigation into these systems is required. The formation of homogeneous layered structures requires heightened understanding of phase separation temperatures, degrees of complementarity, cation effects, and the comparative strength of inter-star bonds. Continued study may allow for the development of DNA nanostar droplets of increased complexity. This may allow for the creation of synthetic cells or micro-reactors with increased functionalities, as well as enhanced understanding of multi-phase cellular coacervates. Further discussion of three-star coacervates as switchable micro-architectures is presented in section 5.2.2.

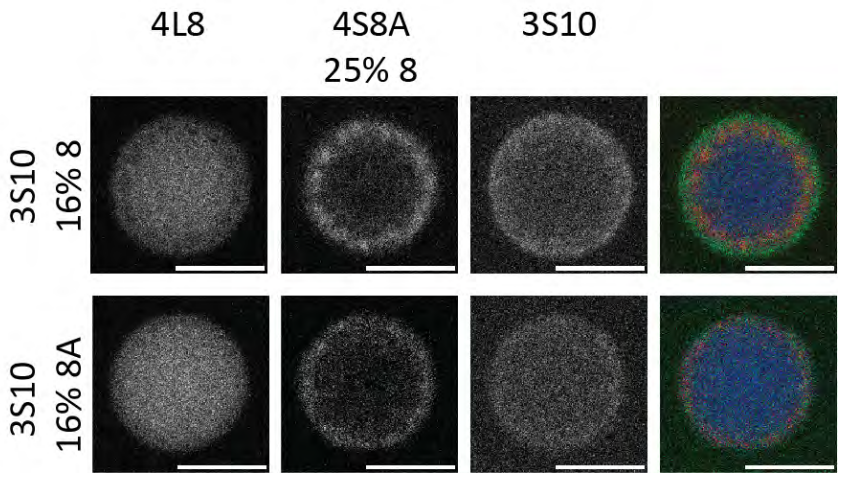

Figure 4.8: 4L8 4S8A (25 %C 8-nt) 3S10 droplets in 0.04 M [Mg^{2+}]. 3S10 nanostars were modified with 16 %C to either 8 or 8A-nt SEs. For ease of visualisation, 4L8 fluorescence is shown in blue, and 3S10 is shown in green. Scale bars 5 μm.

4.3 Targeted capture of biomolecules

In forming core-shell droplets, aims 3.2 and 3.3 require the creation of a selectively permeable outer barrier. Cellular membranes achieve selective permeability through two broad mechanisms - size-based exclusion and active shuttling. In the former case, small molecules are able to passively diffuse through the phospholipid membrane, moving down a concentration gradient. The rate of transport is heavily dependent on particle size and charge, with very few molecules above 1 kD known to permeate through a cellular membrane [200]. The passive movement of particles through a cellular membrane may also take the form of facilitated diffusion, in which molecules osmose through dedicated membrane-spanning channels, or in which the target molecule is bound to a carrier protein which allows its diffusion through the membrane [201]. Alternatively, active transport of molecules through the membrane involves transport pumps, which move molecules against a concentration gradient through the hydrolysis of ATP.

Vesicle membrane-spanning pores have been demonstrated using DNA origami, allowing the passive transport of molecules through a membrane [202] [203]. However, a major aim of this thesis was the creation of core-shell droplets with demonstrable functionality using only DNA nanostars. Therefore, the transport into or exclusion from these droplets will be limited to using size-based exclusion and carrier-facilitated diffusion.

4.3.1 Passive exclusion of dextran

Work in Chapter 2 discussed monitoring the infiltration of dextran polymers as a measure of droplet mesh size (section 2.5.2). It was concluded that 4S nanostars have a significantly smaller mesh pore size in comparison to 3S and 4L. This was attributed to the higher number of inter-particle bonds and the shorter inter-junction distance, respectively. In dense polymer solutions, the rate of diffusion of a solute molecule is determined by the probability of encountering pores in the polymer matrix larger than its hydrodynamic radius [204]. The volume fraction of the polymer and the size of the solute molecule together impact the rate of diffusion - a denser polymer solution will be less likely to form pores of sufficient size, while a large infiltrate will be unlikely to encounter pores of sufficient size. A similar mechanism is thought to apply here, with the rate of dextran infiltration scaling with dextran size and nanostar mesh density.

This assumption was further tested in this chapter by measuring the degree of partitioning of dextran molecules in layered droplets. If a droplet of large mesh size were encapsulated in a shell of denser nanostars, it is expected that the rate of infiltration would be slowed in comparison to the bare droplet. Droplets formed of 4L10 nanostars were compared to 4L10 3S8A and 4L10 4S8B core-shell structures. Earlier work showed 4S nanostars formed a denser network than 3S or 4L, while 3S and 4L networks were comparable in pore size. It was hence hypothesised that a 3S8A shell would not effect the degree of infiltration into a 4L10 core, while a 4S8B shell would decrease the infiltration of dextran particles.

The degree of dextran infiltration after ten hours was measured as the ratio of FITC-dextran fluorescence within the core of a droplet to fluorescence in the bulk solution, termed the partition coefficient (figure 4.9). A small but statistically significant decrease in the partition coefficient was found for 4L10 4S8B droplets in comparison

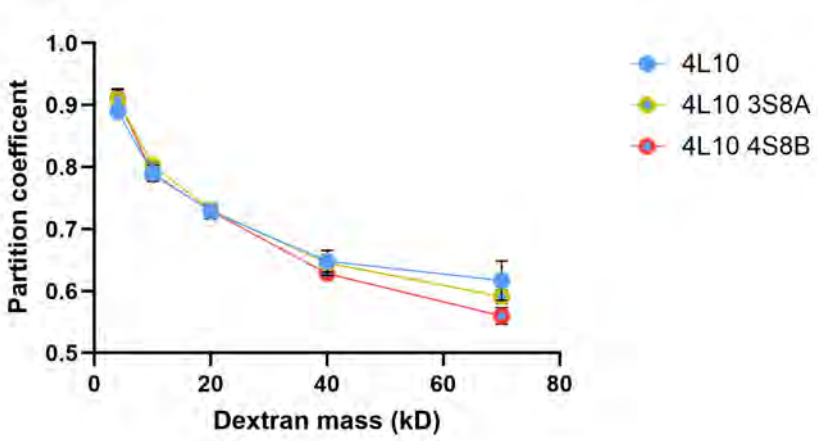

Figure 4.9: Dextran infiltration in 4L10, 4L10 4S8B, and 4L10 3S8A droplets. Partition coefficient measured as the ratio of fluorescence intensity of dextran in the central core and outside of droplets. Shown as mean ± SD of n = 9 droplets.

to 4L10 (Tukey multiple comparisons, $P = 0.0015$) and 4L10 3S8A droplets ($P = 0.0005$). This indicates a decrease in the rate of dextran infiltration through the 4S8B shell, acting as a means of kinetic control. If each system were allowed to proceed to equilibrium over an infinite period of time, the concentration of dextran each the core would be the same regardless of the shell, as partitioning in the core is dependent only on the structure of the core itself.

These results tentatively demonstrate passive transport control in DNA nanostar droplets. However, when considering individual datasets, significant differences in partitioning were only found for the largest infiltrate mass (figure 4.10). At 40 kD dextran, the difference between droplets was insignificant. At 70 kD, all datasets were significantly different (Tukey multiple comparisons test: bare vs 3S8A shell, P = 0.0141; bare vs 4S8B shell, P < 0.0001; 3S8A vs 4S8B shell, P = 0.0026). While these values indicate a significantly lower degree of partitioning in 4L10 4S8B systems, the overall difference is slight and the spread of data is large. This work would thus benefit from additional study, particularly in comparing shells of the same sticky end sequence.

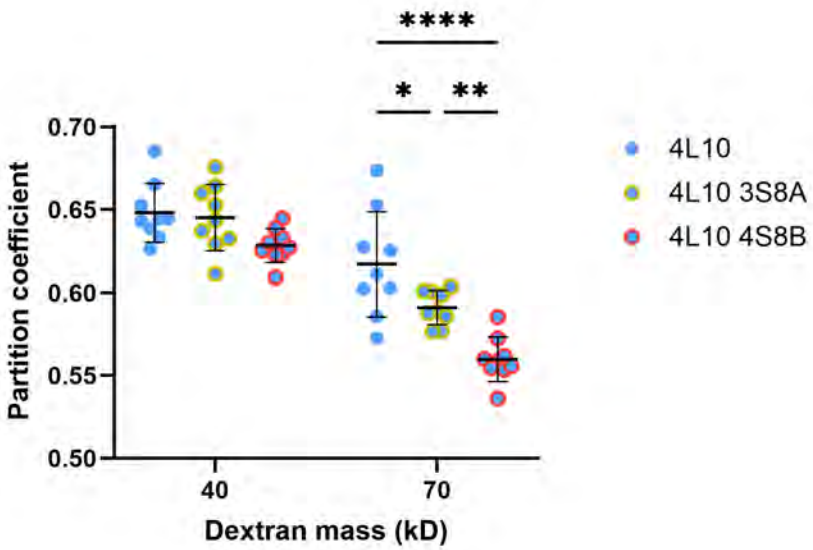

Figure 4.10: Comparison of partition coefficients for dextran of mass 40 - 70 kD. Significant difference is seen between datasets at 70 kD dextran. Mean ± SD = 0.61 ± 0.03, 0.59 ± 0.01, 0.56 ± 0.01 for 4L10, 4L10 3S8A, and 4L10 4S8B, respectively.

The size of excluded infiltrate seen in this system (70 kD) is significantly larger than molecules excluded from cellular membranes (1 kD). This is to be expected, as cell membranes are formed of a phospholipid bilayer, with dense packing and hydrophobic repulsion preventing the infiltration of any large or polar compound. This is vital in separating and protecting the contents of the cell from the external environment. However, when forming a micro-reactor, this impermeability hinders movement of reagents into or out of a vesicle (section 1.3). The synthesis and inclusion of complex membrane-spanning structures are required to allow inter-reactor movement. In comparison, the ease of infiltration into DNA nanostar condensates would allow for the targeted inclusion and movement of large reagents, simplifying the design of multi-stage reaction pathways.

4.3.2 Active inclusion and exclusion of streptavidin

In addition to passive infiltration, we aim to demonstrate functionality in core-shell nanostar droplets through the active control of infiltrate partitioning (aim 3.3). This would demonstrate both chemical addressability of different regions of these droplets, as well as develop cell-like functions of the shell. To study active partitioning of biomolecules, core-shell droplet structures were incubated with fluorescent SA (FITC-SA) functionalised with biotinylated binding sequence oligonucleotides (section A.18. These systems were used in the investigation of streptavidin localisation, exclusion, switching, and carrier-facilitated infiltration.

4.3.3 Sticky end-directed streptavidin localisation

Core-shell droplet systems were prepared using 4S8 3S10 nanostars in either 0.5 M NaCl and 0.05 M $MgCl_2$. Following incubation, droplet solutions were combined with FITC-SA and biotinylated target sequences (section A.18). In order to test the region specificity of compartmentalisation in this system, SA was functionalised with either 8-nt SE, 10-nt SE, or poly-T sequences. These were expected to compartmentalise SA in the core, in the shell, or outside of the droplets, respectively. Following incubation at room temperature for thirty minutes, droplet samples were imaged using confocal microscopy (figure 4.11).

The compartmentalisation of streptavidin can be monitored by the co-localisation of FITC fluorescence and the fluorescence of the droplet. When bound to a biotinylated poly-T oligonucleotide, streptavidin fluorescence within the droplet region was lower than in the bulk solution ($P = 0.67 \pm 0.02$). This indicates exclusion of poly-T-SA from the droplet. In investigating multi-droplet systems, Sato *et al.* and Jeon *et al.* similarly demonstrated the exclusion of streptavidin from nanostar droplets when functionalised with a non-complementary DNA sequence [24] [25].

Pixel profiles were drawn across droplet diameters, and the Pearson correlation coefficient between core, shell, and streptavidin fluorescence intensities were calculated (table 4.1). When streptavidin was functionalised with the sticky end sequence of either the core or shell, it demonstrated a high degree of localisation in the selected droplet region. For instance, in a 4S8 3S10 core/shell system in 0.05 M $[Mg^{2+}]$, streptavidin functionalised with a shell SE sequence (SA-10 nt) was added. The correlation between core and shell was -0.28, while core and SA was -0.49. This indicates anti-correlation of the respective fluorophores. In contrast, the correlation between shell and SA fluorophores was 0.91, indicating a strong localisation of streptavidin to the shell.

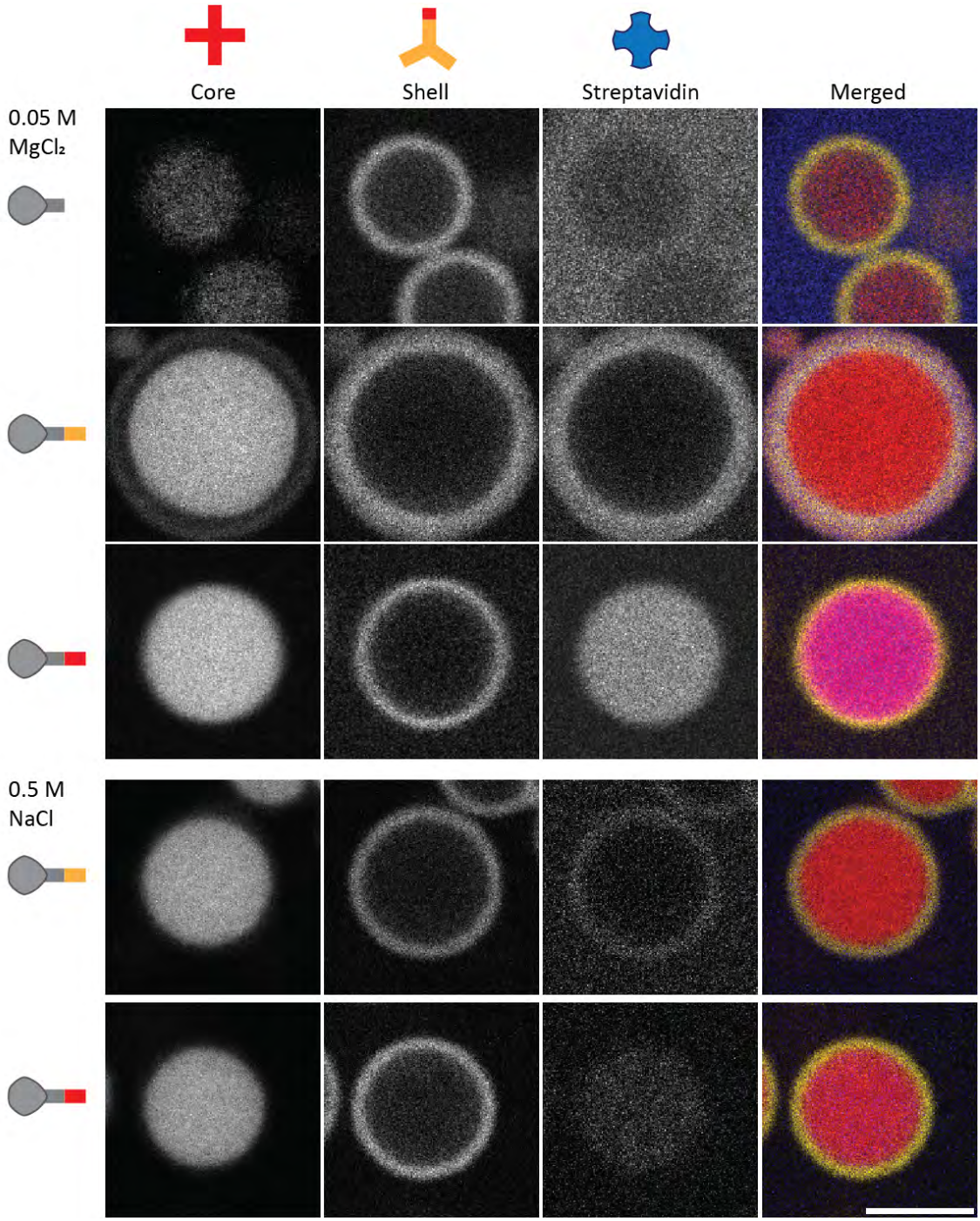

Figure 4.11: Selective capture of functionalised streptavidin. 4S8 3S10 nanostars annealed in 0.5 M [Na^{+}] and 0.05 M [Mg^{2+}] form core shell droplets. Streptavidin functionalised with poly-T ssDNA is excluded from droplets. SA-10 nt SE localises in the shell of droplets, while SA-8 nt SE localises in the core. Scale bars 5 μm.

Target region	Core - Shell	Core - Strep.	Shell - Strep.
	0.05 M $MgCl_2$		
Shell	-0.28 ± 0.14	-0.49 ± 0.10	0.91 ± 0.01
Core	-0.14 ± 0.06	0.90 ± 0.02	0.02 ± 0.04
	0.5 M NaCl		
Shell	-0.15 ± 0.18	-0.38 ± 0.24	0.52 ± 0.12
Core	0.004 ± 0.19	0.77 ± 0.04	0.20 ± 0.07

Table 4.1: Pearson correlation coefficients (P) between core, shell, and streptavidin fluorophore channels. Between -1:1, a higher value corresponds to a greater degree of co-localisation. Streptavidin tends to show high localisation in the target region (green shaded boxes). Data shown as mean ± SD for n=4 repeats.

The degree of localisation varied between magnesium and sodium cations, with a significantly greater fluorescence intensity in 0.05 M [Mg^{2+}] (table 4.1).

Degree of streptavidin capture

Streptavidin is a tetrameric protein, composed of four symmetrically arranged subunits [205]. Each subunit contains a binding site in which biotin may be captured, held in place by eight distinct hydrogen bonds, creating a highly stable duplex [206]. This allows the simultaneous complexation of four biotin molecules to a single SA complex. Thus far, the work in this section has combined FITC-SA with an excess of biotinylated DNA, ensuring a high degree of functionalisation in each protein. Here, the degree of functionalisation required for compartmentalisation was investigated by incubating streptavidin with differing ratios of complementary and non-complementary SEs.

A solution of 4S8 3S10 core-shell droplets was prepared in 0.05 M [Mg^{2+}] and divided into five aliquots. To these were added FITC-SA, followed by varying ratios of 8-nt

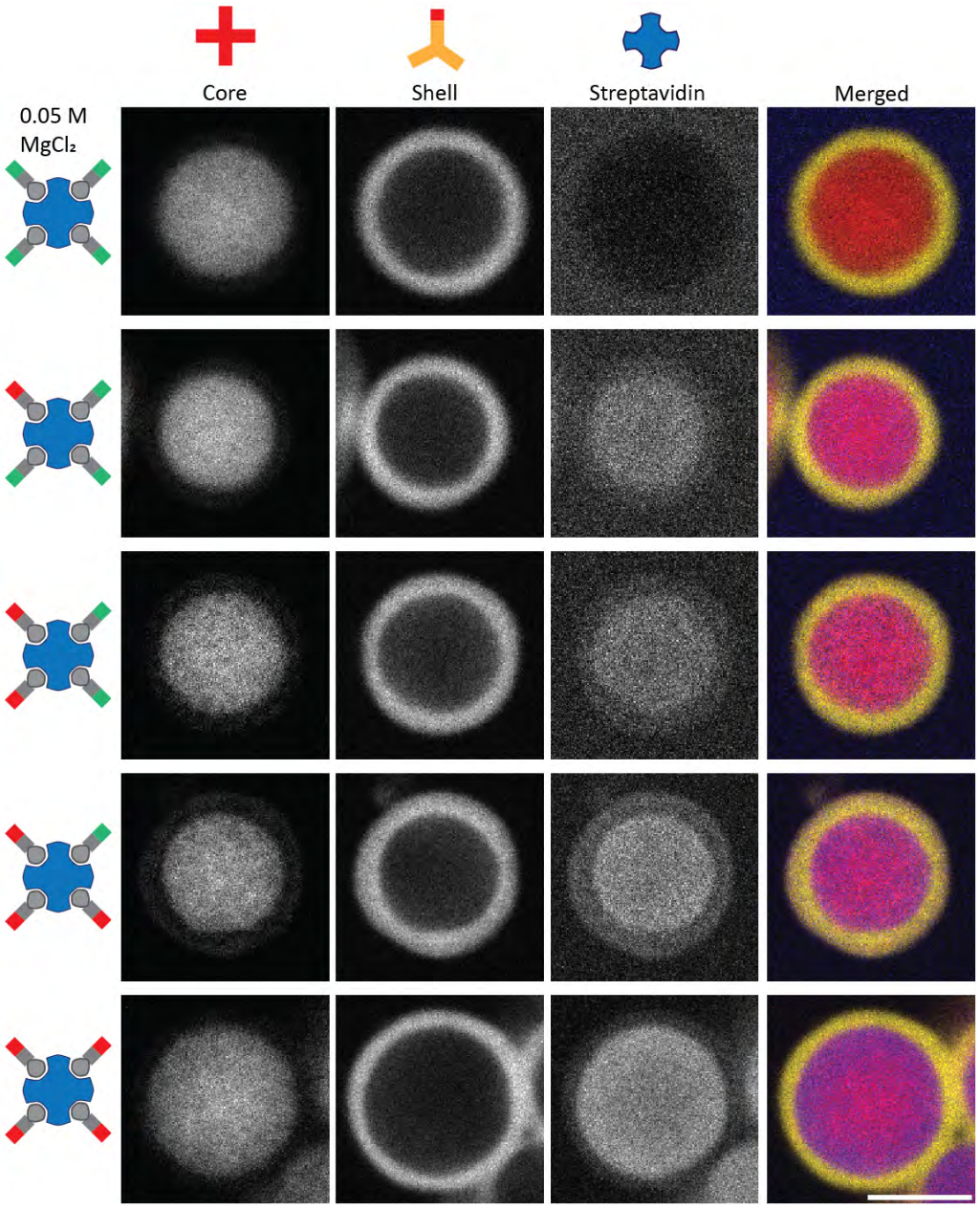

Figure 4.12: Effect of streptavidin functionalisation on degree of compartmentalisation. 4S8 3S10 (16 %C 8-nt) core-shell droplets incubated with streptavidin, functionalised with varying ratios of 8-nt SEs (red) and 8A-nt SEs (green). When functionalised with 100% 8A-nt SEs, streptavidin is excluded from the droplet. Increasing the number of 8-nt SEs increases the localisation in the core. A lower degree of streptavidin capture is seen in the droplet shell, despite lacking 10-nt complementarity, likely hybridised with surfactant stars. Scale bar 5 μm.

and 8A-nt SE biotinylated ssDNA strands. This would result in populations of SA infiltrates with an increasing average affinity for the 4S8 core. It was hypothesised that a majority of streptavidin sticky ends would have to be 8-nt in sequence in order for compartmentalisation to occur.

Confocal imaging of the compartmentalised SA shows a linear increase in localisation with SA-core affinity (figure 4.12). The degree of compartmentalisation was measured as the ratio between FITC fluorescence intensity within a droplet core as compared to the bulk solution. At 100% 8A-nt SE functionalisation, SA was entirely excluded from both core and shell. This was in-line with previous results discussed above, suggesting the protein is excluded through electrostatic repulsion of its non-complementary sequences. Between 25% - 100% 8-nt SE functionalisation, a linear increase in degree of compartmentalisation was seen (figure 4.13).

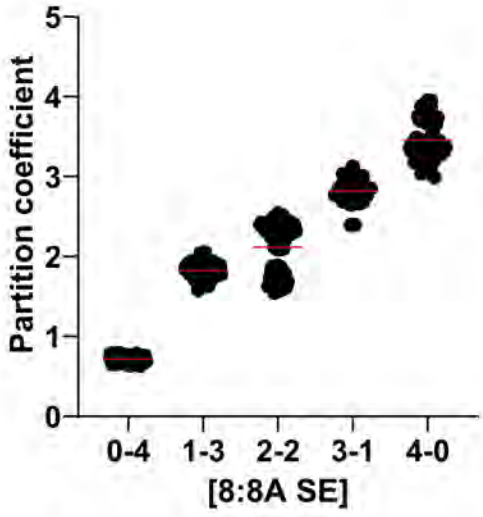

Figure 4.13: Partition coefficients of streptavidin in 4S8 3S10 cores (16 %C 8-nt), with an increasing ratio of 8:8A-nt SE streptavidin functionalisation. Mean shown as red line, n = 25-75. Linear regression of mean ± SD produces R^2 value of 0.92 and non-zero slope p-value < 0.0001, indicating significant relationship between streptavidin functionalisation and degree of partitioning.

It was hypothesised that greater than a 50% degree of 8-nt SE functionalisation would be required to see compartmentalisation of streptavidin. This was based

on the assumption that non-complementary ssDNA sequences appended to the SA would be actively repelled from the droplet, and that this repulsion would be equal in strength to the attraction experienced between complementary sequences. However, here we see infiltration at low average labelling. This could be because the labelling of SA with DNA does not result in homogeneous functionalisation, but a distribution. This may explain the observed infiltration as being due to the small portion of the SA population that statistically has >2 SEs complementary to the core. Alternatively, it could be that the specific SE-SE interaction is stronger than the incorrect SE repulsion. Overall, it was found that the degree of functionalisation of the streptavidin infiltrate offers a method of control over the concentration of compartmentalised protein.

Investigation of the mechanism of core localisation

Notably, localisation of strepatividin in the core was seen despite the presence of a shell. This would suggest that under the current system design, the shell is permeable to infiltrates when they are functionalised with a core-complementary sequence. As was demonstrated above, nanostar droplets exclude streptavidin when it is functionalised with an orthogonal ssDNA sequence. This is in-line with results observed in the literature [24] [25]. The exclusion is attributed to electrostatic repulsion of the non-complementary DNA strands.

These results suggest core-complementary streptavidin experiences a limited degree of attraction to shell nanostars, allowing passage through the shell prior to accumulation in the core. This behaviour was hypothesised to be caused by surfactant stars in the shell, which contain a limited number of core-SE sequences. It is possible that the shell surfactant stars act in a manner akin to plasma membrane carrier proteins, shuttling SA molecules through the shell.

This hypothesis was tested through modification of the core-shell nanostars. If

streptavidin-SE complementarity in the shell allowed for shuttling towards the core, then two different design variations may prevent core compartmentalisation (figure 4.14). First, core-shell droplets were produced using surfactant modification of core nanostars, which would prohibit the presence of core SEs in the shell, rather than the previous used surfactant modification of the shell. Second, mixed-SE cores were produced, in which 25% of core nanostar sticky ends were replaced with an alternate sequence, with streptavidin functionalised with this sequence.

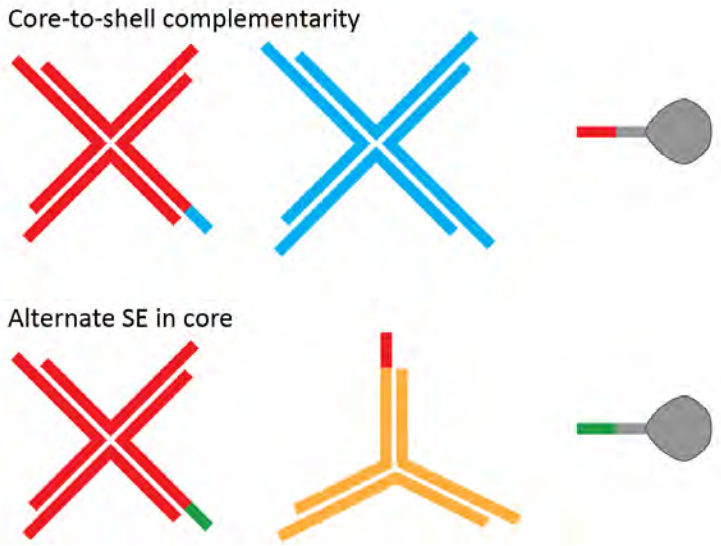

Figure 4.14: Modification of core nanostars in core-shell droplets to investigate streptavidin compartmentalisation.

When a 4S8 4L8B system was prepared using surfactant modification of the shell star, core-shell structures formed in both NaCl and $MgCl_2$ (figure C.3 and A.21). Surfactant modification of core nanostars was then performed, creating a 4S8 core with 25 %C 8-B nt SEs. This system was tested in both magnesium chloride and sodium chloride solutions (figure 4.15). In a 0.05 M magnesium chloride solution, this combination of nanostars created a multi-core structure, in which numerous 4S8 spheres were suspended in a continuous 4L8B droplet. In a sodium cation system, core-shell droplets formed. Under both conditions, 8-nt SE functionalised SA was localised in the 4S8 core.

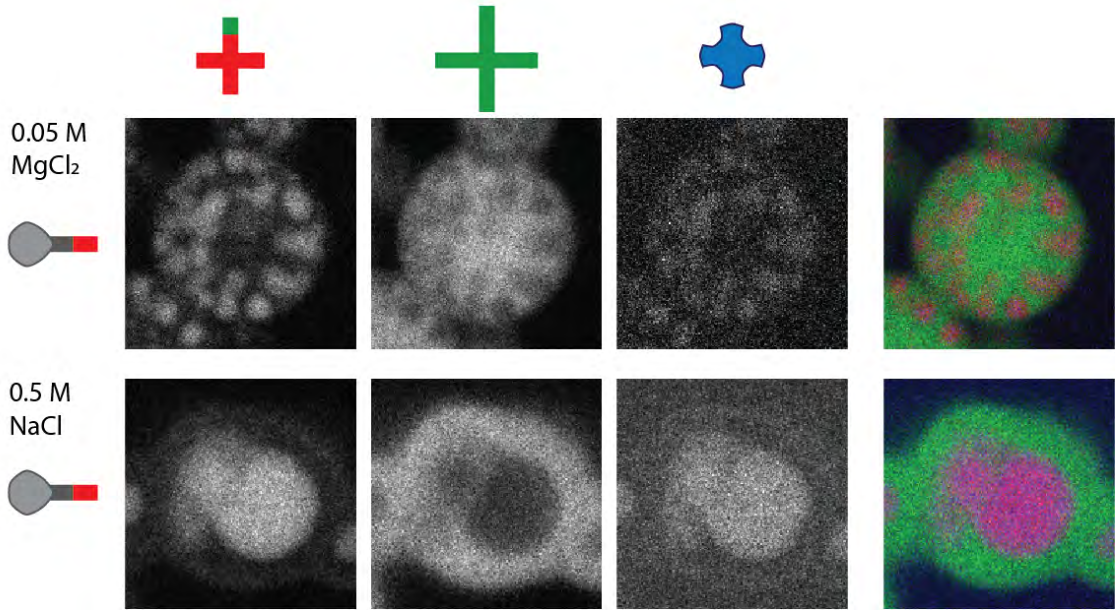

Figure 4.15: Droplets formed from 4S8 (25 %C 8B-nt) 4L8B solutions, showing multi-core structures in 0.05 M [Mg^{2+}] and core-shell structure in 0.5 M [Na^{+}]. Despite surfactant stars being present in the droplet core, streptavidin functionalised with 8-nt SEs localises in the core. For ease of visualisation, 4L8B fluorescence is shown in green shade. Scale bar 5 μm.

If compartmentalisation of streptavidin in the core of the droplet was facilitated by surfactant shell NS shuttling, core NS surfactant modification would theoretically remove this avenue of access. These results imply an alternate route of SA infiltration. However, it is possible that core surfactant nanostars were present in the shell, mimicking the above mentioned carrier mechanism. As described in section 3.4, a portion of surfactant stars in a 25 %C tetravalent nanostar population will contain 50 %C SEs. These nanostars, exhibiting a high degree of complementarity, may infiltrate the second droplet phase. If this were to occur, it would result in the 3S10 shell containing some number of 4S8 surfactant NSs, enabling SA shuttling. Hence, a second method of investigating the shell shuttling hypothesis was required.

Core-shell droplet systems were prepared using 4S8 3S10 nanostars in 0.05 M [Mg^{2+}]. Here, the 3S10 shell possessed 16 %C to the core, while the core nanostars were modified with 25% 8A-nt SEs. As core nanostars were not designed to possess 10-

nt SEs, they should not be present in the shell. Streptavidin was functionalised with either 8-nt or 8A-nt SEs. The former was previously shown to compartmentalise within a 4S8 3S10 core, and was suspected to be shuttled by surfactant shell nanostars. The alternate core SE design only finds 8A-nt SEs in the core, with no cross-complementarity to the shell. If surfactant nanostars indeed act as transport carriers, then 8-nt SE functionalised SA is expected to localise in the core, while 8A-nt SE are not.

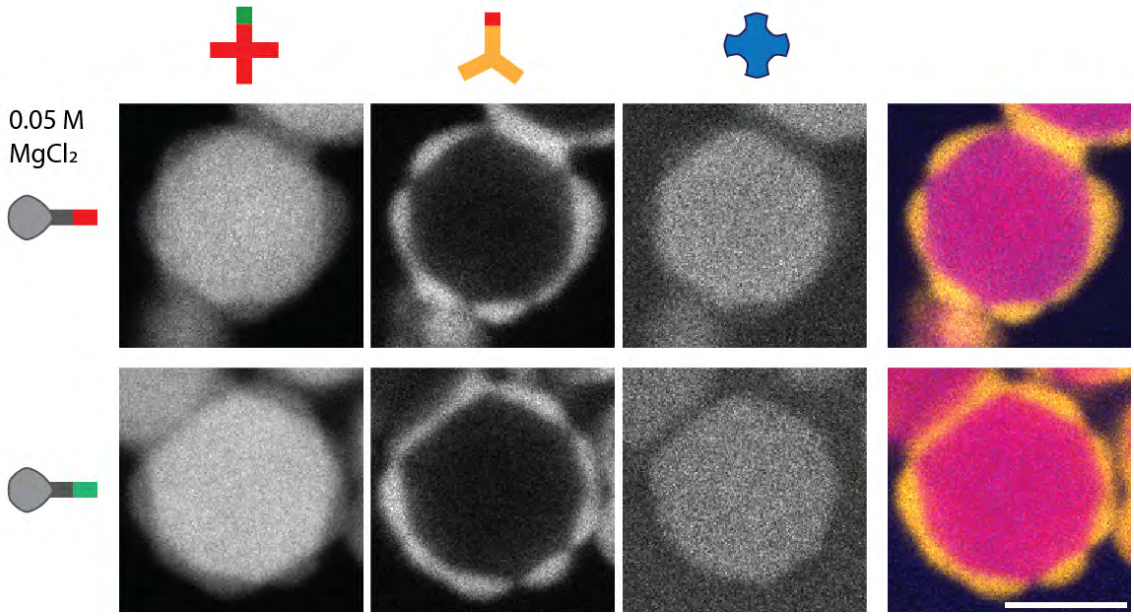

Figure 4.16: Droplets formed from 4S8 (25% 8A-nt) 3S10 (16 %C 8-nt). Surfactant stars are present in the shell, while the core contains 25% alternate 8A SEs. In 0.05 M $[Mg^{2+}]$, streptavidin functionalised with either 8-nt SEs or 8A-nt SEs localises in the core. Scale bar 5 μm.

Droplet systems containing 4S8 25% 8A-nt SE cores and 3S10 16% 8-nt SE shells formed patchy, non-homogeneous shells. They also showed compartmentalisation of both 8-nt SE and 8A-nt SE functionalised streptavidin (figure 4.16). The non-homogeneous appearance of the shell is potentially caused by the lowered effective valency of core, with 25% of core SEs unavailable for binding with the shell. It is possible that the gaps in the 3S10 shell allow for the infiltration of 8-nt and 8A-nt SE streptavidin. However, the prior results suggest that the shell shuttling

hypothesis does not sufficiently explain the observed infiltration of streptavidin into the core (figure 4.11). Therefore, further study of the localisation mechanism of functionalised streptavidin in these systems is required.

Release of sticky end-localised streptavidin

Following demonstration of chemical addressability through selective cargo capture, we further aim to show dynamic control in these systems. This involves imparting dynamic control over the capture and release of cargo molecules, a key feature of complex microreactor systems and synthetic cells. The creation of a switchable system was first attempted using a toehold-mediated strand displacement reaction. As previously described, partially complementary ssDNA sequences may hybridise, but this duplex will dehybridise in favour of a competing strand of higher complementarity, lower energy, or longer length. This concept was used in the work of Leathers *et al.*, who appended long binding sequences to non-SE ends of their nanostar arms. They demonstrated the rapid infiltration of short, partially complementary fluorescent strands through the mesh network of the droplet. These short strands were gradually displaced by longer, slower moving invader strands which had greater complementarity to the binding sequences. Toehold-mediated strand displacement reactions have been used in the creation of computational logic circuits [207] [208], and provide a synthetic mimic of cellular signalling pathways.

The biotinylated DNA used in the functionalisation of streptavidin in this work includes a ten thymine base sequence as a spacer between the sticky end and the biotin modification. In a typical reaction in this work, the poly-T spacer is uninvolved in the capture and localisation of SA in core-shell droplets. In designing a switchable system, the existing spacer was taken advantage of as a toehold, in designing a strand displacement reaction (figure 4.17).

Two distinct core-shell solutions were annealed separately and then combined, con-

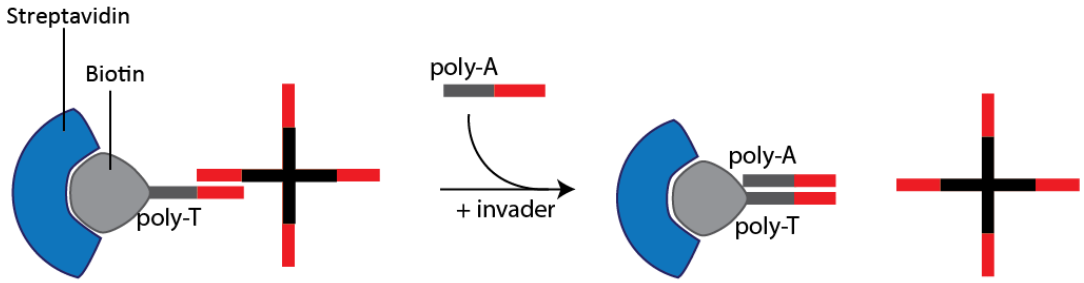

Figure 4.17: Streptavidin conjugated with biotin-polyT-binding sequence may hybridise with nanostars possessing the anti-barcode sequence. An invader strand of polyA-anti-binding sequence is expected to displace the streptavidin-NS bond due to its higher sequence complementarity.

sisting of 4S8 3S10 droplets and 4L8A 3S10 droplets 4.18. The solutions were prepared in a 0.05 M [Mg^{2+}] solvent. Streptavidin was added to the combined droplet solution, followed by biotinylated DNA with a 3:1 8:8A-nt SE ratio. Confocal imaging showed a higher degree of SA capture in 4S8 3S10 cores as compared to 4L8A 3S10 cores, as would be expected from the respective degrees of SA functionalisation.

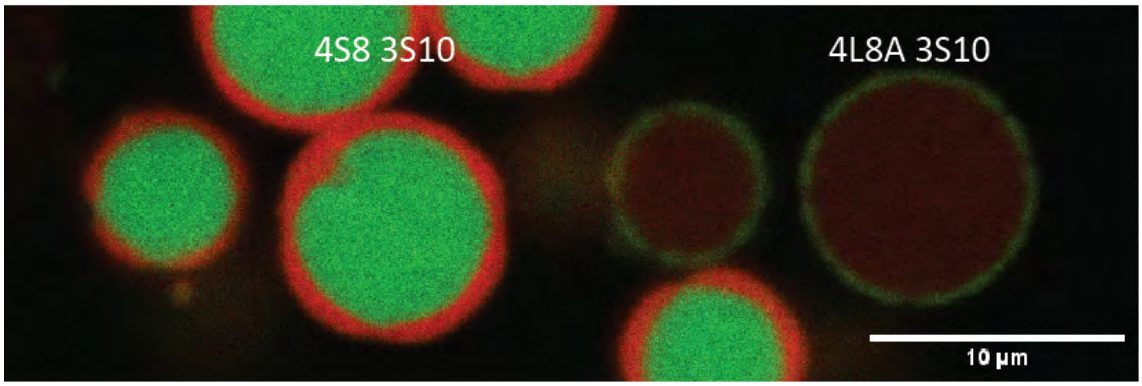

Figure 4.18: Solutions of 4S8 3S10 (16 %C 8-nt SE) and 4L8A 3S10 (16 %C 8A-nt SE) were annealed in 0.05 M [Mg^{2+}]. following annealing, the two droplet solutions were combined. Droplets were functionalised with contrasting fluorophore placements to aid in identification. 4S8 3S10 have a Cy3 (green) core and Cy5 (red) shell, while 4L8A 3S10 have a Cy5 (red) core and Cy3 (green) shell. Scale bar 10 μm.

Following streptavidin compartmentalisation, an invader strand was introduced to the system, consisting of the 8-nt SE and a poly-A sequence. This invader strand was predicted to have a higher binding affinity to the poly-T/8-nt SE biotin sequence than unmodified 8-nt SE sticky ends. Simultaneously, it was not expected to impact

the hybridisation of 8A-nt SEs. Therefore, displacement of SA from 4S8 cores was expected, while 4L8A cores were predicted to remain unchanged.

Confocal images of nanostar droplets pre- and post-invader addition show a significant decrease in 4S8 streptavidin capture (figure 4.19). The degree of capture was quantified as the ratio of FITC-SA intensity in the interior of a droplet to the bulk solution (figure 4.20). A partition coefficient less than 1 indicates exclusion of the cargo; a value of exactly 1 indicates equal concentrations in the droplet and bulk solution; and values greater than 1 indicate compartmentalisation. 4S8 3S10 nanostar droplets experienced a significant decrease in SA compartmentalisation. Following the addition of the invader, the partition coefficient of these droplets fell from 7.53 to 1.15, indicating a near complete removal of SA from the core. A decrease in the compartmentalisation of SA inside 4L8A 3S10 droplets was also noted, with the partition coefficient falling from 2.87 to 1.80. This may be due to destabilisation of 8A-nt SA-nanostar bonds through the binding of the poly-A portion of invader to the biotin poly-T spacer. It would likely not directly displace the 8A-8A SE duplexes, but the steric interference of its presence may lead to a decrease in the binding affinity of SA and nanostar SEs.

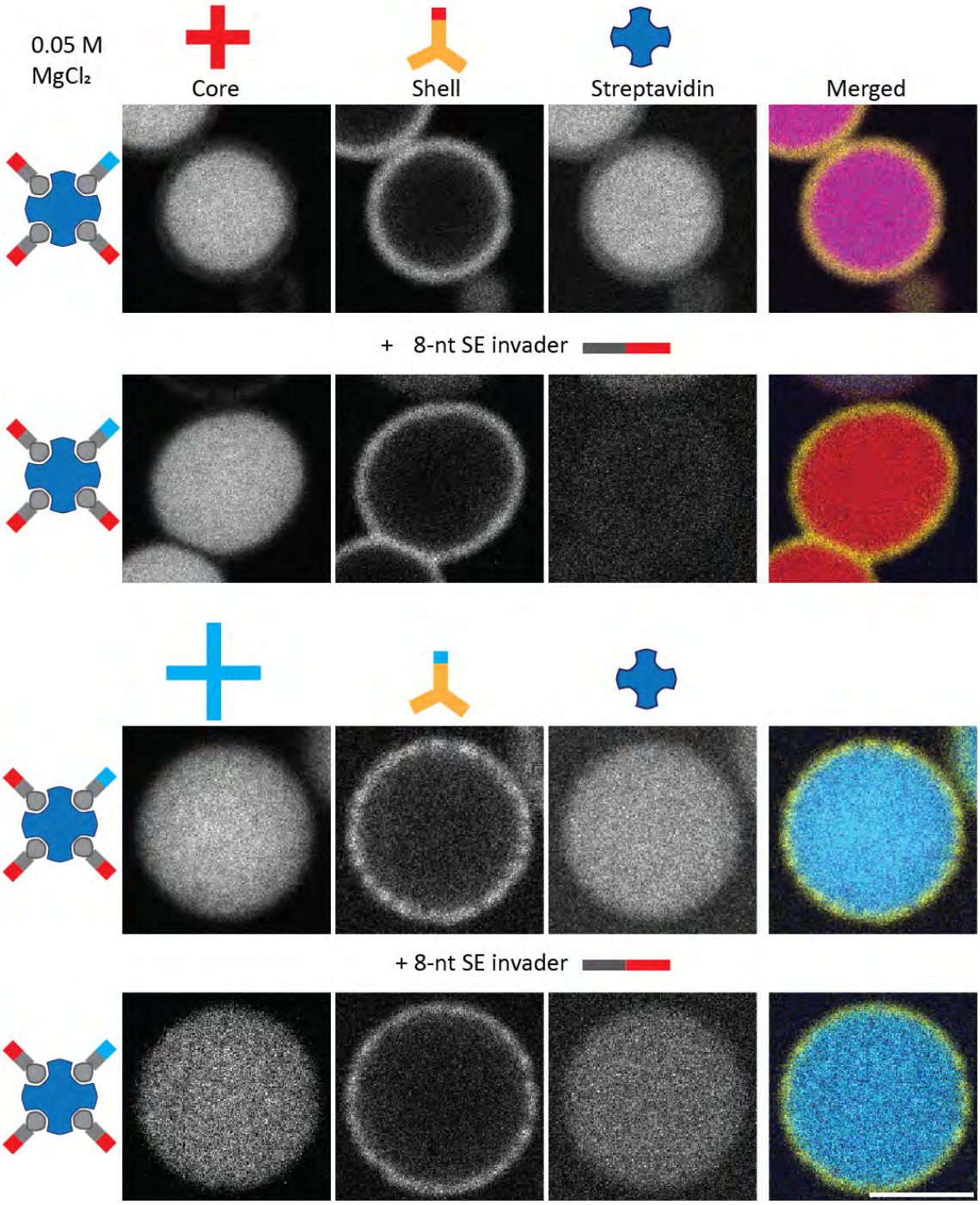

Figure 4.19: Solutions containing both 4S8 3S10 (16 %C 8) and 4L8A 3S10 (16 %C 8A) droplets were combined with 3:1 8:8A-nt SE functionalised streptavidin. Compartmentalisation of streptavidin was seen in both cores. PolyA-8 nt SE invader sequences were added, displacing 8-nt SE streptavidin-4S8 nanostar hybridisation. Streptavidin was displaced from 4S8 3S10 cores, but remained in 4L8A 3S10 cores. Scale bar 5 μm.

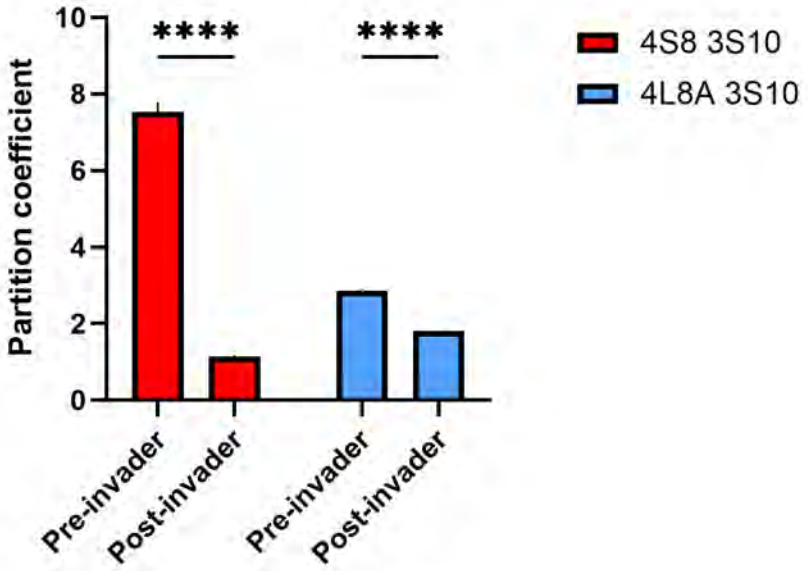

Figure 4.20: Partition coefficient of 3:1 8:8A-nt SE functionalised streptavidin in 4S8 3S10 and 4L8A 3S10 droplet cores, before and after 8-nt SE invader addition. Targeted 4S8 3S10 cores undergo a 84.7% decrease in P from 7.53 to 1.15, while off-target 4L8A 3S10 cores underwent a 37.2% decrease from 2.87 to 1.80. Showing average ± SD of n=3 repeats.

4.3.4 Binding sequence-mediated streptavidin localisation

Thus far, the capture and compartmentalisation of streptavidin has relied on sticky end complementarity between droplet and cargo. As seen in the discussion of surfactant-mediated cargo transport, this makes it difficult to separate out cargo and phase separation effects of changing SE ratios in core or shell. Furthermore, if increased complexity in dynamic systems is desired, the design of these systems will benefit from dedicated cargo capture toehold sequences. In previous results we saw that when changing SE ratio to optimise cargo loading, droplet properties were unintentionally affected, resulting in changes in morphology. Here we aim to optimise cargo binding and morphology independently. Therefore, modified nanostars were produced in which one arm was appended with a unique binding sequence, to which SA capture could be directed.

4S8 and 3S10 nanostars were each modified with a unique binding sequence, termed i and j, respectively (figure 4.21, table A.9). Complementary biotinylated sequences were also procured. These consisted of an i'-biotin sequence, and an i'-j'-biotin sequence. The hybridisation of these sequences was investigated using polyacrylamide gel electrophoresis.

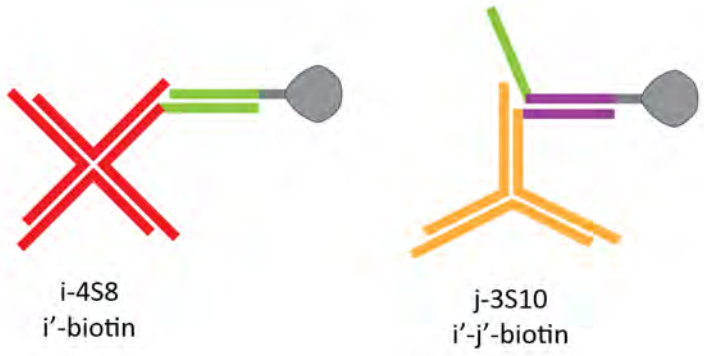

Figure 4.21: Modification of 4S8 and 3S10 nanostars to include cargo capture binding sequences. The non-SE 5' end of strand 1 of each star was appended with a unique binding sequence. Complementary biotinylated sequences allow streptavidin capture by these modified nanostars.

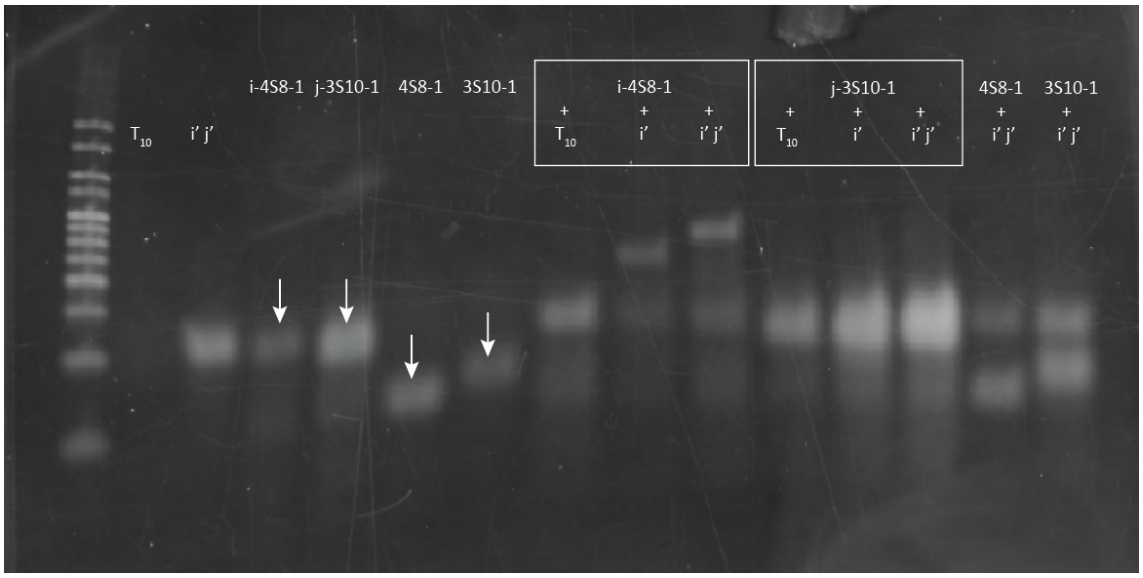

Figure 4.22: Polyacrylamide gel of biotinylated strands and complementary nanostar sequences. Strands were combined at 0.5 μM nanostar strands and 1.5 μM biotinylated strands in 0.5 M [Na^+] at room temperature for 1 hour, and diluted 1:10 prior to loading. Conducted in Bio-Rad 10% Mini-PROTEAN TGX 10% Precast Gel at 180 V for 40 minutes. **Lane contents**: Lane 0: DNA Ladder. Lane 1: poly-T biotinylated strand. Lane 2: i'-j' biotinylated strand. Lane 3: i-4S8 strand 1. Lane 4: j-3S10 strand 1. Lane 5: 4S8 strand 1. Lane 6: 3S10 strand 1. Lane 7-9: i-4S8-1 + poly T-biotin; i'-biotin; i'-j'-biotin. Lane 10-12: j-3S10-1 + poly T-biotin; i' biotin; i'-j' biotin. Lane 13: 4S8-1 + i'-j'-biotin. Lane 14: 3S10-1 + i'-j'-biotin. Arrows indicate single strand bands.

Shown in figure 4.22 are the results of PAGE analysis conducted on i and j oligonucleotides. Unmodified 4S8 and 3S10 strands were used as a control, and were not expected to hybridise to any biotinylated strand. The modified i-4S8 strand was expected to form duplexes with strands containing i'. Similarly, j-3S10 was predicted to hybridise to j'.

DNA strands were combined in solution with an excess of biotinylated strands, and incubated at room temperature for thirty minutes. Lanes 8, 9, and 12 contained functionalised biotin and the complementary strands; hybridisation was thus expected. Conversely, lanes 13 and 14 contained unmodified star strands in combination with functionalised biotin, as controls.

The controls in lanes 1-7 and 10-11 were each observed to contain single sharp bands, as expected. Lanes 8 and 9 contained progressively slower moving bands, in addition to faint secondary bands at their original masses. Lane 12 did not appear to change in position, but showed a significant increase in fluorescence intensity. Lanes 13-14 each contained two bands, combining the positions of lanes 2 & 5 and 2 & 6, respectively.

The controls in lanes 13 and 14 indicate no hybridisation between unmodified nanostar strands and i'-j'-biotin. The increase in mass of lanes 8-9 indicate binding of i-4S8 + i'-biotin and i-4S8 + i'-j'-biotin. The lower mass secondary bands likely result from unbound excess biotinylated strands. Lanes 10-12 concern the hybridisation of j-3S10 with biotinylated strands, wherein hybridisation is only expected in lane 12. However, no secondary structure was seen.

Sequence analysis of the j-3S10 strand using NUPACK reveals the formation of secondary structures within the strand, which would likely decrease the rate of hybridisation with i'-j' 4.23. This secondary structure formation is not expected to affect nanostar hybridisation or droplet formation. The high temperature annealing

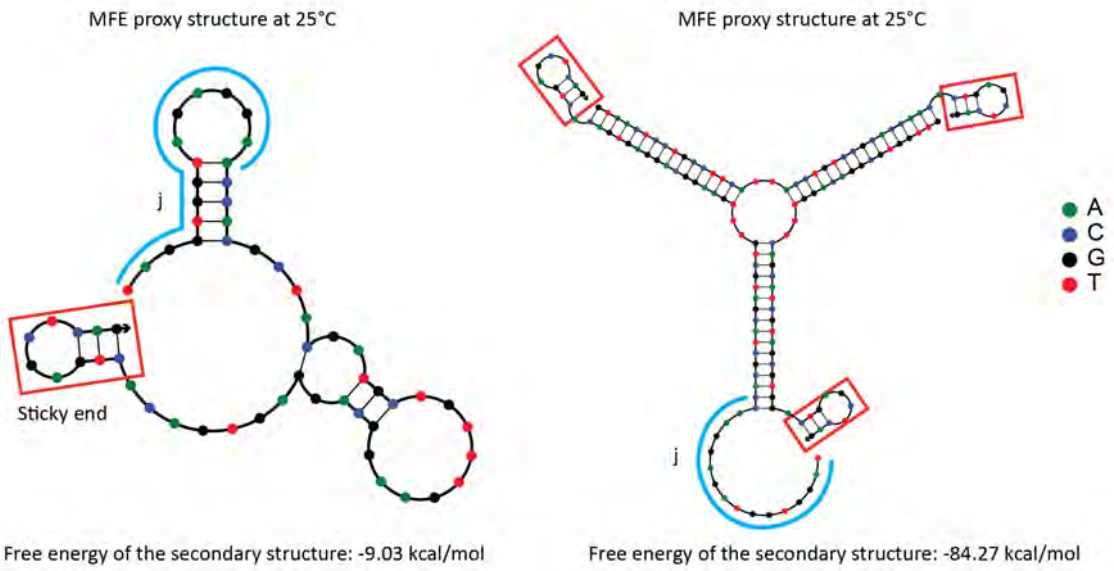

Figure 4.23: NUPACK predictions of secondary structures in j-3S10 strand 1. The j sequence forms a hairpin loop with the 3S10-1 strand when in isolation. This structure is not present upon annealing of the full nanostar. Red boxes indicate palindromic 10-nt SEs. Blue line indicates j region. Simulation performed at 0.5 M [Na^+] and 25 ^oC.

of the nanostars is designed to promote the hybridisation of the full structure design, bypassing the kinetic effects of secondary structures.

Droplet formation using i-4S8 nanostars was investigated, to investigate the degree of modification required for streptavidin capture. Solutions of 4S8 nanostars were prepared in 0.5 M [Na^+], increasing the degree of i modification from 1 - 100%. As the toehold sequence was only applied to a single strand in the star, a 100% i-4S8 structure would consist of three unmodified arms and one arm of approximately double length.

Shown in figure 4.24 are the results of increasing i modification in 4S8 nanostars, when combined with i'-biotin and SA. From 0 - 10%, the expected increase in streptavidin compartmentalisation is seen (P = 0.87, 1.37, 10.74). However, appending a i sequence to 50% of 4S8 strand 1 arms creates in-homogeneous SA compartmentalisation. At 50% i-4S8, a clear gradient is seen in SA compartmentalisation, with the

cargo concentrated at the edge of the 4S8 droplet. A similar effect is seen in 100% i-4S8 droplets, with the confinement of SA to the edge of the droplet significantly more pronounced.

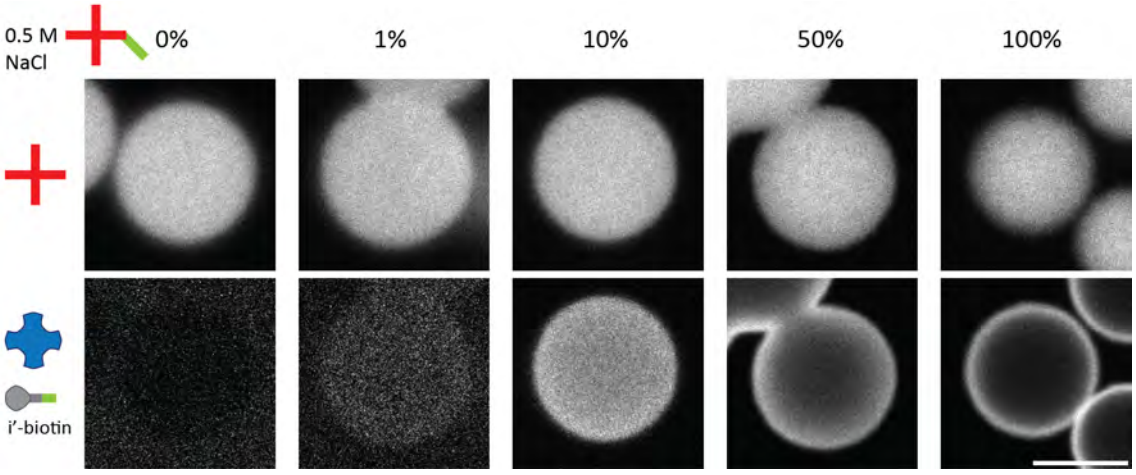

Figure 4.24: Confocal images of i'-streptavidin capture in 4S8 nanostars with increase degrees of i-4S8 modification. Scale bar 5 μm.

Literature results demonstrate the partitioning of large or asymmetric DNA structures to the exterior of nanostar coacervates [160] [22]. In the system investigated in this thesis, one arm of a modified nanostar is extended by 21 nt or 7.14 nm, in comparison to the typical arm length of 16 bp. This possibly accounts for the surface partitioning of streptavidin seen in 50% modified i-4S8. However, systems with modification of every nanostar (100% of strand 1 is appended with i) exhibit increased partitioning. As every nanostar in this system is asymmetrical, asymmetry-based partitioning cannot account for the observed behaviour.

We instead hypothesise that as streptavidin infiltrates through the droplet, it is strongly bound at the surface. Streptavidin is a tetrameric protein, able to complex with four discrete biotin molecules. Additionally, streptavidin is added to the system at 30% of the concentration of the nanostars (1.5 μm SA vs 5 μm NS). Thus, when a droplet contains a high degree of binding sequence functionalisation, infiltrating streptavidin will rapidly complex with biotin at all four binding sites. The

strong biotin-SA bond strength and the multivalency of the 4(NS)-SA complexes is expected to trap streptavidin near the surface of the droplet, resulting in the observed infiltration gradient.

Upon confirming that 10% i modification of 4S8 nanostars allows for homogeneous streptavidin capture in phase-separated droplets, core-shell systems were investigated. Solutions of variously modified 4S8 3S10 NSs in 0.5 M [Na^+] were prepared and incubated with SA and either i'-biotin or i'-j'-biotin. The system was designed such that an i sequence may only be present in the core of a droplet, while a j may only be present in the shell. Surfactant strand replacement and j strand replacement both modify strand 1 of shell 3S10 nanostars. This means that the two structures are mutually exclusive, and surfactant stars cannot possess j complementarity.

This system was used to further explore the question of core infiltration through a non-complementary shell. It was hypothesised that a droplet containing an i-modified core would only experience SA localisation when the shell contained j modifications, and the biotin-SA conjugate possessed i' and j' complementarity (figure 4.25). This would align with the concept of a membrane transport carrier, allowing penetration through the shell only of molecules which contained the appropriate signal sequence.

The hypothesised system functions as follows: a streptavidin bound only to i'-biotin would be electrostatically repulsed by the non-complementary shell. This would occur whether or not the shell contained j sequences. Alternatively, a streptavidin bound to i'-j'-biotin would not pass through a 3S10 shell, but only a j-3S10 shell, with the modified nanostars shuttling the protein towards the core.

The localisation of streptavidin was interrogated through the analysis of individual fluorescence channels. Image channels were separated into core, shell, and SA fluorescence, and the various channels were subtracted from each other to produce

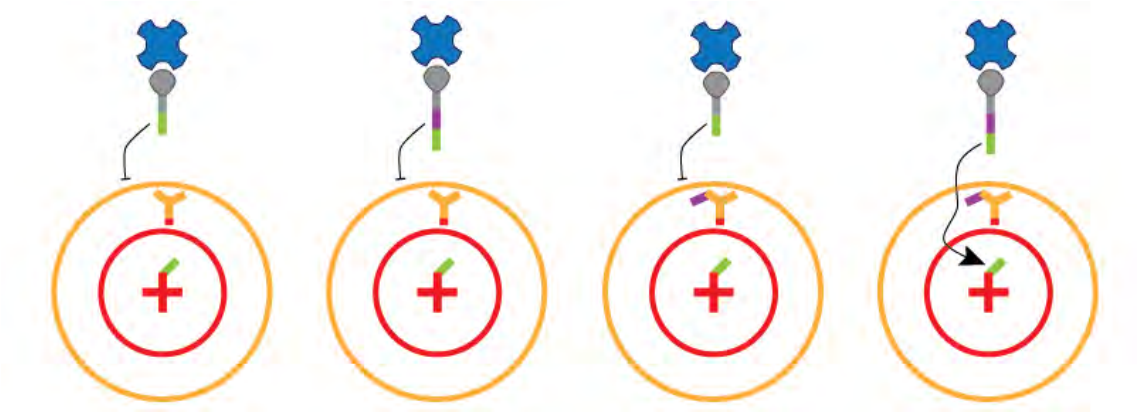

Figure 4.25: Hypothesised streptavidin localisation in core-shell droplets with i and j binding sequences. In an i-4S8 3S10 droplet, i'-SA and i'-j'-SA are not expected to localise in the core due to the shell preventing orthogonal strand infiltration. Similar behaviour is expected in an i-4S8 j-3S10 droplet with i'-SA. In an i-4S8 j-3S10 droplet incubated with i'-j'-SA, the streptavidin may bind to the j-3S10, allowing passage through the shell, and from there be able to localise in the i-4S8 core.

images of the differences (figure 4.26). Considering channels A, B, and C, the degree of co-localisation between A and B can be found by calculating the Pearson correlation coefficient between the subtracted images [A-C] and [B-C]. For instance, to determine if SA is localised in the shell of a droplet, the core fluorescence is subtracted from both the shell and SA channels. If streptavidin is present in the shell, fluorescence will remain in the SA channel after the core subtraction, and so will produce a high degree of correlation to the shell channel. However, if streptavidin was localised solely in the core, then the majority of fluorescence will be removed from the image, and so the correlation between it and the shell will be low. This image processing method was applied to both raw and binarised data.

Image analysis in this manner revealed that i'-SA appeared to compartmentalise in i-4S8 cores, regardless of shell modification (figure 4.27). An i-4S8 j-3S10 core-shell system with i'-j'-SA showed localisation in both the shell ($P_{BW} = 0.69$) and core ($P_{BW} = 0.77$). This is in agreement with section the results of 4.3.3, where SE orthogonality in the shell also did not prevent SA entering the core.

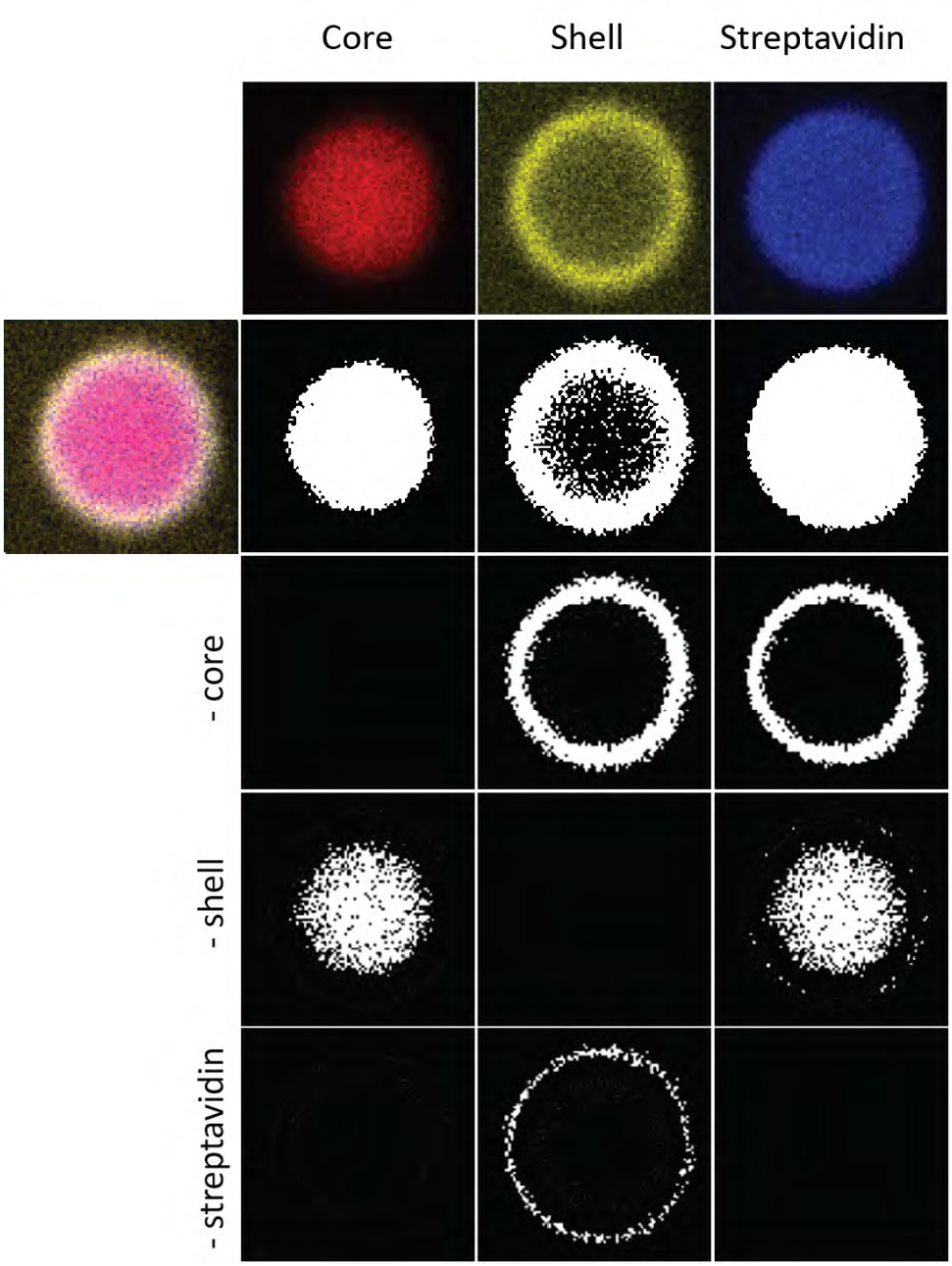

Figure 4.26: Individual channel analysis for quantification of streptavidin localisation. Top row: Image channels of core, shell, and streptavidin. Second row: Binarised image channels. Row 3-5: Binarised core, shell, and streptavidin subtracted from binarised image channels. Localisation of streptavidin in the shell would be calculated as the Pearson correlation coefficient between [shell-core] and [streptavidin-core], such that streptavidin localised in the core region is not considered.

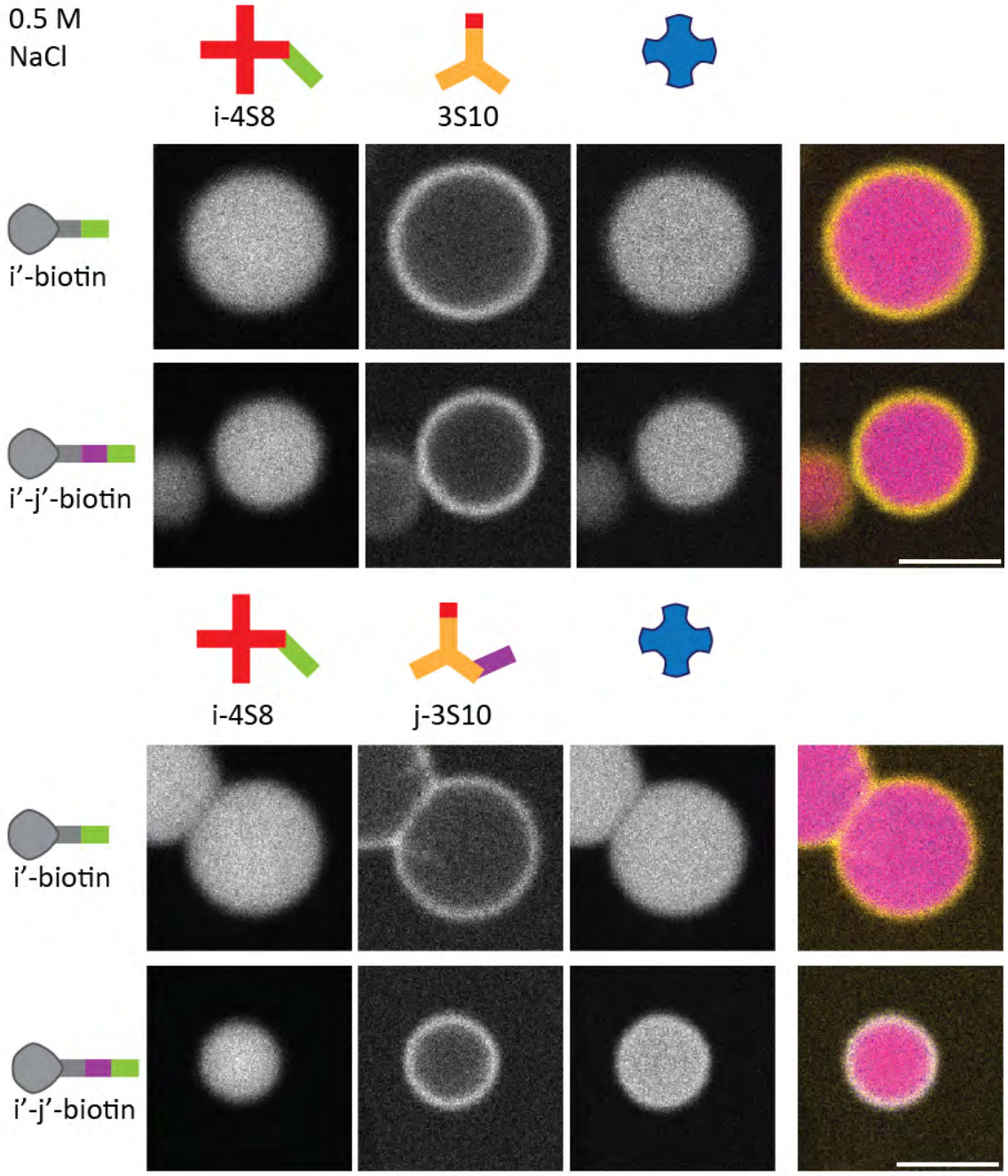

Figure 4.27: Confocal results of experiment outlined in figure 4.25. i'-streptavidin and i'-j'-SA co-localise with the i-4S8 core regardless of shell. Streptavidin also co-localises in the j-3S10 shell when functionalised with i'-j' sequences. Scale bar 5 μm.

Release of binding sequence-localised streptavidin

In a manner similar to the poly-A invader induced switching in section 4.3.3, the release of compartmentalised streptavidin was explored. Streptavidin was localised to an i-4S8 core and j-3S10 shell through the use of i'-j'-SA. An invader strand consisting of the j sequence was then introduced to the solution (figure 4.28). This was expected to compete with j-3S10 binding sequences in binding to the j'-biotin, thereby displacing streptavidin from the shell.

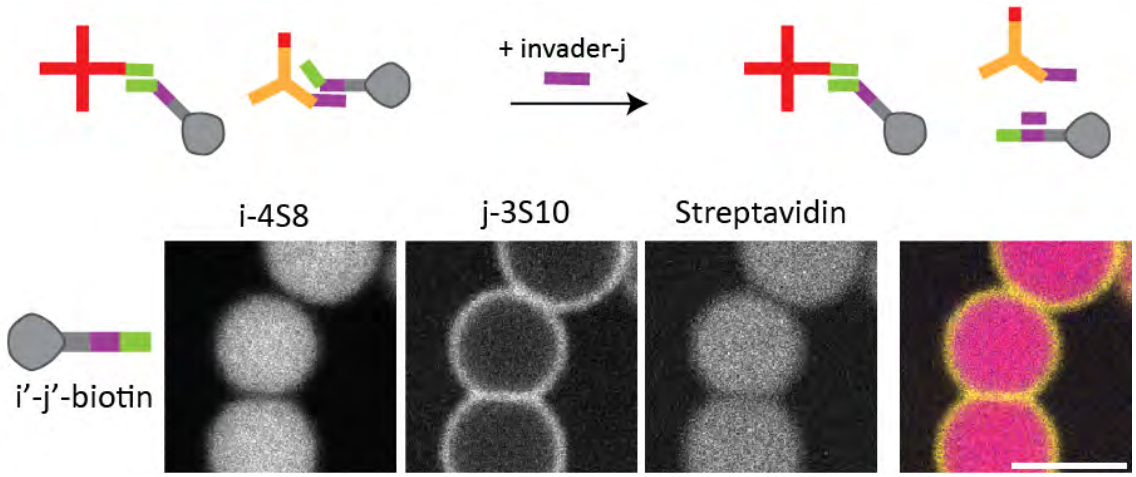

Figure 4.28: Streptavidin localises in the i-4S8 core and j-3S10 shell if functionalised with i'-j' binding sequences 4.27. When a j invader is added to the system and incubated at RT for 3 hours, i'-j'-streptavidin and j-3S10 binding is displaced, removing streptavidin from the shell. Scale bar 5 μm.

Following addition of the invader-j strand, a significant decrease in shell localisation was noted (P_{BW} pre-invader = 0.69, post-invader = 0.38, p < 0.0001). This was accompanied by a slight increase in core localisation of streptavidin (P_{BW} pre-invader = 0.77, post-invader = 0.90, p = 0.0374). This indicates that the invader-j strand was successful in displacing j-3S10 and j'-SA interactions, prompting the transfer of streptavidin out of the shell. This may also account for the increase in core localisation, as the displaced streptavidin would become available for capture in the core.

A typical displacement reaction involves an invading strand of greater complemen-

tarity to the target sequence than the originally bound strand. This may be achieved through the deliberate introduction of mismatched bases, or the truncation of the complementary sequence. Here, the j-3S10 + i'-j'-biotin duplex had a 12-bp complementary region, while the invader + biotin duplex had an 18-bp complementary region (table A.9). The increased length of the complementary sequence in the invader + biotin duplex decreases the free energy of the system, creating a more stable product. Therefore, the formation of an invader + biotin duplex will be favoured over a j-3S10 + biotin duplex. The invader-j sequence included three nucleotides that were complementary to the i region of the i'-j'-biotin sequence. While is is not expected to cause the complete dehybridisation of i-4S8 + biotin duplexes, a slight destabilisation of the duplex is possible.

Analysis of this system in NUPACK was conducted, matching experimental conditions: 5 μM nanostars, including 0.5 μM binding sequence-extended strand 1; 1.5 μM i'-j'-biotin and invader-j; modelled in 0.5 M NaCl at 25 ^{o}C. Analysis was conducted without and with invader-j strands, to match pre- and post-treatment conditions (figure 4.29).

This analysis indicates a significant decrease in j-3S10 + i'-j'-biotin hybridisation upon invader addition. Simultaneously, a significant portion of i'-j'-biotin and invader-j strands were predicted to form a duplexed system (1.48 of 1.5 μM). This simulation does not fully represent the experimental system. For instance, some portion of i'-j'-biotin strands are expected to be compartmentalised in the core, decreasing its availability and increasing the relative concentration of invader-j. Additionally, the NUPACK algorithm is only designed for the analysis of nucleic acids, and therefore cannot take into account electrostatic or steric interference of biotin and streptavidin binding on these systems. Despite this, these results support the experimental observations of invader-triggered strand displacement.

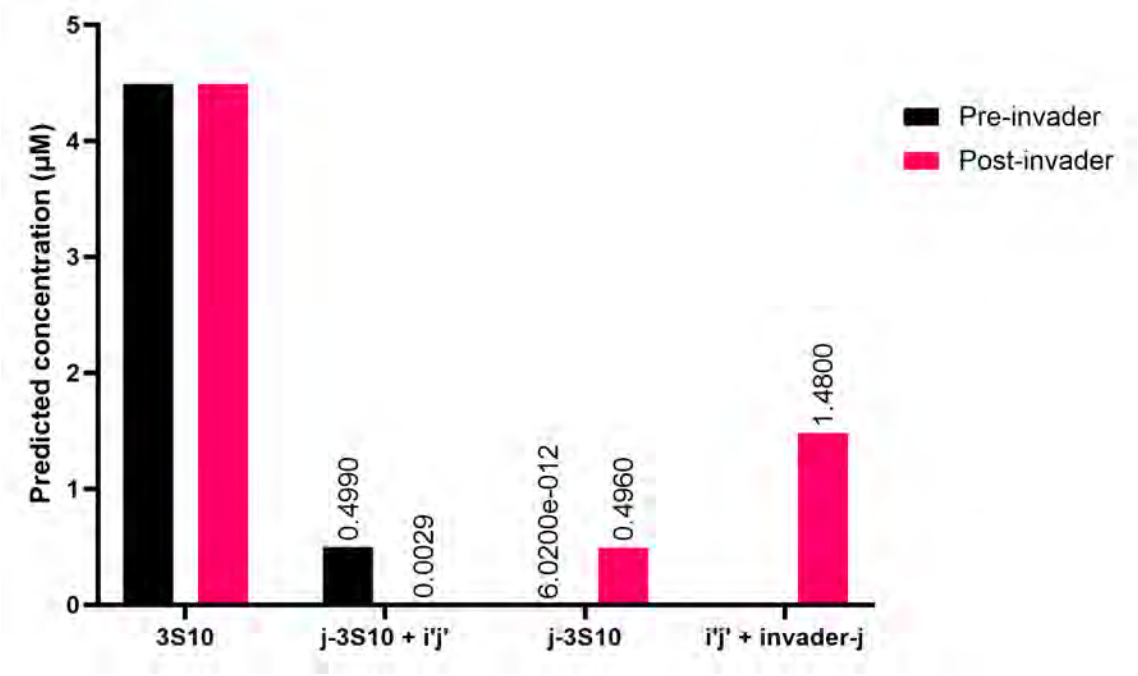

Figure 4.29: NUPACK predictions of 3S10/j-3S10 + i'-j' structure concentration before and after j invader addition. **Pre-invader**, 3S10 and j-3S10+i'-j' are found at a 9:1 ratio, aligning with individual strand concentrations. **Post-invader**, j-3S10+i'-j' is displaced, with i'-j' instead binding to the j invader.

Streptavidin-biotin conjugation prior to droplet mixing

All prior streptavidin compartmentalisation experiments followed the method of annealing droplets, adding SA, followed by biotinylated DNA. The duplexation of biotin-SA is expected to be fast and irreversible, so it was not expected that the order of addition would matter. Under these conditions, it was expected that the un-tagged SA would initially infiltrate throughout the solution; upon addition of biotinylated DNA, these strands would localise to their respective droplet regions, whereupon they would bind to and localise SA. This hypothesis was explored by combining streptavidin with biotinylated DNA for one hour prior to addition to annealed droplet solutions.

In an i-4S8 j-3S10 core-shell droplet combined with i'-SA, cargo compartmentalisation was seen only in the core (figure 4.30). Individual channel analysis revealed no

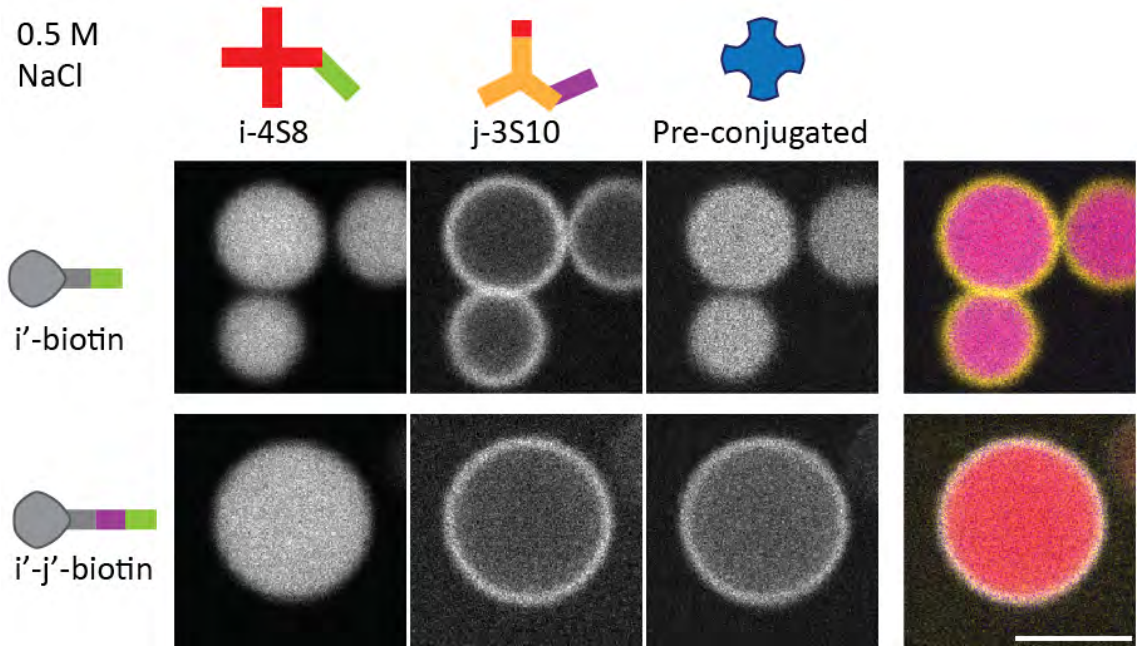

Figure 4.30: Confocal images of i-4S8 j-3S10 core-shell droplets combined with pre-conjugated i'-SA and i'-j'-SA. Results are compared to figure 4.27, where streptavidin and biotin-ssDNA solutions were sequentially added to the droplet solution. i'-SA still sees localisation only in the core. Instead of localising in both core and shell, i'-j'-SA is compartmentalised only in the shell. Scale bar 5 μm.

significant difference in streptavidin localisation when comparing sequential (seq.) and pre-conjugated (PC) streptavidin addition (figure C.17. Both samples had uniformly low shell localisation (P_{BW} seq. = 0.19, PC 0.22, ns) and high core compartmentalisation (P_{BW} seq. = 0.96, PC = 0.95, ns).

When combining i-4S8 j-3S10 core-shell droplets with sequentially added streptavidin and i'-j'-biotin, streptavidin localisation was seen in both the core and the shell (figure 4.27). However, when pre-conjugating the streptavidin and DNA-biotin, streptavidin localisation was seen only in the droplet shell, despite possessing complementarity to the core (figure 4.30). Channel analysis revealed a significant increase in the correlation between shell and SA fluorophores (P_{BW} seq. = 0.69, PC = 0.87, p = 0.002), and a significant decrease in core correlation (P_{BW} seq. = 0.77, PC = 0.35, p < 0.0001) (figure 4.31).

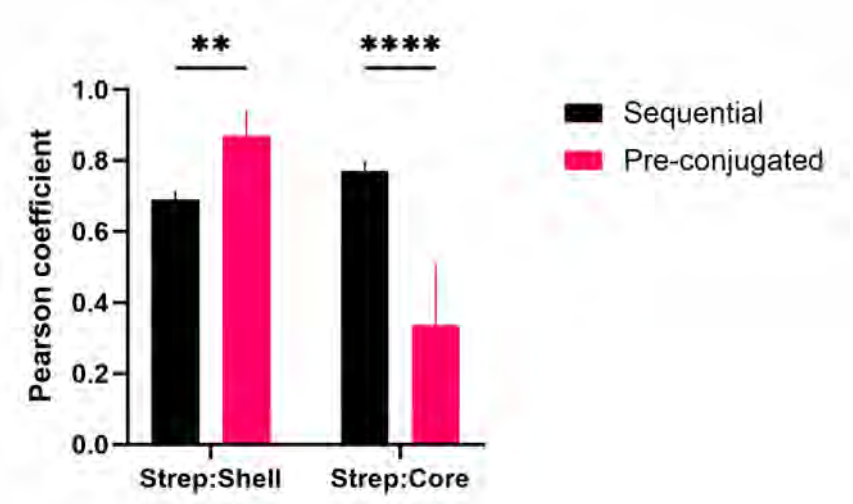

Figure 4.31: i'-j'-SA localisation in i-4S8 core and j-3S10 shell, comparing sequential and pre-conjugated addition. Streptavidin-shell co-localisation significantly increases when pre-conjugating biotin and streptavidin ($p = 0.0020$), while streptavidin-core co-localisation significantly decreases ($p < 0.0001$). Data shown is Pearson correlation coefficient of binarised fluorophore channels. Shell localisation is determined by subtracting core channel from shell and streptavidin, and core localisation is determined by subtracting shell from core and streptavidin. Data shown as average ± SD, n = 4-8.

Until this point, it had been assumed that the shells in NS coacervates would act in a manner similar to cellular membranes. It was hypothesised that core compartmentalisation would only be possible if the cargo possessed an ssDNA sequence complementary to the shell. This drew inspiration from cellular mechanisms such as the nuclear membrane pore, which open only in the presence of recognised structures [209] [210]. In such structures, the membrane is generally impermeable to large, charged molecules. However, membrane-spanning protein complexes have the ability to recognise target molecules and undergo conformational changes, creating a transport channel through the membrane. Passage through this channel is only permitted for molecules of the appropriate properties.

The system developed in this thesis appears to function in a different manner. If a cargo compound is functionalised with a core-complementary sequence, it will compartmentalise in the core. This occurs regardless of the presence of an orthog-

onal shell or the order in which the cargo is functionalised and combined with the system. However, if a cargo molecule is conjugated to core-complementary and shell-complementary sequences prior to addition to a droplet solution, passage into the core will be prevented, with the cargo remaining sequestered in the droplet shell. In this, it appears as though the shell functions as a selective filter, allowing the passage of most infiltrates, but preventing the movement of molecules towards which it has specific affinity.

4.4 Fluorescence Resonance Energy Transfer assays as a measure of droplet mixing

Aim 4 of this thesis proposed the investigation of dynamic reactions in core-shell droplets. Thus far, static functionalities of phase separation, stabilisation, and cargo capture were demonstrated. Limited dynamic functions have been demonstrated in the triggerable release of captured cargo. Further functions may be explored to develop a microreactor system of practical use. These include inciting mixing of encapsulated cores following the dissolution of shells; de-mixing of co-localised droplets; or demonstrating the switching of captured cargo locations. Additionally, the understanding of the energetics of nanostar coacervates may be further developed through quantification of their gelation temperatures (T_g). Each of these proposed reactions may be visually observed through confocal microscopy. However, this is a low-throughput method. A method was thus desired for the simultaneous analysis of multiple samples.

Each of the listed dynamic functions may be monitored through the co-localisation or de-mixing of fluorophores. For instance, a shift in the compartmentalisation of streptavidin between shell and core may be measured as a change in the co-localisation of their respective fluorophores. This physical shift in localisation may be measured through Fluorescence Resonance Energy Transfer (section 1.5.3).

It was hypothesised that FRET may be used to monitor the mixing of nanostar droplets or the localisation of cargo. Given the assumption that the nanostar droplets produced in this thesis undergo a liquid-gel transition, an experimental system was proposed for the identification of this transition temperature (section A.20). If two droplet solutions of identical nanostars were separately annealed and functionalised with different fluorophores, they could be combined and monitored for

mixing. One nanostar population would be functionalised with a donor fluorophore, and the other with the appropriate acceptor. At temperatures $< T_g$, the droplets would be gelated, and nanostars possessing different fluorophores would largely stay separated. If the system was heated, T would eventually surpass the T_g and droplet fusion would be initiated. By monitoring the fluorescence of the donor and acceptor alongside temperature increase, the onset of FRET would signal the intermixing of the two droplet populations. Such an analysis could be performed in a bulk plate reader assay, allowing the simultaneous analysis of multiple systems. This would allow a high-throughput method of estimating droplet gelation temperature. It could additionally allow for monitoring of shell dissolution and core mixing; de-mixing of co-localised cores; or the transfer of compartmentalised cargo.

FRET assays were designed as a proof-of-concept method to determine the gel-liquid transition temperatures of several nanostar droplets (table 4.2). The degree of nanostar gelation at a given temperature appears to scale with both valency and SE strength (section 2.5.1) [24] [165]. Thus, two nanostars of theoretically distinct T_g were chosen, 3S6 and 4S10. Previously, 3S6 droplets had been shown to have high rates of fluorescence recovery at 21 ^{o}C, indicating high internal mobility, and a high degree of deformation, suggesting a low surface tension. Conversely, 4S10 droplets had been shown to have a low internal mobility and high surface tension. Together, these values suggest that at 21 ^oC, 3S6 droplets are near or above their T_g, and 4S10 droplets are below their T_g.

Nanostar droplets were produced under two different conditions. Either Cy3 and Cy5 nanostar solutions were prepared and annealed separately, and mixed immediately prior to the FRET, or the solutions were premixed prior to annealing. The latter condition was expected to produce mixed-fluorophore droplets, which were predicted to produce an immediate FRET response. Conversely, the separate annealing production method would result in separate droplet populations. These were

	Nanostars	Preparation	FRET expected	FRET temperature
1	Cy3 3S6, Cy5 3S6	Premixed, annealed	Yes	Immediate
2	Cy3 4S10, Cy5 4S10	Premixed, annealed	Yes	Immediate
3	Cy3 3S6, Cy5 3S6	Annealed separately, mixed	Yes	Low
4	Cy3 4S10, Cy5 4S10	Annealed separately, mixed	Yes	High
5	Cy3 4S6, Cy5 3S6	Annealed separately, mixed	Yes	Low
6	Cy3 4S10, Cy5 3S6	Annealed separately, mixed	No	-
7	Cy3 4S8, Cy5 3S10	Annealed separately, mixed	No	-
8	Cy3 4S8 3S10 Cy5 4S8 3S10	Annealed separately, mixed	No	-

Table 4.2: Systems investigated in FRET plate reader assays, with expected results and predicted FRET reaction temperature.

expected to fuse and produce a FRET response when the solution temperature rose above the droplet T_g.

The assay compared a number of different nanostar droplet combinations. Solutions of 3S6 nanostar droplets were expected to have a low T_g, thereby fusing and producing a FRET response at a low temperature. Solutions of 4S10 droplets were expected to produce a response at a high temperature, with the higher valency and stronger SEs causing a higher T_g. Both of these nanostar combinations were prepared under premixed and separate annealing conditions, with the premixed condition expected to produce an immediate FRET response as a control value. In order to test mixing of different star bodies with complementary SEs, 3S6 and 4S6 nanostars droplets were combined, and expected to exhibit mixing at a low temperature. Orthogonal nanostar systems were also tested, combining 3S6 and 4S10 nanostars, or 4S8 with 3S10 nanostars, and were not expected to produce a FRET signal. Finally, two 4S8

3S10 core-shell solutions were produced, with non-fluorescent shells and either Cy3 or Cy5 cores. The presence of the shells was expected to inhibit core mixing, even when the system temperature increased above 4S8 T_g, and thus the sample was not expected to produce a FRET response.

The results of the above assays are shown in figure 4.32. The fluorescence of individually excited and detected Cy3 and Cy5 fluorophores are reported as baseline values. In addition, the fluorescence of Cy3 and Cy5 when only Cy3 was excited are shown. A positive FRET signal is expected to take the form of the FRET emission deviating from the baseline emission. A decrease in FRET Cy3 emission and an increase in FRET Cy5 emission would indicate a FRET reaction occuring in the sample. All samples see a gradual decrease in sample fluorescence with increasing system temperature. No change in FRET signal was noted for any system, with all maintaining a consistently low FRET Cy5 emission.

These results would imply that droplet mixing does not occur in any analysed sample within the given temperature range. However, pre-mixed droplets did not exhibit any significant difference in fluorescence intensity when compared to separately annealed droplets. Pre-mixed systems were used as a baseline control as, upon annealing, they produce microscale droplets with homogeneously distributed Cy3 and Cy5 fluorescence. The lack of any detectable FRET response even in pre-mixed systems implies that fluorescence resonance energy transfer does not occur between droplet nanostars in the current system design.

The droplets used in this system are functionalised with fluorophore strands by appending a binding sequence to a non-SE end of an NS arm. This results in a 45-nt length distance between nanostar and fluorophore, with a 24-bp dsDNA sequence and 21-nt ssDNA. This design was chosen such that the presence of a fluorophore would not impact SE-SE binding, by creating a large distance between SE and

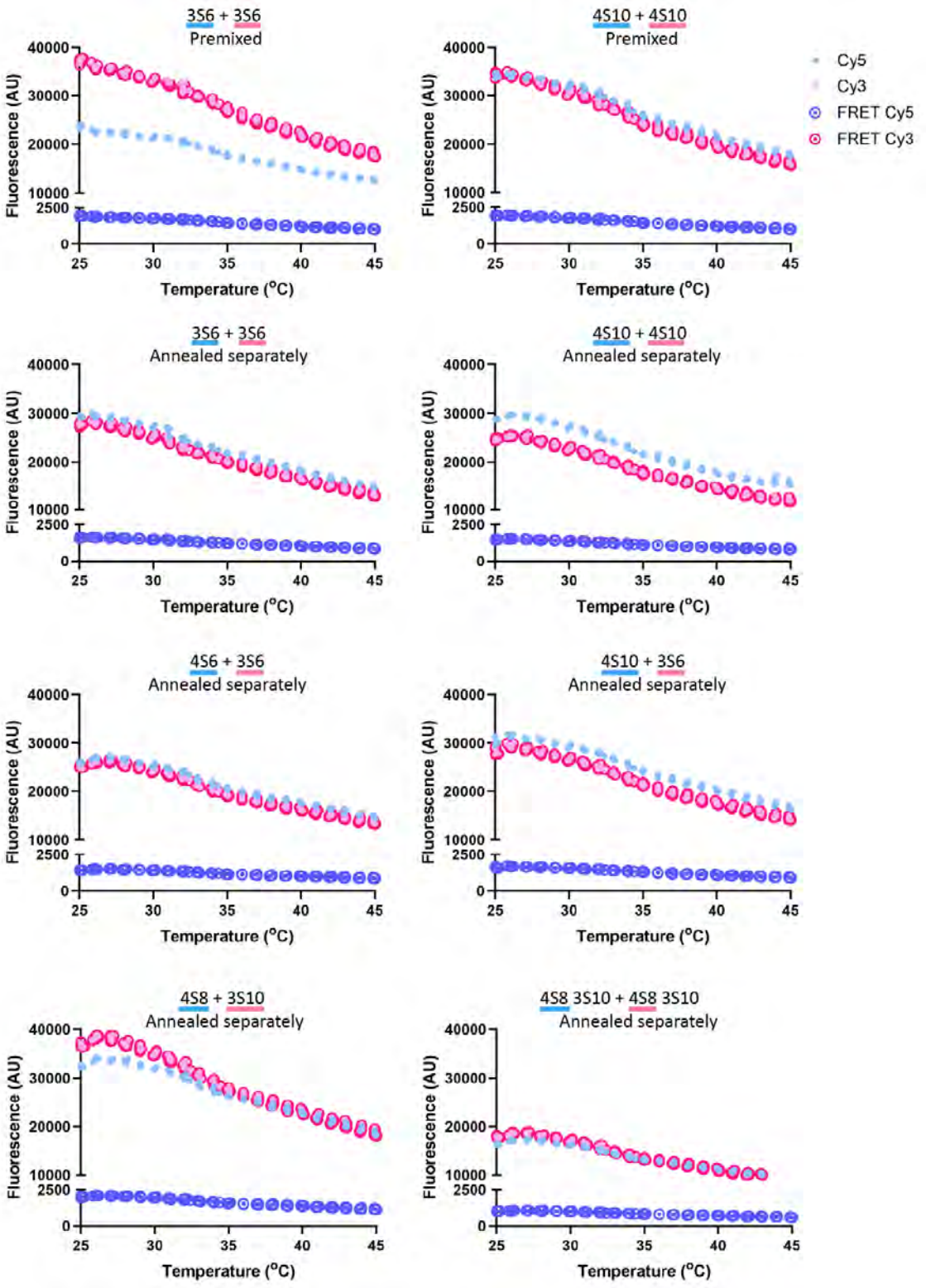

Figure 4.32: Fluorescence intensity at increasing temperatures, as outlined in table 4.2. Cy3 and Cy5 fluorophores were independently excited to provide a baseline. The FRET reaction was conducted by exciting the system at 520 nm, and detecting the FRET Cy3 and FRET Cy5 traces. No FRET response was seen under any experimental condition.

fluorophore. However, this also means that the dimerisation of two fluorophore-modified nanostars may not necessarily bring the fluorophores into close physical contact. As less than 10 nm distance between donor and acceptor is generally required for energy transfer to occur, this flexibility in the design may account for the lack of detected FRET signal.

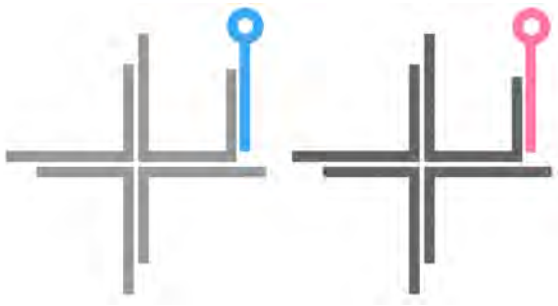

Figure 4.33: Method of fluorophore attachment to nanostars. An ssDNA binding sequence is appended to the 3' end of a nanostar strand. The complementary sequence is functionalised with a Cy3 or Cy5 fluorophore, resulting in fluorophore attachment to the nanostar.

If two nanostars were to meet in solution and hybridise via their SEs, there are seven possible conformers which may form (figure 4.34). Each conformer was assumed to be equally likely, and weighting was calculated as the number of NS-NS interactions that could produce the conformer. These represent a wide range of possible fluorophore-fluorophore distances, with predicts geometric distances between 10 - 57 nm. However, DNA nanostars are not geometric objects, and do not form stiff, linear structures. The possible fluorophore placements were modelled using oxDNA, and the distances between fluorophores calculated. The simulations were conducted using VMMC at 0.5 M [Na^+] and 25 ^{o}C.

The results of simulating fluorophore-fluorophore distances in nanostar dimers are shown in figure 4.35. Nanostars in this work possess high structural flexibility, due to the unpaired bases present at the central junction and SE hinges. In addition, the fluorophore connector system includes a ssDNA sequence, which has a persistence length of approximately 2 nm, in comparison to the 50 nm of dsDNA [178]. These

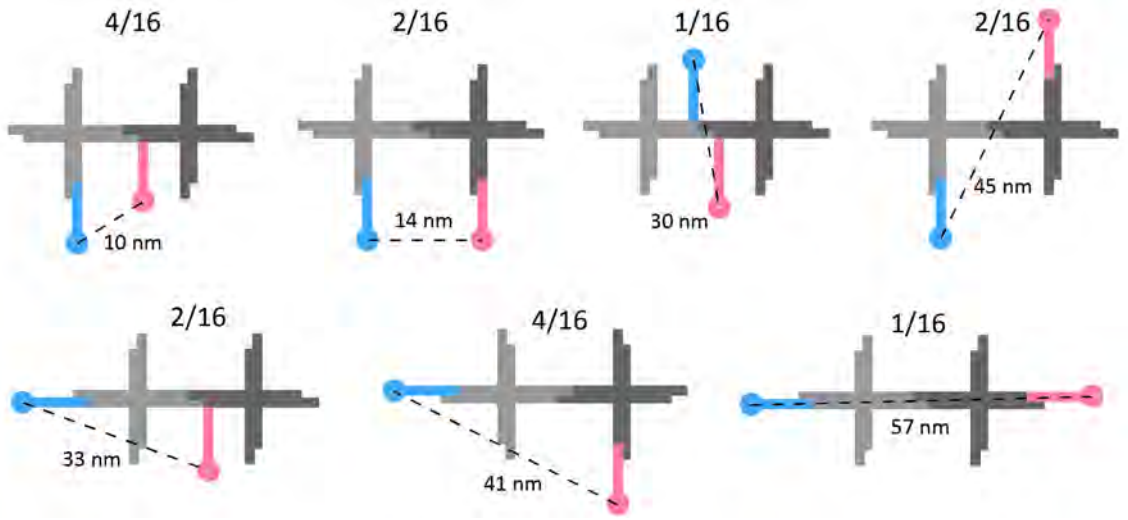

Figure 4.34: When two fluorophore-functionalised nanostars dimerise in solution, there are sixteen potential attachment patterns. Due to the symmetry of nanostar SEs, this results in seven possible conformers of varying probabilities. Conformers are shown with their respective probabilities. Possible fluorophore conformers and distances are highlighted.

considerations combine to create a wide range in simulated fluorophore-fluorophore distances, ranging from 4.45 - 51.9 nm (figure C.18). When weighted by the relative probabilities of the seven dimer conformers, the average inter-fluorophore distance was found to be approximately 29.7 nm. The R_0 of a Cy3-Cy5 FRET pair is 5.4 nm [211]. As described in section 1.5.3, an increase in R_{DA} beyond R_0 leads energy transfer efficiency to rapidly approach zero. Therefore, a system in which the average R_{DA} is 29.7 nm is not expected to have high transfer efficiency.

These simulations suggest that FRET is likely not physically able to occur between dimerised nanostars under the current design. In a phase separated coacervate, nanostars are densely packed, potentially reducing the mean distance between fluorophores. However, preliminary experimental results indicate no FRET reaction occurred, even between pre-mixed droplets. Thus, the current system would likely be ineffective at detecting the fusion or de-mixing of droplets, or the shifting of compartmentalised cargo. To address this limitation, a modification to the nanostar design is proposed in the following chapter (section 5.2.1).

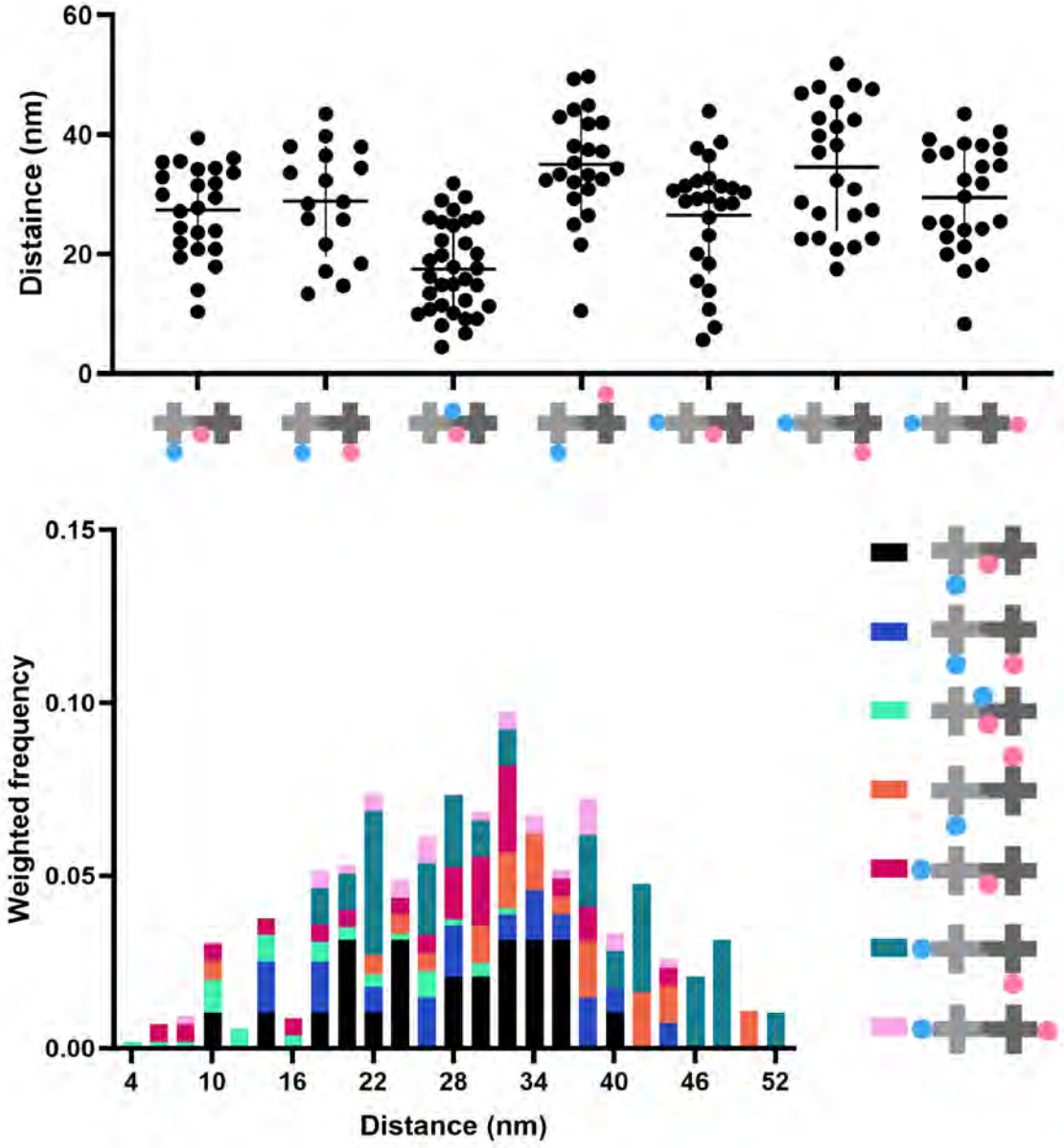

Figure 4.35: Distributions of computationally predicted fluorophore-fluorophore distances in the seven possible dimer conformers. **Top**: Measured distances between fluorophores, shown as individual values with mean and SE. $n = 20$. **Bottom**: Histogram of measured fluorophore distances, weighted by the probability of dimer structure.

4.5 Summary and conclusion

In this chapter, several cell-like functions of core-shell nanostar coacervates were explored, in line with Aim 3 of this thesis.

Sections A.17 and 4.2 continued investigations into NS droplet micro-architecture formation. Aim 3.1 addressed the creation of distinct organelles within core-shell coacervates. The formation of nested co-continuous and three-layered structures was demonstrated, increasing the complexity of available coacervate systems. Further investigation into these systems is required, particularly in the degrees of complementarity between phases, cation effects, and the comparative strength of inter-star bonds. This would allow for further understanding and manipulation of nanostar coacervate systems. This knowledge could potentially be applied to cellular phase separating systems, or be used in the development of synthetic cells. Designs for switchable micro-architectures are developed in section 5.2.2, describing the triggerable formation of organelles in a DNA nanostar synthetic cell.

The passive control of cargo capture in synthetic cells, Aim 3.2, was demonstrated in section 4.3. Numerous methods of control over biomolecule cargo capture in core-shell nanostar droplets were demonstrated. The presence of a dense shell reduced the rate of passive infiltration into the core of a droplet (section 4.3.1). This was thought to occur in a manner akin to volume fraction-mediated solute partitioning in dense polymer solutions, wherein the pore size available for solute infiltration is determined by the random thermal movement of polymer strands. When attempting directed compartmentalisation of cargo compounds, streptavidin molecules were functionalised with an ssDNA binding sequence. This, here termed positive functionalisation, allowed for cargo capture in selected regions of nanostar droplets (sections 4.3.3 and 4.3.4). The portion of total cargo concentration that was captured in the droplet may also be controlled by the degree of functionalisation of the cargo

molecule (section 4.3.3) or the functionalisation of the target nanostars (figure 4.24).

Active control over cargo compartmentalisation was demonstrated, in accordance with Aim 3.3 and Aim 4. The shell was used to actively prevent the compartmentalisation of targeted cargo molecules (section 4.3.4), here termed negative functionalisation. It appeared that negative functionalisation in the shell superseded positive functionalisation in the core, preventing the infiltration of core-targeted compounds. Dynamic systems were demonstrated through the targeted release of captured streptavidin (section 4.3.3 and 4.3.4). Further development of this functionality is discussed in section 5.2.2, in presenting a design for the cyclical switching of streptavidin compartmentalisation.

Finally, Aim 4 drove a method for the monitoring of droplet fusion or cargo compartmentalisation was proposed in section 4.4. Contrary to expectations, FRET response was not found to differ between mixed and separated droplet solutions. Investigation of fluorophore dimer conformers via Virtual Move Monte Carlo simulations was conducted. It was proposed that the current nanostar design is not conducive to the fluorophore spacing required for FRET reactions. Thus, alternative nanostar designs are proposed in section 5.2.1.

The work in this chapter successfully demonstrated higher-order organisation in nanostar coacervates through an increase in micro-architecture complexity. The passive exclusion of infiltrates was demonstrated, with the degree of exclusion tunable with the density of the shell nanostar mesh. Further exploration of this area is warranted. The passive recruitment of functionalised cargo was also demonstrated, with a variety of targeting methods, sequences, locations, and concentrations. Finally, active control over cargo capture was demonstrated, with the selective exclusion or release of compartmentalised cargo. These results set the stage for future works proposed in the following Chapter.

Chapter 5

Conclusions and future works

The central aim of this thesis was the development of a method for the formation of core-shell nanostar droplets. This overarching aim then defined the research aims of each chapter presented herein. The results of these aims and the conclusion of this research are presented below.

Aim 1: Develop understanding of DNA NS droplets by varying the physical characteristics of nanostars

The first aim of this work prompted the investigation of the physical properties of DNA nanostar droplets. Chapter 2 details this research, with nanostars of varying arm length, valency, and binding strength compared. It was found that an increase in nanostar size reduced the mesh size and fluidity of droplets, when varying either the number or length of nanostar arms. The internal fluidity and surface tension of droplets were also found to vary with increasing SE binding strength, with a decrease in NS mobility and an increase in surface tension.

A technique was developed for experimentally determining the phase separation temperature of nanostars. It was found that nanostar arm length did not affect

T_{PS} between 16-23 nt. An increase in the number of nanostar arms from $f = 3$ - 4 was found to lead to droplet formation at a higher temperature. The trends in measured phase separation temperature appeared linked to sticky end binding strength. Trivalent nanostar T_{PS}s approximately aligned with the predicted T_M of their respective sticky ends, while tetravalent nanostars underwent phase separation at higher temperatures. Thus, the thermodynamics of nanostar phase separation and the physical properties of the resulting droplets were explored.

A method was proposed for the experimental determination of droplet gelation temperature, and the monitoring of droplet mixing. Initial experiments in Chapter 4 revealed current star designs are incompatible with the proposed method, and variations in star design are thereafter presented.

Aim 2: Investigate the formation of micro-scale architectures in nanostar droplets

The second aim of this thesis was the development micro-scale architectures in nanostar droplets, particularly core-shell droplets. A systematic investigation of different nanostar combinations was conducted in Chapter 3. Separation of orthogonal nanostar droplets was demonstrated, alongside the mixing of nanostars of distinct size and complementary SEs. It was found that, within the range of values explored, nanostar size did not impact droplet homogeneity when functionalised with complementary SEs. This was contrary to expectations, which predicted the size-based separation of nanostars. When combining orthogonal nanostars, the difference in phase separation temperature was not found to impact the formation of distinct droplet populations. Simultaneously, different nanostars with complementary sticky ends were combined. It was found that regardless of a difference in T_{PS}, complementary nanostars would form mixed droplets.

Nanostar combinations were explored when increasing the degree of complementar-

ity between nanostar populations, through the selective replacement of NS sticky ends. A model was developed for the prediction of patchy or core-shell droplet formation, based on nanostar functionalisation and droplet formation temperature. In nanostar pairs with a low difference in ΔT_{PS}, patchy droplets were found at 16 %C in trivalent-tetravalent systems, or at 25 %C in tetravalent-tetravalent systems. When ΔT_{PS} was increased, core-shell structures were instead produced at these degrees of complementarity.

Three-star droplets were briefly investigated in chapter 4, with further designs proposed in chapter 5. Complex emulsion architectures were demonstrated, including a nested co-continuous structure and three-layer droplet with a patchy interface.

Aim 3: Demonstrate chemical addressability and system stability in core-shell droplets

The core-shell systems were tested for long-term stability. Bare droplets systems, when incubated under conditions of high fluidity, were shown to fuse over time, forming amorphous, mixed structures. When the fluid droplets were encapsulated in a shell, fusion of the cores could be prevented. Future work in this area should include investigations of the filtering capacities of different shells, in modulating the degree of transfer between encapsulated cores.

The presence of a dense nanostar shell was shown to inhibit the passive infiltration of cargo. Core-shell nanostar droplets were shown to possess independently addressable regions when actively compartmentalising functionalised cargo. Streptavidin was shown to localise in either the core or shell of appropriately functionalised droplets. The degree of encapsulation could be modulated by varying the degree of functionalisation of the cargo. A selective filter was demonstrated by creating a system in which a core-directed streptavidin could be excluded from the droplet core by being captured by the droplet shell.

The release of captured cargo was demonstrated through strand-displacement reactions in chapter 4. This functionality was expanded upon in Chapter 5, with designs proposed for the cyclical switching of streptavidin compartmentalisation location. These designs were computationally investigated and validated.

A method was also proposed for the switching of micro-scale architectures through a strand displacement reaction. This system would see a core-shell droplet undergo secondary phase separation in the core, forming chemically distinct organelle regions bound by an outer core. The design was computationally investigated and optimised.

5.1 Final conclusions

The central goal of this thesis was the formation of core-shell nanostar droplets. This goal was successfully achieved. A model describing the formation of core-shell structures was developed, and successfully applied to the formation of over twenty core-shell nanostar combinations. The stability, functionality, and addressability of these systems were then demonstrated. Future avenues of research are proposed below.

5.2 Future work

While the aims of this thesis were largely met, there exist many possible fields of inquiry which could expand upon the results of this work. These may be summarised in three broad directions. First, further investigation of the physical characteristics of nanostar coacervates is warranted. This would provide insight into the phase separation of multi-valent nanostars, and potentially allow for the development of a model LLPS system. Second, as has been previously mentioned, additional dynamic functionalities may be developed. Controllable switching of the chemical addressability or physical properties of nanostar coacervates would heighten their utility as micro-reactors. Finally, this work may be used in the development of an artificial cell, to replicate and explore the physical behaviour of biological systems. Leukocytes are a vital aspect of the immune system, and undergo significant structural changes in their lifespan. The creation of a synthetic leukocyte would allow for enhanced understanding of the interactions and motion experienced by micro-particles in a biological environment.

5.2.1 Investigation of the physical characteristics of nanostar coacervates

Work in Chapter 2 of this thesis developed a method to determine the nanostar formation and phase separation temperatures of LLPS droplet systems (section 2.6). The subsequent formation of two-layer nanostar droplets depended on this technique, as it allowed estimation of the formation temperature profiles of nanostars. Following formation, the various practical uses of these droplets are enabled by their physical characteristics. These features, such as fluidity, surface tension, and internal viscosity, have been found to be affected by the structure of nanostars and the environmental conditions in which the droplets were formed. However, these physical characteristics were only indirectly observed, through substrate contact angle

(section 2.5.1), fluorescence recovery (section 2.5.2), and propensity towards fusion (section 3.7). Methods of more directly measuring these properties would provide a more comprehensive understanding of the system, enabling future applications.

Modifications of nanostar design to allow for Fluorescence Resonance Energy Transfer

These simulations suggest that FRET is likely not physically able to occur between dimerised nanostars under the current design. In a phase separated coacervate, nanostars are densely packed, potentially reducing the mean distance between fluorophores. However, preliminary experimental results indicate no FRET reaction occurred, even between pre-mixed droplets. Thus, the current system would likely be ineffective at detecting the fusion or de-mixing of droplets, or the shifting of compartmentalised cargo. To address this limitation, a modification to the nanostar design is proposed in the following chapter (section 5.2.1).

Experimental work in section 4.4 attempted to develop a FRET assay to identify mixing between nanostar droplets. The physical design of of the nanostars used, particularly in the connection between fluorophore and nanostar, resulted in no FRET response detected under any experimental condition. Thus, a modification to the nanostar design is proposed below.

Buckhout-White *et al.* comprehensively studied Cy3/Cy5 FRET pairs in DNA nanostructures, varying the distance between fluorophores and the ratio of donors to acceptor [211]. They found the Förster distance between the two fluorophores to be 5.4 nm, and determined that FRET efficiency rose when decreasing the distance between donor and acceptor from 1.5xR_0 (8.1 nm) to 0.75xR_0 (4.05 nm). They varied the ratios of donor to acceptor by designing a number of DNA nanostructures, from a simple linear dimer (1:1 D:A ratio) to an eight-armed nanostar with donors at the terminus of each arm and an acceptor at the central junction (8:1 D:A). They

found that in comparison to a reference system of 1:1 D:A with 8.1 nm, a four-armed nanostar of arm length 4.05 nm and 4:1 D:A saw a 60x increase in acceptor fluorescence output. A decrease in donor:acceptor distance always led to an increase in FRET efficiency, while an increase in D:A up to 4:1 also increased efficiency. It must be noted that their nanostar designs did not include sticky ends, and thus the systems did not undergo phase-separation, resulting in a dilute system.

The design of Buckhout-White *et al.* may be adapted to the nanostar systems studied in this work. The arm length of an *S* nanostar is 16 bp, or 5.44 nm (section 2.3). An acceptor fluorophore may replace one unpaired base in the central junction of a nanostar, and the complementary donor fluorophore placed at the end of an SE on a secondary nanostar. If the two nanostars hybridise via their sticky ends, the distance between donor and acceptor would closely align to the Cy3/Cy5 Förster distance of 5.4 nm. The multivalency of nanostars could allow a 3:1 or 4:1 donor:acceptor ratio, further multiplying FRET efficiency. At a distance of 5.4 nm and a 4:1 D:A ratio, Buckhout-White *et al.* saw a $\sim$30X enhancement in Cy5 FRET fluorescence.

It is proposed that the sticky end of one nanostar could be appended with a 3' fluorophore modification, while a second nanostar could have a central junction ssDNA thymine base replaced with a FRET-paired fluorophore. VMMC simulations were conducted on a 4S8-dimer system, at 25 ^{o}C and 0.5 M [Na^{+}]. The distance was calculated between the terminus of the star 1 SE and each of the eight possible positions in the central junction of star 2 (figure 5.1). The closest position, P8, was found to have a mean distance of 6.82 $\pm$ 0.55 nm, while the furthest, P5, had a distance of 7.89 $\pm$ 0.88 nm. Therefore, given the fluorophore-appended SE of nanostar 1 binds to nanostar 2, the simulation data suggests the mean distance between fluorophores will within 1.5xR_0, allowing for possible FRET reactions.

If NS1 and NS2 are both tetravalent stars, 25% of fl-NS1 and fl-NS2 binding events

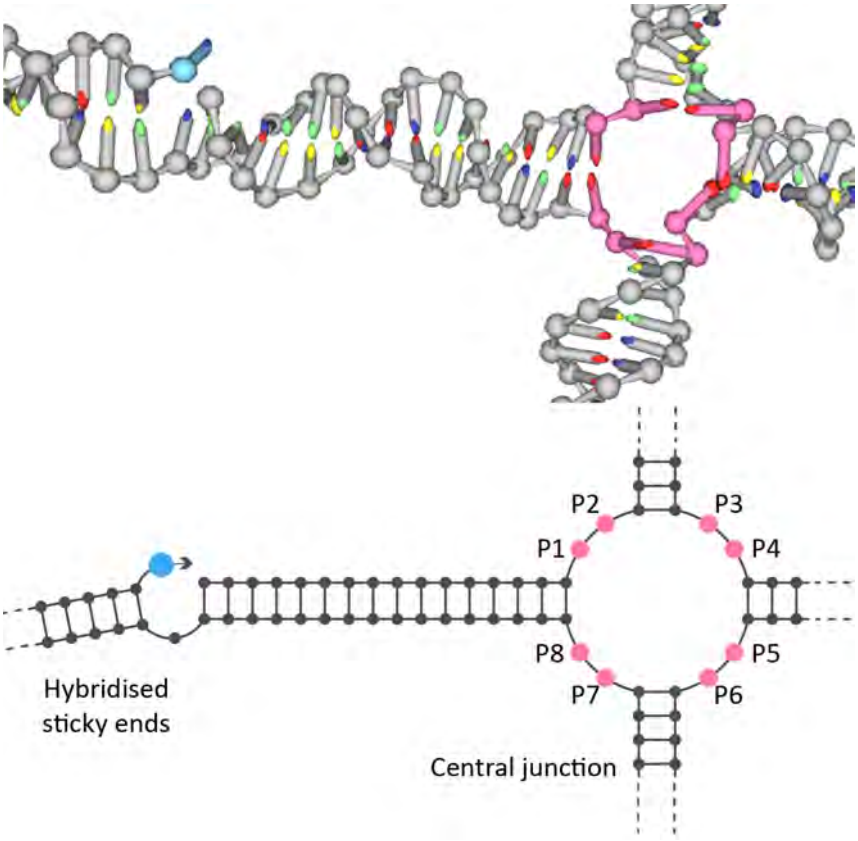

Figure 5.1: Proposed positions of SE appended (blue) and central junction (pink) fluorophores in a dimerised nanostar pair.

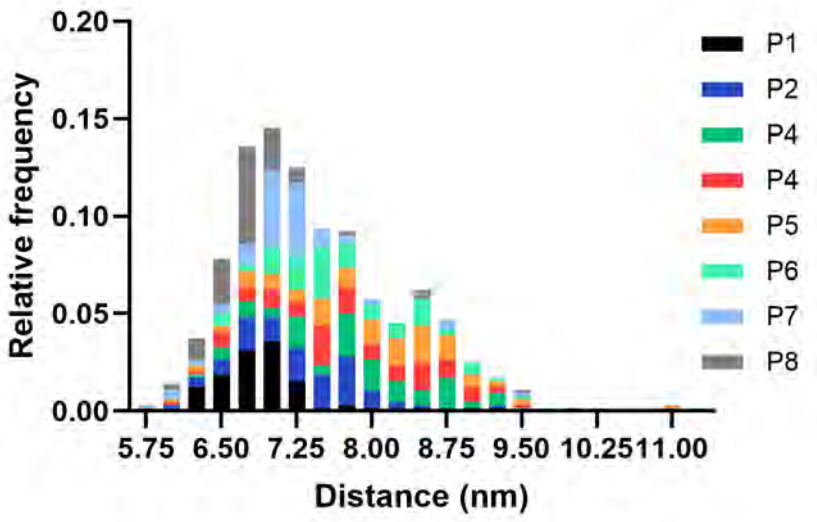

Figure 5.2: Distributions of computationally predicted fluorophore-fluorophore distances in an SE-central junction functionalised dimer system. Histogram of distances, separated by junction fluorophore position, n = 80.

will achieve the correct orientation to allow FRET reactions. In the current experimental system, 1% of nanostars are functionalised with fluorophores. If unmodified and fluorophore-functionalised nanostars have an equal chance of binding to one another, this results in 2.5x10^{-5}% of NS-NS binding events resulting in a FRET reaction. Buckhout-White *et al.* produced 16-nt arm length tetravalent nanostars with an acceptor fluorophore in the central junction and donor fluorophores on each arm terminus [211]. This resulted in a 4:1 D:A ratio, and significantly increased FRET efficiency. Given the multivalency of nanostars explored in this system, similar effects may be expected to be seen. However, the likelihood of five fl-nanostars hybridising in the correct orientation to allow such an interaction is vanishingly small. Therefore, in addition to the proposed modification of fluorophore placements, the fluorophore content of nanostar droplets would likely need to be increased in order to see any significant FRET signal.

The system used in this thesis includes a 1% concentration of fluorophore-functionalised nanostars. Similar nanostar coacervates in the literature use between 1-10% fluorophore content [25] [24] [149] [27]. No distinct difference in coacervate behaviour is noted between their results. However, a further increase in fluorophore concentration may affect the phase separation of nanostars, due to steric or hydrostatic interference. Additionally, Jahnke *et al.* have computationally and experimentally demonstrated a significant shift in ssDNA secondary conformations, depending on the fluorophore with which they are functionalised [212]. Directly modifying the terminus of a ssDNA sticky end may adversely affect the binding efficiency of the nanostar, impacting the phase separation of the system.

Alternatively, instead of modifying an SE terminus and a central junction, the termini of both nanostars could be functionalised with fluorophores. This would greatly reduce the distance between fluorophores - for instance, 3.06 nm in an 8-nt SE system. However, this modification would reduce the proportion of FRET-inducing

binding events between nanostars to just 6.25% of fl-NS1 fl-NS2 hybridisation events. It would also preclude the possibility of multiplying FRET efficiency through increase D:A ratios. Therefore, it is anticipated that an SE-modified junction-modified system, despite the higher distance between fluorophores, would still see a higher overall FRET signal when measured in bulk in a plate reader.

If the proposed system modifications result in an increase in FRET reaction efficiency, a FRET detection system may be used to identify the temperature at which mixing occurs between droplets. This would potentially allow for the identification of droplet gelation temperatures, providing further insight into nanostar system energetics. FRET may also allow quantitative analysis of droplet behaviours such as streptavidin capture; transfer of cargo between cores; or the efficacy of shells in separating cores during heating.

Investigation of droplet viscosity

The internal viscosity of nanostar coacervates can provide insight into SE-SE bond strengths and the liquid-gel state of the droplet. These values were previously investigated using Fluorescence Recovery After Photobleaching, which provides information on the mobility and transfer of nanostars through a droplet (section 2.5.2). This work could be further expanded upon using microrheology, a school of techniques that track the movement of tracer particles through a fluid [213] [214]. Under static conditions, thermal energy will drive Brownian motion. If the fluid is sufficiently viscoelastic, movement of the tracers will be detectable. Microrheological methods track this motion and calculate the mean square displacement of tracer particles over time. This measurement can be used to calculate the viscosity and shear modulus of the fluid.

Jeon *et al.* used this technique in measuring the viscosity of nanostar droplets in varying NaCl concentrations [30]. Fluorescent nanoscale beads were combined in

solution alongside nanostar droplets, resulting in the passive encapsulation of the 200 nm beads. The MSD of the beads was determined using confocal microscopy, which could then be converted to a measure of viscosity using the Stokes-Einstein equation.

Similar techniques could be utilised in measuring the viscosity of nanostar droplets in this work. This would allow quantitative determination of droplet fluidity as it relates to the physical characteristics of nanostars, namely their valency, arm length, and SE binding strength. The relationships between droplet deformability, surface tension, and internal viscosity could then be calculated.

Physical requirements in forming core-shell structures

The degree of complementarity between nanostars appears to contribute towards micro-architecture structure (section 3.5). The required surfactant modifications were experimentally determined as 25 %C in tetravalent stars and 16 %C in trivalent stars, when forming shells around a tetravalent core. When introducing complementarity in the core towards the shell, the degree required remained at 25 %C in tetravalent-tetravalent pairs, but appeared to fall somewhere between 16-20 %C in tetravalent-trivalent pairs (figure 3.21).

While these values appeared to apply to all tested systems, further interrogation of this phenomenon is warranted. If further variation upon nanostar valency was developed, the degrees of complementarity between these systems could be investigated. The requirements for specific micro-architectures could be explored, determining the %C required for core-shell systems, as well as the limits of the effect. This may allow for modelling of why specific degrees of complementarity appear to be required, which may then contribute towards a heightened understanding of multivalency effects in cellular LLPS.

Furthermore, droplet systems containing an increased number of nanostars may be investigated. Given current nanostar designs, two-star systems have been comprehensively explored (Chapter 3). Analysis was conducted on a limited number of three-star systems in NaCl and $MgCl_2$, forming various complex emulsion structures (section 4.2). Further investigations are warranted, in aiming to both develop heightened understanding of these systems, and increase the number available structures.

For instance, systems were produced using three distinct nanostars (NS1, NS2, NS3). When NS3 possessed complementarity to NS2, and NS2 to NS1, annealing produced NS1 cores with co-localised NS2-NS3 shells (figure 4.2, 4.8). When both NS2 and NS3 were complementary to NS1, nested co-continuous or patchy-interface structures resulted (figure 4.5, 4.6). It was proposed that the former condition formed mixed shells due to the surfactant modification of NS2 increasing the effective complementarity of NS3. Therefore, three-layer structures could be attempted either by modulating the degree of NS3-NS2 complementarity, or by changing the direction of complementarity in the systems. If NS1 were modified to be complementary to NS2, and NS3 were complementary to NS2, the relative %C of each pair would be unchanged. This may potentially result in a homogeneous three-layer droplet, allowing for increased complexity in microreactor designs.

Finally, isothermal phase separation may be explored in these systems. This work used a one-step droplet formation mechanism. In these systems, solutions were prepared at their final DNA and cation concentrations, and the annealing process both formed the nanostars and resulted in phase separation (section 2.4). However, nanostar droplet systems have also been formed using a two-step annealing process. In this technique, nanostars are annealed along a temperature gradient at low cation concentration [25] [22]. A later increase in solution cation concentration and incubation at a set temperature allowed for isothermal droplet growth. This method more

closely resembles the formation of liquid coacervates in cellular contexts, in which LLPS occurs under homeostatic conditions.

The formation of core-shell nanostar droplets was hypothesised in this work to rely on the staggered phase separation temperatures of the nanostars. If droplet formation were instead to occur isothermally, instead relying on an increase in cation concentration to trigger LLPS, it is unknown whether similar micro-architectures would still result. It is possible that the same features that have been shown to effect T_{PS} would still contribute to system formation at a constant temperature, with heightened valency or increased SE binding strength allowing for earlier droplet formation. This may then lead to similar micro-architecture formation under isothermal conditions. However, if different thermodynamic processes apply under isothermal conditions, then entirely different structures may form. Investigation of the effect of droplet formation process on the resulting structure is thus warranted.

5.2.2 Design of dynamic systems

The work in this thesis was partially driven by an aim to produce functional microreactors. A defining feature of these systems is their dynamic nature - the ability to modify their structure or behaviour based on received signals. A similar dynamism is desired in this system.

The concentrated environment of nanostar coacervates additionally provides a method of exploring strand displacement kinetics in a concentrated environment. Toehold mediated strand displacement reactions allow an incoming strand to displace the hybridisation of two partially-complementary oligonucleotide, if it possess a higher degree of complementarity to one of the partially-hybridised strands [215]. The invader strand typically includes an additional complementary nucleotide sequence in comparison to the incumbent, termed the toehold. The rate of the TMSD is af-

fected by the length of the toehold region, progressing most efficiently with toeholds of length 6 nt or more.

A number of TMSDs in nanostar coacervates have been demonstrated in the literature [149] [19] [22]. Do *et al.* found a significant increase in the rate of toehold-mediated reactions when confined within a coacervate, as compared to in a bulk solution. They attributed this to the increased local concentration of reagents within the coacervate. Modulation in the nanostar density of these coacervates could allow for investigation of the effect of reagent density on TMSD reaction rates.

The following sections propose multi-stage toehold-mediated strand displacement reactions in core-shell nanostar coacervates. Presented are proof-of-concept systems designed to allow for switchable changes in cargo compartmentalisation and droplet micro-architecture.

Changes in cargo compartmentalisation

The use of strand displacement reactions has been shown to allow the selective capture and release of functionalised streptavidin in core-shell droplets (figure 4.20, 4.29). This concept may be extended in designing a system of switchable localisation, wherein captured cargo is cyclically moved between core and shell (section A.21).

In this design, strand 1 of 3S10 nanostars is extended with a j sequence on the 5' end, forming j-3S10 (figure 5.3). Simultaneously, the 3' end of 4S8 strand 1 is extended with a i binding sequence, forming 4S8-i. In this design, it is assumed that 4S8-i and j-3S10 nanostars will form core-shell droplets.

The modified stars were used in designing a switchable compartmentalisation system (figure 5.4). A j'-(T_{10}) sequence, functionalised with biotin, would allow localisation of streptavidin in the j-3S10 shell. An invader strand (I1) consisting of an (A_4)-j-H-i' sequence is then added to the system. The presence of the poly-A sequence acts as

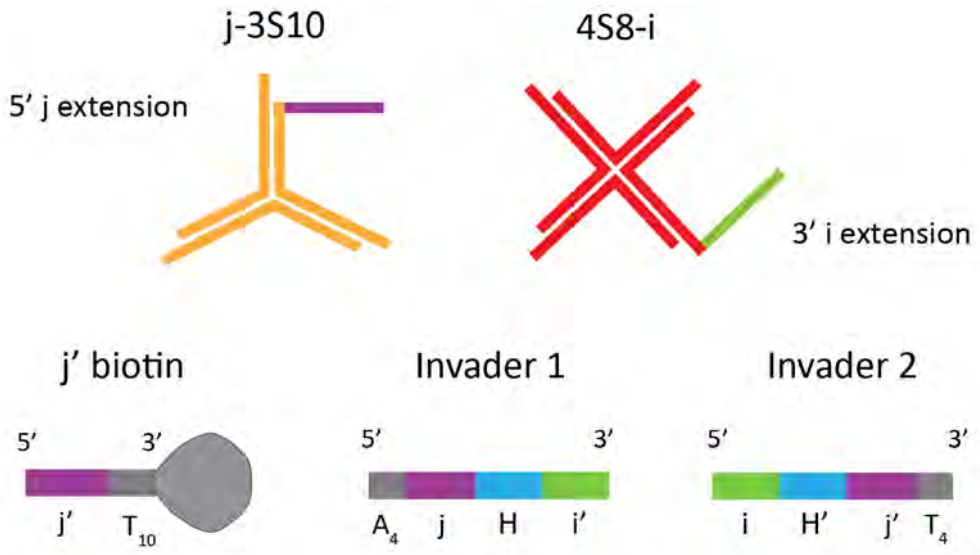

Figure 5.3: Proposed design of switchable localisation system. A 3S10 nanostar is functionalised on the 3' end of strand 1 with a modified j sequence. A 4S8 nanostar is functionalised on the 5' end of strand 1 with a i sequence. Biotin and invader strands, showing relative positions of TMSD binding sequences.

a toehold and allows I1 to displace the j-3S10 + j'-(T_{10})-biotin duplex. The newly formed I1 + biotin complex reveals an ssDNA i', which is predicted to capture the streptavidin in the shell. A second invader sequence (I2), consisting of an i-H'-j'-(T_4) sequence, is then added to the system. The sequences of I1 and I2 are reverse complements, and so the addition of I2 displaces the I1 + biotin complex. This returns the biotin functionalisation to an ssDNA j' sequence, theoretically resulting in a shift of streptavidin to the shell. In order to favour the duplexation of the j and j' regions of I1 and j'-biotin over j-3S10 and j'-biotin, a truncated portion of the invader anti-toehold sequence was appended to the j'-biotin.

The predicted binding interactions of the above system were calculated in NUPACK, at a sodium cation concentration of 0.5 M and a temperature of 25 ^{o}C (section A.22). In order to limit the number of strands involved in the calculation, j-3S10 and 4S8-i nanostars were entered as a single sequence. The sticky end sequences were replaced with poly-A sequences, allowing hairpin loop bends at the terminus of each arm, and the formation of a full nanostar sequence from a single strand (figure A.24).

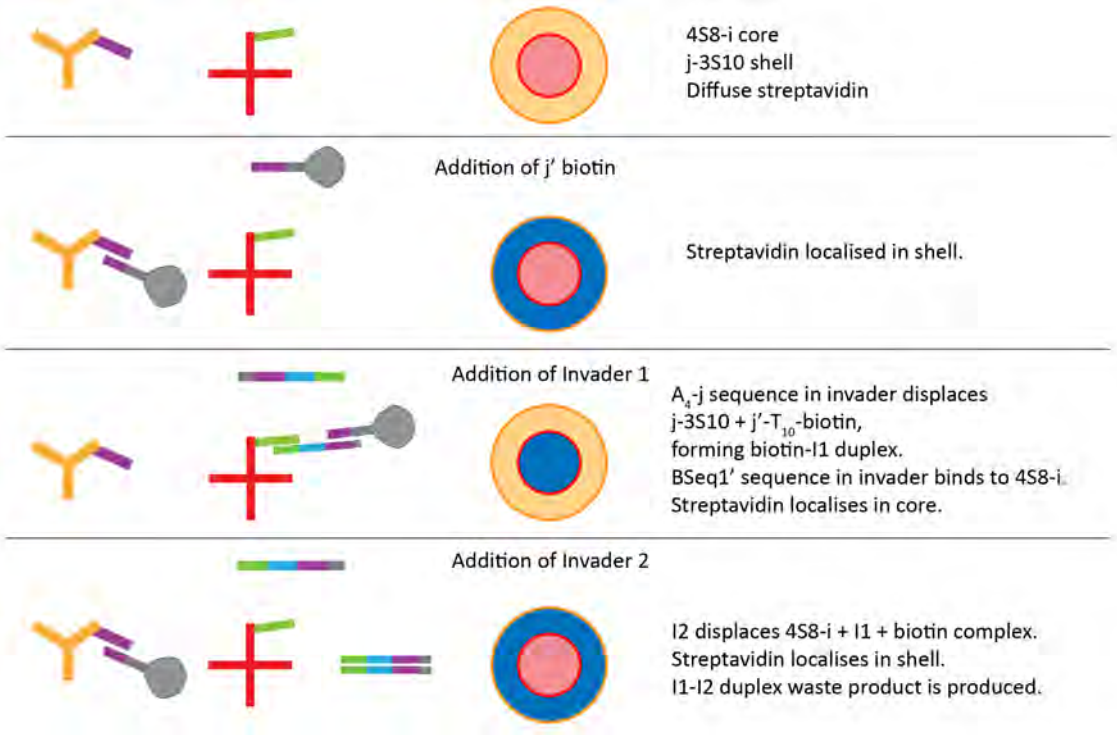

Figure 5.4: Proposed system for the strand displacement-mediated switching of streptavidin localisation. Proposed streptavidin location in core-shell droplet is shown in blue.

Nanostars were simulated at 5 μM concentration, and j'-(T_{10}) (sans biotin) at 1 μM. Invader strands 1 and 2 were added at an excess in comparison to the biotin strand, 1.2 μM. A maximum complex size of five strands was allowed, and each stage of the reaction was calculated.

NUPACK analysis of the proposed system aligned with the predicted displacement steps proposed above (figure 5.5). In step 1, j-3S10 and 4S8-i are both present at maximum concentrations. Step 2 involves the addition to the calculation of j'-biotin. A near-complete hybridisation of j-3S10 and biotin is predicted, alongside a corresponding decrease in j-3S10 concentration. Following this, an excess of I1 is added. The j-3S10 + j'-biotin binding is disrupted, while 4S8-i + I1 + j'-biotin complexes are formed. 4S8-i + I1 complexes are also seen, due to the excess addition of I1. Finally, the addition of I1 returns the system to the state seen in step 2,

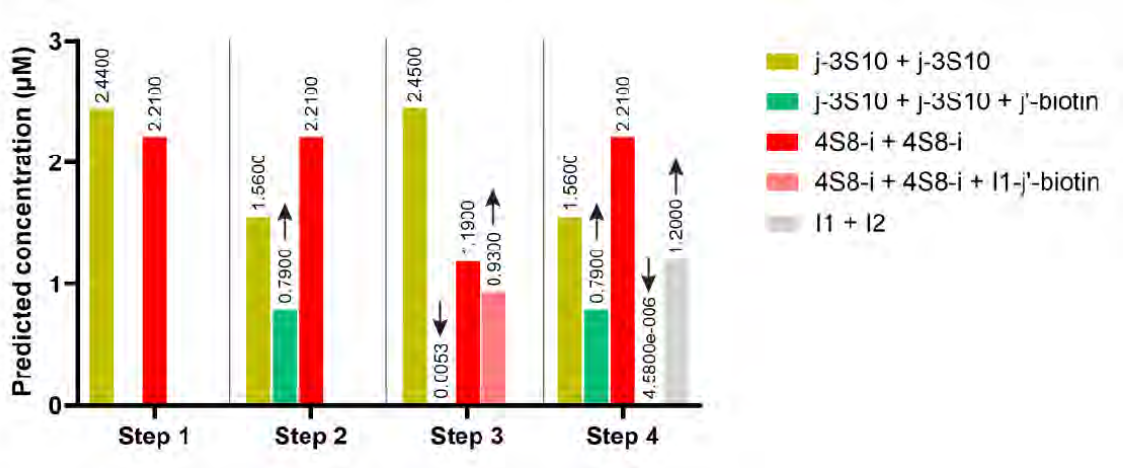

Figure 5.5: NUPACK calculated concentrations of j-3S10, 4S8-i, biotin, and invader strands. **Step 1**: Nanostar dimers of 4S8-i (red) and j-3S10 (green). **Step 2**: j'-biotin addition leads to j-3S10 + j'-biotin duplexation (light green). **Step 3**: Addition of invader 1 in excess displaces j-3S10 + j'-biotin duplexes, and instead forms 4S8-i + I1 + j'-biotin complex (pink). The excess invader forms 4S8-i + I1 duplexes. **Step 4**: Addition of invader 2 displaces all I1 duplexes. The system is returned to step 2, with the production of I1 + I2 dimer waste product (grey).

alongside a I1 + I2 waste product.

Thus far, selective localisation has been experimentally demonstrated, alongside the delocalisation of compartmentalised streptavidin upon invader addition (section 4.3.3, 4.3.4). The above system would allow for cyclical switching between core- and shell-compartmentalised streptavidin.

Changes in micro-architecture

Multi-nanostar mixed droplets have been produced in the literature through the use of surfactant stars [24] [150]. The separation of these co-localised droplets into distinct populations was achieved through the enzymatic or photocleavage-induced passivation of surfactant nanostars. Furthermore, Sato *et al.* demonstrated that passivating only a portion of surfactant stars resulted in the formation of bifacial droplets of distinct nanostar regions (figure 1.20).

This thesis has shown the development of 3 NS core-shell droplets, wherein the core

is a homogeneous mixture of two distinct nanostars (section 4.2). This was achieved through the inclusion of a high proportion of core 1-core 2 surfactant stars. As was previously discussed, these mixed-core droplets may theoretically be induced to switch to a nested co-continuous form, in a manner akin to the work of Sato *et al.* and Tran *et al.* [24] [150]. This would allow for the triggerable separation or mixing of the contents of a micro-reactor. A potential design for such a system is proposed below.

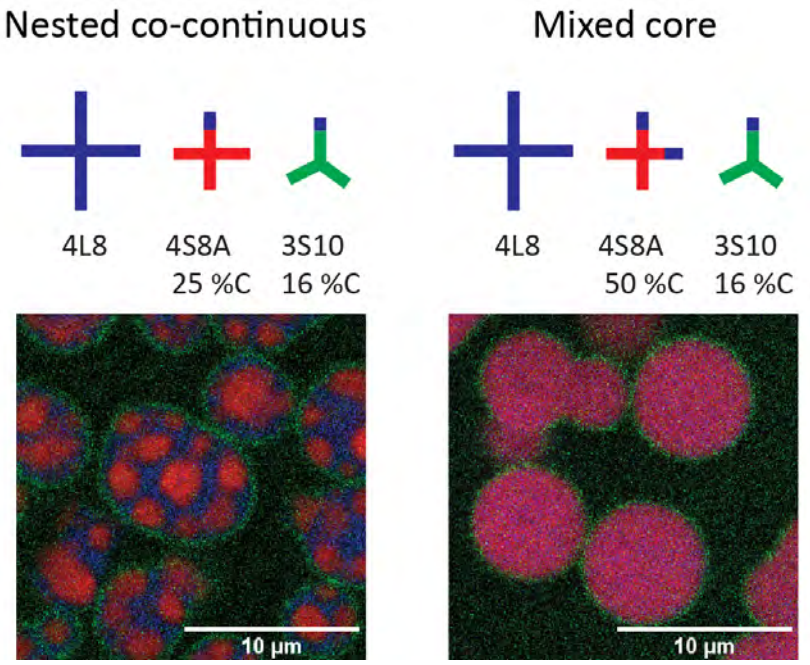

Figure 5.6: A 3S10 shell encapsulates either a co-continuous or mixed core, depending on the %C of the core nanostars.

In the current system, a co-localised core is in a core-shell structure is formed through the annealing of 4L8 4S8A (50 %C 8-nt) 3S10 (16 %C 8-nt) nanostars. A decrease in the degree of complementarity of 4S8A stars to 25 % 8-nt results in a co-continuous core (figure 5.6). In the proposed system, 4S8A surfactant stars would have 50% 8A-nt SEs, 25% 8-nt, and 25% 8-nt with an added toehold sequence. In the initial state, this is expected to form co-localised 4S8A and 4L8 regions. A signal to induce a state change would be added to the system in the form of a switching complex. As shown in figure 5.7, this possesses an 8-nt SE region and the complementary toehold

sequence, allowing binding to the toehold-modified SE in the surfactant star. The second strand of the duplex extends the toehold region and then contains an ssDNA 8A-nt SE. Binding of the switching duplex to a surfactant 4S8A nanostar is intended to reduce the 8-nt SE complementarity to 25 %C.

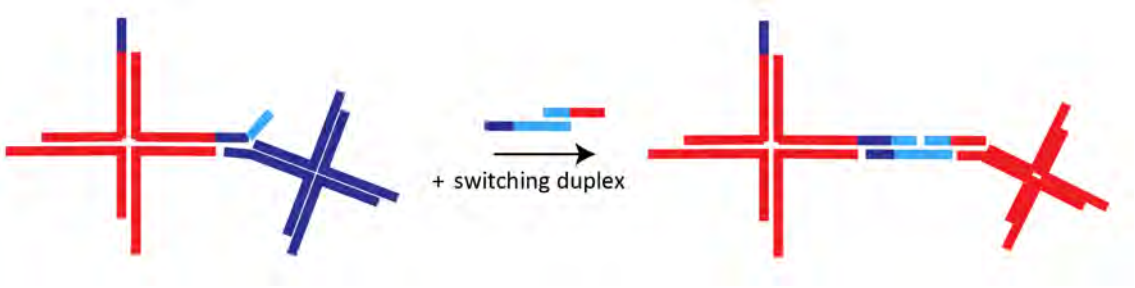

Figure 5.7: Proposed system for the switching of core complementarity. A 4S8A surfactant star has 50% 8A-nt SEs (red) and 50% 8-nt SEs (dark blue). One 8-nt SE is appended with a toehold sequence (light blue). The addition of a switching duplex displaces 4S8A-4L8 dimerisation at the toehold-modified SE, and allows 4S8A-4S8 dimerisation. The degree of complementarity of the surfactant is reduced from 50 %C to 25 %C.

This proposed system was designed and analysed in NUPACK, at a sodium ion concentration of 0.5 M and a temperature of 25 ^{o}C (section A.22). Nanostars were input as a single looped strand. 4S8A and 4L8 nanostars were calculated at concentrations of 5 μM. The surfactant nanostar was input as a 4S8 nanostar, with or without a toehold sequence appended to the 8-nt sticky end. To represent this stoichiometric split, 4S8 and 4S8-t were each modelled at 2.5 μM. Finally, each switch strand was modelled at 2.5 μM.

In the analysed system, prior to adding the switching duplex, 4S8 nanostars were predicted to bind equally to each other and 4L8 nanostars, regardless of toehold presence. Following switch addition, 4S8 nanostars remained bound to 4L8, while 4S8-toehold nanostars were entirely displaced. Simultaneously, prior to switch addition, 4S8 and 4S8-toehold nanostars did not bind to 4S8A nanostars. The addition of the switching duplex saw a duplexation of 96.8% 4S8-t and 4S8A nanostars. Therefore, this proposed system design provides a feasible avenue of exploration for

the switching of droplet micro-architectures.

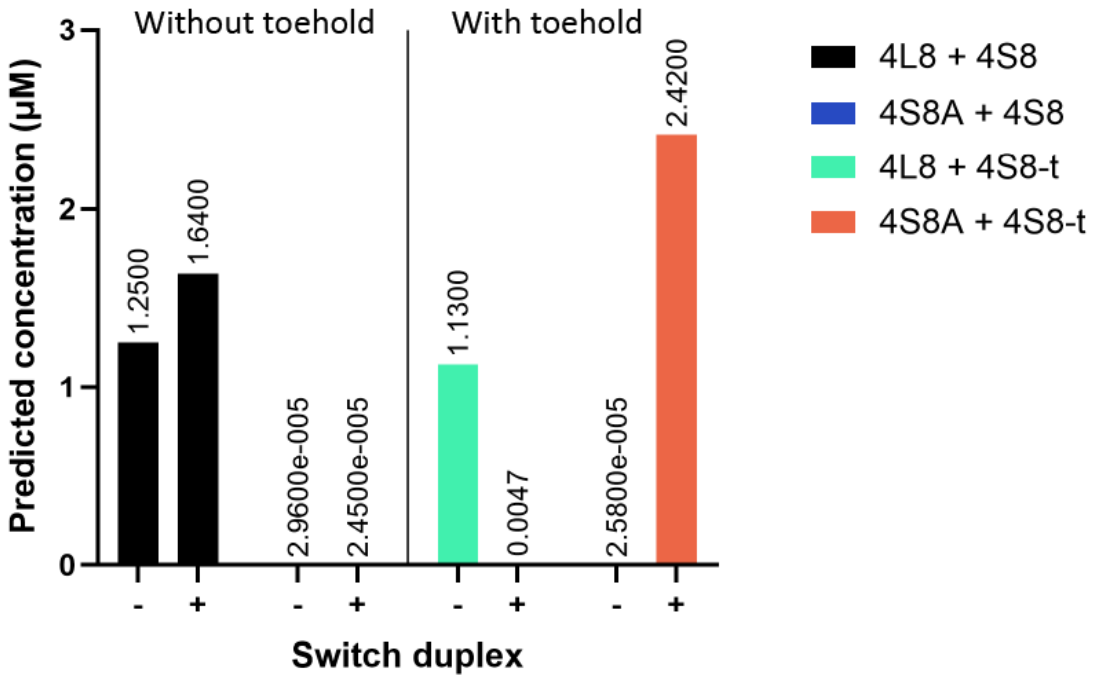

Figure 5.8: NUPACK calculated concentrations of nanostructure complexes, before and after switching duplex addition. A mixed core is expected to form with high 4S8 + 4L8 binding, while a co-continuous structure is expected from 4S8 + 4S8A. **Pre-switch addition**: In surfactant nanostars (4S8), a high degree of duplexation with 4L8 nanostars is seen, regardless of toehold modification. Binding between surfactant stars and 4S8A nanostars is insignificant. **Post-switch addition**, non-toehold surfactant star dimerisation with 4L8 stars is increases. Toehold-appended surfactant stars are displaced from 4L8 nanostar dimerisation, and instead form a surfactant-switch-4S8A complex. Self-dimerisation of nanostars is not shown, accounting for approximately 50% of predicted solution concentration; extended data is shown in Appendix A.29

The switching of surfactant nanostar complementarity via a strand displacement reaction is expected to maintain the total number of nanostars in the system. In comparison, if using the method of Sato *et al.*, the RNase digestion of a portion 4S8A surfactant nanostars would change the relative concentrations of 4S8A and 4L8 nanostars. However, the switching duplex designed in this system effectively extends one arm of the surfactant nanostar by 26 bp or 8.84 nm. In the work of Kengmana *et al.*, a portion of trivalent nanostars were asymmetrical, possessing two arms of 5 nm length, and one of 32 nm length [22]. When the asymmetrical nanostars

represented a fraction of total nanostar content, they were localised to the exterior of droplets, forming an infiltration gradient. While the ratio of arm asymmetry in the proposed surfactant star-switch dimer is only 1:2.5, in comparison to 1:6.5 in Kengmana *et al.*, it is possible that a similar localisation effect of modified surfactant nanostars would be seen. Experimental characterisation would be needed to confirm the extent of this effect.

5.2.3 Development of a synthetic leukocyte

Finally, the results of this thesis will be combined with several other research projects in order to develop a synthetic leukocyte cell. The physical transitions experienced by a white blood cell are numerous (figure 1.1). They include recruitment to the wall of a blood vessel, where they lightly adhere and roll under flow; strong adhesion, upon reaching a region of interest; and deformation from a spherical to amoeboid state.

Microfluidic devices could be developed in which the movement of nanostar coacervates under flow could be investigated [216]. The surfaces of this structure could be patterned with adhered proteins or ssDNA strands, to replicate the areas of inflammation that recruit biological leukocytes [217]. Recruitment could then trigger a strand displacement reaction, inciting a flatting of the coacervate [218].

A proposed schematic for such a system is shown in figure 5.9. A core-shell droplet is lightly adhered to a functionalised surface and rolls under flow. The shell nanostars possess a ssDNA binding sequence, complementary to ssDNA immobilised in selected regions of the microfluidic surface. The tetravalent core nanostars are modified such that one sticky end is extended with a toehold sequence. In the proposed design, the system contains T7 RNA polymerase and dNTPs, under appropriate solution conditions for RNA production.

When the droplet encounters the ssDNA functionalised regions, the shell nanostars strongly bind to the immobilised ssDNA signal strand, and the droplets are arrested. The hybridisation of the signal strand and the shell NS completes a T7 promoter sequence, activating T7 polymerase. The resulting RNA sequence is complementary to the toehold-extended sticky ends of the core. Duplexation of the RNA strand and the core nanostars dehybridises NS-NS binding, effectively reducing the valency of the core nanostars. This is expected to increase the fluidity of the droplet, inducing a state change and initiating a leukocyte-like flatting across the arrest region.

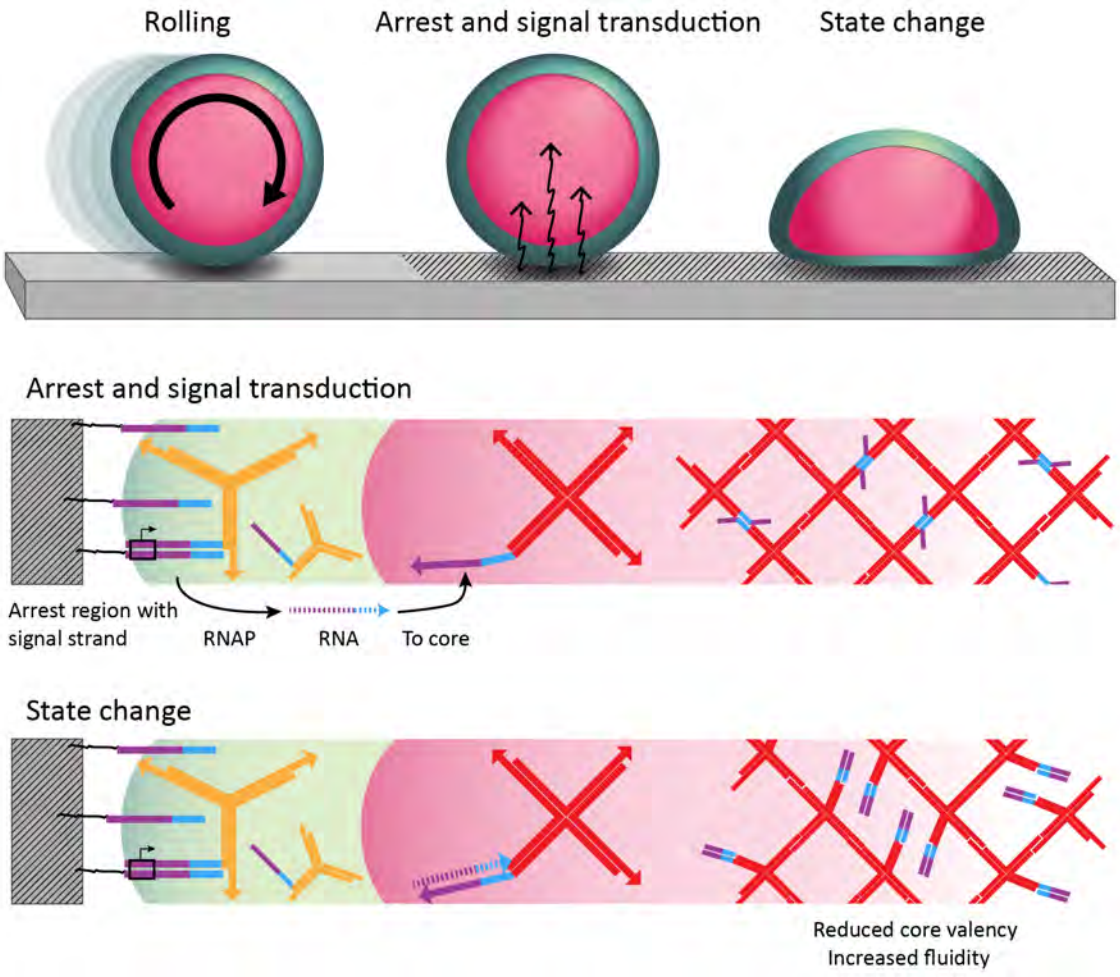

Figure 5.9: Proposed system design of nanostar coacervate synthetic leukocyte, showing physical transitions and strand displacement reactions. The synthetic cell rolls across a surface when experiencing shear forces. When it encounters a functionalised region, its movement is arrested, and the cell flattens across the surface. Arrest is triggered by duplexation of shell and immobilised signal strands. The resulting dsDNA completes a T7 promoter region (black box), allowing activity of T7 polymerase. The resulting RNA sequence triggers a strand displacement reaction in the core, reducing core nanostar valency and increasing droplet fluidity.

Appendix A

Methods

A.1 Design of nanostars in NUPACK software

Intended nanostar structures were input into the Design function of NUPACK using the dot-parens-plus notation, which describes the secondary structures of hybridised oligomers without specifying the base sequence. Constraints were set upon the designs to prevent similarity to each other, i.e. 4L could not contain similar sequences to 3S, 4S could not contain similarity to 4L or 3S. Similar constraints were set to prevent sequence similarity to literature designs.

Nanostar	DPP notation
3S	(16.2(16+)16.2(16+)16.2)16
4S	(16.2(16+)16.2(16+)16.2(16+)16.2)16
4L	(23.2(23+)23.2(23+)23.2(23+)23.2)23

Table A.1: Generic dot-parens-plus notation of nanostar designs, described in section 2.3.

All designs were produced under conditions of 10 μM strand concentration and 0.5 M [Na^+]. Upon producing a sequence design for each nanostar, the software was used to find the predicted melting temperatures and binding strengths of the DNA

complexes. The melting temperature of an oligomer is defined as the temperature at which 50% of bases are predicted to be unpaired. This can be found in NUPACK by predicting structural complexation at a range of temperatures – here, every 1 ^{o}C from 25-95 ^{o}C – and calculating Y = 0.5 from the resulting curve.

A.2 Fluorophore strands

Strand	Sequence (5' - 3')
Cy3 connector Cy3 fluorophore	TTG ATT GTT TCT CTT TGC GTT TCT– AGA AAC GCA AAG AGA AAC AAT CAA AGT CAG AGG GTA CTT ACC ACC/3Cy3Sp/
Cy5 connector Cy5 fluorophore	CTG ATT ATT GTG TGA CAA AAT AA– TTA TTT TGT CAC ACA ATA ATA ATC AGA GAG ATA ACC ATT TTA TAA/3Cy5Sp/
ATTO488 connector ATTO488 fluorophore	AAG GAC CAC CGC ATC TCT ACA– TGT AGA GAT GCG GTG GTC CTT/3ATTO488N/

Table A.2: Sequences of fluorophore connector strands appended to 5' ends of nanostar arms, and the complementary fluorophore sequences.

A.3 DNA droplet preparation and imaging

Except where otherwise specified, DNA droplets were produced using the following standard method:

The designed DNA strands, ordered from IDT DNA Singapore, were received in a dried form, purified by the manufacturer via desalting. Each strand was individually hydrated to 500 μM concentration in MilliQ Type 1 Ultrapure water (MQ) and allowed to resuspend for 24 hours at 4 ^{o}C prior to use. An aliquot of the 500 μM stock solution was diluted in MQ to a 55 μM working solution.

For each star design, two additional strands were also prepared. One, termed the fluorescent strand (Fl.), held a fluorophore (Cy3, Cy5, or ATTO488) bound to a

Solution	Initial concentration	Final concentration	Volume
DNA strands 1-4*	55 μM	10 μM	4 μL
Fluorophore connector	2.2 μM	0.1 μM	1 μL
Fluorophore	2.2 μM	0.1 μM	1 μL
NaCl	2.75 M	0.5 M	4 μL
Water	-	-	4 μL
		Total volume	22 μL

Table A.3: Volumes required in producing a standard single-star solution. *Trimer nanostars lack strand 4; water is added to maintain solution volume.

short ssDNA sequence. Another, the fluorescent strand connector (Fl. conn.), was a modified version of one of the main star strands; appended to the 5' end was the complementary sequence to the Fl. strand sequence. Each of the two were prepared as 2.2 μM solutions. This design allowed the same Fl. strand to be used in multiple configurations.

A volume of 4 μL of each 55 μM working solution was combined; for three stranded stars, an additional 4 μL of MQ was included to maintain solution volume and DNA concentration. To this was added 1 μL of 2.2 μM Fl. and Fl. conn. strands, and 4 μL of 2.75 M NaCl solution. With a final volume of 22 μL, this resulted in 10 μM star concentration, with 0.1 μM fluorescent strands, and 0.5 M NaCl ions. The inclusion of Fl. conn. modified star strands resulted in 1% of stars binding to Fl. strands.

The prepared solution was heated to 95 ^{o}C for five minutes and then cooled at 0.5 ^{o}C/min to 4 ^{o}C in a ProFlex PCR System (Applied Biosystems, USA). Following annealing, the resulting solution was pipetted into a viewing chamber, a 2 mm channel prepared from melted Parafilm® between a white glass microscope slide and #1.5 coverslip. Prior to assembly, each slide was cleaned via sonication for five minutes each in propanol and MilliQ water, followed by drying under pressurised air or nitrogen gas. When injecting sample, the chamber was held such that the glass

surface closest to the microscope objective is the bottom of the chamber; as the polar ends of DNA are attracted to the exposed -OH groups of glass, the coacervate droplets were be drawn by gravity to the lowest glass surface and become lightly adhered, anchoring them for microscopic viewing. The ends of the chamber were then sealed using a two-part epoxy resin, to reduce evaporation.

Sample imaging was performed on a Leica TCS SP8 Multiphoton Microscope, fitted with a white light laser and HyD and PMT detectors. For DNA tagged with Cy3 fluorphores, an irradiating wavelength of 550 nm was used, with a HyD detector set between 560 nm and 630 nm; for Cy5 fluorophores, an irradiating wavelength of 640 nm was chosen, with detection from 650 nm to 740 nm. Images were typically produced at 1024 x 1024 resolution, with an imaging speed of 400 Hz. When analysing images containing both fluorophores, scanning was conducted sequentially – a single line of pixels was irradiated and detected under Cy3 settings, followed by those same pixels being imaged for Cy5 fluorescence. Alternating detection in this manner reduces bleedthrough or false fluorescence from undesired fluorophores, improving the quality of both resultant images. Unless otherwise specified, samples were imaged with a 93x glycerol immersion objective.

As coacervated droplets in solution are distributed throughout the z-axis of the viewing chamber, a single slice within the volume of the sample would provide an inaccurate view of droplet dimensions. Thus, a series of slices moving along the z-axis of the sample was captured, a z-stack, producing a three-dimensional image. Images were captured at 1024 x 1024 resolution, encompassing a volume of 184.70 μm^2 base and 14 μm height. Projecting all slices as a single frame produces a flat image with all droplets represented at their maximum diameter. This allows for statistical analysis without fear of z-position bias.

When interested in fluorophore position rather than an empirical measurement of

droplet size, time-series images were captured at a length of 20 frames. Finding the sum of all slices as a single frames increases sample brightness for more efficient viewing, and will increase the chance of capturing regions of low-intensity fluorescence.

A.4 Poly acrylamide gel electrophoresis

PAGE analysis was conducted on 0-nt SE nanostars annealed under standard conditions, to verify appropriate formation of stars. Combinations from a single strand to a full star were studied to confirm that the chosen strands would only form a full structure when all oligomers of the design were present. Annealed at 10 μM nanostar concentration, solutions were diluted to 100 nM prior to analysis, and combined with Thermo Scientific 6X DNA Loading Dye (Thermo Fisher Scientific, Australia). PAGE was conducted in 10% Mini-PROTEAN® TGX™ Precast Gels (BioRad, Australia). The gels were prepared by conducting a buffer ion exchange: the PAGE cassette was filled with 0.5 X TAE (pH 7) and run at 180 V for twenty minutes to exchange glycine amino acids in the gels with acetate ions. A volume of 10 μL of sample and 1:200 diluted Invitrogen Ultra Low Range DNA Ladder (Thermo Fisher Scientific, Australia) were loaded and run at 180 V for forty minutes. The gels were removed from solution, stained with SYBR Gold Nucleic Acid Gel Stain (Thermo Fisher Scientific, Australia) for ten minutes, and imaged in a BioRad ChemiDoc MP (BioRad, Australia) under SYBR Gold and Cy3 capture wavelengths.

A.5 Dynamic light scattering

Hydrodynamic size (D_h) is the diameter of a theoretical spherical object that diffuses through a liquid solution at the same rate as the measured particles. This technique is equally applicable to spherical and non-spherical objects of interest, and thus can

be applied to the nanostars studied herein [219].

DLS was conducted on 0 SE stars formed under standard conditions using a Zetasizer Ultra (Malvern Panalytical, Australia). The parameters used were a refractive index of 1.5826 and an extinction coefficient of 0.00. All measurements were conducted at 25 ^{o}C using 500 μL of sample and were repeated in triplicate.

A.6 Variation in nanostar flexibility

Further oxDNA analysis was conducted upon variations of the 4S nanostar, in order to investigate the effect of the central unpaired bases (J_{nt}) on nanostar conformation (section 1.6.2). VMMC simulations were run on 4S nanostars with and without unpaired ssDNA hinges at the central junction, termed flexible and inflexible, respectively (figure A.1). Simulations were run for a total of 285 frames. Using the same method as described above, the end-to-end distances of each strand were computed for every configuration. These endpoint distances were analysed per strand to identify any trends in nanostar configuration across the simulated population. Specific conformations were identified, and selected incidences of these conformations were analysed to provide insight into broader trends. This resulted in identification of conformation-switching pathways for inflexible and flexible nanostars, outlining a potential function of the central unpaired junction.

The nanostar studied herein is a modified form of the biological Holliday Junction. Both the HJ and nanostars are generally accepted to adopt one of two conformations – open and linear [220] [146]. In each, two further variations are possible. For the open structure: open bent, wherein each strand adopts a 90^{o} bend at the central junction, and open rotated, where two linear strands form a cross shape and the remaining two bend at the central junction. For the linear structure: anti-parallel linear, where two strands adopt a parallel linear conformation and the attached

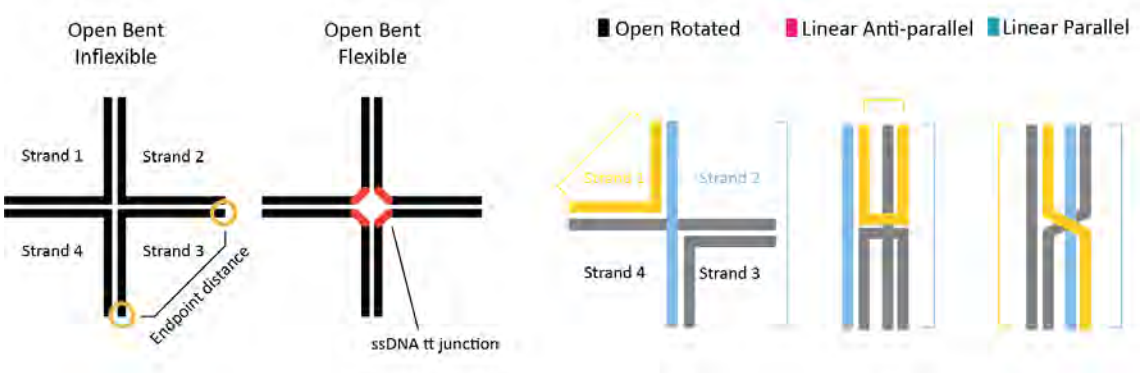

Figure A.1: Nanostar dimensions are measured as the distance between the 3' and 5' ends of each strand. Inflexible and flexible nanostars, shown in an open bent configuration, differ only through the inclusion of unpaired tt hinges at the central junction of each arm. Three additional hypothesised tetramer configurations and the varying endpoint distances seen in each structure.

strands bend in 'U' shapes across this, and parallel linear, with the same internal parallel linear conformation, with the remaining two strands crossing over one another in an 'S' conformation. In the three latter conformations, each possess two linear strands, either perpendicular or parallel to each other. These linear strands do not bind to each other in the nanostar design (e.g., strand 2 + strand 4, figure A.1). Notably, although this investigation concerns a tetrameric particle, a tetrahedral conformation is not expected – earlier simulation studies indicate a tendency towards planarity in nanostars [170].

Of the four theorised nanostar conformations, each is expected to create a distinct pattern of endpoint distances. Linear strands in an inflexible nanostar have a geometric length of 10.88 nm, while a 90^o bent strand has an endpoint distance of 7.69 nm. The additional two J_{nt} bases in a flexible 4S0 NS increase these values to 11.57 nm and 8.17 nm, respectively. A flexible nanostar in an open bent configuration is expected to have endpoint distances of approximately 8 nm for each of its four strands, while an open rotated configuration is expected to have two strands with 11 nm distance and two with 8 nm distance. A parallel linear structure is expected to have endpoint distances close to the maximum value of 11 nm for all four strands,

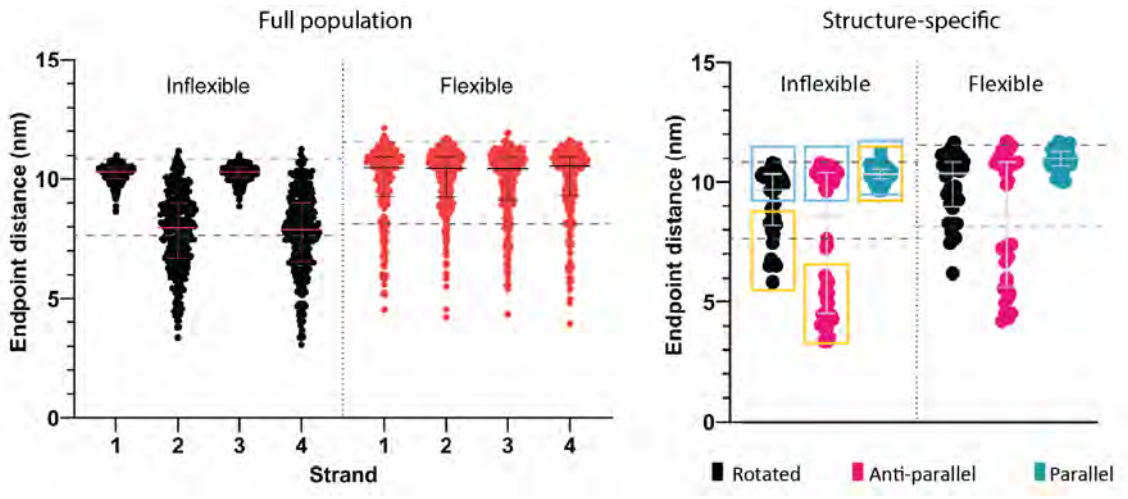

Figure A.2: Distribution of nanostar strand configurations in oxDNA. **Full population**: Endpoint distances of individual strands in inflexible and flexible 4S0 nanostars, shown as individual measurements and median ± 95% confidence interval. Dashed lines show theoretical values for linear and 90^o bent strands. Inflexible nanostars show strong tendency towards linear configurations in strands 1 and 3, while strands 2 and 4 appear more prone to a bent position. Flexible nanostars have similar behaviour for all four strands. **Structure specific**: Strand endpoint distances of flexible and inflexible nanostars, separated by structural configuration. Subset of Full Population data, representing ten frames for each structure. Blue and yellow boxes indicate predicted distances from fig. A.1. Rotated nanostars have high to mid endpoint distances, anti-parallel see binodal high and low, and parallel nanostars have uniformly high endpoint distances across all strands.

and an anti-parallel structure is predicted to have two strands of 11 nm and two of approximately 5 nm, the width of two adjacent DNA helices. Analysis of inflexible and flexible nanostar populations was conducted to determine if any differences in endpoint distances may be identified.

OxDNA simulations were conducted on inflexible and flexible nanostars, with the endpoint distances found for each individual strand in the structure. In simulations of inflexible nanostars, strands 1 and 3 were shown to consistently have a large distance between endpoints with a narrow distribution, while the remaining two strands in the structure appeared to have a broad distribution in their configuration (figure A.2 Full population). The simulated values aligned with geometric predictions for an open rotated structure, in which strands 1 and 3 were always fully

extended. Conversely, flexible nanostars showed no such tendency towards a specific strand conformation, with all strands behaving similarly. These had a broad range of possible distances between endpoints, each weighted toward a higher endpoint distance.

Of the possible nanostar configurations (bent, rotated, parallel, anti-parallel), three were found to commonly occur in VMMC simulations - rotated, anti-parallel, and parallel. Ten frames were identified of each configuration for both flexible and inflexible nanostar simulations and the endpoint distances for these structures plotted (figure A.2 Structure-specific). This revealed consistent behaviours within configurations, regardless of flexibility (table A.4). Parallel nanostars had only narrowly distributed, high distance endpoints. Anti-parallel stars had a binodal distribution of endpoints, corresponding to the linear and crossed strands. The rotated star also saw a binodal distribution, with lessened difference between the nodes. In a rotated configuration, two strands are linearly arranged, accounting for the higher distance node, while the middle distance node corresponds to the strand bent at the central junction. These simulated values aligned with the predicted patterns in endpoint distances for each configuration.

	Inflexible				Flexible			
	S1	S2	S3	S4	S1	S2	S3	S4
Mean (nm)	10.2	7.8	10.2	7.8	9.9	10.0	9.9	9.9
SD (nm)	0.4	1.6	0.3	1.7	1.6	1.3	1.5	1.5
Median (nm)	10.3	8.0	10.3	7.9	10.5	10.4	10.4	10.5

Table A.4: oxDNA simulation 4S nanostar endpoint distances

This may elucidate the distributions seen in the broader populations of the simulations. The symmetric distribution of endpoint distances of strands 2 and 4 in inflexible stars indicates a high incidence of the "bent" position in the rotated configuration. This corresponds well with the appearance of more homogeneous linearity

in strands 1 and 3. The results of the simulations thus suggest that a defined pair of orthogonal strands of an inflexible nanostar tend to remain linear at all times. The remaining pair of strands may move between parallel, rotated, and antiparallel configurations, with a tendency to remain in the rotated configuration (figure A.3). Conversely, the homogeneous distributions of the flexible nanostar suggest no tendency towards linearity for any specific strands; nanostars freely rotate between the two possible variations of the open rotated configuration, with a tendency away from linear structures.

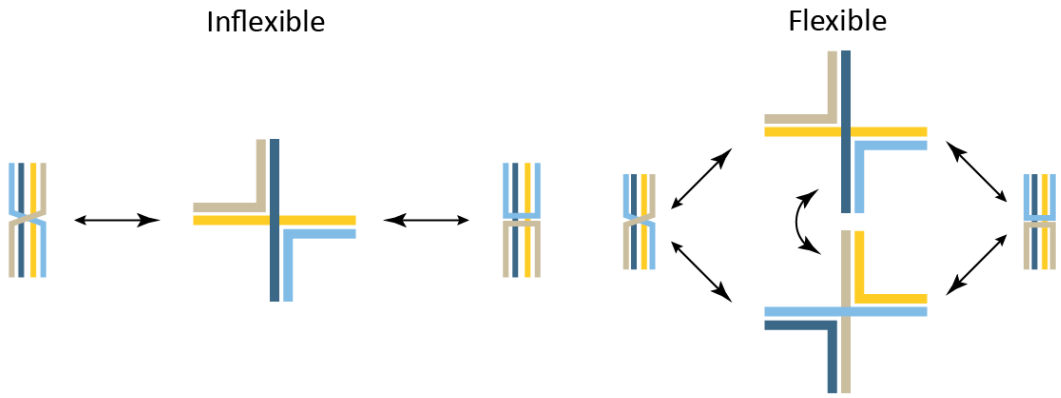

Figure A.3: Proposed structural pathways for inflexible and flexible nanostars. Inflexible nanostars are limited to a single rotated configuration, with occasional transitions to either linear configuration. Flexible nanostars readily switch between either rotated configuration, with a reduced tendency to linear configurations.

These hypotheses are further supported by frequency analysis of the standard deviation of endpoint distances for a given star (figure A.4). For each frame in either simulation ($n = 285$), the endpoint distances of the four strands was calculated. The standard deviation (σ) between these values for the four strands was then found. A low deviation (0-0.5 nm) indicates a similar distance between endpoints for all strands, such as is the case for a parallel configuration. A high standard deviation ($>$ 3 nm) indicates an anti-parallel configuration, while a rotated structure sits between these extremes. Frequency distribution analysis reveals a smooth transition between the three states, rather than a strict structural adherence with no transitory

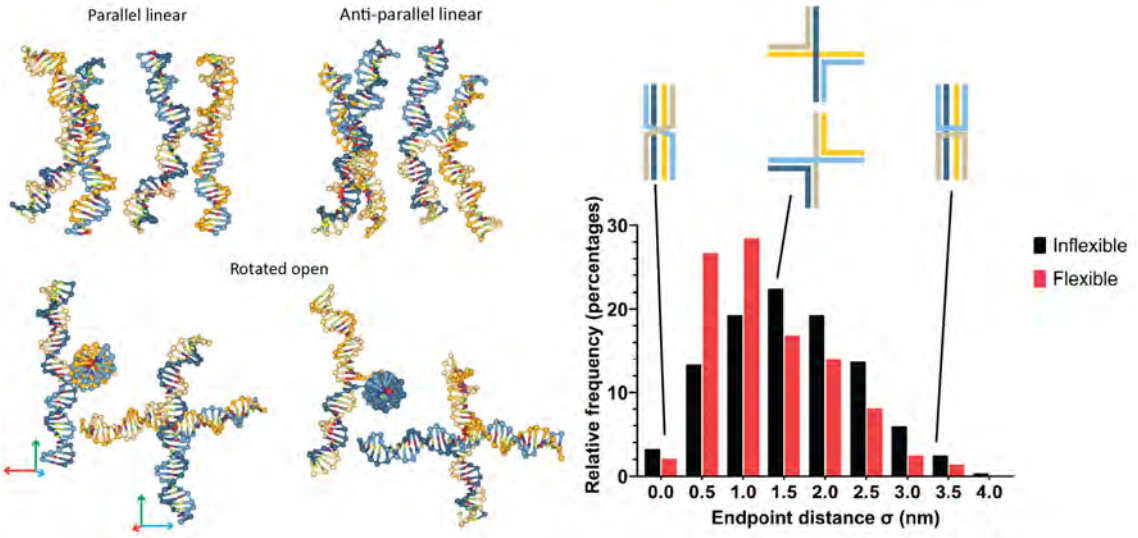

Figure A.4: Example structures of parallel, anti-parallel, and rotated tetramer configurations (oxDNA 2025). Histogram of endpoint distance σ for inflexible and flexible nanostars, indicating the strand-to-strand variability within a single star. Parallel stars are expected to have similar end point distances for all pairs of strands in a star (small sigma), and anti-parallel different distances (high sigma). Open structures are expected to be somewhere in between.

structures, as would be indicated by a trinodal distribution.

Flexible nanostars appear to have the highest occurrence of σ at 0.5-1 nm, corresponding to open rotated configurations with transitory structures between the two variations. Inflexible stars have a symmetric distribution from parallel to antiparallel, with a higher incidence of the two extremes than in flexible stars, as would be suggested by the higher propensity towards linearity (figure A.4). This broad distribution in configurations indicate that even the "inflexible" nanostar is likely to take many conformations, subject to thermal fluctuations in solution.

The simulations were conducted upon single-star systems. In a phase separated droplet, nanostars would be connected via sticky ends to adjacent stars at multiple termini. In a three-dimensional network, junction and termini unpaired bases would allow for bending and rotation of arms to accommodate for the non-planar position of neighbouring stars. An inflexible star lacks the torsional release of central hinges; its

propensity towards linearity would thus disfavour the formation of densely populated nanostar droplets, as suggested by Nguyen *et al.* [146]. Thus, the necessity of promoting the formation of a macroscale phase separated droplet led to the inclusion of unpaired bases at the central junction of each nanostar used in this thesis.

A.7 Measurement of droplet size

Once formed, the size and distribution of droplet radii provide insight into the kinetics of formation. Therefore, the precise and accurate identification of droplet radii is an essential factor of this study.

Confocal microscopy was performed on droplet samples, producing a z-stack file 14 μm in height, of 0.35 μm slice depth. As the droplets formed spherical structures, a single image captured at an arbitrary height may pass through different cross-sections of different droplets, thereby inaccurately representing droplet size. Therefore, each stack was flattened using a `Sum Projection`, in order to represent the maximum diameter of all captured droplets. Four methods of analysis were compared in order to identify the most efficient, least error-prone technique in identifying droplet diameters. The radii and threshold variables were optimised for each method to maximise droplet detection while avoiding false identification.

Methods 2-4 were developed based on a circular Hough Transform algorithm [221]. A CHT, in its most basic form, is defined by three variables – threshold, minimum radius, and maximum radius. An image consisting of outlined objects is analysed. At each point of every edge, circles are traced between the minimum and maximum radii. In the case of a circular object with a radius within the minimum–maximum radii variable range, traces will overlap at the centre point of the circle, allowing identification of the object's outline, even if partially obscured. Each pair of antipodal circular traces that meet at a possible object's centre count as a vote towards the

given combination of centre location and radius value. The ratio of votes an object receives to the resolution of the test – the number of circles drawn on every boundary – provides the Hough score, with non-circular or irregular objects garnering a lower score. When implementing the CHT algorithm, a score threshold is chosen, with all objects garnering a lower score than the threshold being discarded. Thus, through simple estimation of the lowest and highest possible radii of droplets in an image, the position and size of all droplets may be calculated.

Method 1: Klocke

The first method used a custom Python script written by M.A. Klocke, as described in Agarwal *et al.* [222] [27]. This process calculates the area, diameter, and eccentricity of "blobs" in a confocal micrograph, by binarising the image and then tracing the circumference of all bright objects.

Method 2: Summed

Summed z-stacks were analysed using a custom script written in MathWorks MATLAB R2021B, using its CHT-based `imfindcircles` function (figure A.5 B, script B.1).

Method 3: Smith

Summed images were processed to highlight the outlines of droplets (script B.2). These were analysed with the `Circle Hough Transform` plugin in ImageJ FIJI, created by B. Smith for UCB Vision Sciences (figure A.5 C) [223].

Method 4: Binarised

The Klocke binarisation method (section A.8) was also replicated in ImageJ FIJI (script B.3). The resulting binarised images were analysed using the custom MATLAB script (figure A.8 D, script B.1).

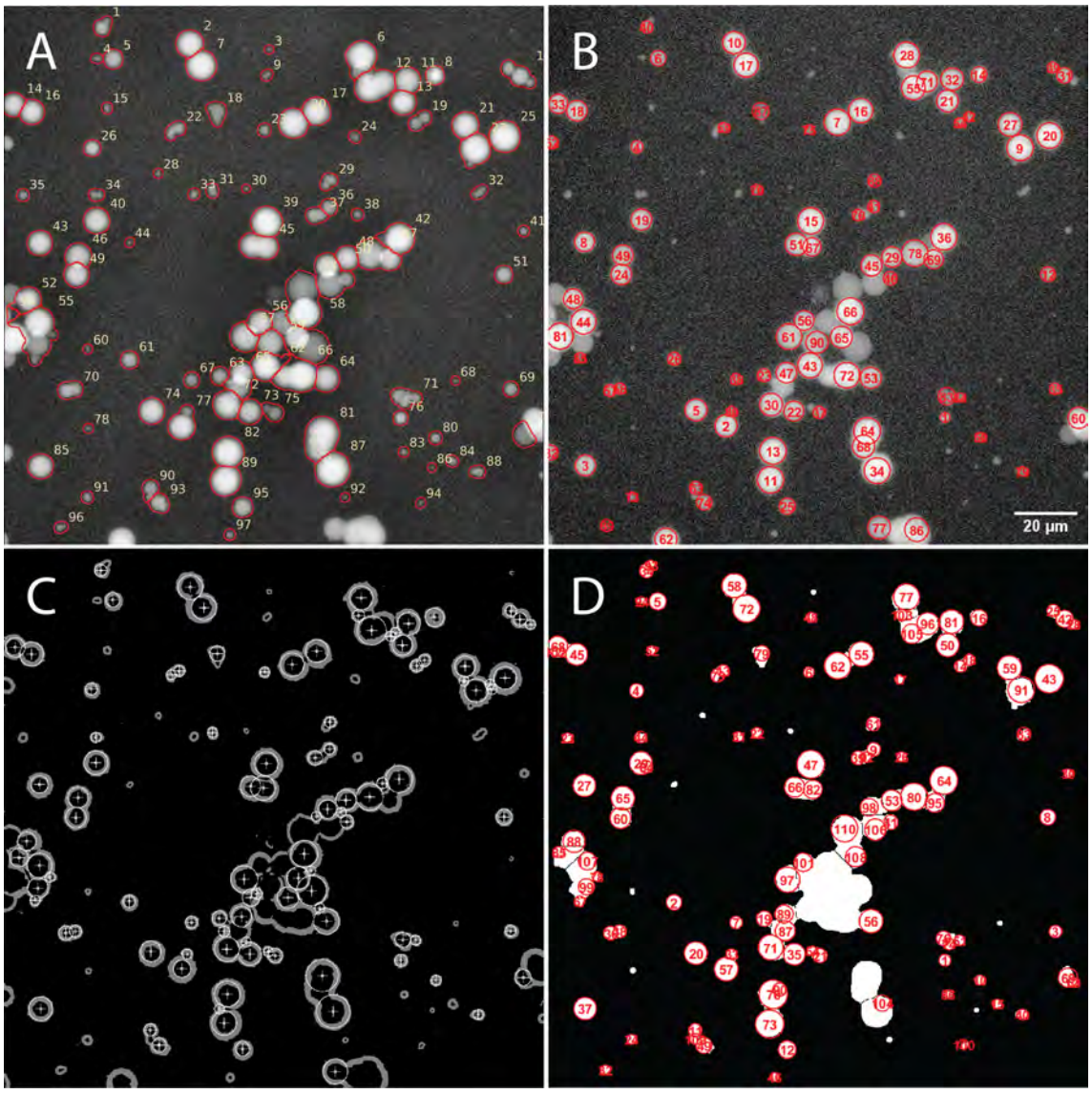

Figure A.5: Algorithmic droplet detection output for Klocke, summed, Smith, and binarised methods. Example is a 4S8 droplet, prepared under standard conditions. Scale 20 μm.

The limitations of each method were explored and compared. Each of the four image processing methods were compared for discernment (successfully distinguishing between adjacent droplets) and accuracy (identifying a high proportion of droplets while avoiding false identifications).

The Klocke method is distinct from the others in that it does not employ a circle-seeking algorithm [222]. Rather, the image is thresholded and all discrete objects outlined as "blobs", with segmentation of larger blobs afforded through a Watershed algorithm. This program was originally intended for identifying the size and eccentricity of objects in a sparsely populated image in order to track the rate of droplet growth over time. As nanostar droplets tend to grow via fusion, transitioning between ovular and circular objects, an algorithm that solely identifies circles would be inappropriate. Considering this, it comes as little surprise that the program was inefficient at discerning between purely circular droplets, especially in more densely packed images. Ovoid or irregular objects were common, combining what can be visually identified as two or more distinct droplets (figure A.6 A). Thus, this algorithm was deemed inappropriate for this application and removed from further consideration.

The image processing workflow of the ImageJ HCT plugin required converting the droplets from solid objects to hollow outlines [223]. When applied to the captured images, this would produce outlines of thicknesses comparable to the smallest droplets. Accordingly, if circle detection parameters were tuned to the size of the smallest droplets, many false detections were found to occur, with droplet outlines themselves recorded as consisting of droplets (figure A.6 B). Conversely, if parameters were tuned to avoid these false positives, the smallest droplets would be excluded from detection, inflating the final size measurement. This issue could be alleviated somewhat through `erosion` of the binarised outlines, but could not be avoided entirely. Furthermore, due to the binarisation of the images, clustered areas

of droplets would often loose interior detail, leading to these droplets being missed by the detection algorithm altogether (figure A.6 C).

Images were also analysed using a custom MATLAB script. This was applied both to binarised images and summed z-projections, with the sum of all layers found in order to maximise apparent diameter and image brightness. The former faced many of the same problems as the Smith ImageJ plugin – in applying the HCT algorithm to a filled outline, central droplets were frequently missed. The computer vision program was unable to discern the featureless regions, while false detections were similarly common, with smaller circles being drawn within larger ones (figure A.6 D). The Summed method, with the benefit of each droplet retaining its shaded appearance instead of flat colour or a simple outline, appeared best able to discern the presence of droplets. However, it was prone to falsely detecting circles in noisy background regions (figure A.6 E). These false detections were addressed through verification of the analysed data, described below.

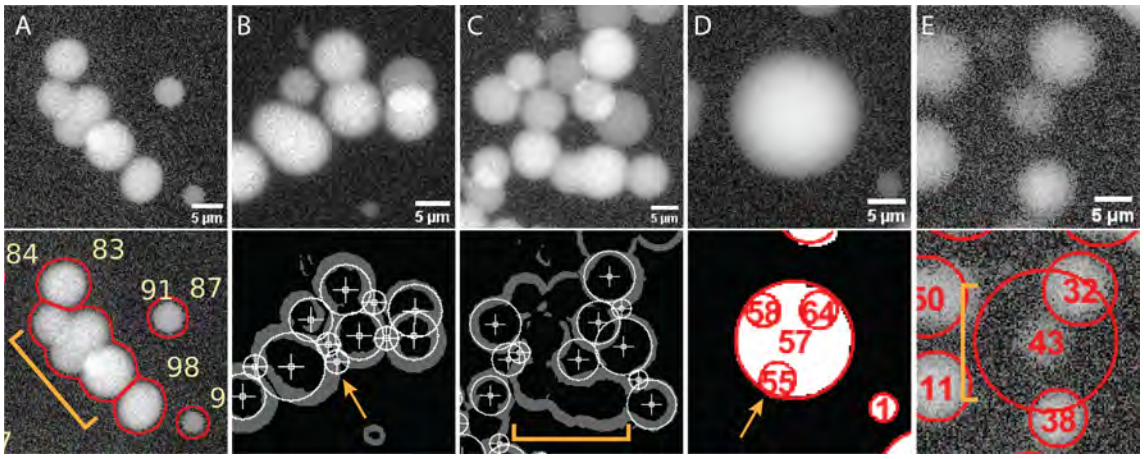

Figure A.6: False detections in algorithmic droplet analysis. A) Adjacent droplets identified as a single object in the Klocke method. B) Drawing a solid outline around droplets in the Smith method created thick boundaries which were themselves identified as circles. C) Areas of aggregated droplets could not be distinguished by the Klocke, Smith, or Binarised methods. D) Circles could be falsely identified within or between other droplets in all methods. E) The Summed method analysed non-thresholded images; noisy background areas could lead to false identification of circles. Scale bars 5 μm.

Following initial droplet detection, verification of the detected droplets was performed. In order to more comprehensively compare the discernment of each detection method, nine random images were chosen and their detection outputs judged for each algorithm. Across all nanostars and droplet appearances, the Klocke algorithm struggled to discern individual droplets in favour of irregular blobs; the Smith method tended to place small circles along the perimeters of droplets; the custom MATLAB script applied to binarised images consistently failed to discern droplets in crowded areas and would place small circles within larger ones. The custom script applied to summed images encountered few incidences of false or merged identification, thus showing the greatest level of discernment.

Systematic verification was conducted on each analysed dataset to improve accuracy. To avoid false positives in droplet detection, the mean pixel intensity within each detected region was compared to the mean intensity of the original image (script B.1, B.4). In the case of analysis methods 3 and 4, the radii and XY-coordinates of detected circles were used to define regions in the original image, which were then compared against the total original image. If the droplet region had more than 1.5 $\times$ the intensity of the image at large, it was counted as likely containing a true droplet, rather than a falsely identified background region. Only verified droplet radii were used in further data analysis. For instance, figure A.6 E shows the results of a Summed detection algorithm, with several accurately identified droplets and one falsely identified region. The mean pixel intensities of regions 11, 32, 38, and 43 were 165.00, 146.77, 160.35, and 92.62, respectively. In comparison to a mean image intensity of 86.73, this produced intensity ratios of 1.90, 1.69, 1.85, and 1.07. Therefore, regions 11, 32, and 38 would be verified as accurately detected droplets, while region 43 would be discarded from the dataset.

Following this verification, the ratio of the mean fluorescence in detected regions to the total image including background regions was compared between the Smith,

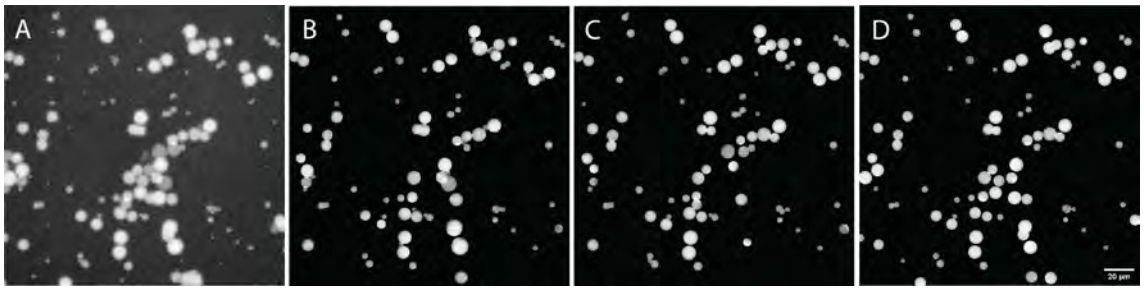

Figure A.7: Original 4S8 droplet image and verified droplet detections in Smith, Binarised, and Summed detection methods. Scale 10 μm.

Binarised, and Summed algorithms (figure A.7). As the droplets are invariably the brightest regions in each image, the greater the number of droplets identified, the higher the mean pixel intensity in the identified region. The proportion of droplets detected in an image can be quantified as the ratio of the sum pixel intensities within the detected regions to the intensity of the image as a whole. A higher ratio indicates that a greater number of droplets have successfully been identified, meaning a lower number of false negative detections occurred. Different sample images contained vastly different densities of droplets and background intensities. An image containing a smaller number of droplets would result in a low droplet:total sum intensity ratio, with the ratio expected to increase with the number of droplets in the image. This ratio was therefore only used as a qualitative comparison between detection methods, rather than a quantitative indication of detection efficiency.

Compared across the full dataset of all droplets, a significant difference in the droplet to image intensity ratio was found between each detection algorithm (figure A.8). A broad range existed within each dataset, with certain images garnering greater or poorer ratios regardless of algorithm, due to droplet density and background intensity. The Summed algorithm showed the highest mean ratio, indicating it consistently identified more droplets than the other detection methods (ANOVA, $P = 0.0197$ vs Smith, <0.0001 vs binarised). Thus, the custom MATLAB script applied to summed z-stack images was henceforth used to analyse all confocal data.

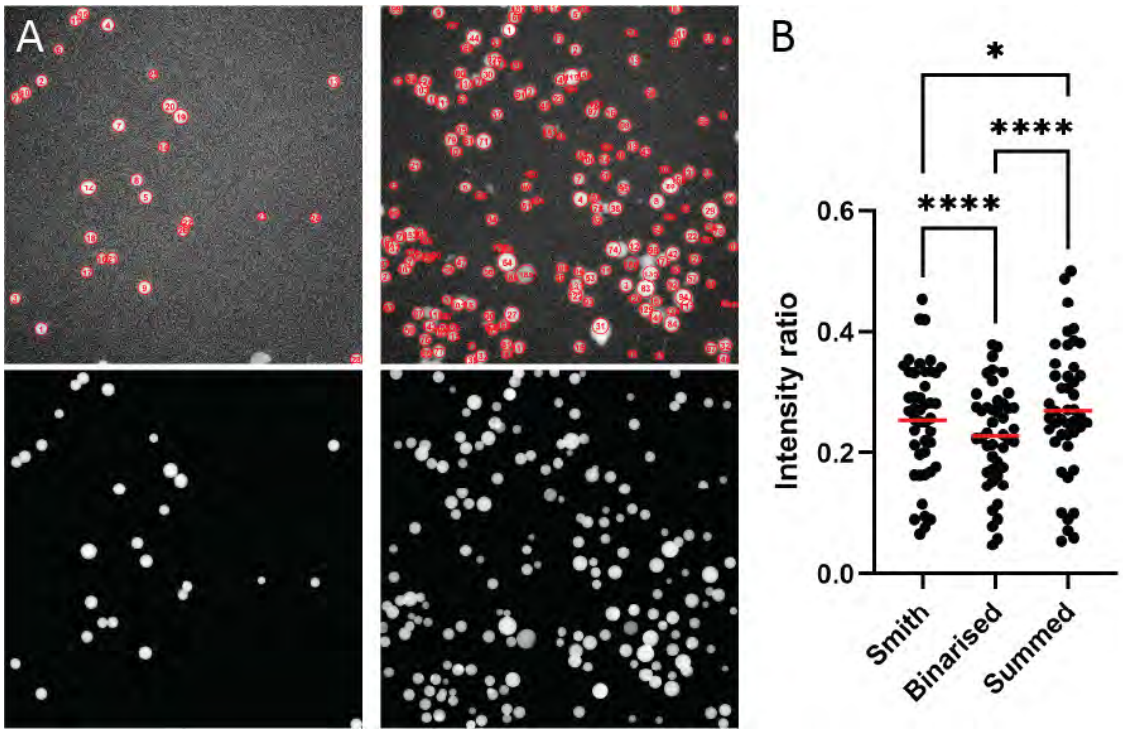

Figure A.8: Droplet:total image pixel intensity may be used to compare the detection efficiency of different droplet identification algorithms. **A**: Depending on droplet density, the ratio of droplet:total image pixel intensity can vary, even with high detection efficiency. Comparing 4L10 and 4S10 NS droplets, detected using the Summed method. Despite the high number of detected droplets in each image, the intensity ratio of the 4L10 image is 0.06, while 4S10 is 0.34. **B**: Comparison of summed droplet intensity to full image intensity for all images analysed using Smith, binarized, and summed detection algorithms, showing individual values and mean.

A.8 Binarisation of droplet images following the Klocke method

1. Confocal z-stack files were flatted using a Sum Projection in order to represent the maximum diameter of all captured droplets (A.9 A);

2. A Gaussian Blur filter was applied at 2σ to remove background speckling or noise, caused by random excitation of fluorophores or overexposed pixels in the detector;

3. The Find Edges command was applied, performing a Sobel edge detection

to define all regions with a large difference in intensity between two adjacent pixels (A.9 B);

4. The image was Auto Thresholded; a number of algorithms are available for this command, each performing a different series of mathematical transformations to produce a thresholded image. Of the available options, the Otsu threshold was chosen (A.9 C);

5. The image was converted to Binary (A.9 E), and was Skeletonised, converting all shapes to single-pixel-thick outlines (A.9 D);

6. The binary operations Fill Holes, Open, and Dialate were performed (A.9 E-H) to, respectively, fill any fully enclosed circles, remove any partial lines, and enlarge the boundaries of the defined objects to better match the original image.

7. Blobs are segmented into separate areas based on estimated nuclei using the Watershed command, which follows the Eucldian distance mapping process (A.9 H).

As shown in figure A.9, droplets of close adjacency tended to be grouped into a single object, despite the use of a Watershed segmentation command.

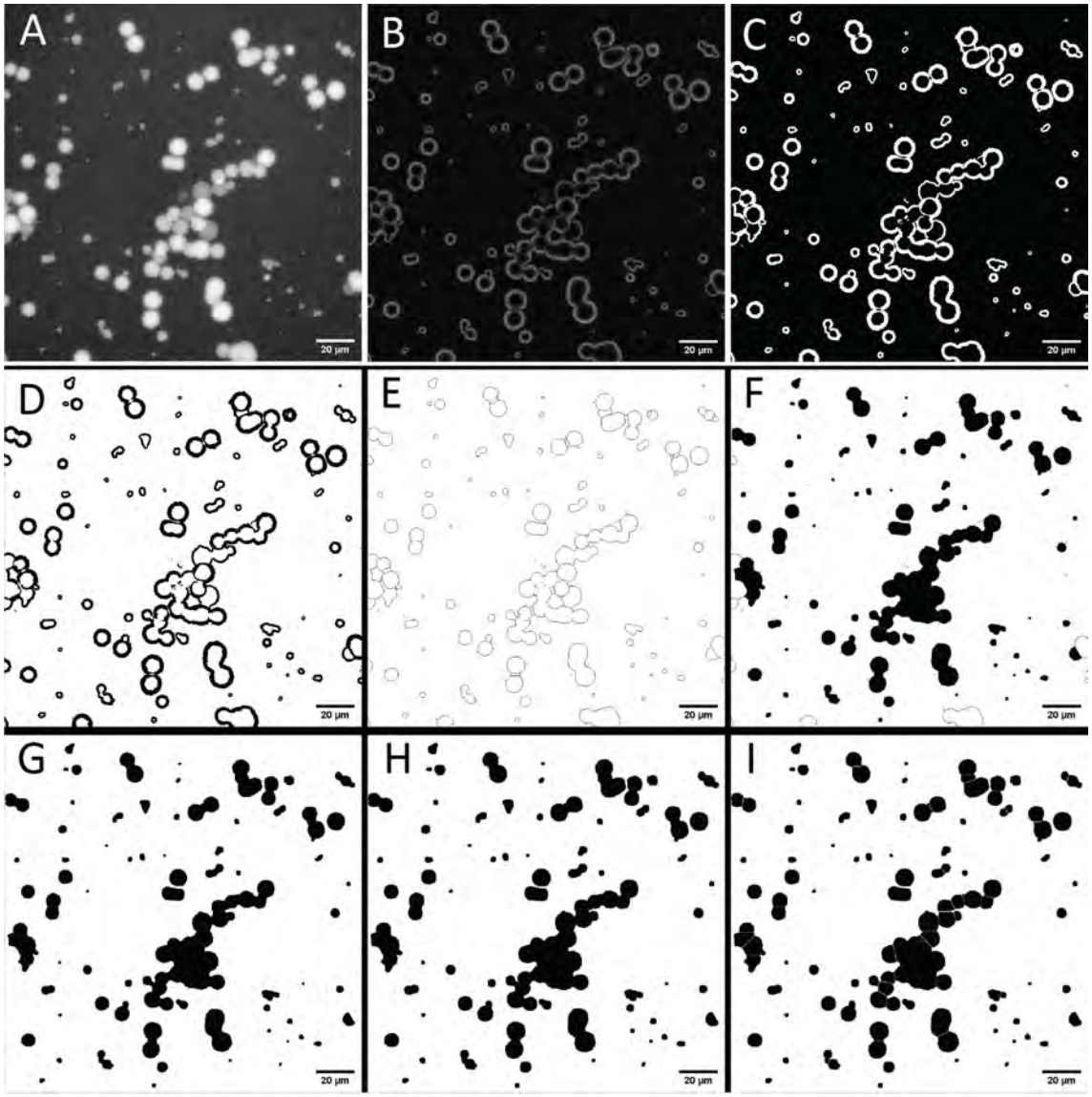

Figure A.9: Droplet image binarisation method, based on the work of Klock in Agarwal *et al.* 2022 [27].

A.9 Fluorescence recovery after photobleaching

When exposed to a sufficiently high energy source of light, fluorophores may be "bleached", undergoing covalent changes whilst in an excited state, rendering them unable to fluoresce [224]. As the subunits of a liquid body are constantly in motion, a small area of fluorophores may be selectively bleached in order to measure the kinetics of this internal diffusion. The rate of fluorescence recovery in the bleached area gives an indication of the rate of motion of the system's subunits, as bleached fluorophores exchange position with surrounding unbleached molecules [225]. A system investigated by FRAP may be either completely or partially mobile. In the former case, all subunits of the system are able to exchange position, and the bleached area will regain close to 100% fluorescence intensity. In a partially mobile system, only a portion of system subunits are mobile (termed the fraction of mobile phase). This occurs in viscoelastic systems, and is seen as fluorescence recovery plateauing well below 100% fluorescence intensity.

FRAP was conducted on droplets produced under standard conditions; using a LEICA TCS SP5 inverted confocal microscope fitted with a 561 nm laser; images were captured between 571 and 621 nm through a 100x oil immersion objective. Samples were heated using a LAUDA Ecoline RE 206 water-heated stage, with slides being acclimated for twenty minutes prior to imaging. Five consecutive frames were captured pre-bleaching to act as baseline images; regions of interest were irradiated to 70% laser power for 30 seconds; recovery was captured for five minutes at 3 s frame^{-1}. The resulting images were analysed using ImageJ; ROI were manually identified, and pixel intensity data extracted using plugin `Create Spectrum JRU v1` [226]. Raw data was then processed to account for photofading and normalised against a reference droplet using the following equations [225]:

$$
\begin{aligned}
C(t) &= R(0)/R(t) \\
I_{correct}(t) &= C(t) \times I(t) \\
I_{noramlized}(t) &= I_{correct}(t) - min(I_{correct})/I_{correct}(0) - min(I_{correct})
\end{aligned}
\tag{A.1}
$$

Normal imaging conditions, although intended to be non-damaging to the sample, will nevertheless bleach some proportion of fluorophores across the imaged area. Therefore, if the fluorescence of the bleached portion of the sample is recorded in isolation, the rate of recovery will be undervalued due to this universal constant level of bleaching. Because of this, a correction factor (C) is calculated for each time point (t) during imaging, by monitoring the fluorescence of a reference unbleached region over time. This is used to correct the measured intensity of the bleached region (I), which is finally normalised against the region prior to bleaching. Multiple datasets were captured for each droplet type, normalised, and averaged; the mean data was then fit using the least sum of squares method to the function:

$$
I(t) = a \times (1 - exp(-t/\tau)) \tag{A.2}
$$

Wherein a and τ are fitting parameters affecting the maximum recovery value and rate of recovery, respectively. From the resulting fluorescence recovery curves, an indication of subunit motility may be deduced. The mobile fraction of a sample is, simplistically put, the portion that recovers fluorescence; that is, the degree of recovered fluorescence in relation to the initial fluorescence value. The immobile fraction are those subunits that are fixed in place – in this case, nanostars that have gelated in the droplet mesh, opposed to those that still experience transient binding of their sticky ends. The greater the mobile portion, the comparatively more liquid the droplet is under given conditions.

A.10 Nanostar mesh sizing using dextran infiltration

A series of variously sized dextrans between 4 – 70 kD in mass, each functionalised with a fluorescein isothiocyanate (FITC) fluorophore (Sigma Aldrich, Australia), were combined in solution with 8, 8-A, and 10 nt SE droplets at 50 μg/mL (Nguyen et al. 2019). Solutions were homogenised and incubated for ten hours at 4 ^{o}C, prior to imaging. The resulting solutions were imaged using a LEICA SP5 confocal microscope, exciting the FITC at 488 nm and capturing the fluorescence from 500 to 550 nm. Images were captured as a series of twenty sequential frames; these were summed, in order to maximise sample signal and minimise random noise. The resultant images had 9 droplets manually selected, with the fluorescence intensity of the FITC channel measured; 9 regions of the bulk solutions were similarly measured, in order to find the partition coefficient of the FITC-dextran.

A.11 Nanostar mesh size using VMMC simulation

The distance between the junctions of two dimerised nanostars was modelled using oxDNA (figure A.10). The tested nanostars, bound through hybridised SEs, ranged from 4S6 to 4L10 NSs. These represented all combinations of nanostar arm lengths and SE lengths. The systems were modelled in 0.5 M NaCl, at 25 ^{o}C, using a VMMC simulation. An unpaired base in the central junction of both nanostars was used as a reference point, and the distance between these two nucleotides found. The simulated distances were compared to the geometrically calculated maximum possible distances between junctions, found using arm length, SE length, and a value of 0.34 nm per base pair.

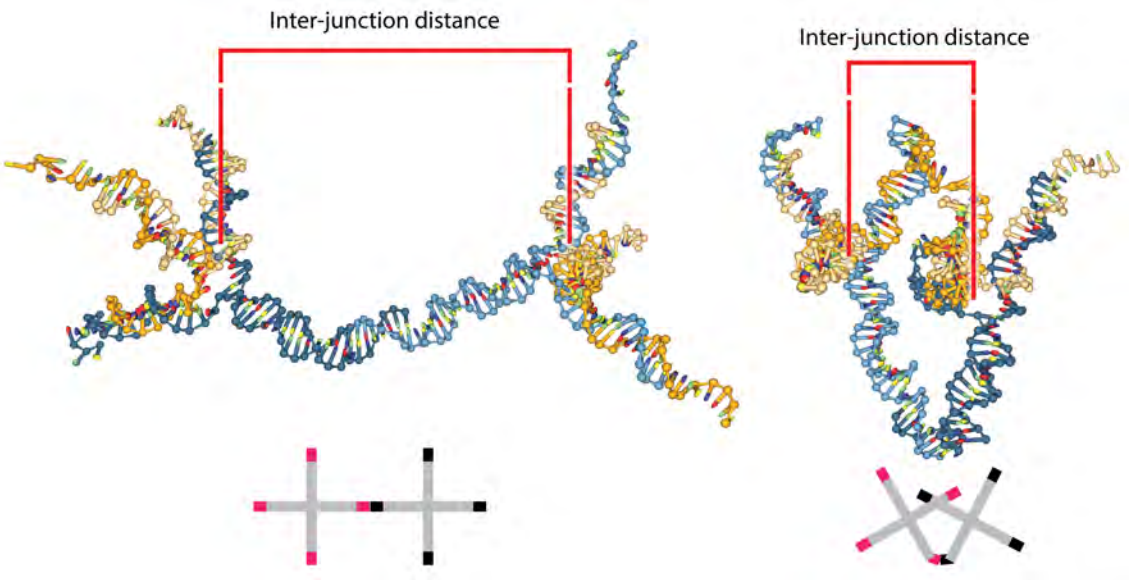

Figure A.10: Example of dimerised 4S8 nanostars modelled in oxDNA, indicating the inter-junction distance as quantified.

The results of the VMMC-modelled interjunction distance aligned closely with the predicted geometric maximum (figure A.11). In a system of two nanostars, most simulation frames saw both connected arms extended to near their maximum length. A small portion of samples saw bending of nanostar arms at the SE unpaired bases, leading to a reduced inter-junction distance (IJD). While such bending appears theoretically possible in a simulated dimer system, nanostars in a phase-separated droplet are part of a three-dimensional mesh. In such a network, most or all sticky ends would be hybridised, meaning bending of a nanostar in one direction would stretch at adjoining stars in other directions. Therefore, we hypothesise that bending of nanostars when in a liquid droplet rarely occurs, and that they tend to be held at close to their maximum IJD. However, the pore size of this network would likely still be less than the IJD, as the disordered nature of the mesh network means inter-connected stars may overlap through adjacent pores.

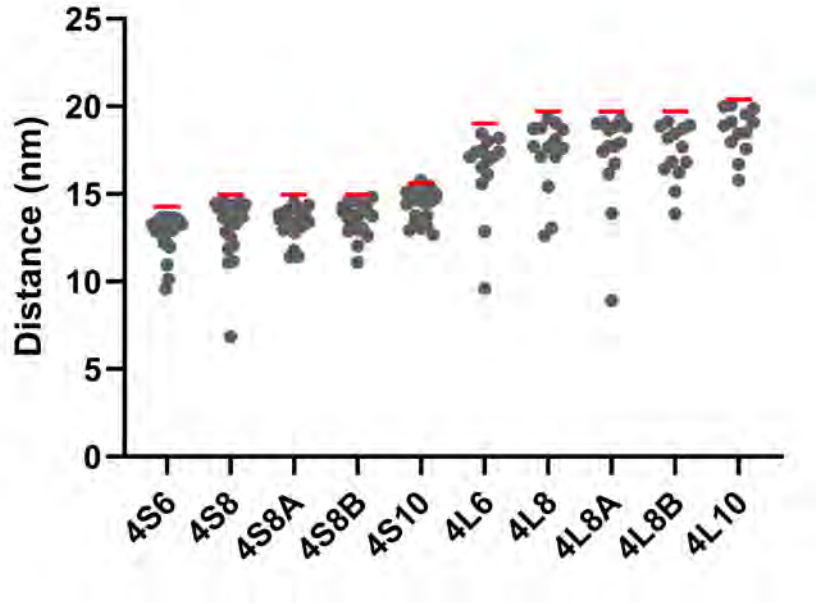

Figure A.11: Inter-junction distances found through oxDNA simulations for 4S6 - 4L10 nanostars. A slight increase in IDJ is seen with increasing SE length, and a significant difference is seen between S-length (16 bp) and L-length (23-bp) nanostars. Simulated results align closely with maximum calculated IJD. n = 18-22.

A.12 Hybridisation of linear DNA

Due to the uncertainty in calculating the hybridisation temperatures of short DNA sequences, hybridisation curve analysis was used to experimentally confirm calculated values.

HCA was first applied to sticky ends in isolation – short, linear, dimerising sequences that would establish a baseline for the technique. Each sequence was initially analysed using the online software NUPACK and DINAMelt, and their respective Analysis and Two State Melting Hybridisation functionalities (table A.5). In each, reaction conditions were set to 0.5 M Na^+ and 40 μM DNA and used to estimate the melting temperatures and free energy. In the case of NUPACK, hybridisation fractions at discrete temperatures are fit to the function

$$y = Y_M \times Y_0/((Y_M - Y_0) \times exp(-k \times x) + Y_0) \tag{A.3}$$

in order to calculate the temperature at which 50% of bases would be hybridised, where Y_0 and Y_M are the minimum and maximum recorded values, respectively. A disparity in estimated melting temperatures was evident between the two methods, demonstrating the difficulties inherent in estimating T_M. The calculated free energy was used as a measure of bond strength, representing the energy released upon hybridisation of the duplex.

Sticky ends strands (IDT DNA, Singapore) were combined in solution at 40 μM, the concentration they would be present at in a 10 μM solution of tetravalent nanostars, at a $[Na^+]$ of 0.5 M NaCl. To these were added three different intercalator conditions (1X SyGreen, 1X SYBR Green, or 0.5X SYBR Green), and hybridisation curves were produced using a Qiagen RotorGene Q (section A.13). Shown in figure A.12 are the resulting fluorescence traces of 6 nt sticky ends using each fluorophore ($n = 4$). The

Sticky end	Sequence	T_M (^{o}C) NUPACK	T_M (^{o}C) DINAMelt	ΔT_M D-N (^{o}C)	$-\Delta G$ (kcal/mol)
6 nt	CGATCG	30.8	28.9	-1.9	6.6
8 nt	CGAGCTCG	48.5	50.2	1.7	10.9
8-A nt	GCGATCGC	51.5	52.8	1.3	11.5
8-B nt	GCTATAGC	33.5	36.4	2.9	8.1
10 nt	CTGAGCTCAG	53.5	52.4	-1.1	12.3

Table A.5: Sticky end sequences, calculated T_M, and $-\Delta G$ at 40 μM strand concentration, 0.5 M NaCl, and 25 ^oC.

fluorescence trace of each repeat was normalised to a scale of 0 – 100% based on its minimum and maximum values. The mean of the four repeats was calculated and fit to the sigmoidal function

$$y = Bottom + (Top - Bottom)/(1 + (IC50/x)^{HillSlope}) \tag{A.4}$$

The high level of agreement between repeats, exemplified by low deviations about the mean, highlights the precision and reproducibility of this technique. As seen in figure A.12, as each system cooled from 95 ^{o}C, each curve maintained low fluorescence until approximately 55 ^{o}C, indicating a low level of hybridisation until this point. Between 55 – 35 ^{o}C there was a rapid increase in fluorescence, signalling the onset of hybridisation, followed by plateauing as the system further cooled.

With melting temperature defined as the point at which 50% of bases are hybridised, the fit curves were used to find the T_M of each trace. In the case of the 6 nt SE, these were 41.8 ± 0.1, 39.3 ± 0.3, and 41.0 ± 0.1 ^{o}C for 1X SyGreen, 1X SYBR Green, and 0.5X SYBR Green, respectively. The difference between the computationally derived melting temperatures (28.9 – 30.8 ^{o}C) and the experimentally determined values emphasises the need for experimental methods. The computationally and experimentally derived hybridisation values for all sticky ends are summarised in

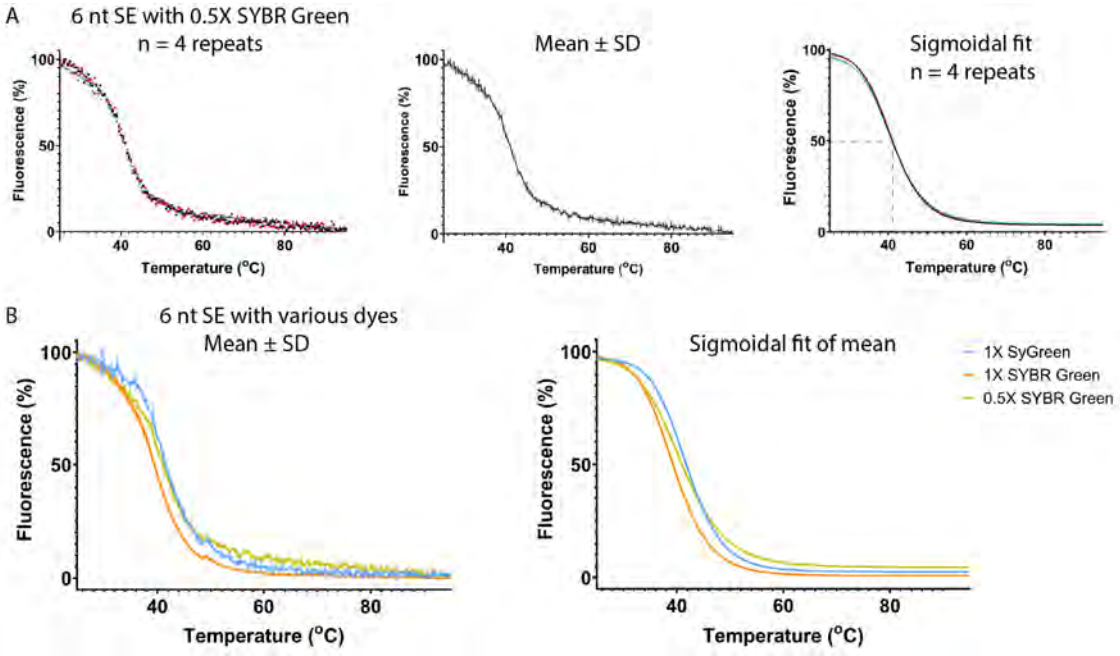

Figure A.12: Statistical analysis of sticky end formation temperature. **A**: Four repeats of hybridisation curves were produced in a RotorGene Q. A low standard deviation between the replicates shows a high repeatability in the data. Data was fit to a sigmoidal curve, and the temperature at a fluorescence intensity of 50% taken as the T_{Hy}. **B**: Process was repeated using different intercalating dye conditions, with a T_{Hy} found for each condition.

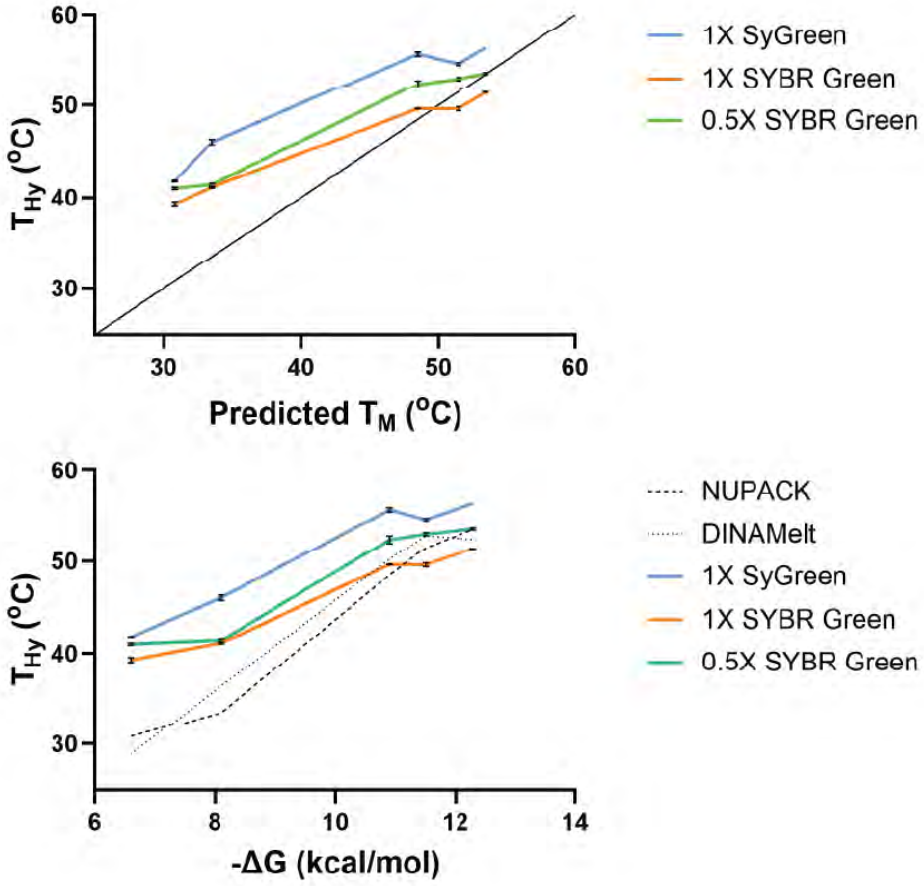

Figure A.13: Experimentally determined hybridisation temperatures of bare SE sequences, plotted against computationally determined melting temperatures (NUPACK) and free energy (DINAMELT). Results compare 1X SyGreen, 1X SYBR Green, and 0.5X SYBR Green fluorophores in a RotorGene Q qPCR system. Data shown as mean ± SD.

figure A.13. While the computational predictions are in closer agreement for stronger sticky end sequences, the low fidelity of prediction for short sequences results in large differences for the weaker 6 and 8B nt SEs.

Two intercalators were used in this work; SYBR Green and SyGreen. Both are asymmetrical cyanine dyes that intercalate within the minor groove of a double stranded helix, allowing for quantification of hybridisation within the system. The SYBR Green dye, provided as a 10,000X concentrate in DMSO, was diluted in MilliQ water and used in solution at 0.5X or 1X concentration. The SyGreen dye

was obtained in qPCR master mix form, a solution containing the dye, Taq polymerase, dNTPs, ROX reference dye, and various proprietary buffer components, the details of which are not available. This system, obtained as a 2X concentrate, was used in solution at a 1:10 dilution to avoid the unknown PCR reaction components interfering with the formation of nanostars; this dilution in hereafter referred to as 1X concentration.

Both SyGreen and SYBR Green are intercalating dyes, which undergo conformational changes when fitting between the nucleotides of dsDNA [189]. These structural changes in the dye cause an exponential increase in their fluorescence response, allowing for the quantitative detection of dsDNA content in a system. The insertion of a fluorophore molecule between the nucleotides of a dsDNA sequence causes a lengthening and partial unwinding of the helix [189] [227] [228]. Zipper *et al.* additionally demonstrated that a second binding mechanism occurs at high concentrations of intercalator: surface binding of the fluorophore to the dsDNA [189]. As the chemical structures and formulations of SyGreen and SYBR Green are proprietary information, their precise chemical interaction with the structure of the dsDNA helix cannot be determined. In the case of ethidium bromide, a commonly used intercalator, this insertion has been shown to increase the melting temperature of the DNA duplex [227]. Additionally, Giglio *et al.* compared four different SYBR Green preparations from different suppliers in analysing the melt curves of a multiproduct PCR reaction [229]. They found that the SYBR Green preferentially bound to one of two targets in most tested reaction conditions, and the measured melting temperature of the targets varied by up to 5 ^{o}C between fluorophore preparations.

In this thesis, a significant difference was found between the hybridisation temperature traces of the three fluorophore conditions (Tukey multiple comparisons test, $P < 0.0001$). As demonstrated by Giglio *et al.*, the same product may present different melting temperatures in a melt curve analysis depending on the fluorophore prepa-

ration. It is possible that a similar effect is seen in HCA here. This may be caused by different DNA-fluorophore interactions between SyGreen and SYBR Green, and different strengths of interaction between 0.5X and 1X SYBR Green.

A.13 Hybridisation curve analysis

Hybridisation curve analysis was conducted using a RotorGene Q Real-Time PCR System (Qiagen, Germany) and a CFX Opus 96 Real-Time PCR System (Bio-Rad, Australia) in section 2.6. DNA solutions were prepared under the same conditions as when capturing confocal micrographs (10 μM nanostructures, 500 mM NaCl), but with the fluorophore and fluorophore connector strands removed; in their place was added an intercalating dye. In a typical analysis, the samples were heated to 95 ^{o}C for five minutes, with the temperature then decreasing at a rate of 0.5 ^{o}C/min until reaching a minimum temperature of 25 ^{o}C; fluorescence was captured every sixty seconds with an excitation energy of 470 $\pm$ 10 nm and a detection range of 510 $\pm$ 5 nm. Samples were studied with n = 4 repeats, and resulting data was normalised to range from 0 – 100% fluorescence intensity.

The resulting fluorescence intensity curves were analysed using a MATLAB script to identify the temperature of phase separation (script B.5). Individual normalised intensity curves were smoothed using a Gaussian function with a window size of 5%. A `findpeaks` algorithm was applied, with parameters chosen to identify the single largest peak in the curve; the corresponding X-value was taken as the phase separation temperature of the sample (figure A.14).

Certain samples did not undergo shifts in fluorescence intensity during annealing (figure A.15). As such, phase separation temperatures could not be estimated using hybridisation curve analysis. This was generally seen in droplets containing 6 or 8B-nt SEs, particularly 3S6 and 3S8B droplets.

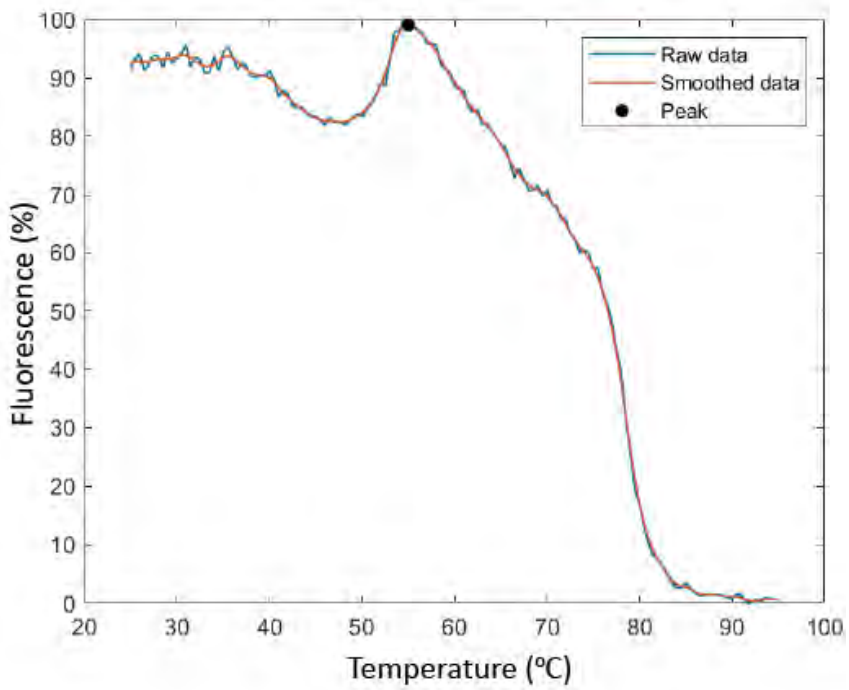

Figure A.14: Example fluorescence intensity curve of a 3S8A nanostar solution prepared under standard conditions (blue). Superimposed are the Gaussian smoothed curve (orange), and the algorithmically detected T_{PS} value (black).

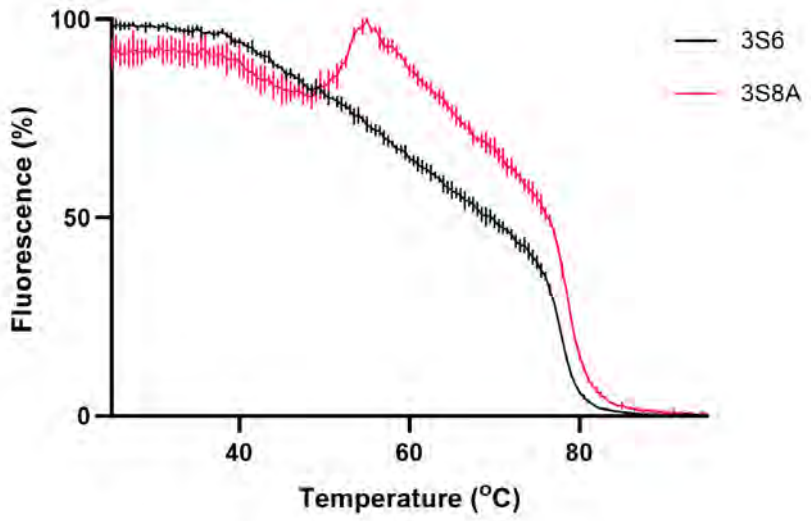

Figure A.15: Fluorescence intensity curves of 3S6 (black) and 3S8A (pink) nanostars prepared under standard conditions (shown as mean ± SD, n = 4). The low SE strength 3S6 nanostar does not exhibit a T_{PS} peak.

A.14 Production of two-nanostar solutions

In multi-nanostar solutions, a volume of 4 μL of each 55 μM strand was combined for each nanostar, alongside 4 μL of 5.5 M NaCl solution and 1 μL each of fluorophore and fluorophore connector strands. For solutions above 0 %C, a portion of the volume of relevant strands was replaced with alternate SE strands, as detailed in table A.6 and table A.7. The resulting solution was annealed and prepared for imaging as detailed in section A.3. In the nomenclature of this work, a 4S8 4L10 25 %C solution contains equimolar concentrations of 4S8 and 4L10 nanostars, with 25% of sticky ends in the 4L stars being complementary to the 4S8. In this chapter, unless otherwise specified, 3S nanostar droplets are false-coloured yellow; 4S droplets are red; and 4L droplets cyan. This is done for visual continuity between images, as depending on the context of various experiments, the same nanostar may be tagged with different fluorophores.

	Original		Replacement	
%C	Strand 1	Strand 2	Strand 1	Strand 2
0	4	4		
6.25	3.5	3.5	0.5	0.5
12.5	3	3	1	1
16	2.72	2.72	1.28	1.28
25	2	2	2	2
50			4	4

Table A.6: Strand replacement in tetravalent stars for 0-50 %C; μL

	Original		Replacement	
%C	Strand 1	Strand 2	Strand 1	Strand 2
0	4	4		
8	3	4	1	
16	2	4	2	
32	2	2	2	2
50	1	1	3	4

Table A.7: Strand replacement in trivalent stars for 0-50 %C; μL

A.15 Calculation of surfactant star probabilities

Case 1: 100% replacement of Strand 1			
Strand 1 100% A	Strand 2 100% B	Strand 3 100% B	Strand 4 100% B
P(A=1)	$1.0(A) \times 1.0(B)^3$		100%
Case 2: 50% replacement of Strand 1 and Strand 2			
Strand 1 50% A 50% B	Strand 2 50% A 50% B	Strand 3 100% B	Strand 4 100% B
P(A=0)	$0.5(B) \times 1.0(B)^3$		25%
P(A=1)	$0.5(A) \times 0.5(B) \times 1.0(B)^2 \times 2$		50%
P(A=2)	$0.5(A)^2 \times 1.0(B)^2$		25%
Case 3: 50% replacement of Strand 1 and Strand 3			
Strand 1 50% A 50% B	Strand 2 100% B	Strand 3 50% A 50% B	Strand 4 100% B
P(A=0)	$0.5(B) \times 1.0(B)^3$		25%
P(A=1)	$0.5(A) \times 0.5(B) \times 1.0(B)^2 \times 2$		50%
P(A=2)	$0.5(A)^2 \times 1.0(B)^2$		25%
Case 4: 25% replacement of Strands 1-4			
Strand 1 25% A 75% B	Strand 2 25% A 75% B	Strand 3 25% A 75% B	Strand 4 25% A 75% B
P(A=0)	$0.75(B)^4$		31.65%
P(A=1)	$0.25(A) \times 0.75(B)^3 \times 4$		42.19%
P(A=2)	$0.25(A)^2 \times 0.75(B)^2 \times 6$		21.09%
P(A=3)	$0.25(A)^3 \times 0.75(B) \times 4$		4.69%
P(A=4)	$0.25(A)^4$		0.39%

Table A.8: Calculation of probabilities of tetravalent star structures based on pattern of sticky end replacement, using discrete probability distributions. It is assumed that the sticky end placements are independent events.

The 4L8B (25 %C 8-nt SE) systems were also replicated in NUPACK, in order to calculate the estimated concentrations of particular complex formations.

```
from nupack import *
model1 = Model(material = 'dna', celsius = 25, sodium = 0.5)

strand1_A = Strand('CAGCCGGTTGCCCTTAAGCTGCGaaGCATCGGCACAAACGACTGCA
↪ TCaCGAGCTCG', name =
↪ 'strand1_A')
strand1_B = Strand('CAGCCGGTTGCCCTTAAGCTGCGaaGCATCGGCACAAACGACTGCA
↪ TCaGCTATAGC', name =
↪ 'strand1_B')
strand2_A = Strand('GATGCAGTCGTTTGTGCCGATGCaaGGCTTCGCCTACAGTCCGGCT
↪ CCaCGAGCTCG', name =
↪ 'strand2_A')
strand2_B = Strand('GATGCAGTCGTTTGTGCCGATGCaaGGCTTCGCCTACAGTCCGGCT
↪ CCaGCTATAGC', name =
↪ 'strand2_B')
strand3_A = Strand('GGAGCCGGACTGTAGGCGAAGCCaaCGCTCGGAGACACGATTGGGC
↪ TGaCGAGCTCG', name =
↪ 'strand3_A')
strand3_B = Strand('GGAGCCGGACTGTAGGCGAAGCCaaCGCTCGGAGACACGATTGGGC
↪ TGaGCTATAGC', name =
↪ 'strand3_B')
strand4_A = Strand('CAGCCCAATCGTGTCTCCGAGCGaaCGCAGCTTAAGGGCAACCGGC
↪ TGaCGAGCTCG', name =
↪ 'strand4_A')
strand4_B = Strand('CAGCCCAATCGTGTCTCCGAGCGaaCGCAGCTTAAGGGCAACCGGC
↪ TGaGCTATAGC', name =
↪ 'strand4_B')

case1 = Tube(strands = {strand1_A:5e-6, strand2_B:5e-6,
↪ strand3_B:5e-6, strand4_B:5e-6}, complexes =
↪ SetSpec(max_size=4), name = 'case1')
case2 =Tube(strands = {strand1_B:2.5e-6, strand1_A:2.5e-6,
↪ strand2_B:2.5e-6, strand2_A:2.5e-6, strand3_B:5e-6,
↪ strand4_B:5e-6}, complexes = SetSpec(max_size = 4), name =
↪ 'case2')
case3 = Tube(strands = {strand1_B:2.5e-6, strand1_A:2.5e-6,
↪ strand2_B:5e-6, strand3_B:2.5e-6, strand3_A:2.5e-6,
↪ strand4_B:5e-6}, complexes = SetSpec(max_size = 4), name =
↪ 'case3')
case4 = Tube(strands = {strand1_B:3.75e-6, strand2_B:3.75e-6,
↪ strand3_B:3.75e-6, strand4_B:3.75e-6, strand1_A:1.25e-6,
↪ strand2_A:1.25e-6, strand3_A:1.25e-6, strand4_A:1.25e-6},
↪ complexes = SetSpec(max_size = 4), name = 'case4')
```

Figure A.16: Predicted complex concentrations based on pattern of sticky end replacement, calculated in NUPACK under experimental conditions of 5 μM [strand] and 0.5 M [Na^+]. Results align with calculated discrete probability distributions in section 3.4.

A.16 Measurement of shell width

The shells produced through different nanostar combinations were observed to vary in thickness. Therefore, a method for quantification of shell width was developed. It was also noted that different images possessed differing degrees of background noise, or a slight infiltration of shell nanostars towards the centre of the core. It was uncertain whether these factors would affect measurements of shell width. Therefore, simulated images of known radius were first generated, with varying degrees of shell width, shell infiltration, and background noise. Different quantification methods were applied to this simulated data in order to benchmark different techniques.

Simulated data was produced using a custom script (script B.7). Images representing confocal images of droplet shell channels were produced with a dense shell of varying thickness and radius. The centres of the simulated shells contained a lower average intensity, to simulate shell infiltration, while low intensity noise was generated across the image background. Each of the four variables (shell width, shell radius, central intensity, background noise) were randomly generated to create a dataset of two hundred simulated images. The images were further processed through the application of a Gaussian filter and the generation of random noise, in order to more closely simulate the appearance of experimental images (figure A.17).

Various shell width detection methods were applied to the simulated dataset, until one was found which could accurately detect shell widths and diameters, independent of background or applied noise. Pixel intensity profiles were drawn across the centre of shell images; in the simulated dataset, twelve profiles were captured for each image. The resulting curves were normalised, and peaks were detected using either a Gaussian, moving median, or LOESS function. The Gaussian method reduces noise by averaging data across a window; the data are weighted in a Gaussian manner. In contrast, the moving median method finds the median of data in a window without weighting. The LOESS function performs a least squares regression analysis, without applying any assumptions about the distribution of the data. Window sizes of 0.1 were selected for each function. Following smoothing, the peak locations and peak

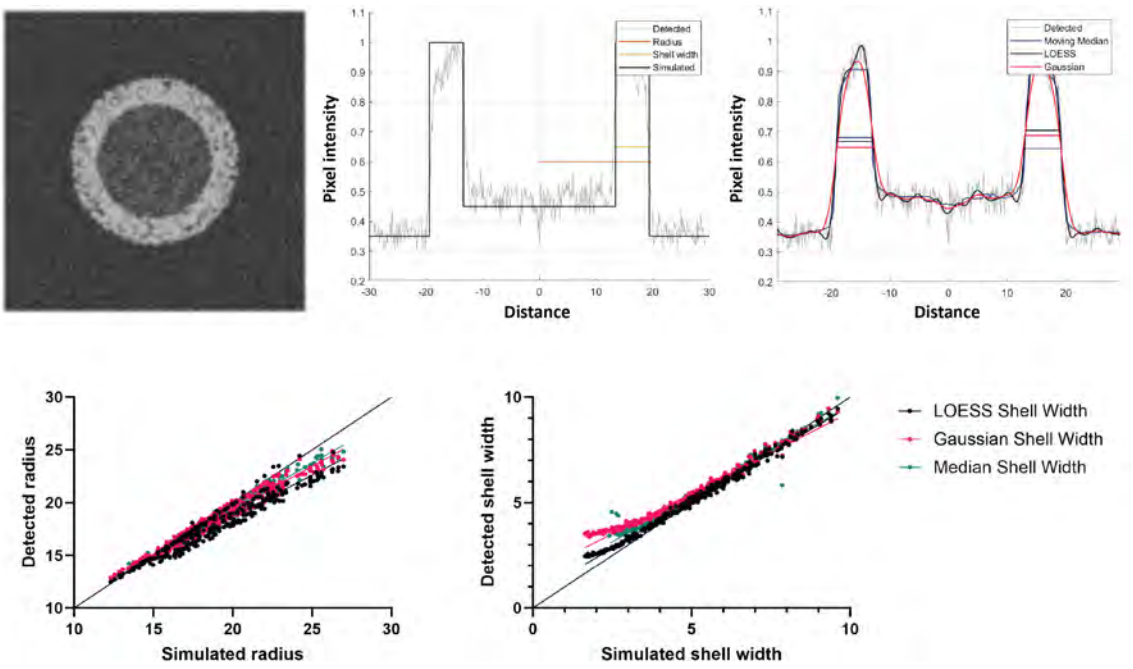

Figure A.17: Process and methods of shell simulation and detection. Example image of simulated data, with blur and noise filters applied. Simulated shell values with detected pixel profile, highlighting radius (orange) and shell width (yellow) values. Detected pixel profile across simulated shell, with Median, LOESS, and Gaussian smoothing algorithms. Comparison of simulated and detected values of shell radius and shell width. Line of identity shows X=Y.

widths of each smoothed dataset were calculated.

The shell width of a sample was calculated as the mean of the FWHM of each peak. The centre of a shell was found as the midpoint between both detected peaks. The diameter of the droplet was the distance between each outer curve at half height, calculated as the midpoint of each peak ± half the FWHM. In the simulated datasets, each of these values was known; therefore, the accuracy of a smoothing and detection method could be found by comparing the known values to the measured data.

Each of the three peak detection methods showed high accuracy when comparing simulated and measured values. In determining shell width, Gaussian, median, and LOESS values produced R^2 values of 0.978, 0.976, and 0.993, respectively, indicating a strong goodness of fit. These values were 0.974, 0.973, and 0.941 in detecting

droplet radius. While the Gaussian and LOESS methods were able to smooth and analyse all three hundred simulated datasets, the moving median method was unable to detect peaks in 10% of images. Additionally, when comparing the sum of residual squares between simulated and detected values, the LOESS algorithm showed the closest agreement with the simulated shell width data (19.7 vs 128.8). Therefore, for all future incidences of shell size analysis, a LOESS smoothing algorithm with a window size of 0.1 was used.

A.17 DNA nanostar droplet systems using magnesium chloride

The system used in this thesis was optimised such that the nanostars would form liquid droplets when annealed at 0.5 M [Na^+]. However, in order to more closely replicate cellular conditions and allow enzyme activity, lower cation concentrations were investigated.

As discussed in section 2.5.3, the majority of nanostars did not phase separate when annealed in the presence of 0.05 – 0.1 M [Mg^{2+}], instead of NaCl. Those which did phase separate formed droplets of high polydispersity and degree of wetting (figure 2.16). A decrease in [Mg^{2+}] to 0.01 M resulted in extended amorphous structures. These cation concentrations are lower than the [Na^+] required for droplet formation, which were 0.5 – 1 M in this system. The work of Jeon *et al.* linked a decrease in [Na^+] to a decrease in droplet surface tension, while Sato *et al.* demonstrated decreasing rates of droplet fusion with decreasing surface tension [30] [165]. If a similar effect occurred in this thesis, then the decrease in [Mg^{2+}] from 0.1 to 0.01 M may cause a reduction in surface tension, thereby reducing the drive for droplet fusion in the system, resulting in the extended structures seen.

To further explore the effect of cation choice on this system, HCA was performed, following the methods described in section 2.6. Nanostar phase separation temperatures were found to follow the same trends as systems prepared in 0.5 M [Na^+],

with slight variances in T_{PS} (figure A.18). The effect of a divalent cation solution on multi-star architectures was also explored. Nanostar combinations that were known to form core-shell (4S8 3S10, 4L10 3S8A, 4S8 4L8B) or patchy structures (4L8 4S8A) in 0.5 M [Na^+] were prepared in 0.05 M [Mg^{2+}] (figure 3.12).

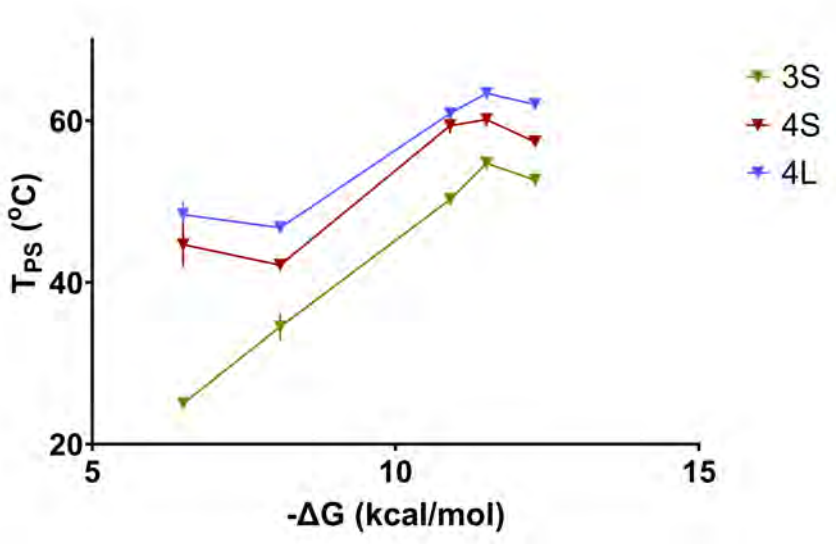

Figure A.18: Phase separation temperatures of nanostars prepared in 0.05 M [Mg^{2+}].

When annealed in the presence of magnesium cations, 4S8 3S10 droplets formed core-shell structures of a 4S8 core and 3S10 shell. However, they displayed a higher degree of infiltration of shell nanostars into the core in comparison to to same system in 0.5 M [Na^+], and the distribution of shell thicknesses was broader (figure A.19). Solutions of 4L10 3S8A nanostars tended to form distinct 3S8A droplets, with only a small portion containing 4L10 cores (figure A.20). Droplets of 4S8 4L8B showed the greatest structural similarity to 0.5 M [Na^+] solutions when prepared in 0.05 M [Mg^{2+}], forming core-shell structures in the majority of imaged droplets. However, when annealed with magnesium cations, the cores of these droplets tended to be less spherical, the shells tended to fuse to form towards multi-droplet aggregates (figure A.21). Finally, 4L8 4S8A droplets were known to form co-continuous particles under standard annealing conditions; when formed in the presence of magnesium, co-continuous particles still resulted, of a smaller mean droplet size (figure A.22).

These results would suggest that similar droplet formation mechanisms occur under

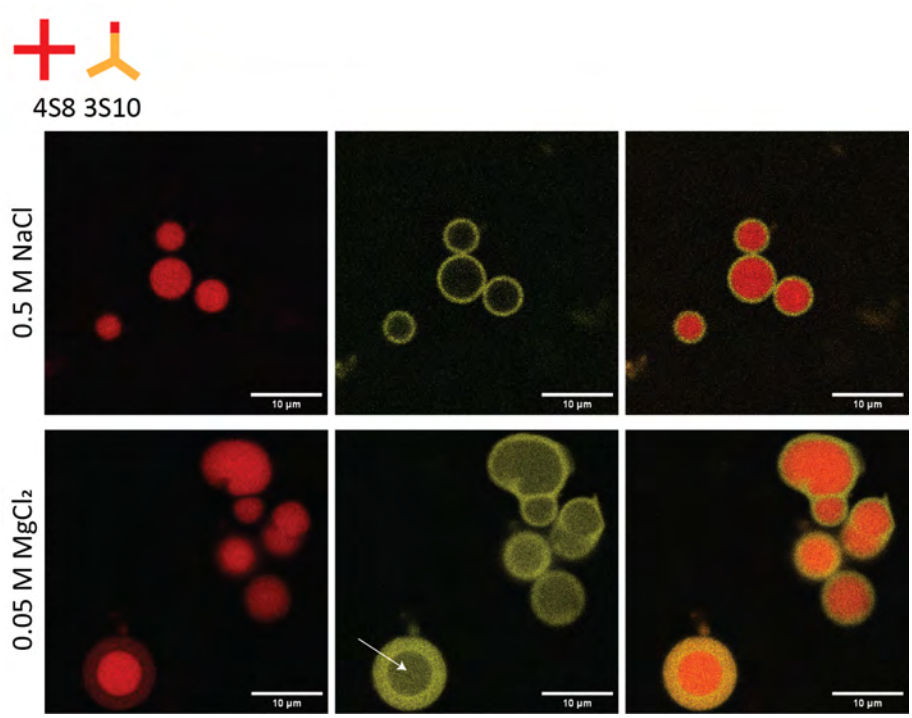

Figure A.19: 4S8 3S10 (16 %C 8-nt) droplets prepared in 0.5 M [Na^+] (ΔT_{PS} = 6.4 ^{o}C) and 0.05 M [Mg^{2+}] (ΔT_{PS} = 13.5 ^{o}C). White arrow indicates shell infiltration into core. Scale bars 10 μm.

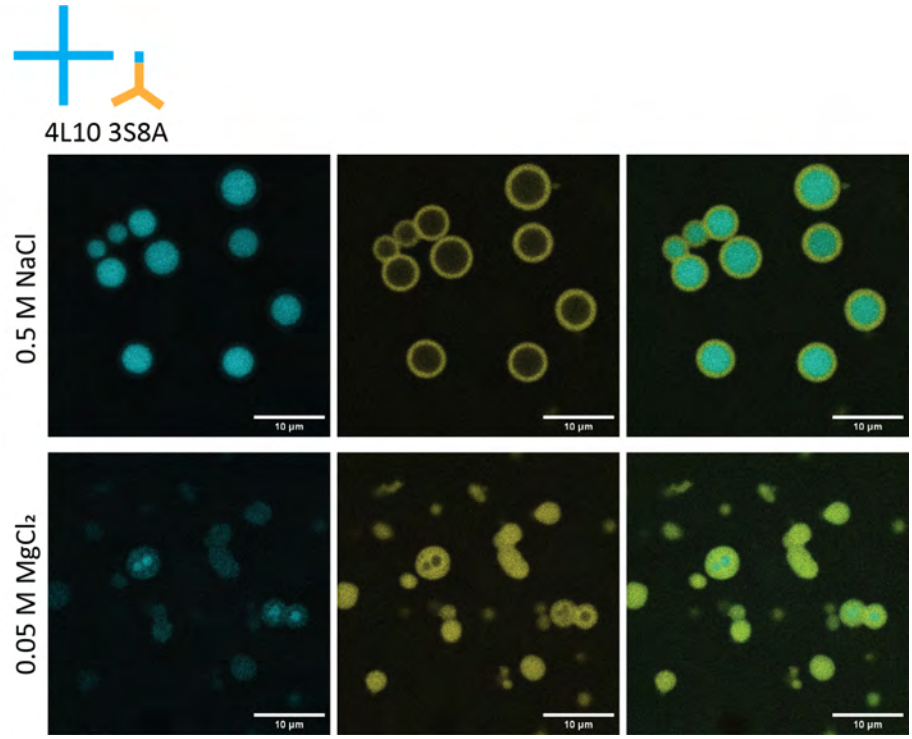

Figure A.20: 4L10 3S8A (16 %C 10-nt) droplets prepared in 0.5 M [Na^+] (ΔT_{PS} = 7.6 ^{o}C) and 0.05 M [Mg^{2+}] (ΔT_{PS} = 11.8 ^{o}C). Scale bars 10 μm.

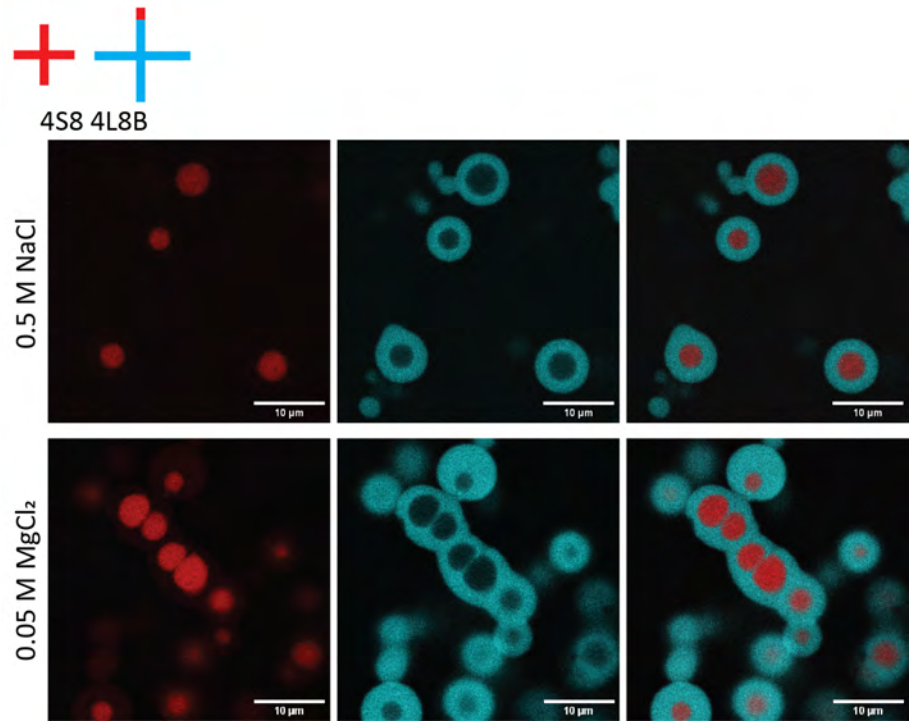

Figure A.21: 4S8 4L8B (25 %C 8-nt) droplets prepared in 0.5 M [Na^+] (ΔT_{PS} = 16.9 ^{o}C) and 0.05 M [Mg^{2+}] (ΔT_{PS} = 12.6 ^{o}C). Scale bars 10 μm.

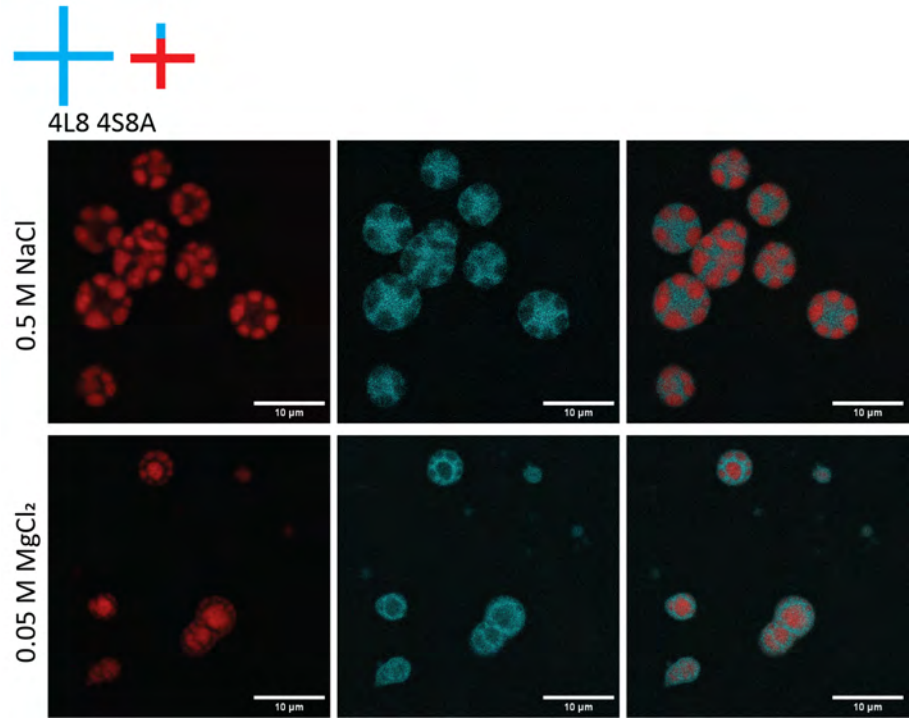

Figure A.22: 4L8 4S8A (25 %C 8-nt) droplets prepared in 0.5 M [Na^+] (ΔT_{PS} = −2.1 ^{o}C) and 0.05 M [Mg^{2+}] (ΔT_{PS} = 0.8 ^{o}C). Scale bars 10 μm.

both annealing conditions, but the degree of interaction between nanostars varies. For instance, the increased infiltration seen in 4S8 3S10 droplets at 25 %C in an $MgCl_2$ solution is comparable to the infiltration seen at 33 %C in NaCl (figure 3.5 vs 3.8). It is possible that the greater shielding afforded by the divalent magnesium cations allows for an increased degree of interaction between partially complementary nanostars. This hypothesised increase in nanostar binding may also explain the enhanced droplet fluidity seen in 4S8 4L8B droplets, which show higher shell-shell fusion in the presence of magnesium cations (figure C.3 vs A.21). However, this would not explain the lack of core-shell formation in 4L10 3S8A systems, the core deformation in 4S8 4L8B, or the smaller size of 4L8 4S8A droplets. Therefore, further study of the interrelated effects of magnesium concentration and inter-star complementarity is warranted.

A.18 Streptavidin localisation

As has been previously discussed in this work, the field of DNA nanotechnology is predicated on the concept of Watson-Crick base-pairing specificity (section 1.5). According to this theory, a strand of ssDNA will only hybridise to its complementary sequence, even when in the presence of non-complementary oligonucleotides. This concept may be further leveraged to create toehold mediated strand-displacement reactions (TMSD) [215]. Two partially complementary ssDNA sequences may hybridise when one is shorter than or contains mismatches to the other. If a fully complementary ssDNA strand is introduced to the system, the partially complementary strand will be displaced in favour of the complete sequence.

The sequence-specificity of DNA binding allows for the selective functionalisation of DNA nanostructures. For instance, nanostars droplets in this work are functionalised with 1% fluorescent strands. In this case, one strand of the nanostar is extended with a specific binding sequence (figure 2.2). The complementary sequence is found in fluorophore-functionalised strands. By appending the appropriate binding sequence to a nanostar, multiple different NS droplets may be visualised using

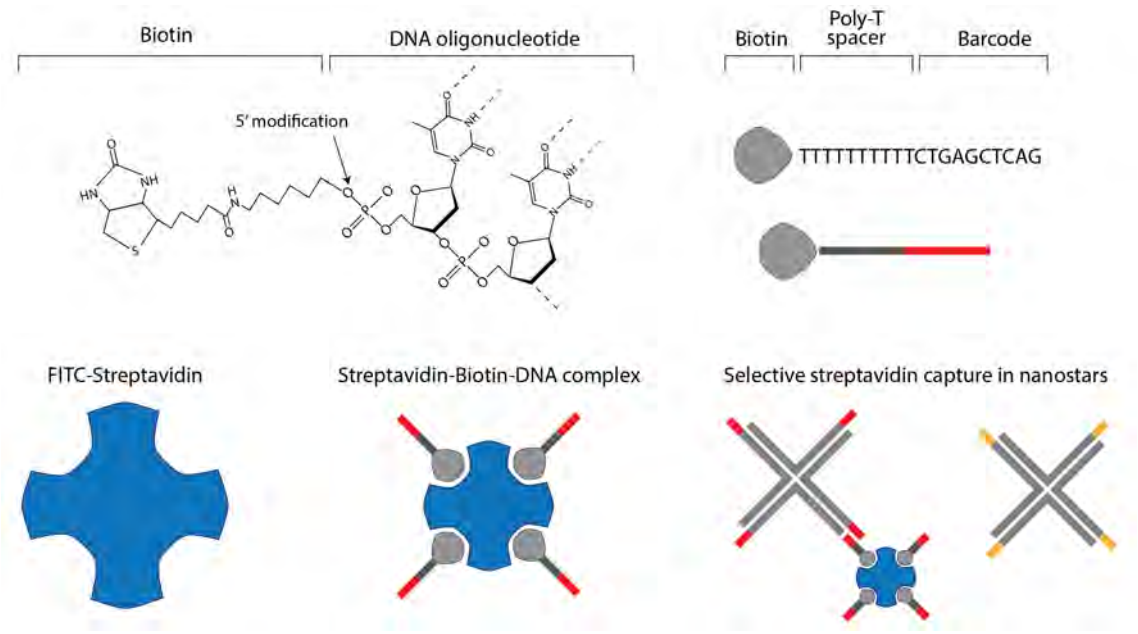

Figure A.23: Chemical structure of 5' modified biotinylated DNA. Illustration of biotinylated DNA, showing biotin (grey pentagon), poly-T spacer (grey line), and binding sequence (red line). Four biotin-DNA duplexes may complex with a streptavidin molecule. A binding sequence-functionalised streptavidin may hybridise to a DNA nanostar exhibiting the complementary sequence.

the same fluorophore strand.

This selective functionalisation was further leveraged in the localisation of biomolecules. Nucleic acids may be biotinylated; that is, an oligonucletide may be produced with a biotin molecule covalently attached to the 5' carbon of a selected base [230]. This biotin may then bind to streptavidin (SA) - a spontaneously occurring reaction with an extremely high bond strength [206]. These interactions allow for the selective binding of SA proteins to DNA nanostructures (figure A.23).

Following droplet annealing, FITC-streptavidin (Thermo Fisher Scientific, Australia) was added to solution for a final concentration of 0.2 mg/ml, followed by ssDNA-biotin conjugate (IDT DNA Singapore) at 1.5 μM. Imaging was conducted on a Leica TCS SP8 Multiphoton Microscope, with FITC excitation at 488 nm and detection between 500 - 540 nm.

A.19 Nanostar arm sequence extensions for streptavidin capture

Strand	Sequence (5' - 3')
i-4S8 strand 1	GCT CTG CAA TGA ACT TAT CCC aTG GAC TAA CGG AAC GGt tAG TCA GGT ATG CCA GCa CGA GCT CG
i'-biotin	GGG ATA AGT TCA TTG CAT AGC ttt ttt ttt t/3Bio/
j-3S10 strand 1	GTG GTA GAG GAA CCA CGC TAC GAT GCT Gtt TGA AGG CAG GAG TGA CaC TGA GCT CAG
i'-j'-biotin	GGG ATA AGT TCA TTG CAT **AGC** TTC CTC TAC CAC **CTA** ttt ttt ttt t/3Bio/
j invader	**TAG** GTG GTA GAG GAA GCT

Table A.9: Sequences used in binding-sequence mediated streptavidin capture and release. **Green**: binding sequence i. **Purple**: binding sequence j. The j invader sequence has greater complementarity to i'-j'-biotin in order to promote invader-biotin binding over j-3S10-biotin.

A.20 Fluorescence Resonance Energy Transfer

The nanostars used in section 4.4 were functionalised with either Cy3 or Cy5 fluorophores. These are extensively used in FRET assays, having a distinct overlap between the emission spectrum of Cy3 and the excitation spectrum of Cy5 [231]. Following annealing, droplets were combined at 4 ^{o}C to a total volume of 40 μl and placed in a Corning 384 Low Flange microplate in a PHERAstar FSX plater reader, whereupon they were heated from 25 - 45 ^{o}C at 3 ^{o}C/hour.

Samples were sequentially irradiated in wavelengths 1) 520, 2) 540, and 3) 635 nm. In condition 1, fluorescence was detected at 570 and 670 nm in order to measure FRET activity. In condition 2, Cy3 fluorescence was detected at 580 nm, and in condition 3, Cy5 fluorescence was detected at 635 nm. The system temperature was increased by 1 degree every 20 minutes, with five measurements taken in every increment.

A.21 Switching of streptavidin complementarity

The following relates to section 5.2.2

```
from nupack import *
model1 = Model(material = 'dna', celsius = 25, sodium = 0.5)

j3S10 = Strand('ATGGTGGTAGAGGAACCACGCTACGATGCTGttTGAAGGCAGGAGTGACa
↪ aaaaTCACTCCTGCCTTCAttACCTGTCCGCACCAACaaaaaGTTGGTGCGGACAGGTttCA
↪ GCATCGTAGCGTGGaCTGAGCTCAG', name =
↪ 'j3S10')
4S8i = Strand('GCTGGCATACCTGACTttCGCAAATTTACAGCGCaaaaaGCGCTGTAAATT
↪ TGCGttCATCACTTGGGACCATaaaaaATGGTCCCAAGTGATGttCCGTTCCGTTAGTCCAa
↪ aaaaTGGACTAACGGAACGGttAGTCAGGTATGCCAGCaCGAGCTCGGCTATGCAATGAACT
↪ GATCCC', name =
↪ '4S8i')
jbiotin = Strand('ggTTCCTCTACCACCATttttttttttt', name = 'jbiotin')
I1 = Strand('aaaaATGGTGGTAGAGGAAcctcttcGGGATCAGTTCATTGCATAGC',
↪ name = 'I1')
I2 = Strand('GCTATGCAATGAACTGATCCCgaagaggTTCCTCTACCACCATtttt',
↪ name = 'I2')

t1 = Tube(strands = {j3S10:5e-6, 4S8i:5e-6}, complexes =
↪ SetSpec(max_size=5), name = 't1')
t2 = Tube(strands = {j3S10:5e-6, 4S8i:5e-6, jbiotin:1e-6},
↪ complexes = SetSpec(max_size=5), name='t2')
t3 = Tube(strands = {j3S10:5e-6, 4S8i:5e-6, jbiotin:1e-6,
↪ I1:1.2e-6}, complexes = SetSpec(max_size=5), name='t3')
t4 = Tube(strands = {j3S10:5e-6, 4S8i:5e-6, jbiotin:1e-6,
↪ I1:1.2e-6, I2:1.2e-6}, complexes = SetSpec(max_size=5),
↪ name='t4')

```

Strand	Sequence (5' - 3')
4S8-i loop	GCT GGC ATA CCT GAC Ttt CGC AAA TTT ACA GCG Caa aaa GCG CTG TAA ATT TGC Gtt CAT CAC TTG GGA CCA Taa aaa ATG GTC CCA AGT GAT Gtt CCG TTC CGT TAG TCC Aaa aaa TGG ACT AAC GGA ACG Gtt AGT CAG GTA TGC CAG CaC GAG CTC GGC TAT GCA ATG AAC TGA TCC C
j-3S10 loop	ATG GTG GTA GAG GAA CCA CGC TAC GAT GCT Gtt TGA AGG CAG GAG TGA Caa aaa TCA CTC CTG CCT TCA ttA CCT GTC CGC ACC AAC aaa aaG TTG GTG CGG ACA GGT ttC AGC ATC GTA GCG TGG aCT GAG CTC AG
j'-biotin	gGT TCC TCT ACC ACC ATt ttt ttt ttt/3Bio/
Invader 1	aaa aAT GGT GGT AGA GGA ACc tct tcG GGA TCA GTT CAT TGC ATA GC
Invader 2	GCT ATG CAA TGA ACT GAT CCC gaa gag GTT CCT CTA CCA CCA Ttt tt

Table A.10: Sequences used in NUPACK simulations of streptavidin localisation switching. **Red**: 8-nt sticky end. **Orange**: 10-nt sticky end. **Green**: binding sequence i. **Purple**: binding sequence j. **Cyan**: toehold.

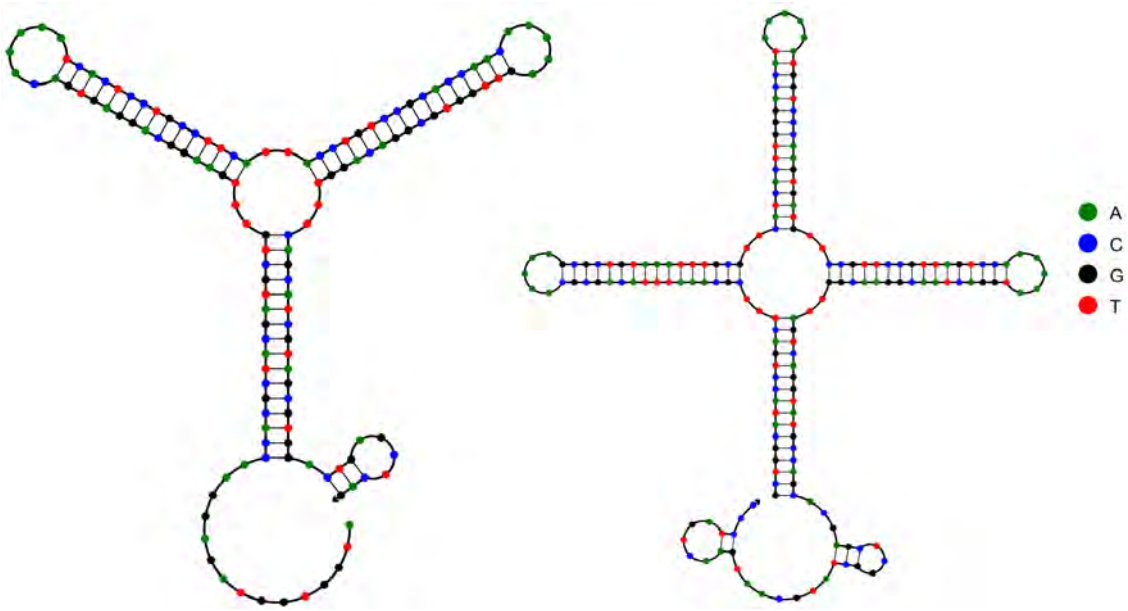

Figure A.24: NUPACK structures of looped j-3S10 and 4S8-i nanostars

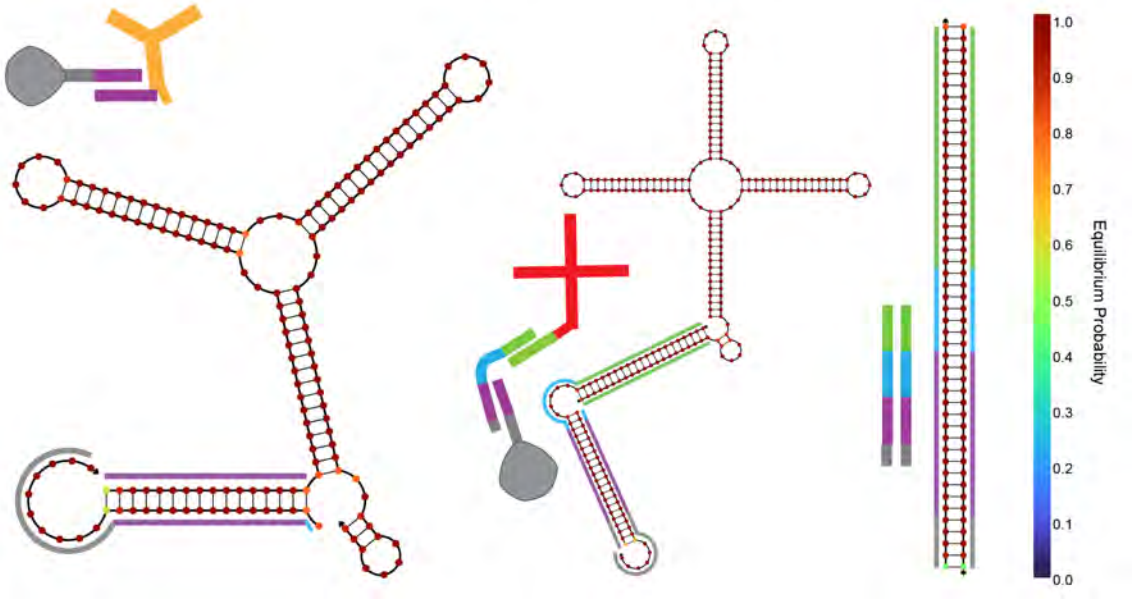

Figure A.25: Secondary structures of **A** j-3S10 and j'-biotin, **B** 4S8-i, I1, and j'-biotin, **C** I1 and I2.

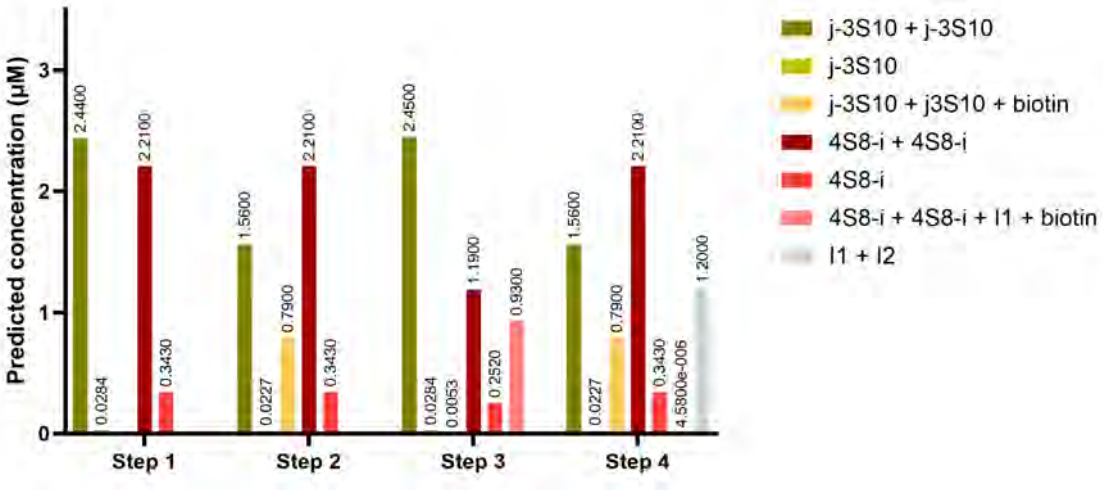

Figure A.26: NUPACK calculated concentrations of j-3S10, 4S8-i, biotin, and invader strands, showing secondary structure concentrations.

A.22 Organelle formation through surfactant switching duplex

The following relates to section 5.2.2.

```
from nupack import *
model1 = Model(material='dna', celsius=25, sodium=0.5)

loop_4S8A = Strand('GCTGGCATACCTGACTttCGCAAATTTACAGCGCaaaaaGCGCTGT
↪ AAATTTGCGttCATCACTTGGGACCATaaaaaATGGTCCCAAGTGATGttCCGTTCCGTTAG
↪ TCCAaaaaaTGGACTAACGGAACGGttAGTCAGGTATGCCAGCaGCGATCGC', name =
↪ 'loop_4S8A')
loop_4L8 = Strand('CAGCCGGTTGCCCTTAAGCTGCGaaGCATCGGCACAAACGACTGCAT
↪ CaaaaaGATGCAGTCGTTTGTGCCGATGCaaGGCTTCGCCTACAGTCCGGCTCCaaaaaGGA
↪ GCCGGACTGTAGGCGAAGCCaaCGCTCGGAGACACGATTGGGCTGaaaaaTCAGCCCAATCG
↪ TGTCTCCGAGCGaaCGCAGCTTAAGGGCAACCGGCTGaCGAGCTCG', name =
↪ 'loop_4L8')
loop_4S8 = Strand('GCTGGCATACCTGACTttCGCAAATTTACAGCGCaaaaaGCGCTGTA
↪ AATTTGCGttCATCACTTGGGACCATaaaaaATGGTCCCAAGTGATGttCCGTTCCGTTAGT
↪ CCAaaaaaTGGACTAACGGAACGGttAGTCAGGTATGCCAGCaCGAGCTCG', name =
↪ 'loop_4S8')
loop_4S8_toehold =
↪ Strand('GCTGGCATACCTGACTttCGCAAATTTACAGCGCaaaaaGCGCTGTAAATTTGC
↪ GttCATCACTTGGGACCATaaaaaATGGTCCCAAGTGATGttCCGTTCCGTTAGTCCAaaaa
↪ aTGGACTAACGGAACGGttAGTCAGGTATGCCAGCaCGAGCTCGaagtgc', name =
↪ 'loop_4S8_toehold')
switch_1 = Strand('gtgatcgattcggcacttCGAGCT', name = 'switch_1')
switch_2 = Strand('cgaatcgatcacaGCGATCGC', name = 'switch_2')

pre_switch = Tube(strands = {loop_4S8A:5e-6, loop_4L8:5e-6,
↪ loop_4S8:2.5e-6, loop_4S8_toehold:2.5e-6}, complexes =
↪ SetSpec(max_size=4), name = 'pre_switch')
post_switch = Tube(strands = {loop_4S8A:5e-6, loop_4L8:5e-6,
↪ loop_4S8:2.5e-6, loop_4S8_toehold:2.5e-6, switch_1:2.5e-6,
↪ switch_2:2.5e-6}, complexes = SetSpec(max_size=4), name =
↪ 'post_switch')
```

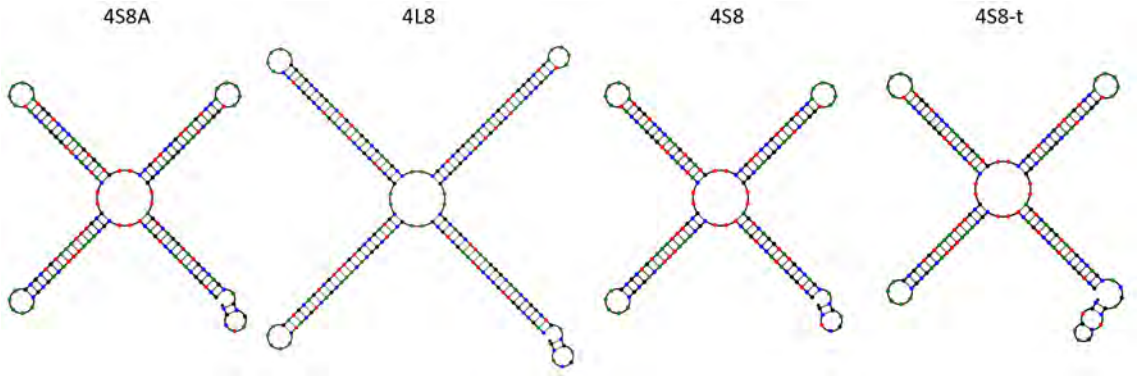

Figure A.27: NUPACK structures of looped 4S8A, 4L8, 4S8, and 4S8-t nanostars.

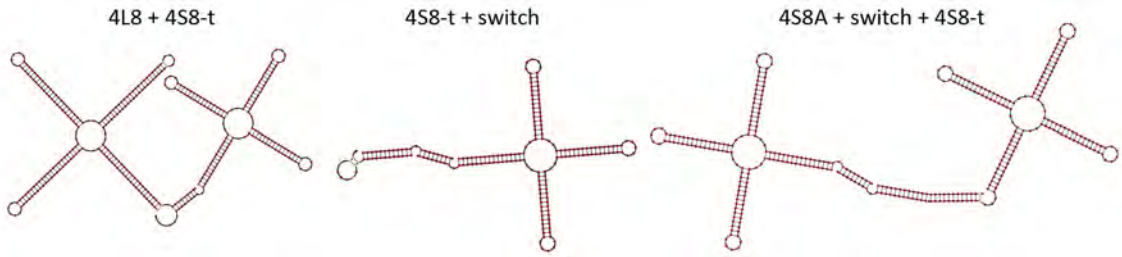

Figure A.28: NUPACK structures showing switch of 4S8-t conjugation from 4L8 to 4S8A, through binding to the switching duplex.

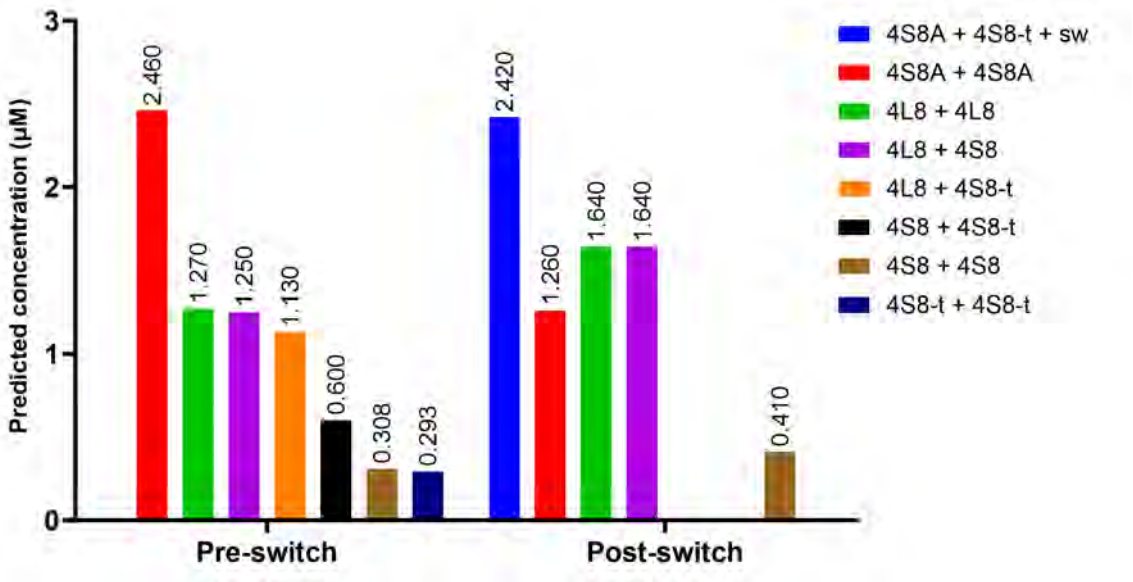

Figure A.29: NUPACK calculated concentrations of nanostructure complexes, before and after switching duplex addition, including secondary structures

Strand	Sequence (5'-3')
4S8A loop	GCT GGC ATA CCT GAC Ttt CGC AAA TTT ACA GCG Caa aaa GCG CTG TAA ATT TGC Gtt CAT CAC TTG GGA CCA Taa aaa ATG GTC CCA AGT GAT Gtt CCG TTC CGT TAG TCC Aaa aaa TGG ACT AAC GGA ACG Gtt AGT CAG GTA TGC CAG CaG CGA TCG C
4L8 loop	CAG CCG GTT GCC CTT AAG CTG CGa aGC ATC GGC ACA AAC GAC TGC ATC aaa aaG ATG CAG TCG TTT GTG CCG ATG Caa GGC TTC GCC TAC AGT CCG GCT CCa aaa aGG AGC CGG ACT GTA GGC GAA GCC aaC GCT CGG AGA CAC GAT TGG GCT Gaa aaa TCA GCC CAA TCG TGT CTC CGA GCG aaC GCA GCT TAA GGG CAA CCG GCT GaC GAG CTC G
4S8 loop	GCT GGC ATA CCT GAC Ttt CGC AAA TTT ACA GCG Caa aaa GCG CTG TAA ATT TGC Gtt CAT CAC TTG GGA CCA Taa aaa ATG GTC CCA AGT GAT Gtt CCG TTC CGT TAG TCC Aaa aaa TGG ACT AAC GGA ACG Gtt AGT CAG GTA TGC CAG CaC GAG CTC G
4S8 loop + toehold	GCT GGC ATA CCT GAC Ttt CGC AAA TTT ACA GCG Caa aaa GCG CTG TAA ATT TGC Gtt CAT CAC TTG GGA CCA Taa aaa ATG GTC CCA AGT GAT Gtt CCG TTC CGT TAG TCC Aaa aaa TGG ACT AAC GGA ACG Gtt AGT CAG GTA TGC CAG CaC GAG CTC Gaa gtg c
Switch duplex part 1	gtg atc gat tcg gca ctt CGA GCT
Swtich duplex part 2	cga atc gat cac aGC GAT CGC

Table A.11: Sequences used in NUPACK simulations of surfactant star complementarity switching. **Red**: 8-nt sticky end . **Blue**: 10-nt sticky end. **Cyan**: toehold 1. **Magenta**: toehold 2.

Appendix B

Custom scripts

B.1 Droplet detection and verification in MATLAB

```
%Find circles in a series of images, compare the circle and background intensities to a series of reference images (useful if finding in binary and comparing to Sum)

D = uigetdir('C:\','Choose an image location');
S = dir(fullfile(D,'*.tif'));
X = uigetdir('C:\','Choose a comparison location');
Y = dir(fullfile(X,'*.tif'));
SavePath = uigetdir('C:\','Choose a save location');
pathName = char(SavePath);
saveFileName = pathName(end-7:end);
baseDataFile = saveFileName + " radii.xlsx";
fullDataFile = fullfile(SavePath, baseDataFile);
intensityDataFile = saveFileName + " intensity.xlsx";
fullIntensityDataFile = fullfile(SavePath, intensityDataFile);
n = 600; %A number arbitrarily higher than the estimated number of droplets
allRadii = reshape(0:n-1,n,1);
allX = reshape(0:n-1,n,1);
allY = reshape(0:n-1,n,1);
setRadii = [1 1];
allIntensity = ["Sample" "Droplet Intensity" "Background Intensity" "Ratio"]';
```

```
20
21  for k = 1:numel(S)
22  % Define image
23      fFname = fullfile(D,S(k).name);
24      OGFile = imread(fFname);
25      compFname = fullfile(X,Y(k).name);
26      compFile = imread(compFname);
27      info = imfinfo(fFname); %extracts image info
28      res = extractfield(info,'XResolution');
29      [fF_path,fFname,fFext] = fileparts(fFname);
30      stringName = convertCharsToStrings(fFname);
31      gaus = imgaussfilt(OGFile,1);
32  % Find circles using the defined variables
33      [Ctrs,radii] = imfindcircles(gaus, [8
        ↪  30],'ObjectPolarity','bright', 'Sensitivity', 0.92,
        ↪  'EdgeThreshold', 0.30);
34      close
35  % Create a figure of the detected circles
36      figure
37      imshow(OGFile)
38      hold on
39      h = viscircles(Ctrs,radii,'EnhanceVisibility',false,'Color','r
        ↪  ','LineWidth',1);
40      hold off
41      for c = 1:length(radii)
42          c_list = num2str(c);
43          text(Ctrs(c,1), Ctrs(c,2), c_list, 'color', 'r',
            ↪  'FontWeight', 'bold', 'HorizontalAlignment',
            ↪  'center','VerticalAlignment', 'middle');
44      end
45  % Export processed image
46      F = getframe;
47      fFnameExt = fullfile(SavePath,[fFname,'_circles',fFext]);
48      imwrite(F.cdata, fFnameExt,'Resolution', res, 'Description',
        ↪  sprintf('ImageJ=1.53q\nunit=um\n'));
49  % Define circle locations
50      M = (radii/res(1))';
51      radiiMicron = (radii);
52      xMicron = Ctrs(:,1);
53      yMicron = Ctrs(:,2);
54  %Set a baseline value against which to compare circle intensities
55      baseIntensity = mean(compFile,"all");
56      empty = drawcircle('Center',[1 1],'Radius',1);
57      cover = createMask(empty);
```

```
58
59  % For all the radii in this column (AKA for this image), execute
    ↪  the following loop, until the radius is 0
60      for m = 1:height(radiiMicron)
61              if radiiMicron(m,1) == 0
62                  continue
63              end
64  % Draw a circle defined by the given X,Y, and radius values
65          blank = drawcircle('Center',[xMicron(m,1),yMicron(m,1)],'R
            ↪  adius',radiiMicron(m,1));
66  % Create a mask on this droplet and find the mean intensity in
    ↪  the circle
67          circle = createMask(blank);
68          testDroplet = compFile.*uint8(circle);
69          testIntensity = mean(nonzeros(testDroplet),"all");
70  % If the intensity of the circle is more than 1.5X the base
    ↪  intensity, add the circle to the overall mask and add the
    ↪  radius to the validated list
71          if testIntensity > 1.5*baseIntensity
72              cover = imadd(logical(cover),circle);
73              setRadii = [setRadii,radiiMicron(m,1)./res];
74          end
75      end
76
77  % Define the overall mask
78      mask = uint8(cover);
79  % Compute total intensity in all validated droplets
80      dropletsMask = compFile.*mask;
81      dropletIntensity = sum(dropletsMask,"all");
82  % Compute total intensity in total image
83      backgroundIntensity = sum(compFile,"all");
84  % Droplet to background ratio
85      intensityRatio = dropletIntensity/backgroundIntensity;
86  % Save intensity data
87      outputIntensity = [stringName dropletIntensity
        ↪  backgroundIntensity intensityRatio]';
88      allIntensity = [allIntensity,outputIntensity];
89      writetable(array2table(allIntensity),fullIntensityDataFile);
90  % Save the analysed image to the validation folder
91      imshow(OGFile)
92      F = getframe;
93      fFnameExt = fullfile(SavePath,[fFname,'_circles',fFext]);
        ↪  %save circles image
94      imwrite(F.cdata, fFnameExt);
```

```
    close()
% Save the validated image to the validation folder
    imshow(dropletsMask)
    L = getframe;
    fLnameExt = fullfile(SavePath,[fFname,'_masked',fExt]);
     ↪  %save circles image
    imwrite(L.cdata, fLnameExt);
% Save the validated radii to the validated folder
    namedRadii = [stringName,setRadii]';
    outputRadii = [namedRadii;ones((n-size(namedRadii,1)),1)];
    allRadii = [allRadii,outputRadii];
    writetable(array2table(allRadii),fullDataFile);
    setRadii=[];
    close()
end
close all
```

B.2 Droplet detection in ImageJ FIJI

```
run("Gaussian Blur...", "sigma=2");
run("Find Edges");
setAutoThreshold("Default dark");
setOption("BlackBackground", false);
run("Convert to Mask");
run("Hough Circle Transform","minRadius=20, maxRadius=100, inc=1,
 ↪  minCircles=1, maxCircles=600, threshold=0.8, resolution=100,
 ↪  ratio=1.0, bandwidth=10, local_radius=10,  reduce show_mask
 ↪  results_table");
```

B.3 Image binarisation in FIJI ImageJ

```
        run("Gaussian Blur...", "sigma=2");
        run("Find Edges");
        run("Auto Threshold", "method=Otsu ignore_black white");
        setOption("BlackBackground", false);
        run("Convert to Mask");
        run("Skeletonize");
```

```
        run("Fill Holes");
        run("Open");
        run("Dilate");
        run("Watershed");
```

B.4 Verification of droplets detected in ImageJ FIJI

```
%As part of ImageJ FIJI droplet detection, export files containing radius, X-coordinate, and Y-coordinate data for each circle.
%Load in files containing radii, X coordinate, and Y coordinate data in pixels as arrays
[F,L] = uigetfile('*xlsx','Choose radii data');
fFpath = [L,F]
pixelRadii = table2array(readtable(fFpath,ReadVariableNames=true));
[F,L] = uigetfile('*xlsx','Choose X coordinates');
fFpath = [L,F]
pixelX = table2array(readtable(fFpath,ReadVariableNames=true));
[F,L] = uigetfile('*xlsx','Choose Y coordinates');
fFpath = [L,F]
pixelY = table2array(readtable(fFpath,ReadVariableNames=true));

%Choose pre-analysed images to export with the output
D = uigetdir('R:\PRJ-KStumbles\LM imaging\','Choose an image location');
S = dir(fullfile(D,'*.tif'));
%Choose the original images to compare against
X = uigetdir('R:\PRJ-KStumbles\LM imaging\','Choose a comparison location');
Y = dir(fullfile(X,'*.tif'));
%Choose a save location
SavePath = uigetdir('R:\PRJ-KStumbles\LM imaging\','Choose a save location');
pathName = char(SavePath);
saveFileName = pathName(end-8:end);

%Files to save radii and intensity data
baseDataFile = saveFileName + " radii.xlsx";
fullDataFile = fullfile(SavePath, baseDataFile);
intensityDataFile = saveFileName + " intensity.xlsx";
```

```
fullIntensityDataFile = fullfile(SavePath, intensityDataFile);

%Create empty arrays in which to hold data
n = 600;
allRadii = reshape(0:n-1,n,1);
setRadii = [1 1];
allIntensity = ["Sample" "Droplet Intensity" "Background Intensity" "Ratio"]';

for k = 1:numel(S)
% Define image
    fFname = fullfile(D,S(k).name);
    OGFile = imread(fFname);
    compFname = fullfile(X,Y(k).name);
    compFile = imread(compFname);
    info = imfinfo(fFname); %extracts image info
    [fF_path,fFname,fFext] = fileparts(fFname);
    stringName = convertCharsToStrings(fFname);
    figure
    imshow(compFile)

%Set a baseline value against which to compare circle intensities
    baseIntensity = mean(compFile,"all");
    empty = drawcircle('Center',[1 1],'Radius',1);
    cover = createMask(empty);

%For all the radii in this column, execute the following loop, until the radius is 0
    for m = 1:height(pixelRadii)
            if pixelRadii(m,k) == 0
                continue
            end
%Draw a circle defined by the given X, Y, and radius values
        blank = drawcircle('Center',[pixelX(m,k),pixelY(m,k)],'Radius',pixelRadii(m,k));
%Create a mask on this droplet and find the mean intensity in the circle
        circle = createMask(blank);
        testDroplet = compFile.*uint8(circle);
        testIntensity = mean(nonzeros(testDroplet),"all");
%If the intensity of the circle is more than 1.5X the base intensity, add the circle to the overall mask and add the radius to the validated list
        if testIntensity > 1.5.*baseIntensity
```

```
            cover = imadd(logical(cover),circle);
            setRadii = [setRadii,pixelRadii(m,k)./5.544]; %This converts the pixel measurement to microns; change based on your resolution
        end
    end
    mask = uint8(cover);

%Compute total intensity in all validated droplets
    dropletsMask = compFile.*mask;
    dropletIntensity = sum(dropletsMask,"all");
%Compute total intensity in full image
    backgroundIntensity = sum(compFile,"all");
%Droplet to background ratio
    intensityRatio = dropletIntensity/backgroundIntensity;

%Save intensity data
    outputIntensity = [stringName dropletIntensity backgroundIntensity intensityRatio]';
    allIntensity = [allIntensity,outputIntensity];
    writetable(array2table(allIntensity),fullIntensityDataFile);
%Save the analysed image to the validation folder
    imshow(OGFile)
    F = getframe;
    fFnameExt = fullfile(SavePath,[fFname,'_circles',fFext]);
    imwrite(F.cdata, fFnameExt);
    close()
%Save the validated image to the validation folder
    imshow(dropletsMask)
    L = getframe;
    fLnameExt = fullfile(SavePath,[fFname,'_masked',fFext]);
    imwrite(L.cdata, fLnameExt);
%Save the validated radii to the validation folder
    namedRadii = [stringName,setRadii]';
    outputRadii = [namedRadii;ones((n-size(namedRadii,1)),1)];
    allRadii = [allRadii,outputRadii];
    writetable(array2table(allRadii),fullDataFile);
    setRadii=[];
    close()
end
close all
```

B.5 Identification of phase separation temperature from hybridisation curve

```
[F,L] = uigetfile('*xlsx','Choose hybridisation curve data');
data = readtable([L,F]);
array = table2array(data);
[R,C] = size(array);
saveLoc = convertCharsToStrings(uigetdir('C:\','Choose a save location'));
tpsData  = ["Sample","Smoothed"];
fullDataFile = fullfile(saveLoc, "computed Tps.xlsx");
xAxis = array(:,1);

for S = 2:C
    yAxis = smoothdata(array(:,S),"gaussian",7);
    [pks,locs] = findpeaks(yAxis, xAxis, minpeakprominence=3, minpeakdistance=40);
    tf = isempty(locs);
        if tf == 1
            locs = 25;
            pks = 100;
        end
    name = data.Properties.VariableNames{S};
    figure
    plot(xAxis,array(:,S),DisplayName="Raw data")
    hold
    plot(xAxis,yAxis,DisplayName="Smoothed data")
    plot(locs,pks,".",markersize=20,color='k',DisplayName="Peak")
    legend(location="northeast")
    title(name)

    saveName = (saveLoc+'\'+S+' '+name+'.png');
    exportgraphics(gca,saveName)
    cname = convertCharsToStrings(name);
    nameLoc = [cname,locs(numel(locs))];
    tpsData = [tpsData;nameLoc];
    writetable(array2table(tpsData),fullDataFile);
close
end

```

B.6 Measurement of deformation as a measure of fluidity

```

close
clear
clc
D = uigetdir('E:\','Choose an image location');
S = dir(fullfile(D,'*.tif'));
SavePath = uigetdir('E:\','Choose a save location');
pathName = char(SavePath);
saveDataFile = "intersections.xlsx";
fullDataFile = fullfile(pathName, saveDataFile);
allAngles = ["Temperature" "Image Number" "Channel" "Circle 1" "C1 radius" "Circle 2" "C2 radius" "Angle" "Intersection area"];

for k = 1:numel(S)
% Define image
    fFname = fullfile(D,S(k).name);
    OGFile = imread(fFname);
        [fF_path,fileName,fFext] = fileparts(fFname);
    stringName = fileName(19:end-20);
    imgNum = fileName(end-2);

    [red,green,blue] = imsplit(OGFile);
% Get resolution information
    info = imfinfo(fFname);
    res = info.XResolution;
% Find circles in shell channel
    blurr = imgaussfilt(red,3);
    imshow(blurr)
    [centers, radii, ~] = imfindcircles(blurr, [30 100], 'Sensitivity', 0.800, 'EdgeThreshold', 0.200, 'Method', 'PhaseCode', 'ObjectPolarity', 'Bright');
    hold on
    g = viscircles(centers, radii, 'EnhanceVisibility', false, 'Color', 'R', 'LineWidth', 1);

% For each pair of detected circles, complete the following
    for a = 1:numel(radii)-1
        for b = 2:numel(radii)

% Find intersects
            [xout,yout] = circcirc(centers(a,1), centers(a,2), radii(a), centers(b,1), centers(b,2), radii(b));
```

```
% If intersection exists, define points of the intersection
                if xout > 0
                    x10 = xout(1) - centers(a,1);
                    y10 = yout(1) - centers(a,2);
                    x20 = xout(2) - centers(a,1);
                    y20 = yout(2) - centers(a,2);
% Find intersect angle
                    ang = rad2deg(atan2(abs(x10*y20-x20*y10),
                     ↪  x10*y10+x20*y20));
                    if ang < 20
                        continue
                    end
                    color = rand(1,3);
% Draw intersect points
                    plot(xout(1),yout(1), 'b.', 'LineWidth', 2,
                     ↪  'MarkerSize', 15);
                    plot(xout(2),yout(2), 'b.', 'LineWidth', 2,
                     ↪  'MarkerSize', 15);
% Draw intersect angle
                    plot([centers(a,1) xout(1)],[centers(a,2)
                     ↪  yout(1)], 'color', color, 'LineWidth',1);
                    plot([centers(a,1) xout(2)],[centers(a,2)
                     ↪  yout(2)], 'color', color, 'LineWidth',1)
                    plot(centers(a,1),centers(a,2), 'k.',
                     ↪  'LineWidth', 2, 'MarkerSize', 25);
% Colour intersect area
                    c1 = nsidedpoly(1000, 'Center',
                     ↪  [centers(a),centers(a,2)], 'Radius',
                     ↪  radii(a));
                    c2 = nsidedpoly(1000, 'Center',
                     ↪  [centers(b),centers(b,2)], 'Radius',
                     ↪  radii(b));
                    h = plot(c1);
                    i = intersect(c1,c2);
                    h.Shape = i;
                    intArea = (area(i))./res^2;
% Add intersect data to list
                    namedAngle = [stringName imgNum "Red" a
                     ↪  radii(a)./res b radii(b)./res ang
                     ↪  intsecDistance intArea];
                    allAngles = [allAngles;namedAngle];
                    writetable(array2table(allAngles),fullDataFile
                     ↪  );
                end
```

```
        end
% Label circles
        for c = 1:length(radii)
            c_list = num2str(c);
            text(centers(c,1),centers(c,2),c_list,'color','r',
            'FontWeight','bold','HorizontalAlignment',
            'center', 'VerticalAlignment', 'middle');
        end
    end
% Output
    f = getframe;
    fFnameExt = fullfile(SavePath,[fileName,'_red angles',fFext]);
    %save circles image
    imwrite(f.cdata, fFnameExt, 'Resolution', res, 'Description',
    sprintf('ImageJ=1.53q\nunit=um\n'));
    figure
    G = montage({blurr,f.cdata},"BorderSize",2,"BackgroundColor","
    w");
    title(fileName(5:end-2));
    F = getframe;
    mFnameExt = fullfile(SavePath,[fileName,'_red angles
    montage',fFext]); %save circles image
    imwrite(F.cdata, mFnameExt);
    close
end
close
```

B.7 Simulation and detection of shells in MATLAB

```
clc
close all
clear

savePath = "C:\Users\karun\OneDrive\Desktop\test\test";
imageOutputFile = ["Sample","Radius","Shell Width"];
parameterDataFile = fullfile(savePath, "sample_parameters.xlsx");
theta=0:0.1:2*pi;
Rad = 10*rand(1,1) + 15; %Create a list of 200 different radii

% Define parameters of circles
```

```
for i=1:numel(Rad)
    saveName ="circle " + i + ".png";
    r = Rad(i);
    e = (0.3)*(rand(1,1)) + 0.1; %Vary shell thickness
    numPoints = rand(1,1)*15000; %Vary background density

% Draw shell
    xcord= r*cos(theta);
    ycord= r*sin(theta);
    figure
    hold on
    n = round(800+(4*r^2)+100*sqrt(e)); %number of points scales
    ↪  with shell thickness to maintain density
    t = 2*pi*rand(n,1);
    gl = 0.7*r+e*r*rand(n,1);
    xshell = gl.*cos(t);
    yshell = gl.*sin(t);
    d = sqrt((xshell.^2) + (yshell.^2));
    plot(xshell, yshell, '*', 'Color', "#BEBEC0", 'MarkerSize', 3)
    axis equal;

% Random noise in the core
% Randomly generate the number of points to exist in the core
    in = round((700.*rand(1,1) + 2000));
    t = 2*pi*rand(in,1);
    rr = mean(gl)*sqrt(rand(in,1));
    x = rr.*cos(t);
    y = rr.*sin(t);
    plot(x,y, '*','Color',"#BEBEC0", 'MarkerSize', 1)

%Random noise in the background
    xlim([-35 35])
    ylim([-35 35])
    for z = 1:numPoints
        xp(z) = (2*35)*(rand(1)-.5);
    end
    for zz = 1:numPoints
        yp(zz) = (2*35)*(rand(1)-.5);
    end
    hold on;
    plot(xp, yp, '.','Color',"#BEBEC0", 'MarkerSize', 1);

% Export the image
    ax = gca;
```

```
    set(gca,'color',"#3A3A3C")
    set(gca,'YTickLabel',[])
    set(gca,'XTickLabel',[])
    exportgraphics(ax,fullfile(savePath,saveName));

% Export the defined parameters
    shellThickness = (max(gl) - min(gl));
    output = [saveName,max(gl),shellThickness];
    imageOutputFile = [imageOutputFile;output];
    writetable(array2table(imageOutputFile),parameterDataFile);
    close
end

% Analyse the simulated image
S = dir(fullfile(savePath,'*.png'));
measuresOutputFile = ["Sample","LOESS Radius","Gaussian
↪  Radius","Median Radius","LOESS Shell Width","Gaussian Shell
↪  Width","Median Shell Width"];
fullDataFile = fullfile(savePath, "measurements.xlsx");

for kk = 1:numel(S)
    fFname = fullfile(savePath,S(kk).name);
    stringName = convertCharsToStrings(S(kk).name(1:end-4));
    img = imread(fFname);

% Apply a Gaussian filter and make the image black and white
    G = rgb2gray(imnoise(imgaussfilt(img,3)));
    theta = linspace(0,300,6);
    profs=[];
%Rotate image and find pixel profiles
    for n = 1:numel(theta)
        rot = imrotate(G,theta(n));
        imshow(rot)
        ax=gca;
        midpoint = floor(mean(ax.XLim));
        p1 = improfile(rot,[midpoint-226,midpoint+226],[midpoint,m⌋
        ↪  idpoint]);
        p2 = improfile(rot,[midpoint,midpoint],[midpoint-226,midpo⌋
        ↪  int+226]);
        profs=[profs,p1,p2];
        close
    end
    meanprof=mean(profs,2);
    R = size(meanprof,1);
```

```
    xAxis = linspace(-29.2444,29.2444,R)';
    data = (meanprof)/(max(meanprof));

% Apply different smoothing algorithms
    f = smoothdata(data,"loess",(R*0.1));
        [~,flocs,fw,~] = findpeaks(f, xAxis, 'MinPeakHeight',
        ↪  0.65, 'MinPeakDistance', 10, 'MinPeakWidth', 2);
    g=smoothdata(data,"gaussian",(R*0.1));
        [~,glocs,gw,~] = findpeaks(g, xAxis, 'MinPeakHeight',
        ↪  0.65, 'MinPeakDistance', 10, 'MinPeakWidth', 2);
    m=smoothdata(data,"movmedian",(R*0.1));
        [~,mlocs,mw,~] = findpeaks(m, xAxis, 'MinPeakHeight',
        ↪  0.65, 'MinPeakDistance', 10, 'MinPeakWidth', 2);

% Calculate shell parameters
    fpeakW = mean(fw);
    mpeakW = mean(mw);
    gpeakW = mean(gw);
    fdiameter=0;
    if numel(flocs)==2
        fdiameter = (flocs(2)+(fw(2)/2))-(flocs(1)-(fw(1)/2));
    end
    fradius=fdiameter./2;
    mdiameter=0;
    if numel(mlocs)==2
        mdiameter = (mlocs(2)+(mw(2)/2))-(mlocs(1)-(mw(1)/2));
    end
    mradius=mdiameter./2;
    gdiameter=0;
    if numel(glocs)==2
        gdiameter = (glocs(2)+(gw(2)/2))-(glocs(1)-(gw(1)/2));
    end
    gradius=gdiameter./2;
% Export calculated values
    measuresOutput =
    ↪  [stringName,fradius,gradius,mradius,fpeakW,gpeakW,mpeakW];
    measuresOutputFile = [measuresOutputFile;measuresOutput];
    writetable(array2table(measuresOutputFile),fullDataFile);
    close
% Export profile images
    figure
    hold
    plot(xAxis,data,'color',"#9E9E9E")
    xlim([-30 30]);
```

```
    ylim([0.2 1.1]);
    xlabel('Distance')
    ylabel('Pixel intensity')
    findpeaks(m(1:R), xAxis, 'MinPeakHeight', 0.65,
    ↪ 'MinPeakWidth', 2, 'MinPeakDistance', 10, 'Annotate',
    ↪ 'extents');
    findpeaks(f(1:R), xAxis, 'MinPeakHeight', 0.65,
    ↪ 'MinPeakWidth', 2, 'MinPeakDistance', 10, 'Annotate',
    ↪ 'extents');
    findpeaks(g(1:R), xAxis, 'MinPeakHeight', 0.65,
    ↪ 'MinPeakWidth', 2, 'MinPeakDistance', 10, 'Annotate',
    ↪ 'extents');
    ax=gca;
    sig_h = findobj(ax, 'tag', 'Signal');
    sig_h(1).LineWidth = 1;
        sig_h(2).LineWidth = 1;
            sig_h(3).LineWidth = 1;
    sig_h(1).Color = 'r';
        sig_h(2).Color = 'k';
            sig_h(3).Color = 'b';
    width_h = findobj('Tag','HalfProminenceWidth');
    if numel(flocs)>0
        width_h(1).LineWidth = 1;
        width_h(1).Color = 'r';
    end
        if numel(glocs)>0
            width_h(2).LineWidth = 1;
            width_h(2).Color = 'k';
        end
            if numel(mlocs)>0
                width_h(3).Color = 'b';
                width_h(3).LineWidth = 1;
            end
    arrow_h = findobj('Tag','Peak');
    delete(arrow_h);
    height_h = findobj('Tag','Prominence');
    delete(height_h);
    legend('Detected','Moving
    ↪ Median','','LOESS','','Gaussian','','Location','northeast')
    ax = gca;
    exportgraphics(ax,fullfile(savePath,(stringName+" plot.png")));
    close
end
```

Appendix C

Additional images

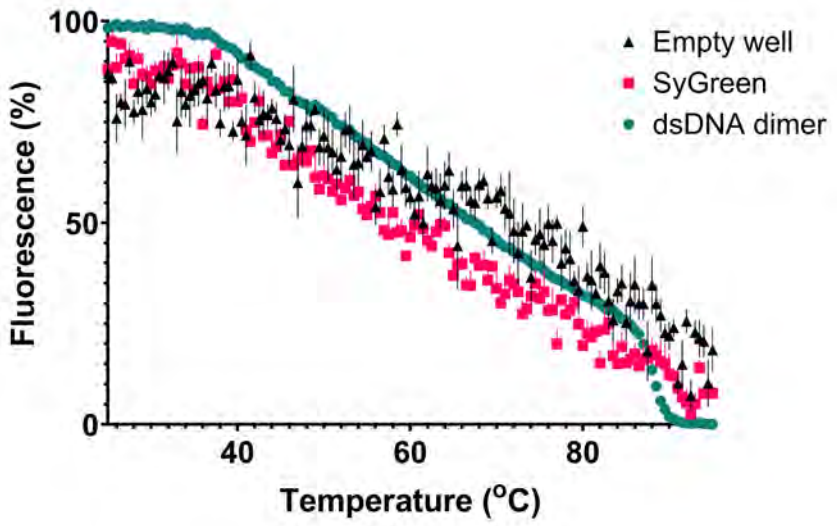

Figure C.1: When capturing fluorescence intensity in an empty sample chamber(black), the RotorGene Q thermocycler detects increasing baseline intensity with decreasing temperature. The same effect is seen when analysing a solution of SyGreen dye in 0.5 M NaCl, lacking any DNA, and in a solution containing linear dsDNA. This likely contributes to the general increasing trend in fluorescence intensity when performing HCA. Normalised fluorescence data shown as mean ± SD, n = 12. Figure relates to section 2.6.

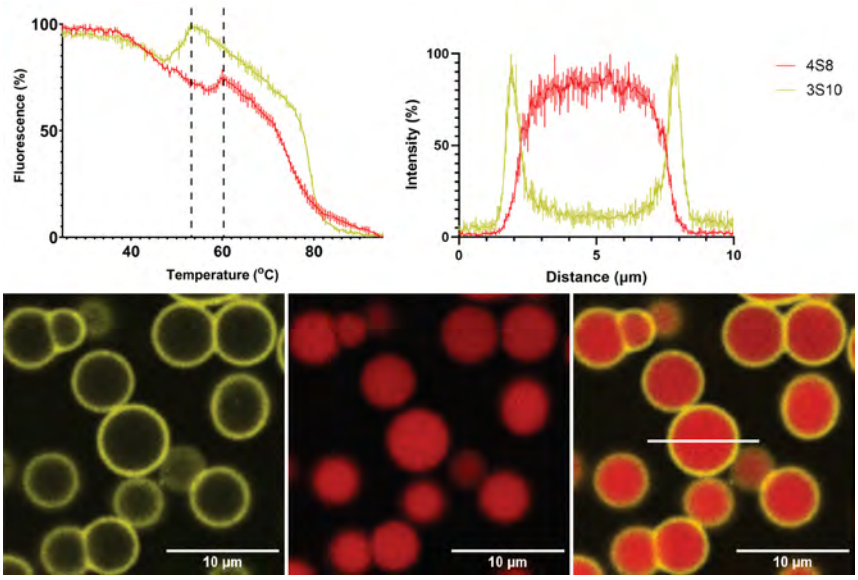

Figure C.2: Core-shell structure of 4S8 3S10 (16 %C 8-nt), with hybridisation curves and representative pixel profile. Average shell width 0.65 ± 0.07 μm. Scale bars 10 μm.

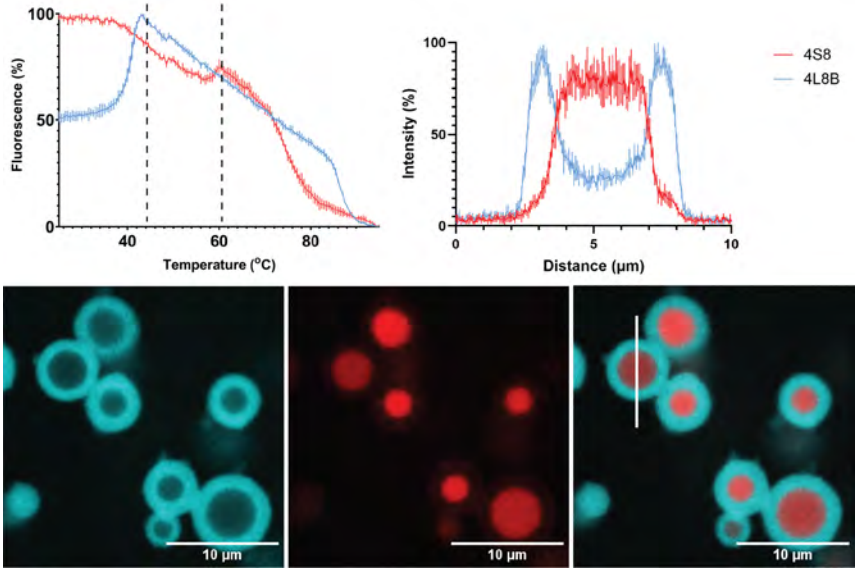

Figure C.3: Core-shell structure of 4S8 4L8B (25 %C 8-nt), with hybridisation curves and representative pixel profile. Average shell width 1.29 ± 0.16 μm. Scale bars 10 μm.

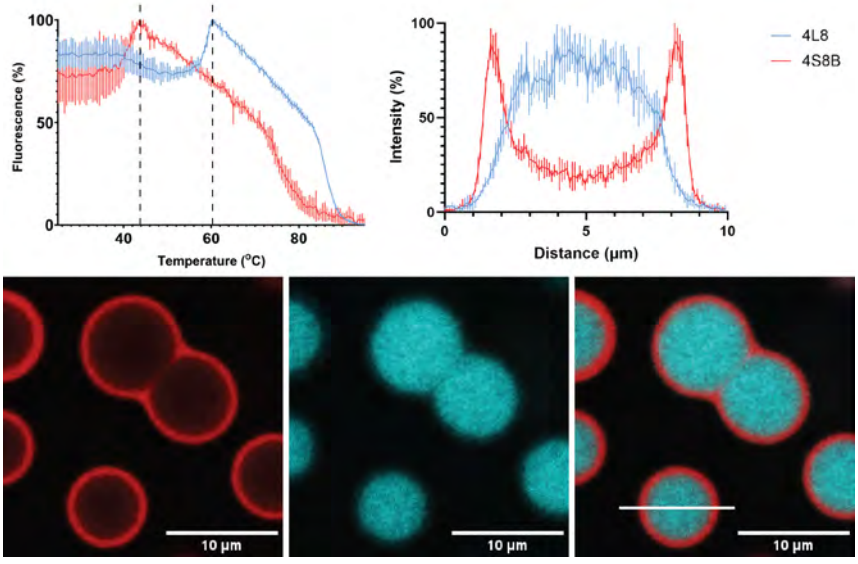

Figure C.4: Core-shell structure of 4L8 4S8B (25 %C 8-nt), with hybridisation curves and representative pixel profile. Average shell width 1.00 ± 0.11 μm. Scale bars 10 μm.

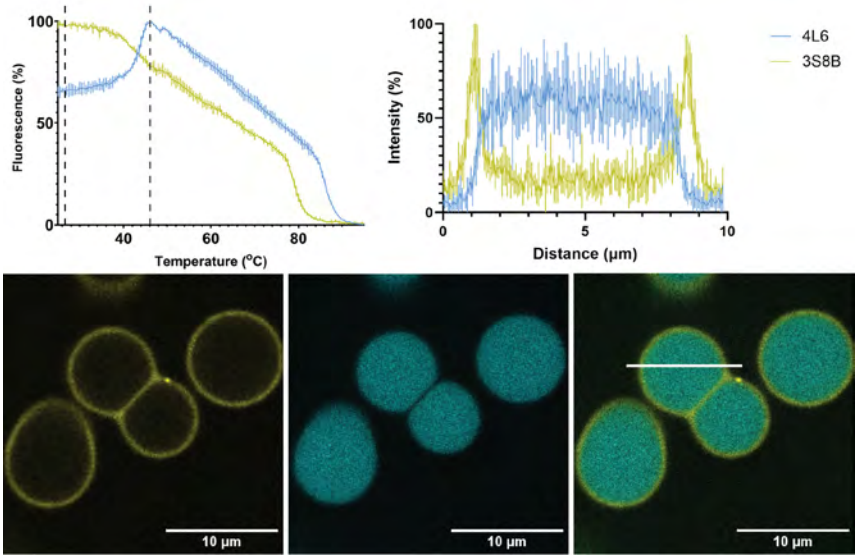

Figure C.5: Core-shell structure of 4L6 3S8B (16 %C 6-nt), with hybridisation curves and representative pixel profile. Average shell width 0.74 ± 0.11 μm. Scale bars 10 μm.

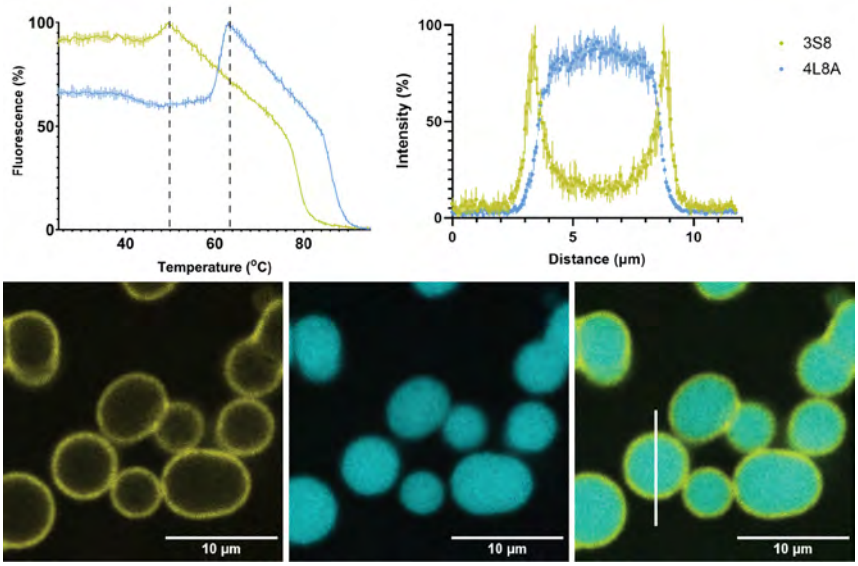

Figure C.6: Core-shell structure of 4L8A 3S8 (16 %C 8A-nt), with hybridisation curves and representative pixel profile. Average shell width 0.71 ± 0.06 μm. Scale bars 10 μm.

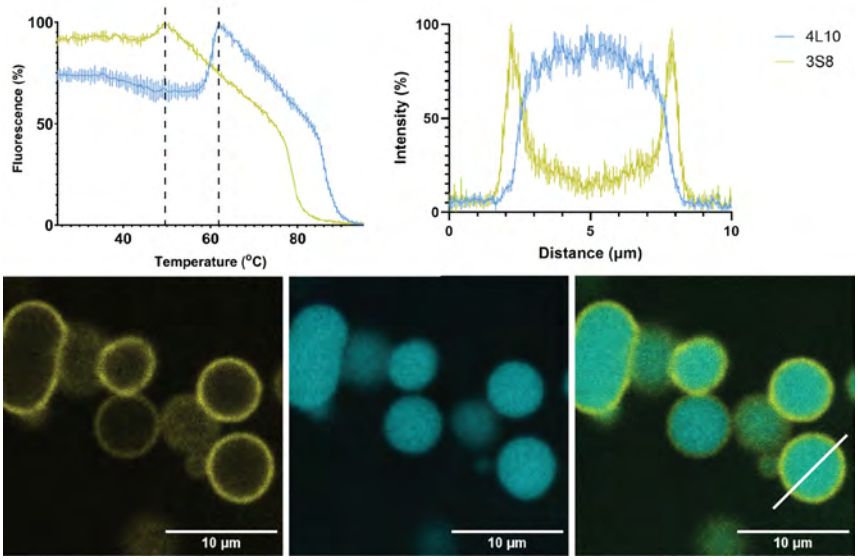

Figure C.7: Core-shell structure of 4L10 3S8 (16%C 10-nt), with hybridisation curves and representative pixel profile. Average shell width 0.70 ± 0.07 μm. Scale bars 10 μm.

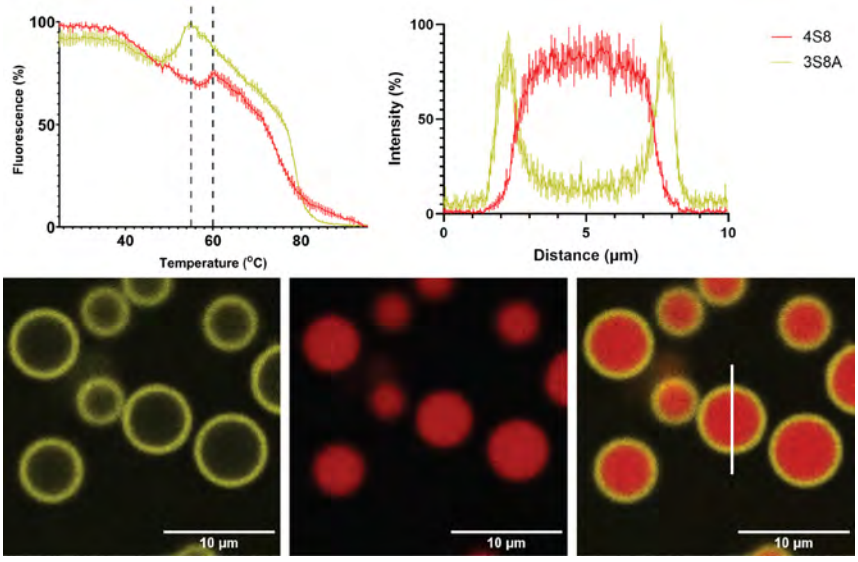

Figure C.8: Core-shell structure of 4S8 3S8A (16 %C 8-nt), with hybridisation curves and representative pixel profile. Average shell width 0.77 ± 0.06 μm. Scale bars 10 μm.

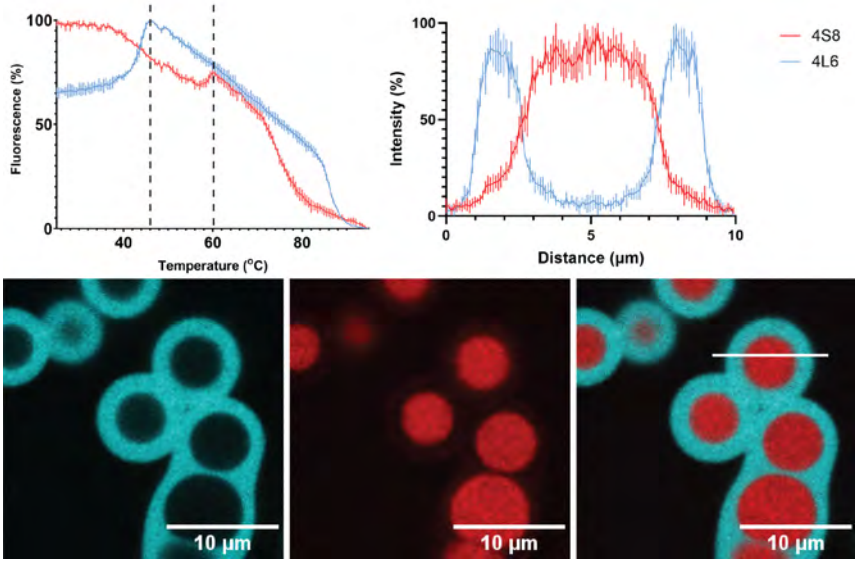

Figure C.9: Core-shell structure of 4S8 4L6 (25 %C 8-nt), with hybridisation curves and representative pixel profile. Average shell width 1.50 ± 0.25 μm. Scale bars 10 μm.

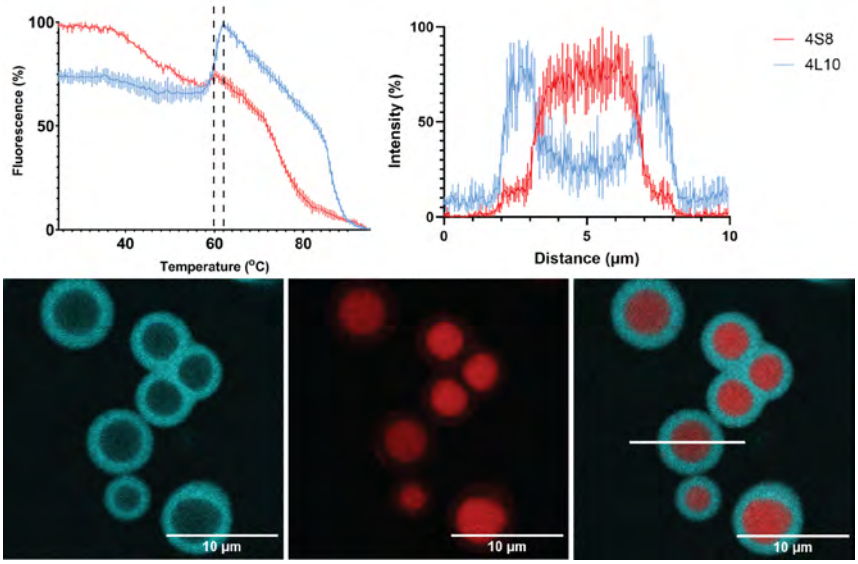

Figure C.10: Core-shell structure of 4S8 4L10 (25 %C 8-nt), with hybridisation curves and representative pixel profile. Average shell width 1.10 ± 0.13 μm. Scale bars 10 μm.

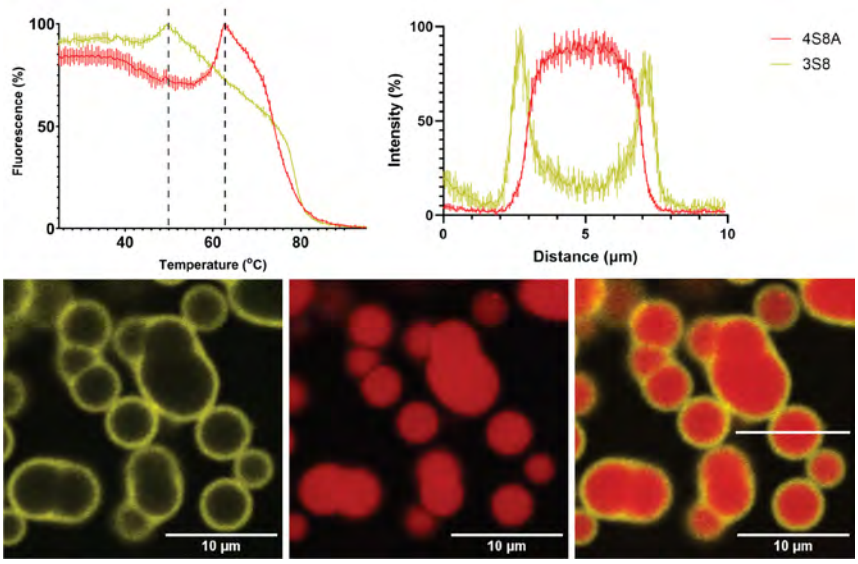

Figure C.11: Core-shell structure of 4S8A 3S8 (16 %C 8A-nt), with hybridisation curves and representative pixel profile. Average shell width 0.73 ± 0.05 μm. Scale bars 10 μm.

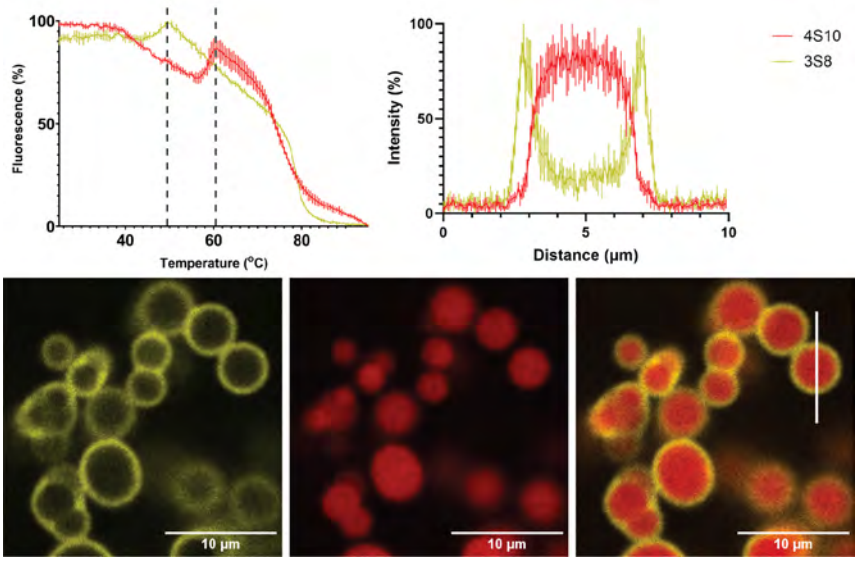

Figure C.12: Core-shell structure of 4S10 3S8 (16 %C 10-nt), with hybridisation curves and representative pixel profile. Average shell width 0.76 ± 0.08 μm. Scale bars 10 μm.

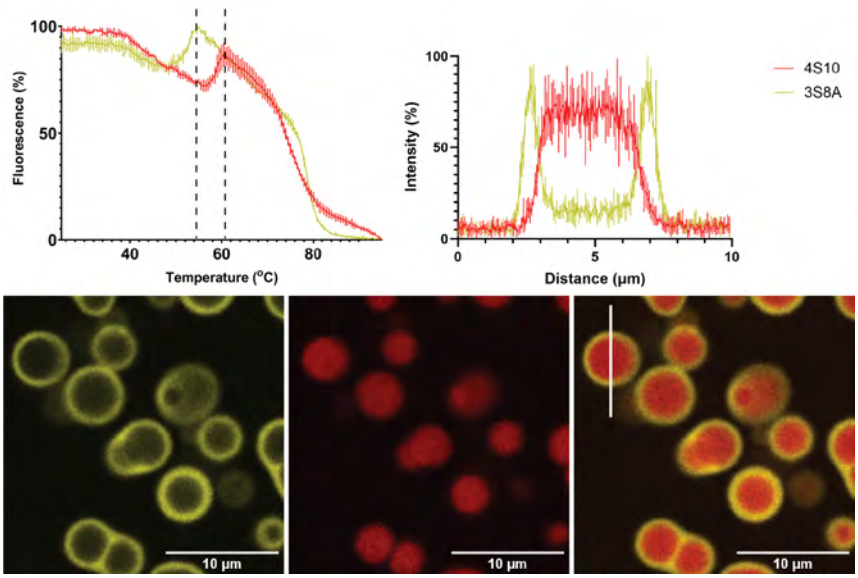

Figure C.13: Core-shell structure of 4S10 3S8A (16 %C 10-nt), with hybridisation curves and representative pixel profile. Average shell width 0.76 ± 0.09 μm. Scale bars 10 μm.

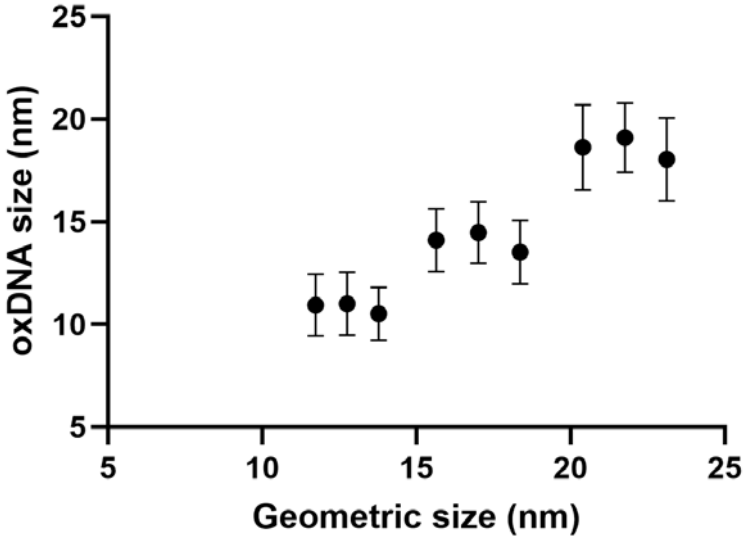

Figure C.14: Predicted nanostar sizes, comparing 2D geometric calculations to oxDNA computational simulations. The palindromic 10-nt sticky ends tended to form hairpin loops when simulated, reducing measured nanostar size. Data shown as mean $\pm$ SD, n = 40-171. Figure relates to section 3.5.4.

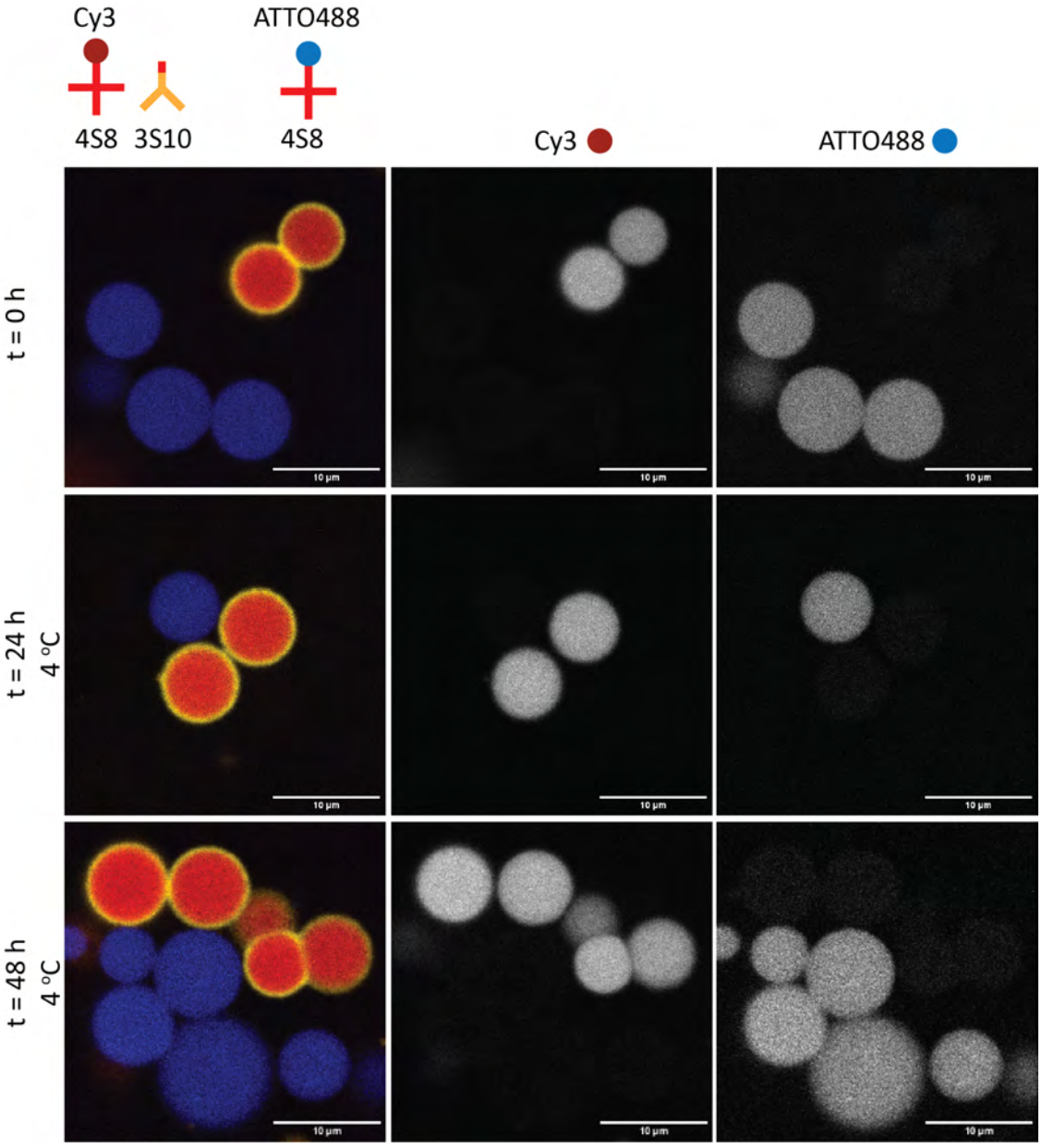

Figure C.15: Bare 4S8-ATTO488 droplets were combined with core-shell 4S8-Cy3 3S10-Cy5 droplets and incubated at 4 ^{o}C for 48 hours. No significant change in fluorophore localisation or droplet appearance is seen. Bare 4S8-ATTO488 droplets are coloured blue; core-shell 4S8-Cy3 3S10-Cy5 are coloured red and yellow, respectively. Scale bars 10 μm. Figure relates to section 3.8.1.

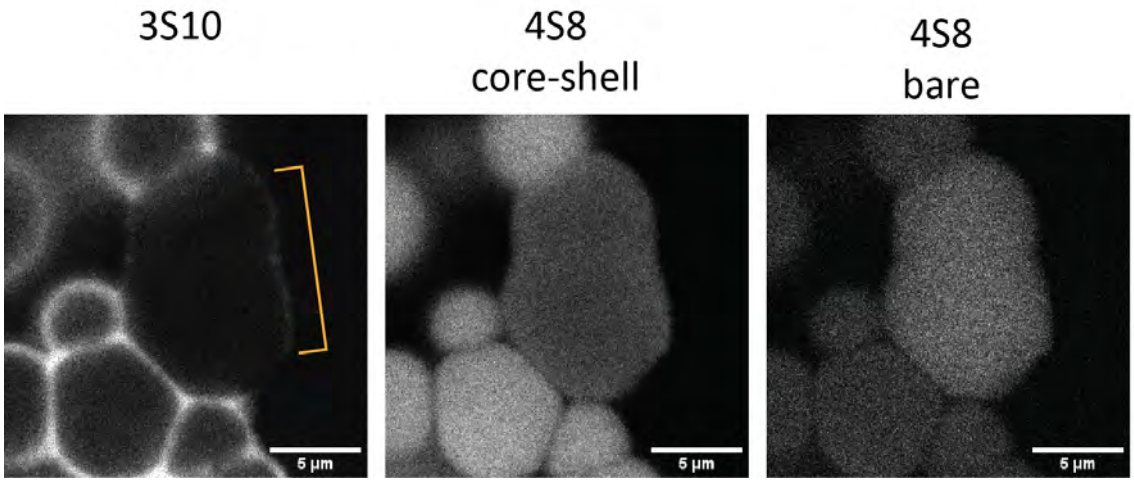

Figure C.16: Bare 4S8-ATTO488 droplets were combined with core-shell 4S8-Cy3 3S10-Cy5 droplets and incubated at 28 ^{o}C for 48 hours. Within 24 hours, a thin membrane of 3S10 nanostars could be seen on the surface of bare 4S8 droplets, indicating isothermal shell formation. However, this thin shell did not prevent the fusion of bare droplets into larger structures. Scale bar 5 μm. Figure relates to section 3.8.1.

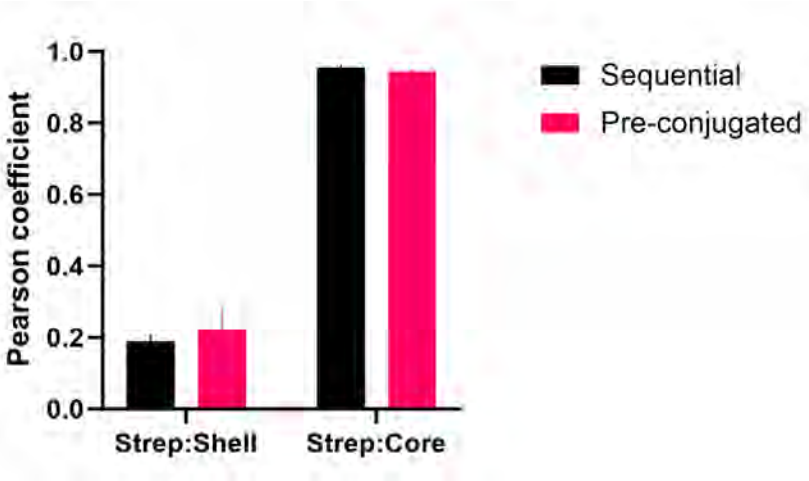

Figure C.17: i'-j'-SA localisation in i-4S8 core and 3S10 shell, comparing sequential and pre-conjugated addition. Streptavidin-shell co-localisation was low under both conditions, while streptavidin-core co-localisation was high. No significant change in localisation was seen between treatment methods. Data shown is Pearson correlation coefficient of binarised fluorophore channels. Shell localisation is determined by subtracting core channel from shell and streptavidin, and core localisation is determined by subtracting shell from core and streptavidin. Data shown as average ± SD, n = 4-8. Figure relates to section 4.3.4.

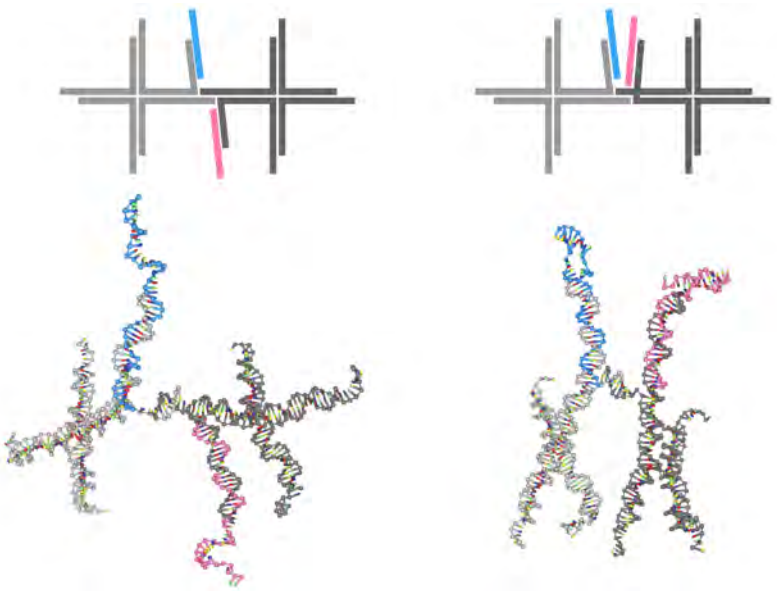

Figure C.18: A fluorophore nanostar dimer of a single configuration may produce vastly different distances between fluorophores, due to the flexibility of the nanostars. Figure relates to section 4.4.

Bibliography

(1) S. F. Banani, H. O. Lee, A. A. Hyman and M. K. Rosen, *Nature reviews. Molecular cell biology*, 2017, **18**, 285–298.

(2) G. M. Whitesides and M. Boncheva, *Proceedings of the National Academy of Sciences of the United States of America*, 2002, **99**, 4769.

(3) B. Alberts, A. Johnson, J. Lewis, M. Raff, K. Roberts and P. Walter, in *Molecular Biology of the Cell. 4th edition*, 2002.

(4) I. D. Kuntz, G. M. Crippen, P. A. Kollman and D. Kimelman, *Journal of Molecular Biology*, 1976, **106**, 983–994.

(5) E. W. Martin and T. Mittag, *Biochemistry*, 2018, **57**, 2478–2487.

(6) C.-C. Chang, C.-L. Pai, W.-C. Chen and S. A. Jenekhe, *Thin Solid Films*, 2005, **479**, 254–260.

(7) Y. Yao, L. Zhang, E. Orgiu and P. Samorì, *Advanced Materials*, 2019, **31**, 1900599.

(8) S. Wang, J. Liu, G. Feng, L. G. Ng and B. Liu, *Advanced Functional Materials*, 2019, **29**, 1808365.

(9) N. C. Seeman, *Current Opinion in Structural Biology*, 1996, **6**, 519–526.

(10) P. W. K. Rothemund, *Nature*, 2006, **440**, 297–302.

(11) J. Schnitzbauer, M. T. Strauss, T. Schlichthaerle, F. Schueder and R. Jungmann, *Nature Protocols*, 2017, **12**, 1198–1228.

(12) N. Qian and J. A. Weinstein, *bioRxiv*, 2023, 2023.08.11.553025.

(13) Y. Wang, I. Baars, I. Berzina, I. Rocamonde-Lago, B. Shen, Y. Yang, M. Lolaico, J. Waldvogel, I. Smyrlaki, K. Zhu, R. A. Harris and B. Högberg, *Nature Nanotechnology*, 2024, **19**, 1366–1374.

(14) A. Kuzyk, K. T. Laitinen and P. Törmä, *Nanotechnology*, 2009, **20**, 235305.

(15) S. H. Um, J. B. Lee, N. Park, S. Y. Kwon, C. C. Umbach and D. Luo, *Nature Materials*, 2006, **5**, 797–801.

(16) S. Biffi, R. Cerbino, F. Bomboi, E. M. Paraboschi, R. Asselta, F. Sciortino and T. Bellini, *Proceedings of the National Academy of Sciences*, 2013, **110**, 15633–15637.

(17) R. Merindol, S. Loescher, A. Samanta and A. Walther, *Nature Nanotechnology*, 2018, **13**, 730–738.

(18) J. Deng and A. Walther, *Chem*, 2020, **6**, 3329–3343.

(19) A. Leathers, M. Walczak, R. A. Brady, A. Al Samad, J. Kotar, M. J. Booth, P. Cicuta and L. Di Michele, *Journal of the American Chemical Society*, 2022, **144**, 17468–17476.

(20) T. S. Harmon, A. S. Holehouse, M. K. Rosen and R. V. Pappu, *eLife*, 2017, **6**, e30294.
(21) S. Alberti, A. Gladfelter and T. Mittag, *Cell*, 2019, **176**, 419–434.
(22) E. Kengmana, E. Ornelas-Gatdula, K.-L. Chen and R. Schulman, *Journal of the American Chemical Society*, 2024, **146**, 32942–32952.
(23) J. Bucci, L. Malouf, D. A. Tanase, N. Farag, J. R. Lamb, R. Rubio-Sánchez, S. Gentile, E. Del Grosso, C. F. Kaminski, L. Di Michele and F. Ricci, *Journal of the American Chemical Society*, 2024, **146**, 31529–31537.
(24) Y. Sato, T. Sakamoto and M. Takinoue, *Science Advances*, 2020, **6**, eaba3471.
(25) B.-j. Jeon, D. T. Nguyen and O. A. Saleh, *The Journal of Physical Chemistry B*, 2020, **124**, 8888–8895.
(26) J. C. Blain and J. W. Szostak, *Annual Review of Biochemistry*, 2014, **83**, 615–640.
(27) S. Agarwal, D. Osmanovic, M. A. Klocke and E. Franco, *ACS Nano*, 2022, **16**, 11842–11851.
(28) N. Yamashita, Y. Sato, Y. Suzuki, D. Ishikawa and M. Takinoue, *ChemBioChem*, 2024, **25**, e202400468.
(29) K. Matsuura, T. Yamashita, Y. Igami and N. Kimizuka, *Chemical Communications*, 2003, 376–377.
(30) B.-j. Jeon, D. T. Nguyen, G. R. Abraham, N. Conrad, D. K. Fygenson and O. A. Saleh, *Soft Matter*, 2018, **14**, 7009–7015.
(31) H. Udono, J. Gong, Y. Sato and M. Takinoue, *Advanced Biology*, 2022, 2200180.
(32) K. Ley, C. Laudanna, M. I. Cybulsky and S. Nourshargh, *Nature Reviews Immunology*, 2007, **7**, 678–689.
(33) Z. Fan and K. Ley, *Biorheology*, 2015, **52**, 353–377.
(34) S. Hanna and A. Etzioni, *Annals of the New York Academy of Sciences*, 2012, **1250**, 50–55.
(35) R. P. McEver and C. Zhu, *Annual Review of Cell and Developmental Biology*, 2010, **26**, 363–396.
(36) B. Alberts, A. Johnson, J. Lewis, M. Raff, K. Roberts and P. Walter, in *Molecular Biology of the Cell. 4th edition*, 2002.
(37) R. F. Bargatze, S. Kurk, E. C. Butcher and M. A. Jutila, *The Journal of Experimental Medicine*, 1994, **180**, 1785–1792.
(38) E. J. Kunkel, J. E. Chomas and K. Ley, *Circulation Research*, 1998, **82**, 30–38.
(39) C. A. Hutchison, S. N. Peterson, S. R. Gill, R. T. Cline, O. White, C. M. Fraser, H. O. Smith and J. C. Venter, *Science*, 1999, **286**, 2165–2169.
(40) B. C. Buddingh' and J. C. M. van Hest, *Accounts of Chemical Research*, 2017, **50**, PMID: 28094501, 769–777.
(41) A. B. Cook, S. Novosedlik and J. C. M. van Hest, *Accounts of Materials Research*, 2023, **4**, 287–298.
(42) N. A. Yewdall, A. F. Mason and J. C. M. van Hest, *Interface Focus*, 2018, **8**, 20180023.

(43) M. Michel, M. Winterhalter, L. Darbois, J. Hemmerle, J. C. Voegel, P. Schaaf and V. Ball, *Langmuir*, 2004, **20**, 6127–6133.
(44) P.-Y. Bolinger, D. Stamou and H. Vogel, *Journal of the American Chemical Society*, 2004, **126**, 8594–8595.
(45) J. W. Hindley, Y. Elani, C. M. McGilvery, S. Ali, C. L. Bevan, R. V. Law and O. Ces, *Nature Communications*, 2018, **9**, 1093.
(46) Y. Elani, R. V. Law and O. Ces, *Nature Communications*, 2014, **5**, 5305.
(47) Q. Xu, Z. Zhang, P. P. Y. Lui, L. Lu, X. Li and X. Zhang, *Materials Today Bio*, 2023, **23**, 100877.
(48) W. Mu, L. Jia, M. Zhou, J. Wu, Y. Lin, S. Mann and Y. Qiao, *Nature Chemistry*, 2024, **16**, 158–167.
(49) S. E. Diltemiz, M. Tavafoghi PhD, N. Roberto de Barros, M. Kanada, J. Heinamaki, C. Contag, S. Seidlits and N. Ashammakhi, *Materials chemistry frontiers*, 2021, **5**, 6672–6692.
(50) A. Schroeder, D. A. Heller, M. M. Winslow, J. E. Dahlman, G. W. Pratt, R. Langer, T. Jacks and D. G. Anderson, *Nature Reviews Cancer*, 2012, **12**, 39–50.
(51) C. Yang, L. Kong and Z. Zhang, *Nano Today*, 2022, **44**, 101481.
(52) J. W. Szostak, D. P. Bartel and P. L. Luisi, *Nature*, 2001, **409**, 387–390.
(53) D. Fayolle, M. Fiore, P. Stano and P. Strazewski, *PLOS ONE*, 2018, **13**, e0192975.
(54) S. Pautot, B. J. Frisken and D. A. Weitz, *Langmuir*, 2003, **19**, 2870–2879.
(55) N.-N. Deng, M. Yelleswarapu and W. T. S. Huck, *Journal of the American Chemical Society*, 2016, **138**, 7584–7591.
(56) S. Deshpande and C. Dekker, *Nature Protocols*, 2018, **13**, 856–874.
(57) H. Nsairat, D. Khater, U. Sayed, F. Odeh, A. Al Bawab and W. Alshaer, *Heliyon*, 2022, **8**, e09394.
(58) M. Dymek and E. Sikora, *Advances in Colloid and Interface Science*, 2022, **309**, 102757.
(59) M. Osawa, D. E. Anderson and H. P. Erickson, *Science*, 2008, **320**, 792–794.
(60) M. Osawa and H. P. Erickson, *Proceedings of the National Academy of Sciences*, 2013, **110**, 11000–11004.
(61) W. M. J. Aumiller, F. Pir Cakmak, B. W. Davis and C. D. Keating, *Langmuir*, 2016, **32**, 10042–10053.
(62) T. Ivanov, T. P. Doan-Nguyen, M. A. Belahouane, Z. Dai, S. Cao, K. Landfester and L. Caire da Silva, *Macromolecular Rapid Communications*, 2024, **45**, 2400626.
(63) S. Koga, D. S. Williams, A. W. Perriman and S. Mann, *Nature Chemistry*, 2011, **3**, 720–724.
(64) Z. Izri and V. Noireaux, *Small*, 2025, **21**, 2403243.
(65) G. M. Whitesides and M. Boncheva, *Proceedings of the National Academy of Sciences of the United States of America*, 2002, **99**, 4769–4774.
(66) B. A. Grzybowski, C. E. Wilmer, J. Kim, K. P. Browne and K. J. M. Bishop, *Soft Matter*, 2009, **5**, 1110–1128.
(67) J. Liu, J. Tang, Z. Tong, G. Teng and D. Yang, *iScience*, 2023, **26**, 106620.

(68) R. Yi, Y. Mao, Y. Shen and L. Chen, *Journal of the American Chemical Society*, 2021, **143**, 12897–12912.
(69) M. Li, M. Liu, F. Qi, F. R. Lin and A. K.-Y. Jen, *Chemical Reviews*, 2024, **124**, 2138–2204.
(70) W. H. Carothers, *Chemical Reviews*, 1931, **8**, 353–426.
(71) P. J. Flory, *The Journal of Chemical Physics*, 1942, **10**, 51–61.
(72) K. Binder, *The Journal of Chemical Physics*, 1983, **79**, 6387–6409.
(73) A. Keller and S. Z. D. Cheng, *Polymer*, 1998, **39**, 4461–4487.
(74) Z. Xu, W. Wang, Y. Cao and B. Xue, *Supramolecular Materials*, 2023, **2**, 100049.
(75) K. G. Soga, J. R. Melrose and R. C. Ball, *The Journal of Chemical Physics*, 1999, **110**, 2280–2288.
(76) S. Brocca, R. Grandori, S. Longhi and V. Uversky, *International Journal of Molecular Sciences*, 2020, **21**, 9045.
(77) J. W. Cahn and J. E. Hilliard, *The Journal of Chemical Physics*, 1959, **31**, 688–699.
(78) M. Naz, L. Zhang, C. Chen, S. Yang, H. Dou, S. Mann and J. Li, *Communications Chemistry*, 2024, **7**, 1–14.
(79) W. Ostwald, *Zeitschrift für Physikalische Chemie*, 1897, **22U**, 289–330.
(80) L. Ratke and P. W. Voorhees, *Growth and Coarsening*, Berlin, Heidelberg, 2002.
(81) A. A. Hyman, C. A. Weber and F. Jülicher, *Annual Review of Cell and Developmental Biology*, 2014, **30**, 39–58.
(82) B. Wang, L. Zhang, T. Dai, Z. Qin, H. Lu, L. Zhang and F. Zhou, *Signal Transduction and Targeted Therapy*, 2021, **6**, 290.
(83) F. Burki, *Cold Spring Harbor Perspectives in Biology*, 2014, **6**, a016147.
(84) F.-M. Boisvert, S. van Koningsbruggen, J. Navascués and A. I. Lamond, *Nature Reviews. Molecular Cell Biology*, 2007, **8**, 574–585.
(85) J. R. Buchan and R. Parker, *Molecular Cell*, 2009, **36**, 932–941.
(86) C. P. Brangwynne, C. R. Eckmann, D. S. Courson, A. Rybarska, C. Hoege, J. Gharakhani, F. Jülicher and A. A. Hyman, *Science*, 2009, **324**, 1729–1732.
(87) G. Wright and J.-B. Sibarita.
(88) S. Z. D. Cheng, in *Phase Transitions in Polymers*, ed. S. Z. D. Cheng, Amsterdam, 2008, pp. 17–59.
(89) W. M. Babinchak and W. K. Surewicz, *Journal of molecular biology*, 2020, **432**, 1910–1925.
(90) P. Li, S. Banjade, H.-C. Cheng, S. Kim, B. Chen, L. Guo, M. Llaguno, J. V. Hollingsworth, D. S. King, S. F. Banani, P. S. Russo, Q.-X. Jiang, B. T. Nixon and M. K. Rosen, *Nature*, 2012, **483**, 336–340.
(91) Y. Lin and X. Fang, *Journal of Genetics and Genomics*, 2021, **48**, 872–880.
(92) V. Nandana and J. M. Schrader, *Current Opinion in Microbiology*, 2021, **61**, 91–98.
(93) W. Ma, G. Zhen, W. Xie and C. Mayr, *eLife*, 2021, **10**, ed. R. H. Singer and J. L. Manley, Publisher: eLife Sciences Publications, Ltd, e64252.

(94) T. Sheth, S. Seshadri, T. Prileszky and M. E. Helgeson, *Nature Reviews Materials*, 2020, **5**, 214–228.
(95) N. A. Yewdall, A. A. M. André, T. Lu and E. Spruijt, *Current Opinion in Colloid & Interface Science*, 2021, **52**, 101416.
(96) G. A. Mountain and C. D. Keating, *Biomacromolecules*, 2020, **21**, 630–640.
(97) T. Lu and E. Spruijt, *Journal of the American Chemical Society*, 2020, **142**, 2905–2914.
(98) R. Dahm, *Developmental Biology*, 2005, **278**, 274–288.
(99) A. D. Hershey and M. Chase, *The Journal of General Physiology*, 1952, **36**, 39–56.
(100) R. E. Franklin and R. G. Gosling, *Nature*, 1953, **171**, 740–741.
(101) J. D. Watson and F. H. C. Crick, *Nature*, 1953, **171**, 737–738.
(102) B. Alberts, A. Johnson, J. Lewis, M. Raff, K. Roberts and P. Walter, in *Molecular Biology of the Cell. 4th edition*, 2002.
(103) J. Poater, M. Swart, F. M. Bickelhaupt and C. F. Guerra, *Organic & Biomolecular Chemistry*, 2014, **12**, 4691–4700.
(104) L. Marky and K. Breslauer, *Biopolymers*, 1982, **21**, 2185–2194.
(105) P. Yakovchuk, E. Protozanova and M. D. Frank-Kamenetskii, *Nucleic Acids Research*, 2006, **34**, 564–574.
(106) G. Khandelwal and J. Bhyravabhotla, *PLoS ONE*, 2010, **5**, e12433.
(107) M. Zacharias, *The Journal of Physical Chemistry B*, 2020, **124**, 10345–10352.
(108) Q. Chi, G. Wang and J. Jiang, *Physica A: Statistical Mechanics and its Applications*, 2013, **392**, 1072–1079.
(109) G. S. Manning, *Biophysical Journal*, 2006, **91**, 3607–3616.
(110) P. Gross, N. Laurens, L. B. Oddershede, U. Bockelmann, E. J. G. Peterman and G. J. L. Wuite, *Nature Physics*, 2011, **7**, 731–736.
(111) K. L. Agarwal, H. Büchi, M. H. Caruthers, N. Gupta, H. G. Khorana, K. Kleppe, A. Kumar, E. Ohtsuka, U. L. Rajbhandary, J. H. Van de Sande, V. Sgaramella, H. Weber and T. Yamada, *Nature*, 1970, **227**, 27–34.
(112) K. Itakura, T. Hirose, R. Crea, A. D. Riggs, H. L. Heyneker, F. Bolivar and H. W. Boyer, *Science (New York, N.Y.)*, 1977, **198**, 1056–1063.
(113) S. L. Beaucage and M. H. Caruthers, *Tetrahedron Letters*, 1981, **22**, 1859–1862.
(114) R. L. Letsinger and W. B. Lunsford, *Journal of the American Chemical Society*, 1976, **98**, 3655–3661.
(115) D. A. Lashkari, S. P. Hunicke-Smith, R. M. Norgren, R. W. Davis and T. Brennan, *Proceedings of the National Academy of Sciences*, 1995, **92**, 7912–7915.
(116) L. E. Sindelar and J. M. Jaklevic, *Nucleic Acids Research*, 1995, **23**, 982–987.
(117) X. Gao, E. LeProust, H. Zhang, O. Srivannavit, E. Gulari, P. Yu, C. Nishiguchi, Q. Xiang and X. Zhou, *Nucleic Acids Research*, 2001, **29**, 4744–4750.
(118) S. Roy and M. Caruthers, *Molecules (Basel, Switzerland)*, 2013, **18**, 14268–14284.
(119) R. A. Hughes and A. D. Ellington, *Cold Spring Harbor Perspectives in Biology*, 2017, **9**, a023812.

(120) R. Holliday, *Genetics Research*, 1964, **5**, 282–304.
(121) N. C. Seeman, *Journal of Theoretical Biology*, 1982, **99**, 237–247.
(122) P. J. Paukstelis, J. Nowakowski, J. J. Birktoft and N. C. Seeman, *Chemistry & Biology*, 2004, **11**, 1119–1126.
(123) J. Zheng, J. J. Birktoft, Y. Chen, T. Wang, R. Sha, P. E. Constantinou, S. L. Ginell, C. Mao and N. C. Seeman, *Nature*, 2009, **461**, 74–77.
(124) R. A. Brady, N. J. Brooks, P. Cicuta and L. Di Michele, *Nano Letters*, 2017, **17**, 3276–3281.
(125) W. Wang, S. Chen, B. An, K. Huang, T. Bai, M. Xu, G. Bellot, Y. Ke, Y. Xiang and B. Wei, *Nature Communications*, 2019, **10**, 1067.
(126) X. Wang, H. Jun and M. Bathe, *Journal of the American Chemical Society*, 2022, **144**, 4403–4409.
(127) R. P. Goodman, R. M. Berry and A. J. Turberfield, *Chemical Communications*, 2004, 1372–1373.
(128) W. M. Shih, J. D. Quispe and G. F. Joyce, *Nature*, 2004, **427**, 618–621.
(129) G. Tikhomirov, P. Petersen and L. Qian, *Nature*, 2017, **552**, 67–71.
(130) J. F. Berengut, C. K. Wong, J. C. Berengut, J. P. K. Doye, T. E. Ouldridge and L. K. Lee, *ACS nano*, 2020, **14**, 17428–17441.
(131) M. T. Luu, J. F. Berengut, J. Li, J.-B. Chen, J. K. Daljit Singh, K. Coffi Dit Glieze, M. Turner, K. Skipper, S. Meppat, H. Fowler, W. Close, J. P. K. Doye, A. Abbas and S. F. J. Wickham, *Science Robotics*, 2024, **9**, eadp2309.
(132) J. Marmur and P. Doty, *Journal of Molecular Biology*, 1962, **5**, 109–118.
(133) E. Protozanova, P. Yakovchuk and M. D. Frank-Kamenetskii, *Journal of Molecular Biology*, 2004, **342**, 775–785.
(134) A. Vologodskii and M. D. Frank-Kamenetskii, *Physics of Life Reviews*, 2018, **25**, 1–21.
(135) J. SantaLucia, *Proceedings of the National Academy of Sciences of the United States of America*, 1998, **95**, 1460–1465.
(136) O. Gotoh and Y. Tagashira, *Biopolymers*, 1981, **20**, 1033–1042.
(137) S. M. Freier, R. Kierzek, J. A. Jaeger, N. Sugimoto, M. H. Caruthers, T. Neilson and D. H. Turner, *Proceedings of the National Academy of Sciences*, 1986, **83**, 9373–9377.
(138) P. Vaitiekunas, C. Crane-Robinson and P. L. Privalov, *Nucleic Acids Research*, 2015, **43**, 8577–8589.
(139) M. E. Fornace, J. Huang, C. T. Newman, N. J. Porubsky, M. B. Pierce and N. A. Pierce, *NUPACK: Analysis and Design of Nucleic Acid Structures, Devices, and Systems*, en, 2022.
(140) B. R. Wolfe, N. J. Porubsky, J. N. Zadeh, R. M. Dirks and N. A. Pierce, *Journal of the American Chemical Society*, 2017, **139**, 3134–3144.
(141) R. B. Sekar and A. Periasamy, *The Journal of Cell Biology*, 2003, **160**, 629–633.
(142) A. Hillisch, M. Lorenz and S. Diekmann, *Current Opinion in Structural Biology*, 2001, **11**, 201–207.
(143) S. S. Vogel, B. W. van der Meer and P. S. Blank, *Methods (San Diego, Calif.)*, 2014, **66**, 131–138.

(144) J. L. Self, A. J. Zervoudakis, X. Peng, W. R. Lenart, C. W. Macosko and C. J. Ellison, *JACS Au*, 2022, **2**, 310–321.
(145) W. Liu, A. Samanta, J. Deng, C. O. Akintayo and A. Walther, *Angewandte Chemie International Edition*, 2022, **61**.
(146) D. T. Nguyen and O. A. Saleh, *Soft Matter*, 2017, **13**, 5421–5427.
(147) O. A. Saleh, B.-j. Jeon and T. Liedl, *Proceedings of the National Academy of Sciences*, 2020, **117**, 16160–16166.
(148) N. Conrad, G. Chang, D. K. Fygenson and O. A. Saleh, *The Journal of Chemical Physics*, 2022, **157**, 234203.
(149) S. Do, C. Lee, T. Lee, D.-N. Kim and Y. Shin, *Science Advances*, 2022, **8**, eabj1771.
(150) M. P. Tran, R. Chatterjee, Y. Dreher, J. Fichtler, K. Jahnke, L. Hilbert, V. Zaburdaev and K. Göpfrich, *Small*, 2023, **19**, 2202711.
(151) M. Walczak, R. A. Brady, L. Mancini, C. Contini, R. Rubio-Sánchez, W. T. Kaufhold, P. Cicuta and L. Di Michele, *Nature Communications*, 2021, **12**, 4743.
(152) J. M. Stewart, S. Li, A. A. Tang, M. A. Klocke, M. V. Gobry, G. Fabrini, L. Di Michele, P. W. K. Rothemund and E. Franco, *Nature Communications*, 2024, **15**, 6244.
(153) G. Fabrini, N. Farag, S. P. Nuccio, S. Li, J. M. Stewart, A. A. Tang, R. McCoy, R. M. Owens, P. W. K. Rothemund, E. Franco, M. Di Antonio and L. Di Michele, *Nature Nanotechnology*, 2024, **19**, 1665–1673.
(154) D. R. Duckett, A. I. H. Murchie, S. Diekmann, E. von Kitzing, B. Kemper and D. M. J. Lilley, *Cell*, 1988, **55**, 79–89.
(155) R. M. Clegg, A. I. Murchie and D. M. Lilley, *Biophysical Journal*, 1994, **66**, 99–109.
(156) A. R. Mount, C. P. Mountford, S. A. G. Evans, T. .-. Su, A. H. Buck, P. Dickinson, C. J. Campbell, L. M. Keane, J. G. Terry, J. S. Beattie, A. J. Walton, P. Ghazal and J. Crain, *Biophysical Chemistry*, 2006, **124**, 214–221.
(157) Y. Li, Y. D. Tseng, S. Y. Kwon, L. d'Espaux, J. S. Bunch, P. L. McEuen and D. Luo, *Nature Materials*, 2004, **3**, 38–42.
(158) K. Matsuura, K. Masumoto, Y. Igami, T. Fujioka and N. Kimizuka, *Biomacromolecules*, 2007, **8**, 2726–2732.
(159) L. Rovigatti, F. Smallenburg, F. Romano and F. Sciortino, *ACS Nano*, 2014, **8**, 3567–3574.
(160) D. T. Nguyen, B.-j. Jeon, G. R. Abraham and O. A. Saleh, *Langmuir*, 2019, **35**, 14849–14854.
(161) S. Okumura, B. N. Hapsianto, N. Lobato-Dauzier, Y. Ohno, S. Benner, Y. Torii, Y. Tanabe, K. Takada, A. Baccouche, M. Shinohara, S. H. Kim, T. Fujii and A. Genot, *Nanomaterials*, 2021, **11**, 293.
(162) Y. A. G. Fosado, *Soft Matter*, 2023, **19**, 4820–4828.
(163) L. Di Michele, B. M. Mognetti, T. Yanagishima, P. Varilly, Z. Ruff, D. Frenkel and E. Eiser, *Journal of the American Chemical Society*, 2014, **136**, 6538–6541.

(164) D. Gao, S. Wilken, A. B. N. Nguyen, G. R. Abraham, T. Liedl and O. A. Saleh, *Soft Matter*, 2024, **20**, 1275–1281.
(165) Y. Sato and M. Takinoue, *Nanoscale Advances*, 2023, **5**, 1919–1925.
(166) S. M. Douglas, H. Dietz, T. Liedl, B. Högberg, F. Graf and W. M. Shih, *Nature*, 2009, **459**, 414–418.
(167) M. Endo, K. Hidaka, T. Kato, K. Namba and H. Sugiyama, *Journal of the American Chemical Society*, 2009, **131**, 15570–15571.
(168) T. G. Martin and H. Dietz, *Nature Communications*, 2012, **3**, 1103.
(169) N. F. Dupuis, E. D. Holmstrom and D. J. Nesbitt, *Biophysical Journal*, 2013, **105**, 756–766.
(170) L. Rovigatti, F. Bomboi and F. Sciortino, *The Journal of Chemical Physics*, 2014, **140**, 154903.
(171) F. Bomboi, S. Biffi, R. Cerbino, T. Bellini, F. Bordi and F. Sciortino, *The European Physical Journal E*, 2015, **38**, 64.
(172) Z. Xing, A. Caciagli, T. Cao, I. Stoev, M. Zupkauskas, T. O'Neill, T. Wenzel, R. Lamboll, D. Liu and E. Eiser, *Proceedings of the National Academy of Sciences of the United States of America*, 2018, **115**, 8137–8142.
(173) J. Gong, N. Tsumura, Y. Sato and M. Takinoue, *Advanced Functional Materials*, 2022, **32**, 2202322.
(174) N. Conrad, T. Kennedy, D. K. Fygenson and O. A. Saleh, *Proceedings of the National Academy of Sciences*, 2019, **116**, 7238–7243.
(175) T. Lee, S. Do, J. G. Lee, D.-N. Kim and Y. Shin, *Nanoscale*, 2021, **13**, 17638–17647.
(176) J. N. Zadeh, C. D. Steenberg, J. S. Bois, B. R. Wolfe, M. B. Pierce, A. R. Khan, R. M. Dirks and N. A. Pierce, *Journal of Computational Chemistry*, 2011, **32**, 170–173.
(177) G. Chakraborty, K. Balinin, G. Portale, M. Loznik, E. Polushkin, T. Weil and A. Herrmann, *Chemical Science*, 2019, **10**, 10097–10105.
(178) E. Roth, A. Glick Azaria, O. Girshevitz, A. Bitler and Y. Garini, *Nano Letters*, 2018, **18**, 6703–6709.
(179) J. Yu, T. Ha and K. Schulten, *Nucleic Acids Research*, 2004, **32**, 6683–6695.
(180) E. Poppleton, M. Matthies, D. Mandal, F. Romano, P. Sulc and L. Rovigatti, *Journal of Open Source Software*, 2023, **8**.
(181) W. K. Spoelstra, E. O. van der Sluis, M. Dogterom and L. Reese, *Langmuir*, 2020, **36**, 1956–1964.
(182) W.-H. Jung, E. Chen, R. Veneziano, S. Gaitanaros and Y. Chen, *Nucleic Acids Research*, 2020, **48**, 12407–12414.
(183) A. Santamaria, S. Hutin, C. M. Doucet, C. Zubieta, P.-E. Milhiet and L. Costa, *Biophysical Journal*, 2024, **123**, 3366–3374.
(184) E. Locatelli, P. H. Handle, C. N. Likos, F. Sciortino and L. Rovigatti, *ACS Nano*, 2017, **11**, 2094–2102.
(185) O. A. Saleh, S. Wilken, T. M. Squires and T. Liedl, *Nature Communications*, 2023, **14**, 3574.
(186) V. Linko and A. Keller, *Small*, 2023, **19**, _eprint: https://onlinelibrary.wiley.com/doi/pdf/10.1
2301935.

(187) A. Bednarz, S. M. Sønderskov, M. Dong and V. Birkedal, *Nanoscale*, 2023, **15**, Publisher: The Royal Society of Chemistry, 1317–1326.
(188) X. Shen, B. Gu, S. A. Che and F. S. Zhang, *The Journal of Chemical Physics*, 2011, **135**, 034509.
(189) H. Zipper, H. Brunner, J. Bernhagen and F. Vitzthum, *Nucleic Acids Research*, 2004, **32**, e103.
(190) V. N. Morozov and V. A. Kuzmin, *High Energy Chemistry*, 2019, **53**, 167–169.
(191) C. Cuniberti and M. Guenza, *Biophysical Chemistry*, 1990, **38**, 11–22.
(192) C. Y. G. Lemetter, F. M. Meeuse and N. J. Zuidam, *AIChE Journal*, 2009, **55**, 1487–1496.
(193) L. Malouf, D. A. Tanase, G. Fabrini, R. A. Brady, M. Paez-Perez, A. Leathers, M. J. Booth and L. Di Michele, *Chem*, 2023, **9**, 3347–3364.
(194) Y. Ji and Y. Qiao, *Communications Chemistry*, 2024, **7**, 1–6.
(195) A. W. Folkmann, A. Putnam, C. F. Lee and G. Seydoux, *Science*, 2021, **373**, 1218–1224.
(196) H. J. Motulsky and R. E. Brown, *BMC Bioinformatics*, 2006, **7**, 123.
(197) K. Lam and E. Tajkhorshid, *Biophysical Journal*, 2020, **119**, 24–34.
(198) Z. Zhang, D. Yomo and C. Gradinaru, *Biochimica et Biophysica Acta (BBA) - Biomembranes*, 2017, **1859**, 1242–1253.
(199) N. Gao, C. Xu, Z. Yin, M. Li and S. Mann, *Journal of the American Chemical Society*, 2022, **144**, 3855–3862.
(200) C. R. Pye, W. M. Hewitt, J. Schwochert, T. D. Haddad, C. E. Townsend, L. Etienne, Y. Lao, C. Limberakis, A. Furukawa, A. M. Mathiowetz, D. A. Price, S. Liras and R. S. Lokey, *Journal of Medicinal Chemistry*, 2017, **60**, 1665–1672.
(201) G. M. Cooper, in *The Cell: A Molecular Approach. 2nd edition*, 2000.
(202) S. Krishnan, D. Ziegler, V. Arnaut, T. G. Martin, K. Kapsner, K. Henneberg, A. R. Bausch, H. Dietz and F. C. Simmel, *Nature Communications*, 2016, **7**, 12787.
(203) S. Groeer, M. Garni, A. Samanta and A. Walther, *ChemSystemsChem*, 2022, **4**, _eprint: https://onlinelibrary.wiley.com/doi/pdf/10.1002/syst.202200009, e202200009.
(204) B. Amsden, *Polymer*, 2002, **43**, 1623–1630.
(205) C. E. Chivers, A. L. Koner, E. D. Lowe and M. Howarth, *Biochemical Journal*, 2011, **435**, 55–63.
(206) F. Liu, J. Z. H. Zhang and Y. Mei, *Scientific Reports*, 2016, **6**, 27190.
(207) C. Chen, J. Wen, Z. Wen, S. Song and X. Shi, *Frontiers in Genetics*, 2023, **14**, DOI: 10.3389/fgene.2023.1120791.
(208) M. A. Jingjing, *Scientific Reports*, 2023, **13**, 15210.
(209) L. Fu, E. N. Weiskopf, O. Akkermans, N. A. Swanson, S. Cheng, T. U. Schwartz and D. Görlich, *Nature*, 2024, **626**, 843–851.
(210) C. F. Dickson, S. Hertel, A. J. Tuckwell, N. Li, J. Ruan, S. C. Al-Izzi, N. Ariotti, E. Sierecki, Y. Gambin, R. G. Morris, G. J. Towers, T. Böcking and D. A. Jacques, *Nature*, 2024, **626**, 836–842.

(211) S. Buckhout-White, C. M. Spillmann, W. R. Algar, A. Khachatrian, J. S. Melinger, E. R. Goldman, M. G. Ancona and I. L. Medintz, *Nature Communications*, 2014, **5**, 5615.
(212) K. Jahnke, H. Grubmüller, M. Igaev and K. Göpfrich, *Nucleic Acids Research*, 2021, **49**, 4186–4195.
(213) T. M. Squires and T. G. Mason, *Annual Review of Fluid Mechanics*, 2010, **42**, 413–438.
(214) Y. Mao, P. Nielsen and J. Ali, *Frontiers in Bioengineering and Biotechnology*, 2022, **10**, 916354.
(215) D. Y. Zhang and E. Winfree, *Journal of the American Chemical Society*, 2009, **131**, 17303–17314.
(216) T. Goh, L. Gao, J. Singh, R. Totaro, R. Carey, K. Yang, B. Cartwright, M. Dennis, L. A. Ju and A. Waterhouse, *Advanced Science (Weinheim, Baden-Wurttemberg, Germany)*, 2024, **11**, e2401524.
(217) K. Coffi Dit Gleize, C. T. H. Tran, A. Waterhouse, M. M. M. Bilek and S. F. J. Wickham, *Langmuir*, 2023, **39**, 343–356.
(218) S. W. Schaffter and R. Schulman, *Nature Chemistry*, 2019, **11**, 829–838.
(219) P. Arenas-Guerrero, Á. V. Delgado, K. J. Donovan, K. Scott, T. Bellini, F. Mantegazza and M. L. Jiménez, *Scientific Reports*, 2018, **8**, 9502.
(220) E. G. Wheatley, S. N. Pieniazek, I. Mukerji and D. L. Beveridge, *Biophysical Journal*, 2012, **102**, 552–560.
(221) J. Illingworth and J. Kittler, *IEEE Transactions on Pattern Analysis and Machine Intelligence*, 1987, **PAMI-9**, 690–698.
(222) M. A. Klocke, *Condensate Detection*, 2021.
(223) B. Smith, *Local Hough Circle*, 2021.
(224) J. Kwon, M. S. Elgawish and S.-H. Shim, *Advanced Science*, 2022, **9**, 2101817.
(225) I. Alshareedah, T. Kaur and P. R. Banerjee, *Methods in enzymology*, 2021, **646**, 143–183.
(226) J. Unruh, *Create Spectrum JRU v1*, 2010.
(227) R. Galindo-Murillo and T. E. Cheatham, *Nucleic Acids Research*, 2021, **49**, 3735–3747.
(228) P. J. Kolbeck, W. Vanderlinden, G. Gemmecker, C. Gebhardt, M. Lehmann, A. Lak, T. Nicolaus, T. Cordes and J. Lipfert, *Nucleic Acids Research*, 2021, **49**, 5143–5158.
(229) S. Giglio, P. T. Monis and C. P. Saint, *Nucleic Acids Research*, 2003, **31**, e136.
(230) P. R. Langer, A. A. Waldrop and D. C. Ward, *Proceedings of the National Academy of Sciences of the United States of America*, 1981, **78**, 6633–6637.
(231) R. Roy, S. Hohng and T. Ha, *Nature methods*, 2008, **5**, 507–516.